Quantum and Dielectric Confinement Effects in Lower-Dimensional Hybrid Perovskite Semiconductors

Claudine Katan, Nicolas Mercier, Jacky Even

Quantum and dielectric Confinement Effects in Lower-Dimensional Hybrid Perovskite Semiconductors

Claudine Katan,[*1] Nicolas Mercier,[2] and Jacky Even[*3]

[1] Univ Rennes, ENSCR, INSA Rennes, CNRS, ISCR (Institut des Sciences Chimiques de Rennes) - UMR 6226, F-35000 Rennes, France

[2] MOLTECH ANJOU, UMR-CNRS 6200, Université d'Angers, 2 Bd Lavoisier, 49045 Angers, France.

[3] Univ Rennes, INSA Rennes, CNRS, Institut FOTON - UMR 6082, F-35000 Rennes, France

Corresponding Author

* Claudine Katan. E-mail: claudine.katan@univ-rennes1.fr

* Jacky Even. E-mail: jacky.even@insa-rennes.fr

ABSTRACT

Hybrid halide perovskites are now superstar materials leading the field of low-cost thin film photovoltaics technologies. Following the surge for more efficient and stable 3D bulk alloys, multilayered halide perovskites and colloidal perovskite nanostructures appeared in 2016 as viable alternative solutions to this challenge, largely exceeding the original proof of concept made in 2009 and 2014, respectively. This triggered renewed interest in lower-dimensional hybrid halide perovskites and at the same time increasingly more numerous and differentiated applications. The present paper is a review of the past and present literature on both colloidal nanostructures and multilayered compounds, emphasizing that availability of accurate structural information is of dramatic importance to reach fair understanding of quantum and dielectric confinement effects. Layered halide perovskites occupy a special place in the history of halide perovskites, with a large number of seminal papers in the 1980s and 1990s. In recent years, the rationalization of structure-properties relationship has greatly benefited from new theoretical approaches dedicated to their electronic structures and optoelectronic properties, as well as a growing number of contributions based on modern experimental techniques. This is a necessary step to provide in-depth tools to decipher their extensive chemical engineering possibilities which surpasses the ones of their 3D bulk counterparts. Comparisons to classical semiconductor nanostructures and 2D van der Waals heterostructures are also stressed. Since 2015, colloidal nanostructures undergo a quick development for applications based on light emission. Although intensively studied in the last two years by various spectroscopy techniques, the description of quantum and dielectric confinement effects on their optoelectronic properties is still in its infancy.

CONTENTS

1. INTRODUCTION

3D hybrid halide perovskites, or ABX$_3$ compounds where A is a small organic (*e.g.* methylammonium MA$^+$, formamidinium FA$^+$) or an inorganic cation (*e.g.* Cs$^+$, Rb$^+$), B a metal Pb^{2+}, Sn^{2+}, Ge^{2+} and X a halogen I$^-$, Br$^-$, Cl$^-$, are now superstar materials for photovoltaic applications and have attracted worldwide efforts from the scientific community since mid-2012. These materials have opened a route towards low-cost manufacture of solar cells while offering currently certified conversion efficiencies of more than 23% at the level of the best known thin film technologies like CIGS (a copper indium gallium selenide material alloy), CdTe or Si and not far from monocrystalline silicon (25%).[1–7] Halide perovskite solar cell technologies use various three-dimensional (3D) alloys in mesoporous and planar architectures either with n-i-p or p-i-n junctions.[8–11] Solar cells with multiple junctions and 2 or 4 terminals, use also a 3D perovskite alloy associated with another perovskite material, CIGS but mostly silicon as a low band gap absorber.[12–17]

Recently, layered halide perovskites[18–20] and colloidal perovskite quantum dots (QD)[21,22] have also revealed great potential for solar cells, although further progresses must be achieved to reach efficiencies on par with their bulk 3D counterparts. Very recently, halide perovskites also demonstrated attractive photo and electroluminescence either as bulk materials or colloidal nanostructures, leading to optically pumped laser devices, with potential for display technology or exhibiting attractive photo-detection capabilities. However, before industrialization of devices based on halide perovskites, a number of serious technological locks have still to be solved, *e.g.* related to photo-stability, degradation under ambient conditions, the potential toxicity of lead and upscaling of device size.[5]
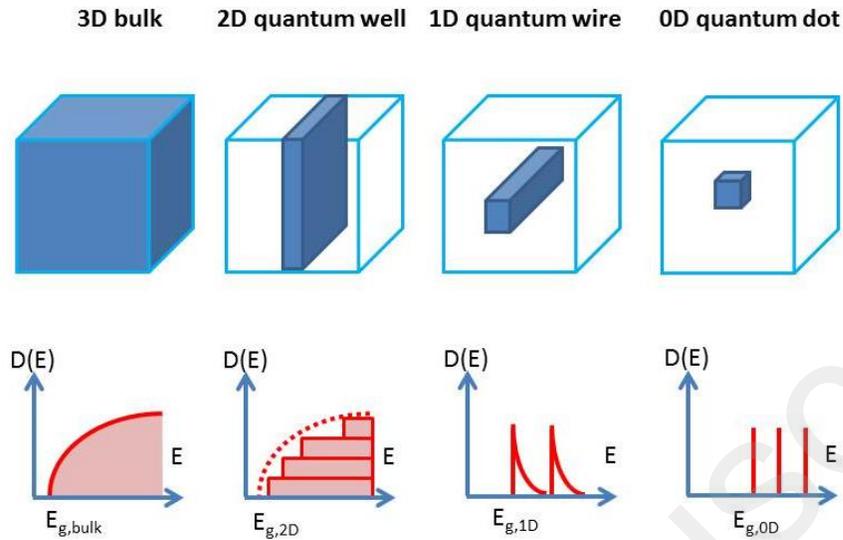
Figure 1. Schematic representation of a three-dimensional (3D) bulk semiconductor and the related two-dimensional (2D), one-dimensional (1D) and zero-dimensional (0D) quantum nanostructures. The joint density of states D(E) between the conduction band (CB) and the valence band (VB) is represented as a function of the energy, assuming infinite confinement potentials and an effective mass model for both the CB and the VB. The quantum confinement also results in an increase of the electronic band gaps when compared to the bulk material. The 3D density of states (DOS) can be reconstructed by merging 2D DOS related to electronic subbands both in the CB and VB.

Prior to the perovskite fever, especially in the 1980s and 1990s, most experimental efforts on halide perovskites were focused on chemistry, structural and optical characterizations of layered halide perovskites. Chemical engineering of the organic part led to an extensive exploration of the possible structural organizations and optical properties of these hybrid compounds.[23–25] Given the diversity of structural networks attainable with metal halides, we stress here that the minimum structural condition needed to be grouped under the terms "perovskite network or perovskite sub-network" is to maintain some component of

6

corner-sharing metal halide octahedra. Quantum and dielectric confinement effects were identified very early as a relevant factor underlying the unusual optoelectronic properties of monolayered and multilayered perovskites, among which the room temperature emission from excitonic resonances provides one notable example.[26–29] The concept of quantum confinement is widely used for heterostructures and nanostructures made of classical semiconductors, especially quantum wells (QW). For epitaxially grown classical semiconductor nanostructures, the dimensionality and size of the nanostructure have direct consequences on the electronic band gap and joint Density Of States (DOS) close to the band gap (Figure 1).

A schematic QW picture was introduced for layered perovskites yielding a simple and efficient framework to perform analogies with classical semiconductor heterostructures.[26,29,30] Progress on the understanding of their electronic structures[31–33] was strongly connected to detailed experimental investigations of their excitonic properties. Moreover, D. Mitzi and coworkers obtained important conceptual advances, developing a technological approach for tin-based layered halide perovskites leading to the demonstration of transistor devices and to impressive anisotropic carrier transport properties.[34–37] Researchers from Greece,[29,38,39,33,23,40–45] and Japan,[26,46,27,31,47–52,32,53–58] were the other most important contributors to the field at its early stage. The vast majority of the studies on low dimension halide perovskite structures were initially dedicated to monolayered systems such as A'_2BX_4 compounds (where A' is typically an extended non-conjugated primary ammonium cation, $R-NH_3^+$). These systems correspond to n = 1, where n is the number of vertically and periodically ordered perovskite octahedra sheets sandwiched between organic barriers. Monolayered compounds offer extended chemical engineering possibilities by

7

comparison with 3D halide perovskites. They also afford an ideal platform to investigate fundamental physical processes in a hybrid 2D system with self-organized vertical growth.[59–76]

Until very recently, experimental studies on pure multilayered halide perovskites (n>1) were scarce as a consequence of growth and purity issues and were basically limited to bilayered systems (n = 2).[28,31,29,52,32,61,77,18,78,19,79–88] Thanks to new synthetic routes,[80] phase-pure higher n-members have recently been obtained leading to breakthroughs reported in Nature[20] and Science.[89] These achievements are related to three major experimental advances demonstrated for $A'_2A_{n-1}B_nX_{3n+1}$ multilayered perovskites known as Ruddlesden-Popper phases:

- Synthetic control to achieve phase purity and new methodologies for thin film material growth with well-defined crystallographic structures and orientations;

- Major progress in photoconversion efficiency of layered halide perovskites for photovoltaics from about 4% to 15.4%, along with increased stability against illumination and moisture;

- Detailed investigations of localized versus delocalized and light induced electronic states in thin films and ultrathin exfoliated crystals.

Similar demonstrations are now expected for many other multilayered halide perovskites.

All the recent progresses on multilayered halide perovskites reveal that a change of paradigm is occurring at the moment in a similar manner as the one observed for 3D halide perovskites in the past few years.[90] The understanding of the optoelectronic properties of multilayered halide perovskites may indeed greatly benefit from concepts developed in the

realm of conventional semiconductors, based on solid-state physics,[64,65,67,90–94] and may open the route towards new applications. Such studies may provide guidance for new synthetic targets and open the route towards new applications as well as help answering a number of fundamental open questions. The possibilities offered by monolayered and multilayered perovskites for various applications are now intensively explored,[86,88,95–102,102–140] as well as various fundamental properties beyond the initial studies essentially based on structural, excitonic and carrier transport properties.[85,141–165]

Initial results on perovskite solar cells were obtained using hybrid halide perovskite QD[1,2], but these nanostructures were rapidly overshadowed by bulk thin films of 3D materials to enhance absorbance. Recently, colloidal perovskite QD clearly demonstrate potential for light emission and photovoltaic applications,[21,166] which led to the resurgence of interest in these nanostructures. Colloidal halide perovskites nanostructures indeed show great promises for applications,[167,168] and thus also deserve some attention as part of this review, even so quantum and dielectric confinements have been yet little explored by the scientific community in these new colloidal nano-objects. Beside colloidal QD, colloidal quantum wire (QWr), quantum rods (QR) and quantum nanoplatelets (QNPL) are also investigated. In this review, we choose the International System of Units (S.I.), unless explicitly stated otherwise, and use bold typeface for vector and tensor quantities in the present manuscript.

9

2. A CHEMICAL AND STRUCTURAL VIEWPOINT

Summary: Perovskites are defined by a framework of corner-sharing octahedra. The <100>, <110> and <111> layered perovskite series are obtained by cutting the 3D mother structure in planes perpendicular to the <100>, <110> and <111> directions. Most of the crystallographically characterized multilayered perovskites belong to the <100> series.

2.1. Perovskite networks

2.1.1. Introduction

The perovskite type structure ABX_3, which refers to the mineral $CaTiO_3$, can be described as a three-dimensional (3D) anionic network of corner-sharing BX_6 octahedra counter-balanced by cations (Ca^{2+} in $CaTiO_3$) filling the space defined by eight adjacent corner-sharing BX_6 octahedra. In the case of halide-based perovskites, X^- is a halide, B^{2+} is a divalent metal and A^+ an inorganic cation such as Cs^+, Rb^+ or an organic cation. In this last situation, the related compounds are called hybrid perovskites or organic-inorganic perovskites. While the archetype compound is $(CH_3NH_3)PbI_3$ ($CH_3NH_3^+$ = methylammonium, MA^+), a lot of other 3D hybrid perovskites ABX_3 are known where A^+ is MA^+ or the formamidinium (FA^+) organic cations, B^{2+} is Pb^{2+}, Sn^{2+}, Ge^{2+}, Cu^{2+}, Mn^{2+}, Cd^{2+}, Cr^{2+}, Zn^{2+}, etc.., and X^- is I^-, Br^- or Cl^-.[169,24] Moreover, a lot of derived compounds have been successfully prepared these recent years thanks to different substitutions on the A, B or X sites. Particularly, 3D perovskites based on mixed organic cation MA^+/FA^+ or even $MA^+/FA^+/Cs^+$ (triple cation approach), mixed metal cation (ex : Pb^{2+}/Sn^{2+}), and mixed halides (ex : I^-/Br^-) have been developped.[8–10] Finally, it is worth noting that in the search of lead-free materials, the strategy consisting of replacing 2 Pb^{2+} cations by one M'^+ and one M''^{3+} cations has led to 3D double perovskite $A_2M'M''X_6$ of Elpasolite type.[170] Nevertheless, if the 3D structural dimensionality is retained in these mixed metal hybrid

perovskites, the electronic dimensionality is lowered.[171] Most colloidal perovskite nanostructures share the same crystallographic structures as the corresponding 3D bulk perovskites. The cubic, tetragonal, and orthorhombic polymorphs are observed, but surface effects may adjust their relative stabilities.[167]

The lower-dimensional perovskites are characterized by a non-3D anionic inorganic framework of corner-sharing octahedra, meaning that these networks can be described from the mother ABX_3 structure by the dimensional reduction concept: adding a certain amount of AX per ABX_3 unit, a decondensation of the 3D network will occur leading to a lower-dimensional perovskite network.[172] For instance, the addition of one AX per ABX_3 unit leads to a A_2BX_4 compound based on a 2D corner-sharing octahedra network. Thus, a lot of different kinds of low-dimensional perovskite networks can be imagined, but with the exception of a few atypical cases, all known networks are mainly the <100>- and <110>-oriented layered perovskites, and to a less extent the <111>-oriented perovskites (Figure 2), and several 1-D networks which derive from the layered perovskites. The description of lower-dimensional perovskites in terms of <100>, <110> and <111> families had been reported by D. Mitzi as soon as in 1999,[24,173] and updated by the same author in 2016.[25] The different networks of each of these families can be obtained by cutting the ABX_3 mother structure in planes perpendicular to the <100>, <110> and <111> directions, every n, m or q layers leading to B_nX_{3n+1}, B_mX_{3m+2} and B_qX_{3q+3} anionic frameworks for the <100>-, <110>- and <111>-oriented families, respectively.

2.1.2. The <100>, <110> and <111> layered perovskite series

Another way to describe the <100>- and <110>-oriented low-dimensional perovskites (Figure 2) consists of removing neutral « $B^{(II)}X_2$ » units from the mother structure, or substituting $(B^{(II)}X)^+$ units by organic cations. This point of view can be very interesting to design and

11

prepare new hybrid perovskites. In the case of the <100>-oriented family, the removal of one BX_2 plane every n+1 layers leads to B_nX_{3n+1} $(B_{(n+1)}X_{3(n+1)} - BX_2)$ networks. For instance, the removal of one BX_2 plane every three layers $(A_3B_3X_9)$ leads to the $A_3B_2X_7$ bilayer perovskite. The general formula of such <100>-oriented hybrid perovskites are $(A')_2(A)_{n-1}B_nX_{3n+1}$ or $(A'')(A)_{n-1}B_nX_{3n+1}$. When the interlayer cations is a monocation (A'^+), typically a primary ammonium cation $R-NH_3^+$, a head-to-tail arrangement of organic cations in the interlayer space occurs, involving that two adjacent layers are staggered to each other, usually by (½ ½). When the interlayer is a dication (A''^{2+}), typically a primary diammonium cation $(NH_3-R-NH_3)^{2+}$, the staggered situation can also be encountered. However, dications favor the eclipsed situation of consecutive layers (Figure 2). Finally, when n > 2, the perovskite network can also be considered as resulting from the combination of (n-2) BX_3 inner layers, (as in the mother 3D structure) and two BX_4 outer layers, here also leading to the general formula of B_nX_{3n+1}. In the case of the <110>-oriented family, the substitution of $(BX)^+$ cationic units in the (110) planes by organic cations $(A'^+$ or ½ $A''^{2+})$ every m+1 layers leads to B_mX_{3m+2} $(B_{(m+1)}X_{3(m+1)} - BX)$ networks. For instance, the substitution of one $(BX)^+$ by one A^+ cation every three layers $(A_3B_3X_9)$ leads to the $A_4B_2X_8$ layered perovskite. Compounds belonging to this class of hybrid perovskites are quite rare, and only one series with m =1 to 4 has been described,[35] the general formula being $(A')_2(A)_mSn_mI_{3m+2}$ where A^+ and A'^+ are methylammonium and iodoformamidinium, respectively. The m = 2 member of this <110> family is the most common since a few have been described recently. The formula can be $(A')_2(A)_2B_2X_8$, as in the case of the iodostannate hybrid, $(A)_4B_2X_8$ (one example: A^+ = guanidinium; X= I^- ; M = Pb^{174} or Sn^{175}), or $(A'')_2B_2X_8$ perovskites (A'': dications, Figure 2). The m = 1 member of the <110> series, BX_5, is special since it is a 1-D network consisting of trans-connected BX_6 octahedra. This network has been

crystallized either with two kinds of cation, as in $(NH_2C(I)=NH_2)(NH_2CHNH_2)SnI_5$,[176] or by one kind of cation, as in $(CH_3SC(=NH_2)NH_2)_3PbI_5$.[43] The case of the <111>-oriented perovskites is particular because there is no known 2D networks based on divalent B(II) metal ions, but only with trivalent M(III) ions (M = Bi, Sb). Thus, the related materials $(CH_3NH_3)_3Bi_2Br_9$[177] or $(NH_4)_3Sb_2I_9$[178] based on $M^{(III)}_2X_9$ q= 2 <111> networks can be conceptually obtained by the substitution of 3 B^{2+} cations of the mother structure $(A_3B_3X_9)$ by two M^{3+} cations, the vacancies being ordered in (111) planes (Figure 2).
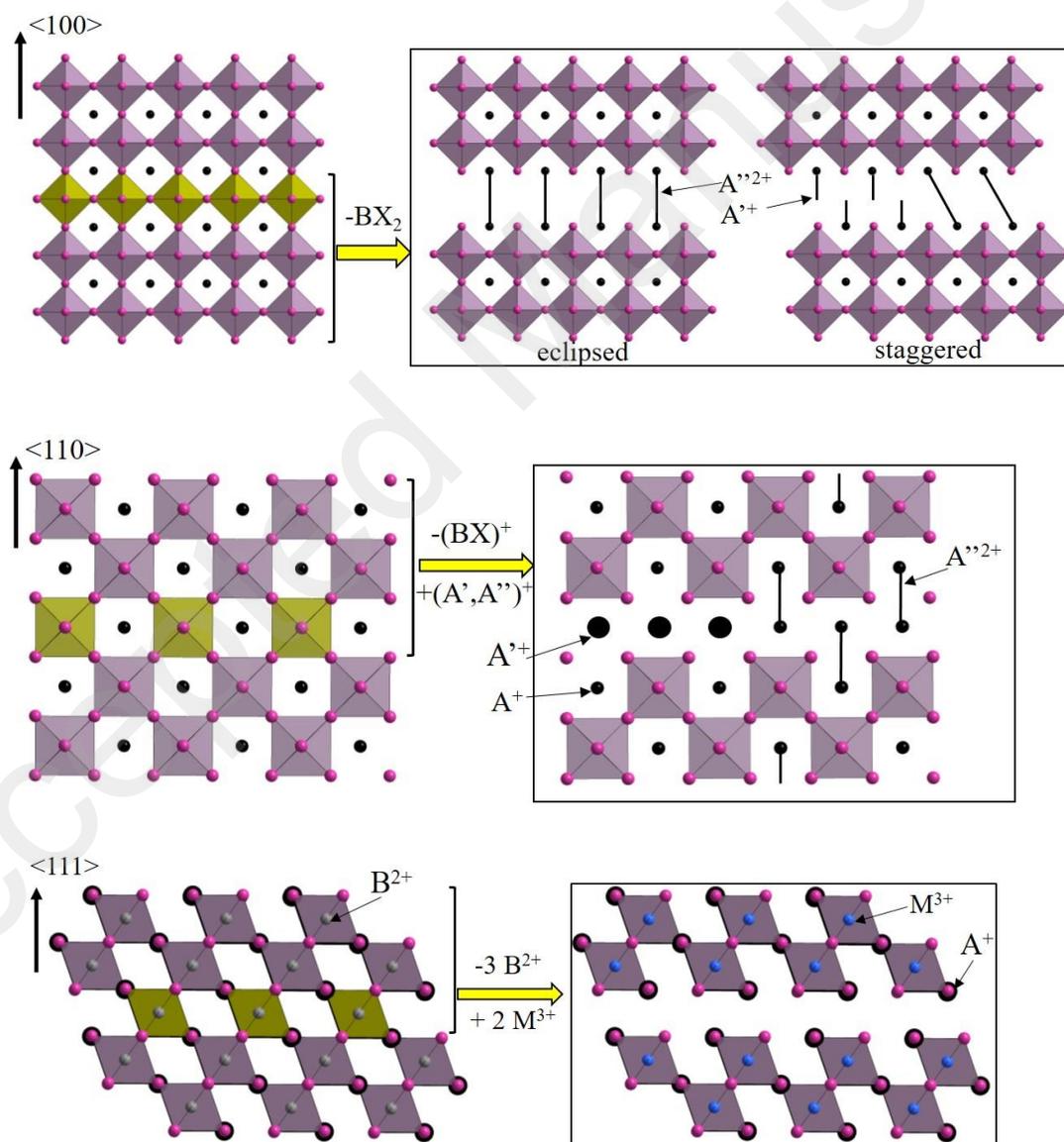
Figure 2. The <100>- (top), <110>- (middle) and <111>-oriented (bottom) low-dimensional perovskites conceptually defined from the mother ABX_3 perovskite structure (left) by elimination or substitution processes. A'^{+} and A''^{2+} are monocations and dications, respectively. B^{2+} and M^{3+} are divalent and trivalent metal ions, respectively. (top) For the <100>-oriented family, the removal of one BX_2 plane every n+1 layers leads to B_nX_{3n+1} networks. (middle) For the <110>-oriented family, the substitution of $(BX)^{+}$ cationic units in the (110) planes by organic cations $(A'^{+}$ or ½ $A''^{2+})$ every m+1 layers leads to B_mX_{3m+2} networks. (bottom) For the <111>-oriented perovskites, $M^{(III)}_2X_9$ q= 2 <111> networks can be conceptually obtained by the substitution of 3 B^{2+} cations of the mother structure ($A_3B_3X_9$) by two M^{3+} cations, the vacancies being ordered in (111) planes.

If substitutions on the B and X sites of the 3-D BX_3 perovskite network have led to a lot of derived 3-D perovskites, such substitutions have also been carried out for the low-dimensional perovskites, particularly for the halide component. The preparation of a mixed halide solid solution is of high interest to tune electronic, optical or magnetic properties of corresponding hybrids. As a first example, we can mention the early work of Y. Susuki and H. Kubo (1983) who analyzed the Cl^{-} and Br^{-} distribution in the quasi-two-dimensional perovskite ferromagnets $(CH_3NH_3)CuCl_{1-x}Br_x$.[179] Later, in order to clarify the role of the halide in the superexchange mechanism of halochromate perovskite ferromagnets, C. Bellitto et al. reported on the mixed halide material $(C_6H_5CH_2NH_3)CrBr_{3.3}I_{0.7}$ exhibiting a 3-D ferromagnetic ordering at 51 K.[180] In the 1990s, G. C. Papavassiliou and N. Kitazawa brought an important contribution to the field by investigating the mixed crystals of $(A)_2PbBr_xI_{4-x}$ and $(A)_2PbCl_xBr_{4-x}$ (A= $C_6H_5CH_2NH_3^{+}$,[181,182] $C_{10}H_{21}NH_3^{+}$)[29] showing the shift of the exciton band to the blue region by replacing I by Br, or

14

Br by Cl. More recently, M. G. Kanatzidis et al. prepared the first mixed halide multilayered 2D perovskite $(EA)_4Pb_3Br_{10-x}Cl_x$ (<100>/n = 3 ; EA^+= ethylammonium). They show that the content of Cl^- (x) has a drastic influence on the distortions of the perovskite network and consequently on the luminescence properties (white emission) of related materials.[84] Finally, we can notice the first hybrid perovskite containing a pseudohalide anion, $(CH_3NH_3)_2PbI_2(SCN)_2$. First prepared as crystallized powders and thin films for solar cells application,[183,184] its crystal structure has unambiguously revealed the layered nature of this compound, the terminal iodides of the ideal n = 1 PbI_4^{2-} layers being substituted by the SCN^- pseudohalide anions leading to $PbI_2(SCN)_2^{2-}$.[185] If a low band gap was first assigned to this material (1.55 eV), it has been further shown that this value was wrong,[185] and finally measured around 2 eV.[186]

2.1.3. Atypical perovskite networks

Atypical hybrid perovskites are based on corner-sharing octahedra networks which cannot be deduced from the ABX_3 mother structure by simple cuts along (100), (110) or (111) planes. The first example is the series of "rooflike" networks. These networks are isomers (same formula as $BX_4 = BX_{4/2}X_2$ resulting from the corner-sharing of four halides, while two halides are terminal), including two types of octahedra, those with the two terminal halides in trans-position, as in the n = 1 members of the <100> series, and those with the two terminal halides in cis-position, as in the m = 2 member of the <110> series (Figure 3). They can be described as corrugated layers of « $n' \times n''$ rooflike » type where n' and n" are the number of octahedra composing each half of the roof. Thus, a 4×4 rooflike network is encountered in $(NH_3-(CH_2)_5-NH_3)SnI_4$[187] (Figure 3, left), while a 3×3 rooflike network is encountered in $\alpha(H_2DMEN)PbBr_4$[95] (DMEN = 2-(dimethylamino)ethylamine) (Figure 3, middle). Recently, the first asymmetrical 3 x 2 rooflike

network has been crystallized with both formamidinium and guanidinium (Gua$^+$) cations, (FA)(Gua)PbI$_4$.[188] Another example is the Pb$_4$I$_{14}$ network of Figure 3 (right) found in (MA,HEA)$_6$Pb$_4$I$_{14}$ (MA$^+$, methylammonium, HEA$^+$, ethanolammonium).[189] It can be easily described from the ABX$_3$ mother structure by the substitution of one (PbI)$^+$ unit every five units by an organic cation A$^+$ leading to A$_6$Pb$_4$I$_{14}$ (= A$_5$Pb$_5$I$_{15}$ − (PbI)$^+$ + A$^+$). In the structure, the (PbI) vacancies are ordered, leading to a unit cell volume 5/4 bigger than the unit cell volume of (CH$_3$NH$_3$)PbI$_3$ (Figure 3, right). From a structural point of view, the perovskite network remains 3-D because the corner-sharing mode occurs in the three directions of space. However, as underlined by the red color of crystals, the electronic dimensionality is certainly lowered. This can be rationalized considering that chains of *trans*-connected octahedra are encountered only along the *c* direction, while along the (2*a* + *b*) and (*a* − 2*b*) directions, an alternation of four *trans*-connected octahedra and one Pb^{2+} vacancy occurs. Finally it must be noted that a solid solution can be obtained and it is shown that this material, preferentially named (MA,HEA)$_{1+x}$Pb$_{1-x}$I$_{3-x}$ to highlight the lead and iodide deficient PbI$_3$ mother network, can exist in the x = 0 to 0.2 range. x= 0 corresponds to the (CH$_3$NH$_3$)PbI$_3$ while x = 0.2 corresponds to the Pb$_4$I$_{14}$ (Pb$_{0.8}$I$_{2.8}$) based compound where only organic cations fill cavities. For 0<x<0.2, cavities contains organic cation as well as lead and iodine.[189]

16
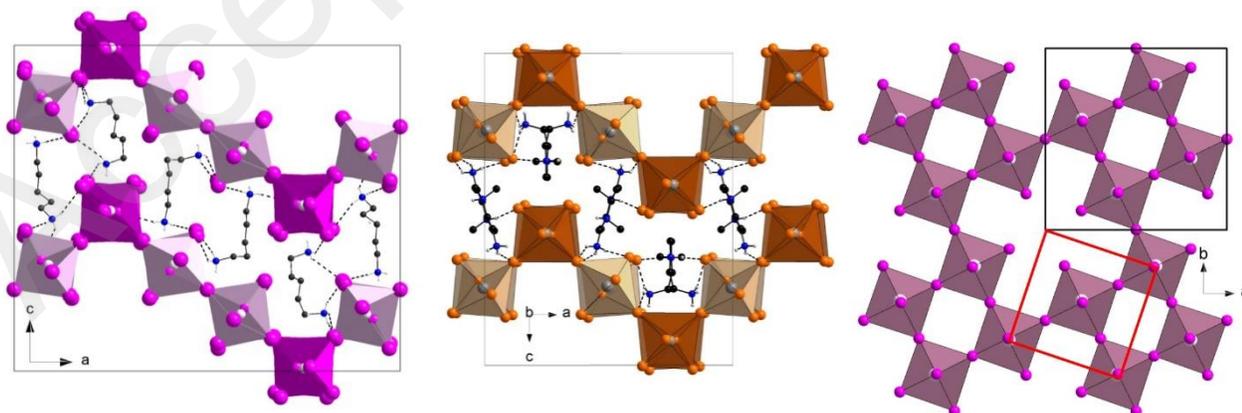
Figure 3. Atypical perovskite networks : (left) 4×4 rooflike network in $(NH_3\text{-}(CH_2)_5\text{-}NH_3)SnI_4$, (middle) 3×3 rooflike network in $\alpha(H_2DMEN)PbBr_4$ (DMEN = 2-(dimethylamino)ethylamine), and (right) Pb_4I_{14} $(Pb_{0.8}I_{2.8})$ lead and iodide deficient BX_3 perovskite network in $(HEA, MA)_{1.2}Pb_{0.8}I_{2.8}$ $(HEA^+ :$ ethanolammonium ; $MA^+ :$ methylammonium).

2.1.4.   Halometallate structures with perovskite sub-networks

Perovskite networks are one sub-class of the more general family of B(II)/X(-I) halometallate networks which can be defined as anionic networks of corner, edge or face-sharing B_xX_y polyhedra. Among these networks, some are built in a large amount through the corner-sharing mode of octahedra, which is the signature of perovskite sub-networks. In Figure 4 three of them are reported. The first two structures are 2-D anionic networks of corner- and face-sharing octahedra. However, they are better described as 1-D $B_n'X_{4n'+2}$ perovskite ribbons[190,191,192] linked together by B^{2+} cations. In $(PPA)Pb_2I_7$ $(PPA^+ =$ phenylpropylammonium), two octahedra thick ribbons of (Pb_2I_{10}) are alternatively linked to four octahedra thick ribbons of (Pb_4I_{16}) by Pb^{2+} leading to the Pb_2I_7 network (or $Pb_8I_{28} = Pb_2I_{10} + Pb_4I_{16} + 2\ Pb^{2+}$). In $(PBA)Pb_2I_7$ $(PBA^+ =$ phenylbutylammonium), three octahedra thick ribbons of (Pb_3I_{14}) are linked together by Pb^{2+} leading to the Pb_2I_7 network (or $Pb_4I_{14} = Pb_3I_{14} + Pb^{2+}$) (Figure 4). If these networks are 2-D from a structural point of view, DFT calculations clearly show that there is a quantum confinement effect: the calculated band edges are flat along the [010] confinement direction, while the electronic wave functions corresponding to the states at the band edges are confined to the regions of ribbons of corner-sharing octahedra.[193] Thus, from

an electronic point of view, these materials can be considered as 1-D and comparable to 1-D perovskites $B_{n'}X_{4n'+2}$. The first member of this series characterized by $B_{n'}X_{4n'+2}$ ribbons linked by B^{2+} cations is the B_3X_{10} network resulting from B_2X_{10} (n' = 2) ribbons fused by B^{2+} ions, as found for instance in $(AESBT)Pb_3I_{10}$[194] (AESBT = 5-ammoniumethylsulfanyl-2,2'-bithiophene) or $((CH_3)_3S)Pb_3Br_{10}$, this last material interestingly exhibiting a broadband emission with a massive Stokes shift.[195]

Halometallate networks can also result from corner and edge-sharing octahedra. For instance in $(H_2Aepz)_3Pb_4I_{14}$ (Aepz = 2-(2-aminoethyl)-pyrazole)[196] the Pb_4I_{14} bilayer network can be described as perovskite ribbons linked together through edge-sharing mode (Figure 4, right). In the same chemical system H_2Aepz-Pb-I, the n = 1 member of the <100>-oriented family has also been obtained, $(H_2Aepz)PbI_4$. While it is well known in the <100> series that the band gap decreases from the monolayer BX_4 to the bilayer B_2X_7 compounds (see section 3.1), the band gap of the bilayered compound $(H_2Aepz)_3Pb_4I_{14}$ is larger than the band gap of the monolayer compound $(H_2Aepz)PbI_4$. This is most probably indicative of effect of quantum confinement in the regions of ribbons of corner-sharing octahedra, meaning that the electronic dimensionality doesn't correspond to the 2-D structural dimensionality.
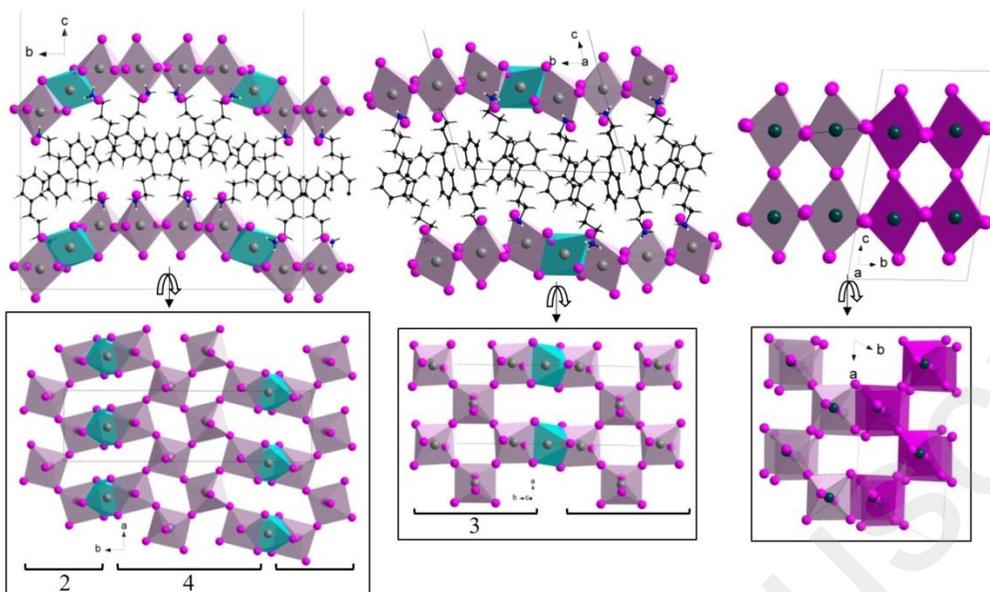
Figure 4. Layered halometallate networks built from ribbons of corner-sharing octahedra linked together either by Pb^{2+} ions (blue octahedra), in $(PPA)Pb_2I_7$ $(PPA^+ = phenylpropylammonium)$ (left) and $(PBA)Pb_2I_7$ $(PBA^+ = phenylbutylammonium)$ (middle), or through edge-sharing mode in $(H_2Aepz)_3Pb_4I_{14}$ $(Aepz = 2-(2-aminoethyl)-pyrazole)$ (right). Adjacent ribbons appear as light pink octahedra and pink octahedra.

2.2. Formation of perovskite networks / choice of organic cations

2.2.1.　Introduction

Due to the labile halide ligands, metal halide complexes are involved in fast dissociation and association in solution. The large number of different anionic halometallate anions, 0-D, 1-D, 2-D or 3-D that are found in the solid state, can be explained by a condensation of BX_n polyhedra during the crystallization process depending on several parameters. The stoichiometry of reagents is one of these parameters. Ideally, we could expect that the mixture of 1 BX_2 and 1

AX affords a ABX_3 compound, and that 1 BX_2 and 2 AX gives a A_2BX_4 compound, but it is not a rule. Many examples show that two or more different compounds can be obtained together, as in the system $SnI_2/CH_3-(CH_2)_{11}NH_3^+$ where both $(CH_3-(CH_2)_{11}NH_3)SnI_4$ and $(CH_3-(CH_2)_{11}NH_3)SnI_3$ are crystallized.[197] Moreover, as syntheses are often carried out with an excess of X^- anion in order to easily solubilize the BX_2 salts, the concentration of X^- is also a key parameter.[198] Finally, the importance of the stoichiometry is nicely illustrated by the preparation of different members of the layered <100>-oriented perovskites $(CH_3(CH_2)_3NH_3)_2(CH_3NH_3)_{n-1}Pb_nI_{3n+1}$ (n = 1 to 4). Thus, the n = 1-4 materials are prepared as pure phases in HI solution from the stoichiometric reaction of CH_3NH_3Cl and PbO, while half the expected stoichiometry is used for the n-butylamine (limiting reagent).[80] If in that case the formation of multilayered perovskites was expected because suitable cations were used, the nature of the BX_3^- or BX_4^{2-} networks of ABX_3 or A_2BX_4 materials prepared from any A^+ organic cation, is not predictable in many cases. The nature of the organic cation(s) is a crucial key point in the formation of the anionic halometallate network. For instance, in the case of a ABX_3 compound, BX_3^- can be either a 3-D perovskite network, a 1-D chain of face-sharing octahedra,[199] a 2-D sheet of MoO_3 type,[197] etc… all these networks being isomers. Besides the nature of A^+, the pressure or temperature can influence the nature of the anionic network. For instance, the network found in $(FA)PbI_3$ is either a 1-D chain of face-sharing octahedra at room temperature, or a 3-D perovskite above 150 °C.[199] Different types of perovskite networks can also be isomers. Thus, the BX_4^{2-} anion can be the n = 1 member of the <100>-oriented family, the m = 2 member of the <110>-oriented family, or one of the exotic 4×4, 3×3 or 3×2 rooflike networks (Figure 3). All these networks can be stabilized by non-bulky $R-NH_3^+$ or $^+H_3N-R-NH_3^+$ primary ammoniums, meaning that the nature of the R groups, particularly their ability to make intermolecular interactions, will template one

20

inorganic anion rather than one of its isomers. As another example of isomeric networks, we can cite the $B_2X_7^{3-}$ anion found as the n = 2 member of the <100>-oriented family (Figure 2), the atypical lead and iodide deficient $B_{1-x}X_{3-x}$ (x = 0.2) network (Figure 3), and the above described halometallate structures with perovskite sub-networks (Figure 4).

2.2.2. <100>-oriented layered perovskites
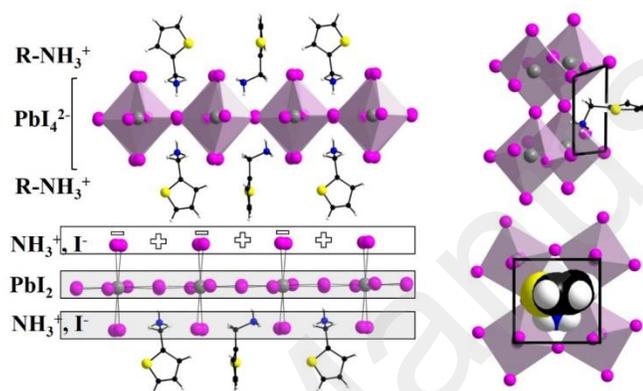
Figure 5. Organic-inorganic interface in a n = 1 <100>-oriented perovskite (example of (2-methylammonium-thiophene)$_2$PbI$_4$) highlighting the cationic size (right) and charge (left) criteria necessary for organic cations to template the perovskite network.

Not only the <100>-oriented perovskites are by far the more common family of hybrid perovskites, but the prediction of achievement of such structures by selecting suitable cations is certainly much higher than for any other halometallate network. These B_nX_{3n+1} networks are characterized by terminal halides which define a square-like grid of anionic charges. On the other hand, suitable organic cations, typically non bulky primary (di)ammonium R-NH$_3^+$ or $^+$H$_3$N-R-NH$_3^+$, will form organic layers with ammonium heads defining a set of positive charges counter-balancing the anionic charges of the inorganic layers. Thus, if such hybrids are well defined as perovskite layers separated by organic cations, they can also be considered as neutral blocks (n > 1) or neutral PbI$_2$ layers (n = 1) ended by NH$_3^+$,X$^-$ planes in order to highlight the

21

ionic interaction at the organic-inorganic interface that finally guides the formation of such structures. This is illustrated in Figure 5 for the ((2-methylammonium)thiophene)$_2$PbI$_4$ <100>/n = 1 compound.[200] Besides the necessity to have a cationic head, the size of organic cations is also a key point. There is no restriction in length, meaning that the distance between adjacent perovskite layer can be tuned depending on the length of selected organic cations, as shown by a series of perovskites based on long alkylammonium cations.[201] However, their width, or cross-sectional area must fit in the surface defined by four adjacent terminal halides as illustrated in Figure 5 for the thiophene derivative cation. The great number of BX_4^{2-} (n = 1) based perovskites, especially for Pb^{2+} and Sn^{2+} ions is also explained by some degree of freedom of this soft network in order to accommodate different organic cations and hydrogen bonding schemes.

Three main structural features characterize the degree of distortion of the network. The first one is relative to the geometry of the BX_6 polyhedron. While an octahedral nature reveals the stereo-inactivity of the Pb^{2+} or Sn^{2+} ns^2 lone pair, a non-octahedral geometry usually reveals the lone pair stereo-activity, as found in (EDBE)PbCl$_4$ (EDBE : 2,2'-(ethylenedioxy)bis(ethylammonium)).[202] This structural feature is considered as responsible of self-trapped excitons in (EDBE)PbCl$_4$ and some other chloro- and bromo-plumbate perovskites, and consequently to a broadband white emission of these promising perovskites. The two other degrees of distortion are the in-plane and out-of-plane distortions.[203] These distortions as well as the octahedral nature of the metal complexes, have direct impact on the electronic properties of related materials. The weaker they are the smaller is the band gap.[76,203–206]
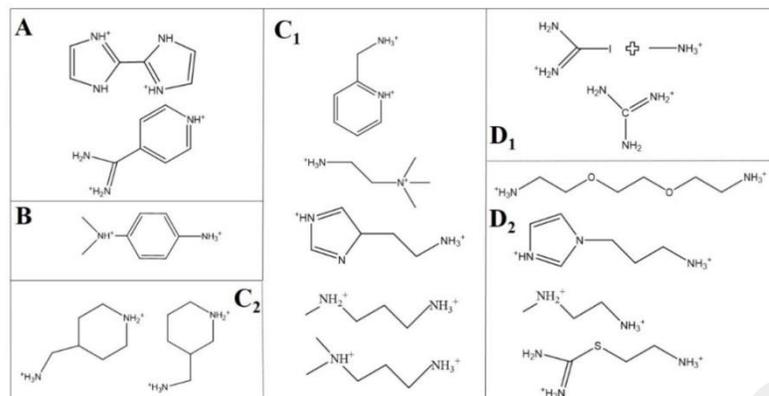
Figure 6. A, B, C₁ and C₂: Non all primary ammonium dications affording <100>-oriented perovskites (A, no primary ammonium; B, one primary ammonium; C₁ and C₂, one CH₂-NH₃⁺ fragment). D₁ and D₂: cations affording <110>-oriented perovskites.

If most of the <100>-oriented perovskites have been stabilized by primary ammonium mono- or dications $R-NH_3^+$ or $^+H_3N-R-NH_3^+$, other cations can template these perovskite networks. With the exception of the non-primary ammonium biimidazolium and 4-amidinopyridinium cations (Figure 6, A), leading to PbI_4[207] and $PbBr_4$[208] based layered perovskites, respectively, and the N,N-dimethylphenylene-p-diammonium ($DPDA^{2+}$) dication in $(DPDA)PbI_4$ (Figure 6, B), all are dications that possess one $-(CH_2)-NH_3^+$ fragment.[209] The C_2 cations shown in Figure 6 have stabilized a series of multilayered (n>1) perovskites,[204] and it is worth noting that they have all the same orientation in the interlayer space, meaning that all primary ammonium are in interaction with a perovskite sheet while all piperidinium fragments are in interaction with the adjacent perovskite sheet (Figure 7). In contrast, in the n = 1 perovskite, a head-to-tail situation of cations in the interlayer space is encountered, as well as between cations which are on both sides of the perovskite layer, as illustrated in Figure 7. This is

23

usually the best compromise for the inorganic layer to host the bulky non-primary ammonium head.[25]
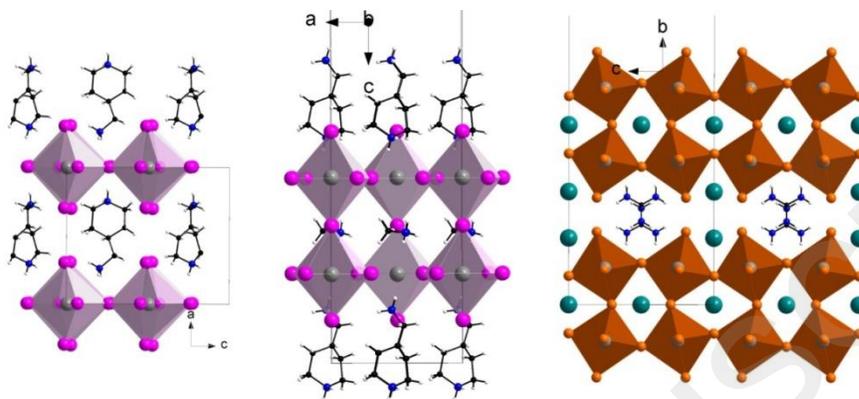
Figure 7. Structures of the n = 1 (4AMP)PbI$_4$ (left) and the n = 2 (4AMP)(MA)Pb$_2$I$_7$ (middle) perovskites (4AMP : 4-(methylammonium)piperidinium) showing the different molecular arrangement in the interlayer space. Structure of the Cs$_2$(C(NH$_2$)$_3$)Pb$_2$Br$_7$ perovskite with alternating ordering of cations in the interlayer space (right).

The first layered perovskite incorporating two kinds of well-ordered cations in the interlayer space is the n = 1 iodostannate hybrid (5FPEA,NEA)SnI$_4$ (5FPEA$^+$ = 2,3,4,5,6-pentafluorophenethylammonium, NEA$^+$ = 2-naphtylenethylammonium). More recently, other examples including multilayered (n> 1) hybrids have been reported: Cs(Gua)PbX$_4$ (X = Br, I) and Cs$_2$(Gua)Pb$_2$Br$_7$ (Gua = guanidinium, Figure 7)[210] as well as (Gua)(MA)$_n$Pb$_n$I$_{3n+1}$ (n = 1, 2, 3).[83] Interestingly, these perovskites adopt a higher crystal symmetry than most 2D perovskites, which consequently leads to lower band gap with the same perovskite layer thickness n.[83]

The polarizability is also a main characteristic of organic cations that can influence the properties of layered hybrid perovskites.[211] More specifically, depending on the nature of the interlayer organic cation, the electronic and dielectrical confinements can be tuned (vide infra). Organic cations based on neutral electron rich conjugated cycles will be more polarizable, thus

decreasing the electronic and dielectric confinement in perovskite layers. Several hybrid perovskites based on acene alkylammonium or thiophene alkylammonium cations have been reported. Besides the well-known 2-phenethylammonium cation based on a single benzene ring,[38] and its functionalized derivatives,[212] cations based on a naphtyl group (two fused benzene rings), have also led to n = 1 perovskites.[213] Thiophene alkylammonium type cations with one,[200] two,[194] or four[214] thiophene units have also led to n = 1 hybrid perovskites. Another strategy to tune the electronic and dielectric confinement in these layered materials is through intercalation of highly polarizable molecules. The intercalation process of neutral molecules within layered perovskites have first been demonstrated by D. Mitzi for a series of iodostannate perovskites incorporating benzene or hexafluorobenzene molecules.[215] More recently, the reversible incorporation of diiodide molecules into a n = 1 layered perovskite through a post-synthetic process has been demonstrated: the exposure to vapor of diiodide of $(IC_6H_{12}NH_3)PbI_4$, where $IC_6H_{12}NH_3^+$ is the iodohexylammonium cation, led to $(IC_6H_{12}NH_3)PbI_4.2I_2$ (Figure 8). Furthermore, the authors demonstrated that the dielectric characteristics of the intercalated compound are very different from those of the non-intercalated compound, involving a reduction of the electronic confinement in these 2D hybrid perovskites.[69]
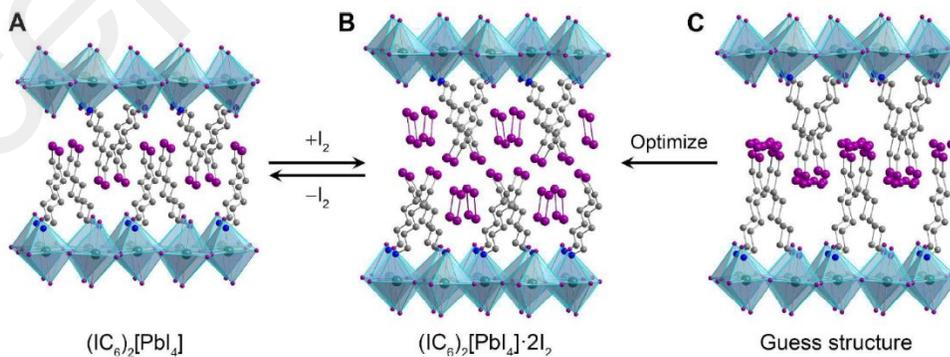
Figure 8. Intercalation of I_2 in the interlayer space of the hybrid perovskite $(IC6)_2PbI_4$ (A) ($IC6^+$: iodohexylammonium). C is the initial guess structure of the I_2 intercalation compound, and B is its DFT geometry-optimized structure. Reprinted with permission from ref [69] - Published by the Royal Society of Chemistry

If the criteria of charge and size that fulfill non bulky primary ammonium $R-NH_3^+$ or diammonium $^+H_3N-R-NH_3^+$ are necessary, they don't ensure systematic achievement of perovskite phases. This can be illustrated by a series of hybrids obtained with phenalkyl ammonium cations. If the phenethylammonium cation affords multilayered perovskites,[18,28] the phenepropylammonium and the phenebutylammonium cations don't. Due to a longer alkyl chain (one or two supplementary CH_2 units), a head-to tail arrangement of molecules interacting together in the interlayer space occurs, which, combined to the quite bulky phenyl group, involves a decrease of the positive charge density at the organic-inorganic interface. The set of positive charges cannot fit with the set of negative charges brought by terminal halides of the n = 1 perovskite layer. As a consequence, a condensation of the BX_6 octahedra within the inorganic layers occurs during the crystallization process in order to equal the set of positive charges defined by the organic cations, finally leading to Pb_2I_7 halometallate structures with perovskite sub-networks. The resulting structures $(PPA)Pb_2I_7$ and $(PBA)Pb_2I_7$ are built from different inorganic networks, but both are based on corner- and face-sharing octahedra (Figure 4).[193] Another similar case involves two thiophene based cations. If the 2-methylammonium-thiophene afford the monolayer perovskite (Figure 5),[200] the longer 5-ammoniumethylsulfanyl-2,2'-bithiophene cation led to a Pb_3I_{10} halometallate structure with a perovskite sub-network (corner- and face-sharing modes) as a result of a molecular head-to-tail arrangement.[194] Non-bulky

primary ammonium cations which possess heteroatoms along the molecular skeleton (O, S) or at the end (I, Br, CN…) can also preclude the formation of perovskite layers due to abilities of heteroatoms to make specific interactions through their free electron pairs. An interesting example is the series of hybrids obtained with the cystaminium $(NH_3(CH_2)_2SS(CH_2)_2NH_3)^{2+}$ cation. Depending on experimental conditions, the layered perovskite $(NH_3(CH_2)_2SS(CH_2)_2NH_3)PbI_4$[216] as well as a series of hybrids based on 1D $Pb_{n'}I_{4n'+2}$ (n' = 2, 3, 5) perovskite networks have been obtained. [192,190]

2.2.3. B_2X_8 m = 2 <110>-oriented layered perovskites

The layered compounds (m > 1) belonging to the <110>-oriented perovskites are rare and only m = 2 members have been structurally characterized. It is important to notice that the corresponding $B_2X_8^{4-}$ network and the BX_4^{2-} n = 1 / <100> are isomers meaning that for a given ratio « organic cation/BX_4 », both perovskites are in competition. The comparative structural analysis of both networks as well as the structural analysis of the m = 2 $B_2X_8^{4-}$ perovskites can be of interest, first to understand why the n = 1 <100> network is preferentially formed, but also to design new <110> perovskites in the future. Organic cations which have stabilized <110> perovskites are depicted in Figure 6 (D1 and D2). As regards <100> and <110> networks, two main differences can be stressed. The first is the density of anionic charge at the organic-inorganic interface, which can be defined as the number of terminal halides by surface unit. The charge density is higher in the <110> network. In fact, while the distance between two adjacent terminal halides is roughly $d = (2 \times d(\text{B-X}))$ for the <100> network, the average distance is lower for the <110> network since there are two types of distances, $d = (2 \times d(\text{B-X}))$ along one direction (for instance *a* direction, Figure 9a) and $d = (2 \times d(\text{B-X}) \times \cos 45°)$ along a

perpendicular direction (**b** direction in Figure 9a). The second difference concerns the interaction between organic cations and the inorganic anion. For the <100> BX_4^{2-} network, all cationic heads will be ideally localized within the inorganic network entering through square windows defined by four adjacent terminal halides (Figure 5). In contrast for the <110> network there will be two different situations. One cationic head will be localized within the inorganic layer entering through rectangular windows defined by four adjacent terminal halides whereas the other will take place in the interlayer space next to edges of metal halide octahedra (Figure 9). The structural analysis of the first reported m = 2 compound, $(NH_2C(I)=NH_2)_2(MA)_2Sn_2I_8$,[39] is of interest. Besides the fact that the smaller methylammonium cation is located in the inorganic layer while the bigger iodoformamidinium cation lies in the interlayer space, it is interesting to notice that the iodoformamidinium cation interacts through hydrogen bonding with terminal iodides of both adjacent layers (Figure 9a, dashed lines). This situation has been confirmed in the structure of the Pb analogue reported recently,[217] and a similar feature occurs in $(H_2D2d)_2Pb_2Br_8$ (D2d : 2-(aminoethyl)isothiourea)[218] and $(H_2D2b)_2Pb_2Br_8$ (D2b : N-(3-aminopropyl)imidazole))[219] (Figure 9b). In the structure of $(H_2D2c)_2Pb_2Br_8$ (H_2D2c : N-methylethane-1,2-diammonium; Figure 9d)[202] the primary ammonium head in the interlayer space is also interacting with terminal bromides of two adjacent layers. A special feature of this structure is the presence of the secondary ammonium within the perovskite layer while the primary ammonium is located in the interlayer space. Finally, the structure of $(EDBE)_2Pb_2Br_8$ (EDBE : 2,2'-(ethylenedioxy)bis(ethylammonium), Figure 9c)[202] is the only one based on a symmetric dication. This is quite surprising since, as expected for such a symmetric cation, the chloride compound $(EDBE)PbCl_4$ is a <100> perovskite. This may be related to the presence of

hydrogen bonds between one activated H atom, of a CH_2 unit next to the oxygen heteroatom, and terminal bromides, which are then stabilized as in all the other existing m = 2 structures.
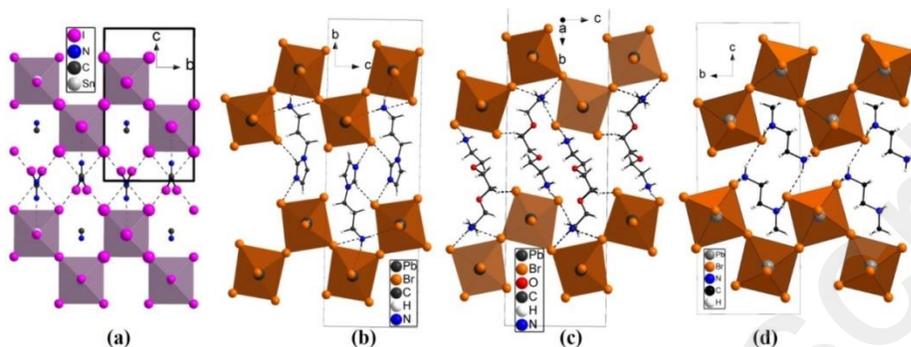
Figure 9. Structures of m = 2 <110>-oriented perovskites, $(NH_2C(I)=NH_2)_2(MA)_2Sn_2I_8$ with N…I contacts (d < 3.70 Å) as dashed lines (H atoms not located) (a), $(H_2D2b)Pb_2Br_8$ (D2b : N-(3-aminopropyl)imidazole) (b), $(EDBE)_2Pb_2Br_8$ (EDBE : 2,2'-(ethylenedioxy)bis(ethylammonium)) (c) and $(H_2D2c)_2Pb_2Br_8$ (H2D2c : N-methylethane-1,2-diammonium) (d) showing the hydrogen bonding at the organic-inorganic interface.

2.3. Multilayered <100>-oriented perovskites

2.3.1.   Introduction

The multilayered <100>-oriented perovskites (n > 1) have emerged as a promising class of light-absorbing materials for solid state photovoltaics due to a higher stability against humidity than their 3D analogues, while keeping a high power conversion efficiency up to 15.4% when a suitable preferential orientation of layers perpendicular to the substrate occurs.[20,220–223] Successful preparation of phase pure n > 2 multilayered perovskite[80] combined to thin films preparation using hot-casting methods[11] represents a breakthrough, pushing the 2D halide perovskites as serious candidates in the field of PSCs. The first multilayered hybrid perovskite, $(PEA)_2(MA)Pb_2I_7$ with n = 2, has been discovered by J. Calabrese, D. L. Thorn et al. in 1991.[28]

29

They anticipated that this new material belongs to a more general family of multilayered halide perovskites: « *... and we began to suspect that the cubic perovskite (MeNH₃)PbI₃ and the layered perovskite (RNH₃)PbI₄ are actually two extremes of a hitherto unknown structural series (RNH₃)₂(MeNH₃)ₙ₋₁PbₙI₃ₙ₊₁. Here n = ∞ corresponds to the cubic perovskite compound (MeNH₃)PbI₃ and n = 2, 3,.. (« bilayer, « trilayer »,...) describe structures not previously known for any organic amine-metal halide system.* ». In the next paragraph, we will highlight some structural features of n > 1 multilayered hybrid perovskites (B = Pb, Sn, X = I, Br) which have been crystallographically characterized so far.

Table 1 : <100>-oriented multilayered hybrid perovskites (n > 1) : nature of the inorganic network B_nX_{3n+1}, nature of organic cations in the perovskite sheet (MA^+ or FA^+) and in the interlayer space (left column) and space group (SG) (MA^+ : methylammonium, FA^+ : formamidinium, PEA^+ : phenethylammonium, M-PMA^+ : 4-methyl-benzylammonium, BA^+ : butylammonium, EA^+ : ethylammonium, ac-BA^+ : ammonium 4-butyric acid, $ThMA^+$: 2-methylammonium thiophene, Gua^+ : guanidinium, $3AMP^{2+}$: 3-(methylammonium)piperidinium, $4AMP^{2+}$: 4-(methylammonium)piperidinium).

Cations in the interlayer space	n = 2	n = 3	n = 4
PEA⁺	[a] Pb_2I_7/MA — P-1	[l] Pb_3I_{10}/MA — P1	[ref] B_nX_{3n+1}/A — SG
M-PMA⁺	[b] Pb_2I_7/MA — Pbcn		
BA⁺	[c] Pb_2Br_7/FA — Cmc2₁	[m] Pb_3Br_{10}/MA — Cmc2₁	
	[d] Sn_2I_7/MA — Ama2	[n] Sn_3I_{10}/MA — Cmca	
	[e] Pb_2I_7/MA — Cc2m	[e] Pb_3I_{10}/MA — C2cb	[e] Pb_4I_{13}/MA — Cc2m
EA⁺		[o] Pb_3Br_{10}/EA — C2cb	
ac-BA⁺	[f] Pb_2I_7/MA — C2cb		
Gua⁺ + Cs⁺	[g] Pb_2Br_7/Cs — Cmmm		
ThMA⁺	[h] Pb_2I_7/MA — Aba2	[p] Pb_3I_{10}/MA — Cmc2₁	
Gua⁺ + MA⁺	[i] Pb_2I_7/MA — Bmm2	[i] Pb_3I_{10}/MA — Imma	
3AMP²⁺	[j] Pb_2I_7/MA — Ia	[j] Pb_3I_{10}/MA — Pa	[j] Pb_4I_{13}/MA — Ia
4AMP²⁺	[j] Pb_2I_7/MA — Ia	[j] Pb_3I_{10}/MA — Pc	[j] Pb_4I_{13}/MA — Ia
⁺H₃N–(CH₂)ₘ–NH₃⁺	[k] Pb_2I_7/MA — m=8 Cc, m=9 Cc	[k] Pb_3I_{10}/MA — m=8 Pc, m=9 Pc	[k] Pb_4I_{13}/MA — m=8 Cc

n = 5: [q] Pb_5I_{16}/MA — C2cb

[a] ref. 28, [b] ref. 42, [c] ref. 224, [d] ref. 175, [e] ref. 80, [f] ref. 225, [g] ref. 210, [h] ref. 200, [i] ref. 83, [j] ref. 204, [k] ref. 226, [l] ref. 18, [m] ref. 227, [n] ref. 35, [o] ref. 95, [p] ref. 220, [q] ref. 82

31

2.3.2. Crystallographically characterized structures

The <100>-oriented multilayered perovskites $(A')_2(A)_{n-1}B_nX_{3n+1}$ or $(A'')(A)_{n-1}B_nX_{3n+1}$ that have been crystallographically characterized are mainly n = 2, n = 3 and n = 4 members of the series but also n = 5 for one structure. Several structural data of multilayered hybrid perovskites, where the inorganic network is based on Pb^{2+} or Sn^{2+} and I^- or Br^-, are reported in Table 1: nature of the inorganic network B_nX_{3n+1}, nature of organic cation(s) in the perovskite sheet and in the interlayer space along with the corresponding space group. We first notice that the organic cation in the inorganic sheet is in most cases the methylammonium cation. Two compounds are exceptions: in $(BA)_2(FA)Pb_2Br_7$ the formamidinium cation takes place in the $Pb_2Br_7^{3-}$ layer,[224] while in $(EA)_4Pb_3Br_{10}$, the ethylammonium cation is present in the $Pb_3Br_{10}^{4-}$ sheet.[84] If this last multilayered perovskite is unique, since only one type of cation is present both in the interlayer space and in the perovskite sheet (in that case, A' = A), the presence of the quite big ethylammonium cation occupying the perovskite cages is surprising and unprecedented. In fact, in the 3D $APbX_3$ perovskites, the only known cations that can fit in the perovskites cages are MA^+, FA^+ and Cs^+. The incorporation of the larger size cation of EA^+ into the n = 3 perovskite sheet is explained by a highly distorted perovskite network, with quite strong distortion of PbI_6 octahedra (Pb-I bond distances in the 2.98-3.31 Å range), which finally allows to accommodate the extra $-CH_2-$ group of ethylammonium cations. For a long time, only primary ammonium monocations have afforded multilayered <100>-oriented perovskites, the head to tail arrangement of organic cations in the interlayers leading roughly to a (½ ½) shift of adjacent layers in the layer plane. Recently, a few series of Pb_nI_{3n+1} (n = 2-4) multilayered hybrids with dications in the interlayer space have been crystallized. The dications are either the long alkyldiammonium $(NH_3-(CH_2)_m-NH_3)^{2+}$ (m = 8, 9)[226] or the shorter dications of $3AMP^{2+}$ (3-

(methylammonium)piperidinium) and $4AMP^{2+}$ (4-(methylammonium)piperidinium).[204] In hybrids based on these last cations, due to their dicationic nature as well as their short length, no shift between adjacent perovskite layers is observed. A main characteristic of some of these perovskites is their enhanced electronic dimensionality as underlined by band structure calculations which reveals a band dispersion along the perovskite layer stacking direction.[83] The key factor is the short halogen-halogen contacts between apical halogenes of adjacent layers ($d = 4.00$ Å in (4-AMP)(MA)$_3$Pb$_4$I$_{13}$). This feature is especially expected when short cations such as $3AMP^{2+}$ and $4AMP^{2+}$ or Gua^+ and MA^+ fill the interlayer space. A singular feature of most of these multilayered perovskite is their acentric and polar nature as they mainly crystallize in the monoclinic *m* and orthorhombic *mm2* crystal classes (deduced from space groups given in Table 1). One exception is the first reported multilayered perovskite (PEA)$_2$(MA)Pb$_2$I$_7$ described in the P-1 space group.[28] However, the statistical disorder which affects some atoms may indicate that a lower symmetry could be refined. A few years later, the acentric nature of a n = 2 perovskite compound based on 2-methylammonium thiophene cation, by highlighting the acentric nature of the bilayer perovskite network, has been unambiguously demonstrated.[200] Next, using the ammonium 4-butyric acid cations that forms supramolecular dimers in the interlayer space leading to an acentric organic layer, it was shown that the monolayer compound was centric due to a symmetry center located in the perovskite layer, while the n = 2 hybrid perovskite built from bilayer perovskite sheets along with the acentric organic layers was acentric and polar.[225] Recently, the relative energies of some multilayered perovskites in both the centrosymmetric and non-centrosymmetric structures were computed. It has been found that the acentric structures were lower in energy, and that this trend was even more significant when the number of layers, n is increased.[80] This is in agreement with similar calculations on (CH$_3$NH$_3$)PbI$_3$ that predicted the

acentric structure (*I4cm*) to lay slightly lower in energy compared to the centric (*I4/mcm*) structure.[228] Not only most of these compounds are acentric, but they are also polar, meaning that they may exhibit ferroelectric properties. If ferroelectricity in low-dimensional hybrid halobismuthate based on 1D BiI_3Cl_2 perovskite network has been evidenced a few years ago,[229] some 2D hybrid perovskites ferroelectrics have been reported recently, either monolayered[230,231] or multilayered materials, $(BA)_2(MA)_2Pb_3Br_{10}$[227] and $(BA)_2(FA)Pb_2Br_7$.[224] In $(BA)_2(MA)_2Pb_3Br_{10}$ an order-disorder transition occurs at 315 K, the BA^+ cations being disordered in the centro-symmetrical high temperature phase while they become ordered in the polar low temperature phase. At the same time, the inorganic network that adopts a highly symmetrical configuration above 315 K undergoes structural changes corresponding to a re-orientation and tilting of $PbBr_6$ octahedra.[227]

(a)   (b)   (c)   (d)
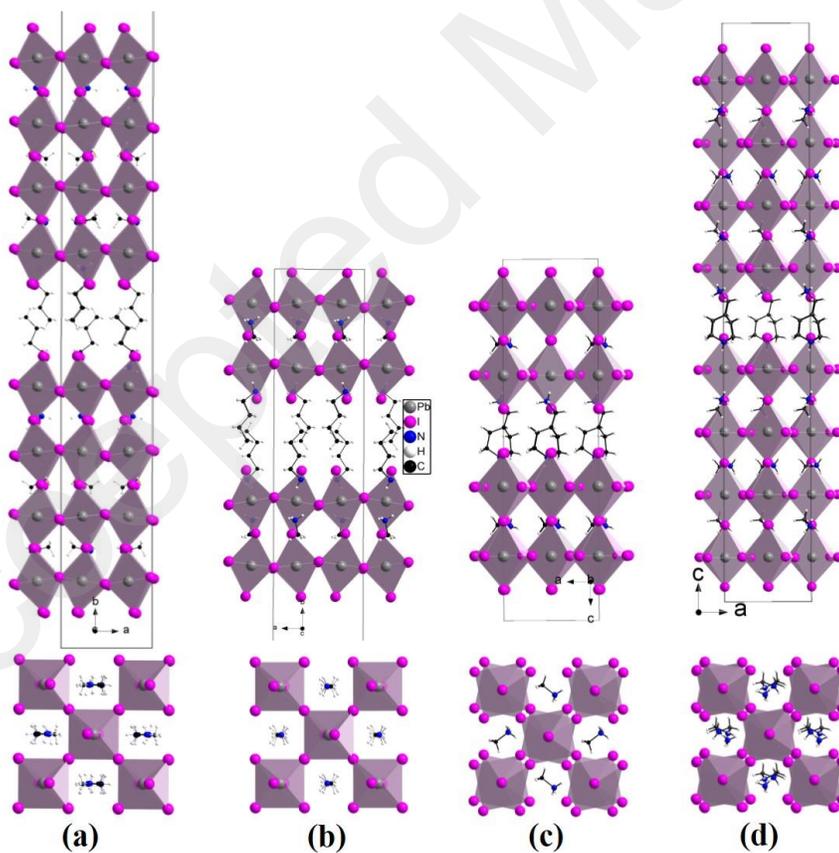
Figure 10. Structures of n = 2 and n = 4 <100>-oriented perovskites, $(BA)_2(MA)_3Pb_4I_{13}$[80] (BA⁺ : butylammonium, MA⁺ : methylammonium) (a), $(BA)_2(MA)Pb_2I_7$[80] (b), $(4AMP)_2(MA)Pb_2I_7$[204] (4AMP²⁺ : 4-(methylammonium)piperidinium) (c) and $(4AMP)_2(MA)_3Pb_4I_{13}$[204] (d) : general view (top) and view of one inorganic multilayer along the perpendicular direction (bottom).

If a large number of n = 1 <100>-monolayer perovskites have been stabilized by a variety of organic cations, the number of known <100>-multilayered perovskites are currently comparatively low. Then the question arises: could all organic cations that have afforded monolayered compounds stabilize multilayered materials? As already underlined, the n = 1 layer can be highly distorted (in-plane and out-of-plane distortion, octahedra distortion) in related materials depending on the nature of organic cations in the interlayer space. In contrast, and even if an out-of-phase tilting of octahedra is observed in the tetragonal room temperature structure of the 3D $(CH_3NH_3)PbI_3$, the distortions are limited with Pb-I-Pb bond angle greater than 164°. As a consequence, it can be expected that cations that induce only weak distortions in the monolayer perovskite network shall be well suited to afford multilayered materials. The n = 2 multilayered compound is unique since it is built from two outer layers, and, if distortions of in-plane type are the most commonly observed, large out-of-plane and in-plane distortions can also occur, as in $Cs_2(C(NH_2)_3)Pb_2Br_7$ (Figure 7, right).[210] The n > 2 multilayered compounds are different in account of the presence of two types of layers, outer layers and inner layers (one or more), the latter being comparable to layers of 3D bulk materials. Figure 10 shows an overall view, as well as that of one inorganic multilayer along the perpendicular direction, of n = 2 and n = 4 structures of BA/MA/Pb/I and 4AMP/MA/Pb/I compositions. It is first interesting to notice that the bilayer conformation is quite different in both $(BA)_2(MA)Pb_2I_7$ and $(4AMP)_2(MA)Pb_2I_7$. In

the BA$^+$ based material, layers exhibit out-of-plane distortions (δ = 7.18°), the MA$^+$ cation is roughly parallel to the stacking axis while only the ammonium part of BA$^+$ cations lie in the inorganic sheet, the CH$_2$ group lying in the plane defined by apical iodides (Figure 10b). On the contrary in the structure of (4AMP)$_2$(MA)Pb$_2$I$_7$, layers exhibit in-plane distortions (Pb-I-Pb bond angle $\approx$ 156°) but no out-of-plane distortions (Figure 10c). The second interesting feature is the similar type of distortions occuring in the n= 2 and n= 4 structures for both systems. In (4AMP)$_2$(MA)$_3$Pb$_4$I$_{13}$, only in-plane distortions are observed, but with increased Pb-I-Pb bond angles compared to those observed in the bilayer compound, particularly for the inner layers (160° and 162°) (158° and 158.7° for the outer layers). As in the structure of (BA)$_2$(MA)Pb$_2$I$_7$, only out-of plane distortions are observed in the structure of (BA)$_2$(MA)$_3$Pb$_4$I$_{13}$, but here also the network is less distorted in the n = 4 structure (δ = 6.08°-6.50°) than in the n = 2 structure (Figure 10a).

Given that different types of cations, namely ThMA$^+$ or PEA$^+$, including a thiophene or a phenyl group, BA$^+$ and (NH$_3$-(CH$_2$)$_m$-NH$_3$)$^{2+}$ (m = 8, 9) based on an aliphatic chain, 3AMP^{2+} and 4AMP^{2+} dications, including a non-primary ammonium head, and both Gua$^+$ and MA$^+$ in the interlayer space, have afforded n = 2-4 multilayered hybrid perovskites, shows that a large variety of cations can potentially stabilize such multilayered materials. However, other factors than steric considerations can preclude the formation of multilayered perovskites. In fact, during the synthetic process, by using a small (A = MA$^+$ or FA$^+$) cation and a longer one (for instance monocation A'$^+$), there is a competition between the formation of the expected multilayered perovskite and the formation of both the 3D ABX$_3$ compound and the monolayer (A')$_2$BX$_4$. The nature of the monolayered material (for instance based on highly distorted layers) and its high thermodynamic stability can favor the disproportionation into n = 1 and the 3D perovskite.

3. MULTILAYERED HALIDE PEROVSKITES: QUANTUM CONFINEMENT

Summary: The description of 3D halide perovskites basic electronic structures represents currently a major challenge for nowadays theoretical first-principles approaches due to the importance of relativistic effects, many-body effects, the dynamics of the organic cations and the coupling to low energy lattice excitations. For lower-dimensional perovskite networks, this is an even more challenging goal. Therefore, the understanding of quantum confinement effects in low dimensional structures and nanostructures is still at an early stage and is capitalizing on concepts and tools, including empirical methods, initially developed for conventional semiconductors.

3.1. Electronic band structure

Reviewing the main features of the electronic structure of hybrid halide perovskites is an essential prerequisite to understand the subtle interplay between their organic and perovskite components and to investigate effect of quantum and dielectric confinement. This section aims at providing basic considerations, such as those related to the atomic composition of the band edge electronic states, and related key findings that should also help to bridge the gap between solid state physics and molecular chemistry concepts.

3.1.1. Brief overview of theoretical approaches and relation to experiments

Band gap (alternatively bandgap) is among the most frequently used physical term to characterize the capabilities of a given material for a wide range of applications as well as to

37

conduct comparison between experimental and computed data, especially that derived from electronic structure calculations. To avoid any confusion, we introduce the following terminology:

- The HOMO-LUMO gap, which correspond to the energy difference between the highest occupied molecular orbital (HOMO) and the lowest unoccupied molecular orbital (LUMO) of an isolated (0D) species.

- The DFT gap ($E_{g,DFT}$), which corresponds to the energy difference between the highest occupied valence band (VB) state and the lowest empty conduction band state (CB) that is computed using Kohn-Sham (KS) Density Functional Theory (KS DFT)[232] and does not account for electron removal or addition neither for electron promotion from a VB state to a CB state.

- The transport or electrical or fundamental gap ($E_{g,trans}$), which corresponds to the energy difference between uncorrelated free electrons and holes; experimentally, this is to a good approximation accessible through ultraviolet photoemission spectroscopy (UPS) that provides information on the occupied VB states and inverse photoemission spectroscopy (IPES) for the empty CB states. It is related to the difference between ionization potential and electron affinity. As such, it can be computed to a good approximation using total energy (E_{tot}) differences: $E_{g,trans} = E_{tot}(N + 1) + E_{tot}(N - 1) - 2E_{tot}(N)$, with N the number of electrons in the system, or better based on Many-Body Perturbation Theory (MBPT)[233] such as the quasiparticle self-consistent GW theory[234] (sc-GW).

- The optical band gap energy ($E_{g,opt}$) is experimentally determined in many cases from photoluminescence (PL) experiments or the observation of a

resonance in optical absorption spectroscopy. It consists in the continuum band gap (E_g) corresponding to the lowest allowed interband absorption minus the exciton binding energy (E_b) corresponding to the energy required to form a bound exciton (electron-hole pair). In direct band gap semiconductors, the continuum band gap E_g usually matches the transport band gap $E_{g,trans}$. Noteworthy, the continuum gap may or not imply contributions from phonons either related to self-energy corrections or to interactions between the free electrons and holes with lattice phonons.

To some degree of accuracy, these quantities may be computed using various methods ranging from fully empirical ones[235] to self-consistent first-principles calculations including relevant treatments to account for many-body interactions and electron-phonon coupling.[93,236–240] The simplest approach is based on linear combinations of atomic orbitals (LCAO)[241] with mainly three variants with the Hückel and Extended Hückel theories (EHT)[242–244] for quantum chemists and the tight-binding (TB) model[245] for physicists. Currently, the most widely used and versatile technique is based on DFT within which the problem of j interacting electrons can be solved through a set j one-electron Schrödinger-like KS equations by introducing an effective potential.[232] Unfortunately, its exact form is unknown and a broad variety of approximated exchange-correlation density functionals (xc-kernel) have been developed over the last decades, the simplest being the local density approximation (LDA),[246,247] and the step above includes gradient corrections (GGA).[248] Noteworthy, KS DFT is a ground state theory and it has been shown that none of the band gaps experimentally measured can be derived from a single KS DFT band-structure calculation, even with the exact density functional. More recently, alternative realizations of DFT have been developed within generalized Kohn-Sham (GKS) schemes.[249–251] It has been demonstrated that the GKS band gap provides a better approximate to $E_{g,trans}$ than

the KS band gap, and that it equals $E_{g,trans}$ for a given approximate functional. For instance, those containing a fraction of exact exchange (*e.g.* HSE),[252] the so-called hybrid functionals, are currently attractive computationally-efficient alternatives to many-body techniques.

DFT has proved efficient to afford useful structure-properties relationships for many classes of semiconductors as long as an appropriate xc-kernel is implemented. For instance, in such cases, computed VB and CB densities of states (DOS) can be compared to DOS derived from UPS and IPES, respectively. Unfortunately, when using standard xc-kernels such as PBE[248] for the archetype $CH_3NH_3PbI_3$ compound, DFT computed band gaps show a fortuitous agreement with the experimental optical band gap.[91] This is a direct consequence of two opposite but huge error compensations between many-body and relativistic effects.[253] In fact, due to the large atomic number of lead (to a lesser extent for tin and halogens), spin-orbit coupling (SOC) has a dramatic effect on the electronic structure, inducing a large reduction of the band gap. The combination of no SOC with PBE leads to a fortuitous cancellation for the Pb bands but not for any other bands, thus the entire band structure will be incorrect in its details. To accurately estimate the band structure and continuum band gap, one needs to include the relevant many-body interactions that can be obtained using sc-GW, or alternatively to a cheaper computational cost by a one-shot GW correction (G_0W_0 approximation). Last, to account for excitonic effects, one needs to describe bound states that are well accounted for when solving the Bethe-Salpeter Equation (BSE) describing the bound states of a two-body relativistic system.[254] This can be performed at various levels of theory (*vide infra*), *e.g.* within the framework of DFT or that of semi-empirical approaches such as the TB model.

An alternative approach to investigate electronic excitations (*e.g.* optical properties) relies on time-dependent DFT (TD-DFT).[255,256] In the last two decades, TD-DFT schemes have been

extended to periodic solids[257] but have yet rarely been applied to halide perovskites.[253] In the context of photovoltaics, it has proved efficient for many dyes, for instance to compute optical absorption of TiO_2/Dyes interfaces.[258] Among the few TD-DFT studies on halide perovskites that also include non-adiabatic molecular dynamics (NAMD)[259–262] except for the optical properties of the prototypical OD Cs_4PbBr_6 compound,[260] effort has primarily concerned 3D networks to rationalize absorption spectra,[263] the exciton [259,262] and excited state geometries in the presence of defects.[264] Noteworthy, none of these TD-DFT investigations includes SOC, which is believed to have no significant harmful effect on structural optimization,[264] but sizeable impact is expected as far as optical properties are concerned. [64,91,92,262]

3.1.2. Ways to handle the organic cations

For most of the organic cations (primary non-conjugated ammonium cations) used to stabilize 3D and lower dimension halide perovskites, their HOMO-LUMO gap is significantly larger than the transport gap of the inorganic framework and, therefore, the molecular states do not contribute to the top of VB (VBM for valence band maximum) and bottom of the CB (CBM for conduction band minimum). This has been noticed at the early stage, with for example the use of an isolated $(PbX_6)^{4-}$ charged cluster [265] or a single $(SnI_4)^{2-}$ layer[38,203] to compute the electronic structure of halide perovskites. This was assessed for lower dimension halide perovskites in the seminal work by Koutselas et al. who performed ETH calculations with and without the amines and showed that the band gap did not change.[33] Over the decades, alternative strategies have been explored with for example the use of a uniform background charge density in self-consistent LCAO modeling of 2D and 3D perovskites achieving fair comparison with VB DOS experimentally derived from UPS.[265] Many computational tricks have also been explored in

41

the context of DFT computations, with compensation background charge densities or substitution of the organic cation by an alkali metal. In 2007, Sourisseau et al. reported that for 2D (X-$(CH_2)_2$-$NH_3)_2PbI_4$ (X = Cl, I), the best agreement with computed DOS and electronic band gaps is obtained when putting a sodium atom on the ammonium site.[205]

In the case of hybrid 3D halide perovskites, this leads in a situation conducive to computations as the organic cations are disordered near room temperature (both in cubic and tetragonal phases) as they do not fit the site symmetry.[91–93] This trick has also proved efficient for the modeling of lower dimension halide perovskites, both at the early stage and still recently, as it allows modeling the numerous disordered layered structures and at the same time reduces the computational cost. Replacement of the organic cation by a Cs^+ at the position of the ammonium group also helped developing model structures to introduce composite approaches designed to afford band alignments and dielectric profiles (section 3.2 and 4.4, respectively) or to rationalize effect of octahedral tilting on the band gap in layered perovskites (section 3.1.3.3).

However, such approximations will break down in several situations especially when dielectric confinement is at work. In fact, whereas R-NH_3^+ have low static dielectric constant of about 2 to 3, it may be significantly increased for bifunctional organoammoniums, non-primary ammoniums or as a result of intercalating species. Next, explicit account of the cations is a prerequisite for structural optimization. Noteworthy, most of the computed properties depend intimately on the structure of the perovskite framework (vide infra) and thus we stress that raw DFT structural optimization even with the most suited xc-kernel (*e.g.* corrected for dispersion forces) will afford the ground state static structure at zero kelvin (0 K). Moreover, explicit account of the A, A' and A'' cations is mandatory whenever information on lower-lying states is desired, as illustrated recently when comparing UPS VB DOS in BA-based 2D perovskites[266] or

investigating VB DOS broadening in 3D perovskites.[267] The same holds whenever detailed information is desired on higher-lying CB states.[266] Besides, it has recently been demonstrated based on molecular dynamics simulations that the organic molecule can be highly dynamic in layered halide perovskites inducing dynamic potential fluctuation and subsequent wave function localization. [268]
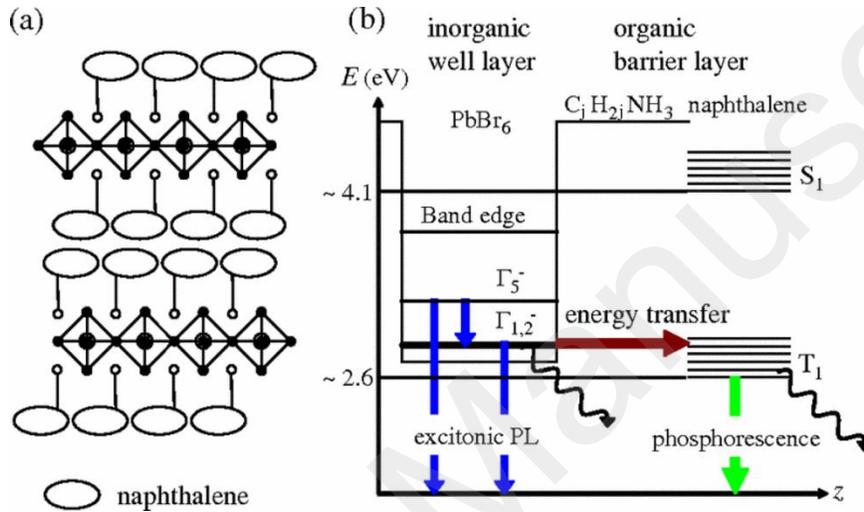
Figure 11. Schematics of the crystal structure of naphthalene-incorporated layered perovskite-type QW materials. It merges the Wannier and Frenkel pictures which are suited for the excitons in the inorganic and the organic parts, (a) Energy diagram and energy transfer dynamics of ($C_jH_{2j}NH_3PbBr_4$) (b). Reprinted with permission from ref [269]. Copyright 2008 American Physical Society.

Last but not least, quite a few lower dimension halide perovskites containing active organic cations have been reported (section 2.2 and ref. [25,270]). As early as in 1999, Mitzi et al. suggested possible energy transfer between the inorganic framework and the organic moiety for more conjugated cations, namely a quaterthiophene chromophore.[214,271] This has recently been confirmed using GKS DFT calculations including SOC, revealing a type II band alignement.[272]

43

Among others, charge separation between the organic ammonium-propyl-imidazole (API) layer and the inorganic $PbBr_4$ one has been suggested to occur on the band edge states on the basis of early DFT computations lacking SOC.[219] Recent GKS DFT results with SOC included have belied this conclusion, showing that the optical response of single-layered Pb-based perovskites with single-π-conjugated layers such as ammonium-propyl-imidazole or phenylethylammonium is dominated by states localized within the perovskite layer.[240]

The description of energy transfer between the inorganic framework and the organic moiety is a complex question that has not yet received a clear theoretical framework. However, a qualitative picture has emerged from pioneering experimental works on this topic.[273,274,214,269,25,270] An appropriate description entails the merging of the Wannier and Frenkel models which are suited for the excitons in the inorganic and the organic parts, respectively. Prospective schematic energy level diagrams mix energy levels related to singlet and triplet molecular states with monoelectronic states that are expected to describe the CB and VB edges of the inorganic QW.[274,25] A few recent attempts have been conducted in this direction.[240,272,274,] For instance, it has been shown from DFT simulations[206] that chlorine-based systems shall present larger electronic band gaps and band alignments close to a type II QW. Even though it may favor mixing of inorganic and organic electronic wavefunctions, it shall only partially explain the results of a comparative study on the halide substitution using Cl/Br/I.[273] The schematic descriptions of energy levels must be refined in order to introduce quantitatively the electron-hole pair states for both the inorganic and the organic parts (Figure 11).[269] More, the singlet-triplet splitting of the Frenkel exciton as well as triplet-triplet coupling are expected to play a major role in the process of energy transfer. Finally, relevant wavefunction overlaps between the two excitonic states must be carefully introduced, in order to explain the resonant

44

optical nonlinearities. In fact, progresses have recently been made for the description of the Wannier exciton of the inorganic QW, including realistic dielectric profiles and the leakage of the spinor states into the organic barrier derived from DFT simulations (vide infra).[275] A further step is necessary to introduce exchange energy into such simulations, using monoelectronic spinor states. Together with a correct description of the molecular excitonic states, it may lead to a more satisfying theoretical framework for situations where the organic cation plays an active role, *i.e.* largely beyond a mere cationic charge compensating molecule.[25,276,277]

3.1.3. Electronic band edge states

3.1.3.1 Basics of the atomic composition of band edge states

As early as in 1978, Heidrich et al. developed an empirical LCAO model for $CsPbI_3$ by analogy with thallous halides and computed the first band diagram of halide perovskites.[278] This early work, based on the ansatz that the average band energies can be approximated by energies of the free ions corrected by Madelung shifts, already stressed that the electronic band gap of the cubic *Pm3m* phase is direct but at the Brillouin Zone (BZ) boundary, namely at the R-point ($\mathbf{k}_R = (1/2,1/2,1/2)$), and that SOC and crystal field may split the possible transitions of optical spectra. At a first sight, the fact that the band gap shows up at the BZ boundary can be grasped considering a linear chain of atomic orbitals (Figure 12).[279] Noteworthy, in this simple picture, only the main orbitals that contribute to VBM and CBM have been considered namely the p-orbitals of the halide atom with the s-orbitals of the metal for the VBM and the p-orbitals of the metal for the CBM (vide infra). Figure 12 introduces further the concept of band-folding illustrated in Figure 13 for the pseudo-cubic phase of a 3D halide perovskite. In the first BZ associated to the primitive unit cell of the cubic *Pm3m* space group, the DFT band structure

drawn along its principal directions indeed reveals a direct band gap at the R-point. With the very same crystallographic positions but representing the band structure along principal directions of the first BZ of the orthorhombic *Pnma* unit cell evidences the band folding from BZ edges R, M (($\mathbf{k}_M = (1/2,1/2,0)$))) and X ($\mathbf{k}_X = (0,1/2,0)$) to the BZ center Γ ($\mathbf{k}_\Gamma = (0,0,0)$). Further comparison to the true orthorhombic structure highlights the connections between the two band structures and additional effect related to the structural distortions (strain). Thus, depending on the unit cell used to compute band dispersion, the shape may appear different and the band gap may or not show up at the BZ center.
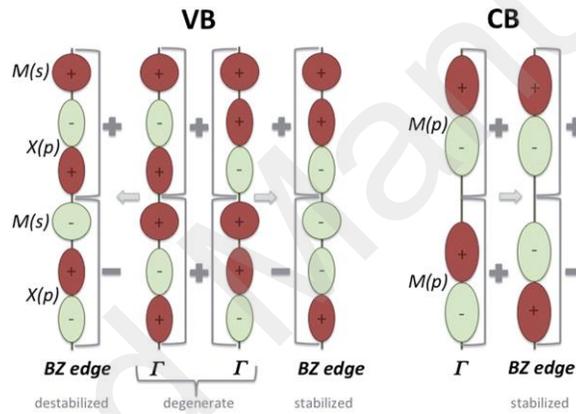
Figure 12. Atomic orbital hybridization and band folding in the Brillouin zone (BZ) exemplified on the simplest scenario, which consists of a linear chain. Left panel: hybridization between the p-orbitals of the halogen, X(p), and the s-orbitals of the metal, M(s). The valence band maximum (VBM) corresponds to the anti-bonding combination (left) that shows up at the BZ edge when the unit cell is built from one halogen and one metal (grey bracket). Upon unit cell doubling in real space (two grey brackets), the two combinations shown left and right fold back to the Γ point, centre of the new BZ. Right panel: hybridization between the p-orbitals of the metal, M(p). The conduction band minimum (CBM) corresponds to the bonding combination (right) that shows up at the BZ edge when the unit cell is built from one metal (grey bracket).

Upon unit cell doubling, this combination folds back to the Γ point, centre of the new BZ.

Reprinted with permission from ref [279] – Published by the Royal Society of Chemistry.
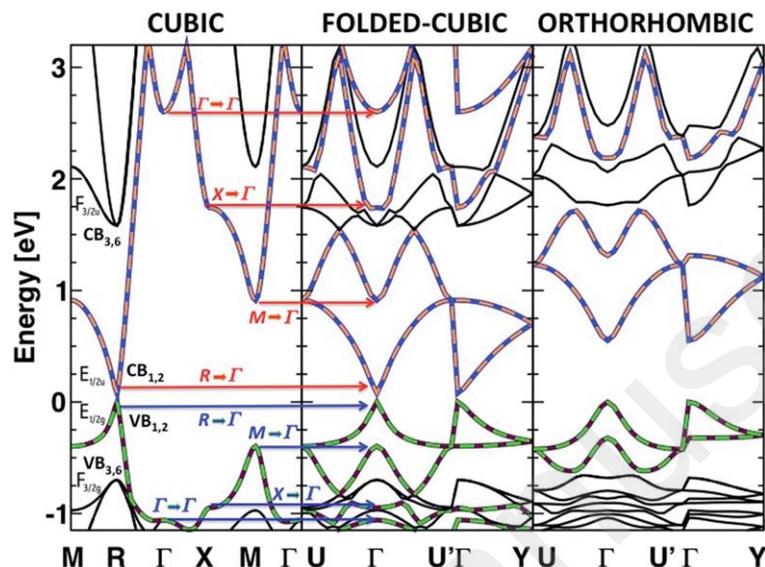
Figure 13. Band folding in the Brillouin zone (BZ) shown for $CH_3NH_3PbI_3$ with DFT calculations including spin–orbit coupling (SOC). Left panel: electronic band diagram calculated for the cubic Pm3m (space group no. 221, Z = 1) crystal structure and represented along principal directions of the first BZ with irreducible representations of the double group. Middle panel: the very same band structure represented along principal directions of the first BZ of the orthorhombic Pnma unit cell (space group no. 62, Z = 4) evidencing the band folding from R, M and X to Γ, which results in an apparent 4-fold increase of the number of bands. Right panel: electronic band diagram calculated for the real low-temperature orthorhombic Pnma crystal structure shown along principal directions of its first BZ. It highlights effects of structural distortions on the band structure, namely the increased band-gap and the change in effective masses at the VBM and CBM. It is noteworthy that the band mixing remains moderate as a direct consequence of the large splitting of $CB_{1,2}$ and $CB_{3,6}$ (left panel) induced by SOC whereas such

The initial LCAO model was refined in 1981 with inclusion of spin-orbit coupling and the s-orbitals of Cs, leading to a Hamiltonian matrix of 28×28.[280] Despite irrelevant calibration of Cs-orbitals, it allowed to attribute the main feature of available experimental optical spectra and ultraviolet photoemission data, stressing the impact of a van Hove singularity at the M-point of the BZ. Since then, several other tight-binding models were devoted to 3D halide perovskites among which the work by Umebayashi et al. [265] who provided the bonding diagram of a $[PbI_6]^{4-}$ cluster, the 3D crystal $CH_3NH_3PbI_3$ as well as for the 2D crystal $(C_4H_9NH_3)_2PbI_4$ (Figure 14). In the zero-dimensional system the higher occupied states were shown to be composed of σ-antibonding hybridization between metal s-orbitals and halogen p-orbitals. The lowest unoccupied states were stated to consist in metal p-orbitals hybridized either with halogen s-orbitals (σ-antibonding) or p-orbitals (π-antibonding). The later hybridization, even of moderate strength in metal halide crystals, was not taken into account in the early studies and their respective weight (also σ- versus π-antibonding) are seldom made clear.

3.1.3.2 Electronic structure in 3D networks

Considering further TB modeling of cubic 3D halide perovskites [281] clearly reveals that the CBM at the high symmetry R-point of the BZ has a σ-antibonding character with

$$E_{CBM(R)} = \frac{E_{sX}+E_{pB}}{2} + \frac{\sqrt{(E_{pB}-E_{sX})^2 + 16V_{pBsX}^2}}{2}, \tag{1}$$

where E_{sX} and E_{pB} are the atomic energies and V_{pBsX} the overlap integral related to the p-orbitals of the metal (pB) and the s-orbitals of the halide (sX). Due to the stronger hybridization between metal s-orbitals (sB) and halogen p-orbitals (pX), the picture was clear from the early stage with

$$E_{VBM(R)} = \frac{E_{sB}+E_{pX}}{2} + \frac{\sqrt{(E_{pX}-E_{sB})^2 + 48V_{sBpX}^2}}{2}. \tag{2}$$

These expressions highlight several main features of the band diagram of 3D halide perovskites, for instance the reversed ordering of band edge states (VBM and CBM) as compared to tetrahedrally bonded semiconductors [64,91]. They also provide a chemically intuitive tool to get a proper grasp of both halide (X) and metal (B) substitution based on atomic energies.[282] For example, when Pb is replaced by Sn, E_{sB} becomes less negative leading to a smaller band gap. Alternatively, substitution of I by Br (or Cl) leads to sizably more negative values of E_{pX} and the band gap significantly opens. Moreover, from expression (2) it is also easy to anticipate that for fixed lattice parameters (constant Pb-Pb distances) the band gap will

49

increase with increasing octahedral rotation or tilting (Pb-I-Pb angles deviating from $180°$) [228,283] as a result of a decrease of the overlap integral V_{sBpX}. Effect of lattice strain (Δa: small change of the lattice parameter a) can also be anticipated from such a simple TB model: [281]

$$\delta E_{CBM(R)} \approx \frac{-16V_{pBsX}^2}{\sqrt{(E_{pB}-E_{sX})^2+16V_{pBsX}^2}}\frac{\Delta a}{a} \tag{3}$$

and

$$\delta E_{VBM(R)} \approx \frac{-48V_{sBpX}^2}{\sqrt{(E_{pX}-E_{sB})^2+48V_{sBpX}^2}}\frac{\Delta a}{a}, \tag{4}$$

showing that the largest variation is expected at the VBM, which is stabilized when the lattice parameter increases leading to a band gap increase.

Moreover, due to the presence of atomic species with large atomic numbers, relativistic effects and for instance spin-orbit coupling have a dramatic effect on the band diagrams. Combined to symmetry considerations, this complexifies further the band diagram as illustrated by the schematic energy diagram reported by Tanaka et al. (Figure 15).[284] More recently, DFT calculations confirmed the major role of SOC evidencing the large splitting (Δ_{SOC}) of the first degenerated conduction levels ($CB_{1,2}$ and $CB_{3,6}$ in Figure 14), the CBM transforming to 2-fold $E_{1/2u}$ degenerate spin-orbit split-off states ($CB_{1,2}$): $\left|1/2,1/2\right\rangle = \frac{1}{\sqrt{3}}\left|(X+iY)\uparrow\right\rangle + \frac{1}{\sqrt{3}}\left|Z\downarrow\right\rangle$ and

$\left|1/2,-1/2\right\rangle = \frac{1}{\sqrt{3}}\left|(X-iY)\downarrow\right\rangle + \frac{1}{\sqrt{3}}\left|Z\uparrow\right\rangle$.[91] Corresponding spinorial components will be illustrated in the next section on a typical monolayered halide perovskite (Figure 16). This giant change of the whole electronic band structure has drastic effects on the electronic band gap, which changes according to

$$E_{CBM(R)} = \frac{E_{pB}+E_{sX}-2\Delta_{SOC}/3}{2} + \frac{\sqrt{\left(E_{pB}-E_{sX}-2\Delta_{SOC}/3\right)^2+16V_{pB,sX}^2}}{2} \tag{5}$$

within the TB model,[281] but also on effective masses and on the optical absorption through a renormalization of the oscillator strengths.[91] In fact, the $CB_{1,2}$ lead to a strong and isotropic optical transition with the even $|S\rangle$-like doubly $E_{1/2g}$ degenerate VBM states that undergoes a threefold decrease due to SOC.[92] Expression (5) and the one relevant to VBM combined with atomic energy levels tables also provide an intuitive way to grasp changes due to relativistic effects subsequent to metal and halide substitution.[279]
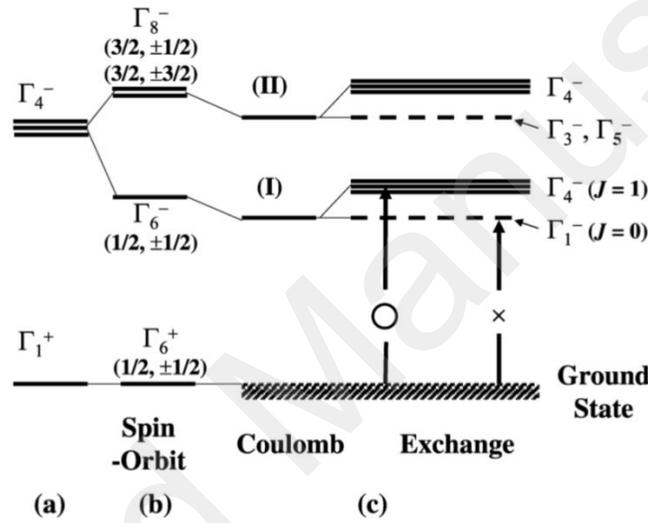
Figure 15. Schematic electronic energy diagram of 3D crystals for both monoelectronic and electron-hole pair (excitonic) states.[284] Notice that a similar diagram including the correct monoelectronic irreducible representations at the R point instead of the irreducible representations at the Γ point quoted here is given in ref.[92,285] (a) The CB and VB have Γ_4^- and Γ_1^+ symmetry, respectively. (b) With the spin–orbit interaction, the CB splits into fourfold Γ_8^- and twofold Γ_6^- states, while the VB transforms as twofold Γ_6^+ in double representation. (c) The lowest-energy exciton is split by the Coulomb and exchange interactions into sixfold Γ_4^- and twofold Γ_1^- states and transitions to these states are optically allowed and forbidden, respectively. Reprinted from ref[284], Copyright 2003, with permission from Elsevier.

3.1.3.3 Electronic structure in 2D networks (n = 1, <100> networks)
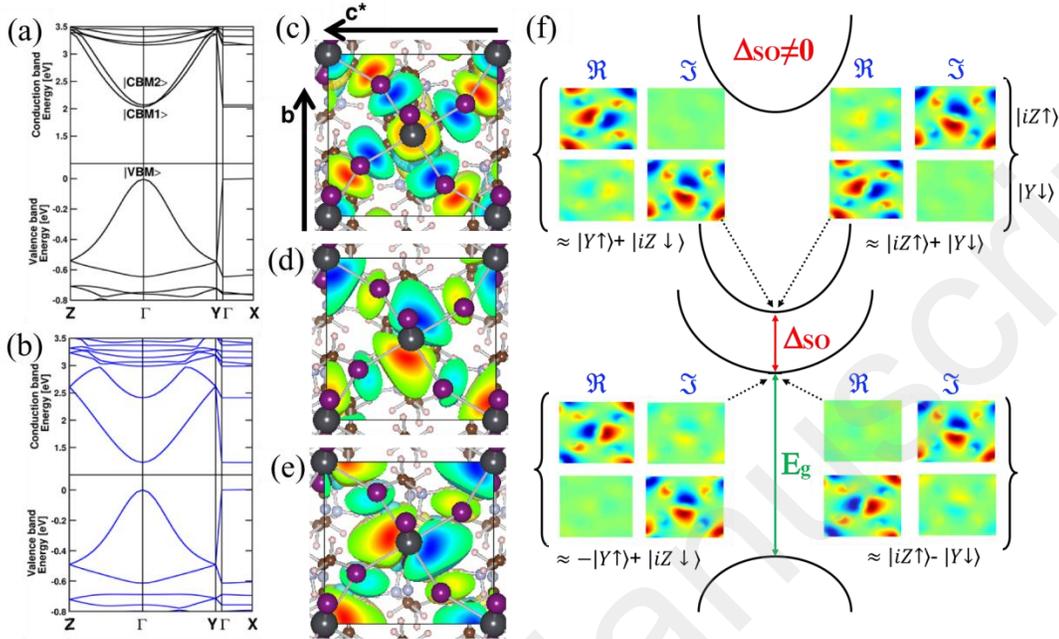
Figure 16. Electronic properties of ([pFC₆H₅C₂H₄NH₃]₂PbI₄) from DFT calculations. Band structure computed (a) without and (b) with SOC with energy levels referenced to the VBM. Both highlight the absence of dispersion and thus electronic coupling along Γ-X. Comparison of both band structures highlight the effect of SOC on the band gap, bandwidth and effective masses. Comparison to Figure 13 also illustrate the band gap increase related to quantum confinement. (c-e) Electronic wave functions (computed without SOC) of VBM, CBM1 and CBM2 as represented in the bc* plane illustrating the σ-antibonding character of the in-plane hybridization between p-orbitals of halide and s-orbitals of metal in VBM (c) and p-orbitals of metal with s-orbitals of halide for CBMs (d,e). (f) Schematic representation of the electronic band diagram when considering effect of SOC (Δ_{SO}) with ($\Re$) real and ($\Im$) imaginary parts of the complex spinorial components of CBM1 and CBM2 (top panels: spin up components; bottom panels: spin down components). Reprinted with permission from ref [64]. Copyright 2012 American Physical Society.

As for 3D perovskite crystals, the band gap of layered halide perovskite may or not show up at the center of the BZ depending on the space group and the unit cell used to compute the band structure. The simplest approximation to investigate lower dimension halide perovskite consists in considering an isolated single charged inorganic moiety. This was implemented by G. Papavassiliou and coll. as early as in 1994 on a single $(SnI_4)^{2-}$ <100> layer based on EHT.[38] They underlined the main features of the band structure edge states, with VBM largely composed of in-plane σ-antibonding combination of halide p-orbitals and metal s-orbitals, whereas the CBM was found to be primarily composed of out-of-phase hybridization between the metal and halide p-orbitals. A decade later, DFT calculations revealed that CBM involves both halide p and s-orbitals and concluded that CBM remains composed primarily of σ-antibonding states.[265] In 2005, Knutson and Mitzi highlighted the different symmetry allowed in-plane hybridizations at the high symmetry points of the BZ, for instance CBM consisting of hybridization between metal p-orbitals and halogen p or s-orbitals at the Γ- or M-point, respectively.[203] All these early works did not account for SOC but already stressed effect of quantum confinement on the band gap, bandwidth, DOS and the flat dispersions revealing absence of electronic coupling along the stacking axis. The first quantitative inspection of SOC in monolayered <100> halide perovskites conducted in 2012 revealed its impact on electronic (summarized in Figure 16) and optical properties.[64] To conclude on the orbital nature of the band edge states in <100> monolayered perovskites, VBM can be clearly thought as a σ-antibonding combination between the p-like equatorial and axial halide orbitals and s-like metal ones whereas the situation is more involved for the CBM as a result of SOC. CBM retains features of bonding interaction between metal p-

like orbitals, antibonding interactions between the latter and s-like orbitals of equatorial halogens and p-like orbitals of axial ones.

All the early studies on monolayered <100> perovskites also underlined another important factor that directly influences the band gap value, band diagram and related optical properties, namely the structural distortions of the inorganic perovskite layer.[38,265,203,205] Knutson et al. investigated the band structure of a series of idealized $(SnI_4)^{2-}$ perovskite <100> sheets using EHT to decipher the crystal orbital origin related to in- and out-of-plane angular distortion and demonstrated that the in-plane Sn-I-Sn bond angle has the greatest impact on the band gap.[203] This effect is similar to the one already discussed for 3D frameworks based on expressions (1) and (2) or (5) when considering SOC. More recently, it has been further quantified based on DFT calculations using a <100> Cs_2BX_4 model structure having rigid octahedral with D_{4h} symmetry,[76] which is illustrated in Figure 17. This model provides a synthetic view for structure-band gap relationships not only for monolayered <100> perovskites,[76,206] but it has also proved useful for qualitative assessments in multilayered ones.[84,204] Figure 17 shows that the band gap significantly opens upon octahedral tilting, mainly as a result of a lesser antibonding character of the VBM that gets stabilized. In addition, octahedral tilting leads to reduced hybridization and in turn to significant reduction of VBM and CBM bandwidths.
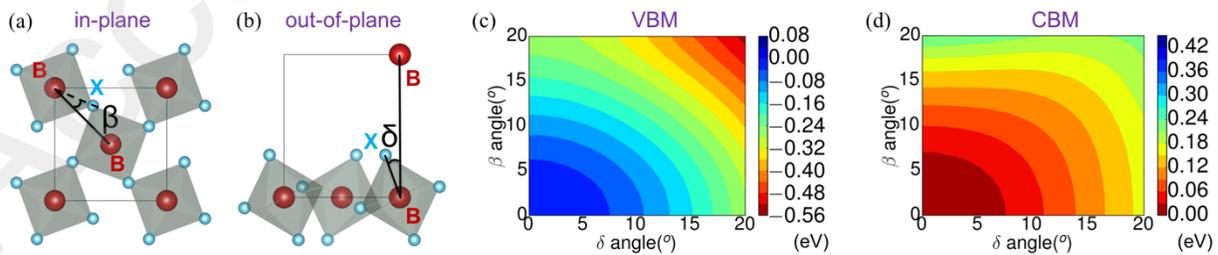
Figure 17. Cs_2BX_4 model to rationalize impact of octahedral tilting on band edge states. The model is composed of rigid $[BX_6]_2^-$ octahedra of D_{4h} symmetry.[76] Two angles characterize the

structural distortions: (a) β corresponds to the in-plane projection of the B-B-X angle and (b) δ corresponds to the out-of-plane B-B-X tilt angle. Color maps (c) and (d) report the variation of VBM and CBM state energies as a function of β and δ. They have been computed for B = Pb and X = I for a Pb-I distance of 3.18 Å using DFT and including SOC according to Ref. [206]. *They reveal the larger impact of octahedral tilting on VBM (c) as compared to CBM (d) and the systematic band gap increase with structural distortion independently of any change in quantum or dielectric confinement.*

The straightforward trends provided by such a model to experimentalists having on hand series of related crystal structures prompt its extension to <110> and <111> layered perovskites as well as implementation of more quantitative levels of theory (*e.g.* sc-GW, HSE or DFT-1/2). It may also be useful to further inspect a range of B-B in-plane distances as well as anisotropy in B-X bonds (apical versus equatorial), even so the effect of lattice strain has been demonstrated to have lesser impact then octahedral tilting (vide supra). Besides and to the best of our knowledge, a full TB model providing analytical expressions similar to (1)-(5) derived for 3D frameworks and tacking symmetry into account has still to be worked out for layered halide perovskites, whilst it is anticipated to afford similar sounded insight to the understanding of structure-properties relationships as well as an efficient tool to address large size structures, heterostructures and nanostructures.

3.1.3.4 Electronic structure and confinement effects
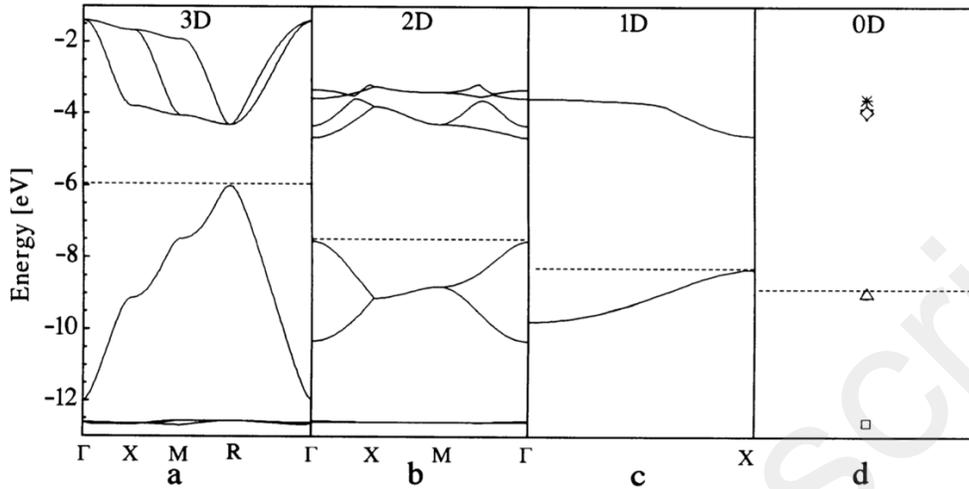
Figure 18. Electronic band structures of (a) $CH_3NH_3PbI_3$, (b) $(C_9H_{19}NH_3)_2PbI_4$, (c) $(NH_2C(I)=NH_2)_3PbI_5$ and (d) $(CH_3NH_3)_4PbI_6 \cdot 2H_2O$. Dashed line indicates the position of E_{Fermi}. Reprinted with permission from ref [33] Copyright 1996 IOP Publishing.

In 1996, Koutselas et al. performed ETH calculations on a series of hybrid halide perovskites of various dimensions ranging from 3D down to 0D.[33] A modification of the Slater orbital exponent for the I 5p orbitals was used to obtain a close agreement between the calculated band gap and the experimental band gap in the case of the 3D network. This pioneering work demonstrated many of the main features of the band diagram of lower dimension halide perovskites. Figure 18 highlights: (i) the direct band gap, (ii) the increase in band gap, (iii) the decrease of bandwidth and (iv) the rise in DOS with decreasing dimensionality and thus effect of quantum confinement. As already mentioned in section 2.3, it is only recently that series of phase-pure multilayered halide perovskites have been achieved and crystal structures made available. These provide a fair playground to further investigate effect of quantum confinement based on electronic structure calculations. Figure 19a reports the band structures computed for a series of $(CH_3(CH_2)_3NH_3)(CH_3NH_3)_{n-1}Pb_nI_{3n+1}$ multilayered perovskites with n = 1 to 4.

56

Quantum confinement leads to a systematic decrease of the band gap with increasing thickness (n-value) of the perovskite layer sandwiched between the organic cations along with the increased number of subbands that equals the number n of octahedra in the perovskite layer. Similar systematic decrease has also been computed for model structures $A_{n+1}M_nX_{3n+1}$ (A = Cs,MA; M = Pb,Sn; X = I, Br, Cl).[81,286] Corresponding local densities of states (computed within a small energy range close to the band edges) also reveal localization of electron and holes on specific sheets of the perovskite layer. The specific localization depends mainly on the amount of octahedral tilting within each layer, VBM being localized on the sheet with smallest octahedral tilting (Figure 17). Noteworthy, the density isosurfaces illustrate the knot spin texture[287–289] of CBM subsequent to inclusion of SOC.
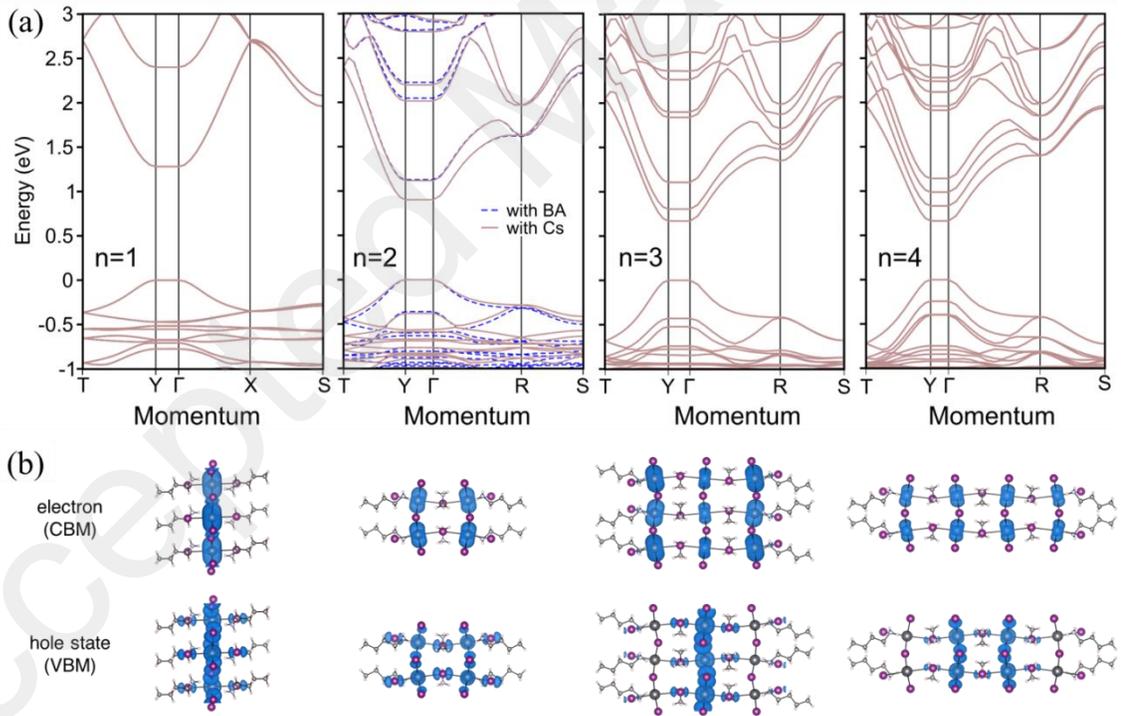
Figure 19. DFT computed electronic properties of $(CH_3(CH_2)_3NH_3)(CH_3NH_3)_{n-1}Pb_nI_{3n+1}$ with n = 1 to 4 including SOC. (a) Computed band structures for the experimental crystal structures obtained by replacing the organic cations $(CH_3(CH_2)_3NH_3)$ with Cs^+ (brown). Comparison to the

real structure is shown for n = 2 (dashed blue). (b) Corresponding local densities of states at CBM and VBM, evidencing the knot spin texture of CBM and localization on different perovskite sheets. Adapted with permission from ref [275]. Copyright 2018 NPG Publishing group.

We further stress that such localization on specific sheets is obtained based on static structures usually obtained from X-Ray diffraction. However, from molecular dynamics simulations[268] and proton NMR[290] there is clear evidence that both A and A' cations undergo a fast disordered dynamics (ps timescale), which has been suggested to lead to potential fluctuation sufficiently large to induce further localization of the band edge states.[268] This also impels us to reconsider differently our view of hydrogen bonding in these intriguing hybrid halide perovskites. Meanwhile, when using static *average* structures, replacement of the molecules having a dipole with an alkali metal such as Cs^+ may help to decipher whether the specific localization is mainly related to the specific dipolar orientations of the organic cations (*e.g.* $CH_3NH_3^+$ Figure 19b) on hand or primarily to the detailed structure of the inorganic perovskite framework. Last but not least, we also suggest that caution be exercised when implementing DFT structural optimization of low dimensional hybrid halide perovskites. In fact, it may lead to significant structural distortions such as larger β and δ tilt angles (Figure 17a,b) that have been shown in section 3.1.3.3 to have a direct impact on their electronic structure with for instance increased band gaps (Figure 17c,d) that should not be traced back to quantum confinement. Changing the crystallographic space group for DFT structural optimization may induce additional structural distortions with direct impact on computed electronic properties.[291,292] Another way to possibly tune confinement effects is to play with the thickness and composition of the organic layer that sandwiches the perovskite ones. It turns out that for most of the investigated layered structures, the first has minor effect on the computed electronic band

structure. For instance, in the series of alkylammonium lead iodide monolayers having from 4 up to 10 (and from 10 up to 18) carbon atoms in the alkyl chain, the increased size of the organic barrier does hardly alter band edge states and band gaps of the electronic band structure computed for the experimental room temperature structures.[94,206,262] The band gap jump between the two sets of chain length can be traced back to a phase transition (section 3.2) that induces larger out-of-plane octahedral tilting (Figure 17).[206] This is indicative of very small contribution from confinement effects and is in contradiction with results based on DFT optimized structures. For instance, predictions relevant to the room temperature optoelectronic properties of layered perovskites after systematic DFT structure optimization,[293] must be considered with caution. Similar procedures are known to lead to sizeable variations of the band structure, band gap and effective masses in the case of 3D halide perovskites.[294–296]

For small interlayer cations, especially for eclipsed configurations, electronic coupling between the perovskite layers may occur and lead to sizeable band dispersion in the direction of reciprocal space corresponding to the stacking axis, [83,204] thus reducing effect of quantum confinement. The nature of the organic cation in the interlayer may also have significant influence on the band diagram due to varying dielectric constants of the organic layer. This is illustrated in Figure 20 using an extreme case where, the dielectric contrast is reversed after I_2 intercalation in $(IC_6)_2[PbI_4]$ (Figure 20c-d).[69] The DFT band gap remains direct but is shown to decrease by 110 meV, (Figure 20a-b; 230 meV when including self-energy corrections, see section 4.3) and a set of narrow bands appears close to the Fermi level originating from the guest I_2 molecules. These bands show limited interaction with the levels of the inorganic layer and $(IC_6)_2[PbI_4]·2I_2$ can be considered as a weakly coupled composite. Halogen intercalation also reduces significantly the CBM bandwidth, which in turn increases its effective mass.
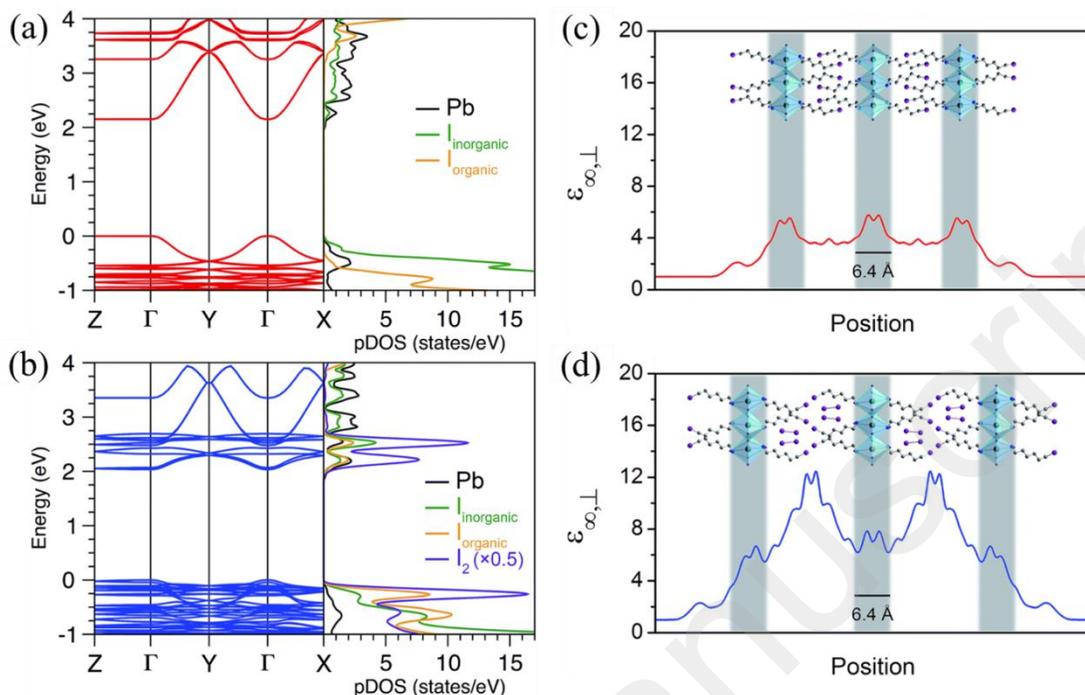
Figure 20. DFT computed electronic and dielectric properties for (a),(c) (IC$_6$)$_2$[PbI$_4$] and (b), (d) after I$_2$ intercalation leading to (IC$_6$)$_2$[PbI$_4$]·2I$_2$. (a), (b) Band structure and projected density of states. (c), (d) corresponding calculated high-frequency dielectric profiles $\epsilon_{\infty,\perp}$ computed from slabs of (c) (IC$_6$)$_2$[PbI$_4$] and (d) (IC$_6$)$_2$[PbI$_4$]·2I$_2$. Here, $\epsilon_{\infty,\perp}$ is the high-frequency dielectric constant perpendicular to the direction of layer propagation. Dark green, purple, blue, and grey spheres represent Pb, I, N, and C atoms, respectively. Hydrogen atoms are omitted for clarity. Reprinted with permission from [69] – Published by the Royal Society of Chemistry.

3.1.3.5 Rashba effect in layered halide perovskites

A pending question is: are Rashba or Dresselhaus effects predicted so far by DFT for 3D halide perovskites also observable in layered halide perovskites? A spinor-splitting leading to such effects is generally expected when the spatial inversion symmetry is broken, while the time-reversal symmetry still holds for all the electronic states.[93] In layered heterostructures of classical

60

semiconductors, it yields spin-related splitting properties in all the directions perpendicular to the stacking axis because the stacking axis usually coincides with a symmetry axis. On the contrary, the stacking axis and the symmetry axis are predicted to be perpendicular in many practical cases in multilayered perovskites. A spin degeneracy is then expected to remain along one of the in-plane axis.[66,297] Recent experimental results indicate that the observation of a Rashba or Dresselhaus effect might be possible in layered compounds (Figure 21).[298,299]

(a)

(b) inner branch   outer branch

[100]
[010]

(c)
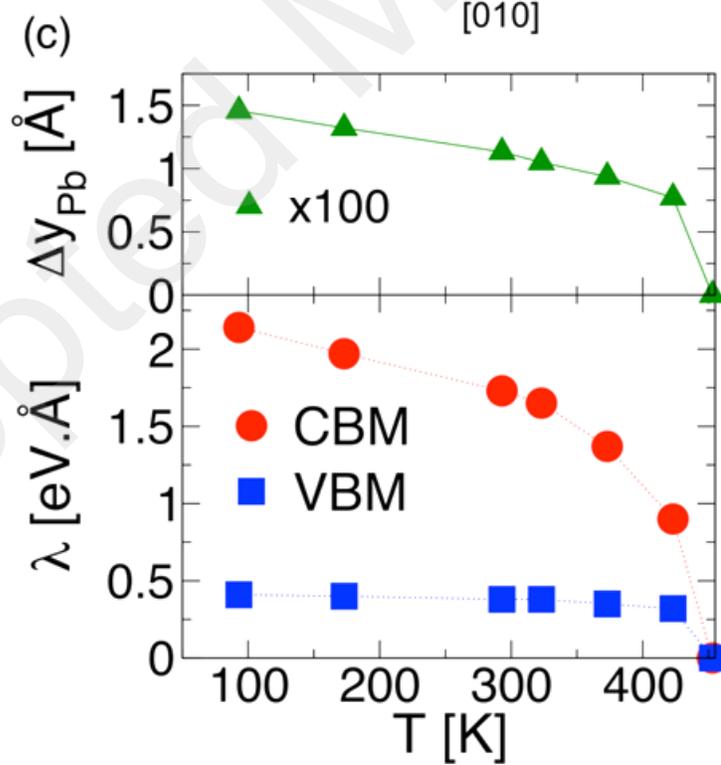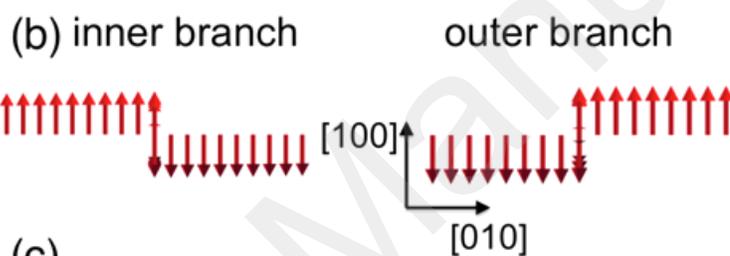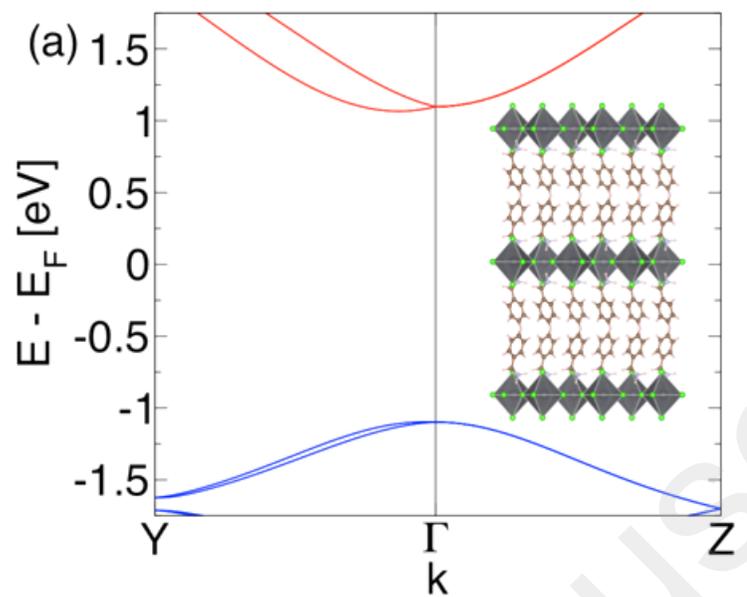
Figure 21. (a) Band structure of Bz2PbCl4 in the low temperature Cmc21 phase, computed with SOC. Blue and red bands correspond to occupied and unoccupied bands, respectively. (b) Spin textures for the inner and outer branches of the conduction band. (c) Temperature dependence of the Pb displacement along y and computed Rashba parameters for the conductionand valence bands. Reprinted with permission from ref [66]. Copyright 2015 American Chemical Society.

3.1.4. Effective masses from band structures

Among the input parameters of models aiming at investigating effect of quantum and dielectric confinement as well as for device empirical simulation including transport simulations, the effective mass of charge carrier is an essential ingredient. The commonly used unit of measurement is the rest mass m_0 of an electron (9.109 10^{-31} kg or 5.486 10^{-4} amu). It can be derived from electronic band structure calculations considering the band curvature near a high symmetry point of the BZ. As for other materials, deriving effective masses from DFT calculations raises technical issues. First and foremost, it relies on the assumption of parabolic band curvatures near the critical point and in the general case the effective mass has a tensor character as a result of anisotropy. In 3D halide perovskites, it has been demonstrated that the accuracy of effective masses much depends on the level of theory of the DFT approach,[93] and reliable estimates require self-consistent implementation of both relativistic (SOC) and many-body effects (sc-GW).[300] This may lead to erroneous conclusions, as for instance those derived for multilayered perovskites of varying n-value.[61] Unfortunately, implementation of SOC concomitantly with sc-GW is out of reach for most of the lower dimension halide perovskites as it is already a computationally challenging task for their 3D analogues.

Now, it has been shown that there is a direct relationship between the DFT computed band gaps and effective masses.[301] Using this relation of proportionality, the computed single particle DFT effective masses can be multiplied by the ratio between the experimental and DFT electronic band gaps. This procedure helped to reach good agreement between predicted and experimental effective masses for the $(CH_3(CH_2)_3NH_3)(CH_3NH_3)_{n-1}Pb_nI_{3n+1}$ series with n = 1 to 4 (Table 2). We also remind that this does not take the influence of thermal effects on the effective masses into account.

Table 2. DFT computed band gaps ($E_{g,DFT}$), experimental continuum band gaps ($E_{g,exp}$), experimental and DFT computed reduced masses $\mu = \left(\frac{1}{\mu} = \frac{1}{m_e} + \frac{1}{m_h}\right)$, as a function of n for $(CH_3(CH_2)_3NH_3)(CH_3NH_3)_{n-1}Pb_nI_{3n+1}$ multilayered perovskites.[275] Computed masses are given for the [100] in-plane direction and [001] (except [010] for n = 1) out-of-plane direction, before ($\mu_{r,DFT}$) and after ($\mu_{r,scaled}$) band gap correction. The experimental exciton reduced mass, $\mu_{r,exp}$, is derived from fitting the diamagnetic shifts obtained from magneto-absorption spectroscopy to semi-empirical simulations of the Wannier-Mott exciton as described in Ref. [[275]].

n	infinity	1	2	3	4
$E_{g,DFT}$ (eV)	0,41	1,28	0,91	0,67	0,66
$E_{g,exp}$ (eV)	1,55	2,80	2,44	2,25	2,15
$\mu_{r,exp}$	0,104[302]	0,221	0,217	0,201	0,196
μ_{DFT} [100]	0,054 (0,049[a])	0,106	0,086	0,063	0,056
μ_{DFT} [001]	0,041 (0,037[a])	0,109[b]	0,080	0,061	0,059
μ_{scaled} [100]	0,204 (0,186[a])	0,233	0,231	0,212	0,182

| μ_{scaled} [001] | 0,155 (0,140[a]) | 0,238[b] | 0,216 | 0,206 | 0,191 |

[a] computed from DFPT

[b] computed for the [010] direction

3.2. Concept of quantum confinement applied to multilayered halide perovskites

Before discussing the concept of quantum confinement applied to multilayered halide perovskites, it is useful to revisit some assumptions implicitly made by many authors performing theoretical analyses of the electronic structure of layer halide perovskites. Noteworthy as shown in the previous section, DFT simulations of the electronic properties of layered halide perovskite materials, usually assume the existence of a periodic lattice and a perfect lattice translational symmetry along the stacking axis for layered halide perovskites. 3D periodic Bloch functions are used to describe the electronic wavefunctions of the equivalent superlattice close to the electronic band gap: $\psi_{e,\mathbf{k}}(\mathbf{r}_e) = \frac{e^{\mathbf{k}.\mathbf{r}_e}}{\sqrt{V}} u_{e,\mathbf{k}}(\mathbf{r}_e)$ with a truly 3D periodic Bloch functions $u_{e,\mathbf{k}}(\mathbf{r}_e)$, where k is the 3D wavevector inside the BZ of the periodic lattice, V a normalization volume and $\mathbf{r}_e$ the position of the electron in real space. Such Bloch functions implicitly enforce delocalization of monoelectronic states along the stacking axis, although DFT studies on monolayered halide perovskite show that in most cases resulting superlattice effects are negligible.[64,65,76,69] Without electronic coupling between the inorganic perovskite layers, flat dispersions of the electronic bands are computed from the BZ center Γ to a point located at the edge (**Y** for example, Figure 19a) along the direction of the stacking axis. Monoelectronic states at the bottom of the CB or the top of the VB are thus degenerated along this line, and any superposition of the solutions corresponding to the k wavevectors between Γ and **Z,** shall then be considered as a possible solution as well. An opposite view consists in considering the perovskite

65

sheets as isolated entities from the electronic viewpoint leading to an alternative description of the electronic states close to the electronic band gap by:

$$\psi_{e,\mathbf{k}_t}(r_{te}, \mathbf{z}_e) = \frac{e^{\mathbf{k}_t \cdot \mathbf{r}_{te}}}{\sqrt{A}} u_{e,k_t}(\mathbf{r}_{te}, \mathbf{z}_e) \qquad (6)$$

with in-plane 2D periodic Bloch functions $u_{e,k_t}(r_{te}, \mathbf{z}_e)$ and $\mathbf{k}_t$ is the in-plane component of the wavevector, where A is a normalization surface, r_{te} the in-plane position of the electron and $\mathbf{z}_e$ the position along the stacking axis. In that case, the lack of out-of-plane periodicity or electronic coupling between the layers allows charge localization along the stacking axis. This description of monoelectronic states has been chosen for the simulation of the Wannier excitons.[31–33,275] Carrier localization close to only one perovskite sheet for both electron and hole may be justified in that case by the attractive electron-hole interaction. In practical cases, even weak superlattice effects may indeed lead to charge localization along the stacking axis as a result of thermal or defect-induced fluctuations of the vertical ordering. Strong electron-phonon interaction leading to polaron formation,[303,304] is another example where carrier localization along the stacking may occur. In order to analyze the localization of electronic states in the stack by DFT, very large supercell calculations including local lattice distortions and defects, as well as molecular dynamics[268] will be certainly useful in the future and lead to more realistic simulations of monoelectronic states.

In classical multiple QW systems, a 3D DOS can be reconstructed by merging 2D-like DOS related to electronic subbands both in the CB and VB (Figure 1), as a result of i) an increase of the QW thickness (n in the case of multilayered halide perovskites, *e.g.* Figure 19), ii) a superlattice effect related to electronic coupling between QW (influence of the organic barrier

for multilayered perovskites), iii) both effects occurring simultaneously. In the future, understanding how the crossover occurs in terms of electronic structures between monolayered (n = 1) and 3D (n = ∞) halide perovskites, and how the 2D DOS merges into a 3D-like DOS in that case is of great interest. A complete symmetry analysis of the electronic structure of multilayered perovskites is also still lacking, although the spinors have been described for monolayered compounds (Figure 16).[64]
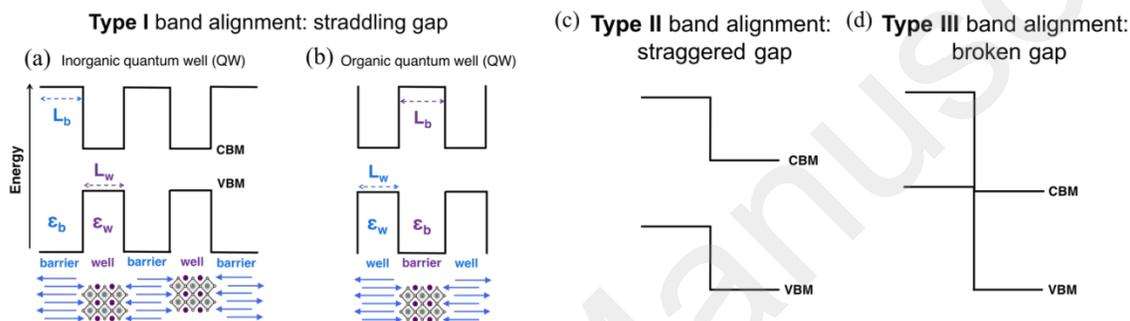
Figure 22. Schematic view of the three types of possible band alignments relative to VBM and CBM states of each material building the whole superlattice. (a) and (b) Type I band alignment in QW made of a well and a barrier of width and dielectric constant L_w/L_b and $\varepsilon_w/\varepsilon_b$, respectively: (a) Most common band alignment observed in hybrid halide perovskites illustrated for a layered structure where semiconducting perovskite sheets (mainly inorganic) alternate with organic layers having much wider band gaps. (b) Wider band gap perovskite and organic cation with smaller HOMO–LUMO gap result in the well/barrier roles of the organic and inorganic parts being switched. (c) and (d) Alternative band alignments obtained when shifting the electron affinity of the organic cation relative to the perovskite sheet, either affording a (c) type II alignment with a staggering of the energy levels or (d) a type III alignment having a broken gap.

For layered halide perovskites, the quantum confinement concept was discussed initially in terms of QW by several authors giving an appealing qualitative guidance for the researchers involved in the field of layered perovskites.[26,38,30] A favorable situation for optoelectronic properties corresponds to the so-called type I QW case (Figure 22a), where both electrons and holes are confined within the well, leading to an enhancement of the radiative recombination and stronger binding energies for the exciton than in a 3D material. Changing the QW thickness gives also additional flexibility to tune the emission energy. The validity of a type-I QW to decribe layered halide perovskites has been evaluated quantitatively using a specifically designed DFT-based approach.[94,206] This approach shows that most known multilayered halide perovskite structures correspond to type I QW with very deep confinement potentials in a composite W/B structure (Figure 23c). Except a few cases related to short organic cations in the barrier (section 3.1.3.4), the electronic coupling between the perovskite sheets vanishes and the electronic band gap of the heterostructure does not depend strongly on the barrier thickness. In fact, figure 23 reports the computed band alignments for various $(C_jH_{2j+1}NH_3)_2PbI_4$ compounds with $4 \leq j \leq 18$. The electronic band gap computed for the RT crystallographic structures, undergoes a step-like increase for $j \geq 10$. This increase is related to a change of the molecular conformations leading to an increase of the in-plane and out of-plane tilt angles, being well reproduced within a Cs_2PbI_4 model structure (section 3.1.3.3 and Figure 17), *i.e.* without need of a quantum confinement effect.
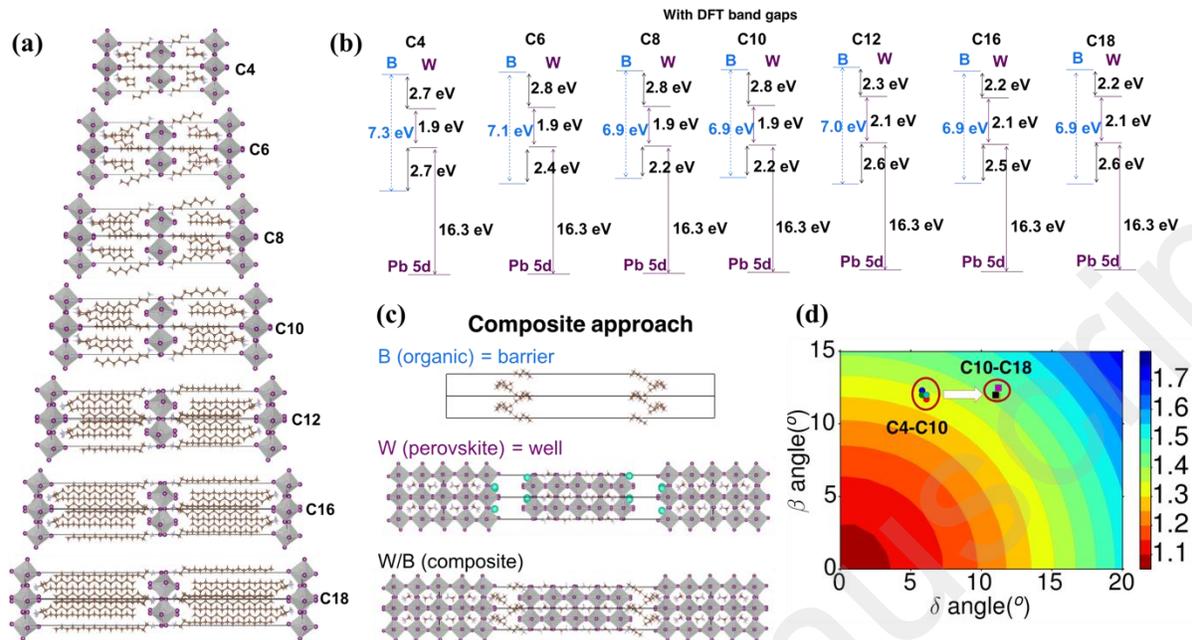
Figure 23. Band alignment for various barrier thicknesses. (a) Structures of $(C_jH_{2j+1}NH_3)_2PbI_4$. Cj next to the structures refers to the number (j) of carbon atoms in the alkyl chain. (b) Computed band alignments for the alkyl-based structures shown in panel a, taking crystallographic data recorded at room temperature. Since all the experimental band gaps are not available for the series, DFT band gaps for CB lineup were used. (c) Schematics of the composite model used to perform band alignment calculations defining the organic barrier (B), the perovskite well (W) of the whole composite structure (W/B). (d) Computed band gaps plotted on the 2D color map illustrating the variation of the band gap with octahedral in-plane (beta) and out-of-plane (delta) tilt angles for a Cs_2PbI_4 model structure (Figure 17). Adapted with permission from ref[206]. Copyright 2018 American Chemical Society.

To compute the variation of the monoelectronic subband energies, the electronic band gap [61] or the envelope functions of the edge states,[32] it may appear appealing, at first sight, to use the type I QW picture (Figure 22a) together with an empirical transverse effective mass

69

Hamiltonian for the out-of plane carrier motion. The validity of such an approach can be inspected considering the series of BA-based multilayered perovskites. Figure 24 reports the band gap energy variation of $(C_6H_{13}NH_3)_2(CH_3NH_3)_nPb_nI_{3n+1}$ with n = 1-4 as a function of the QW width using a transverse effective mass model.[61] The confinement potentials used for the calculation are indicated as inset in the figure. A seemingly fair agreement is obtained with the reported experimental values, except for an overestimation of the band gap for the thinnest (n = 1) compound.
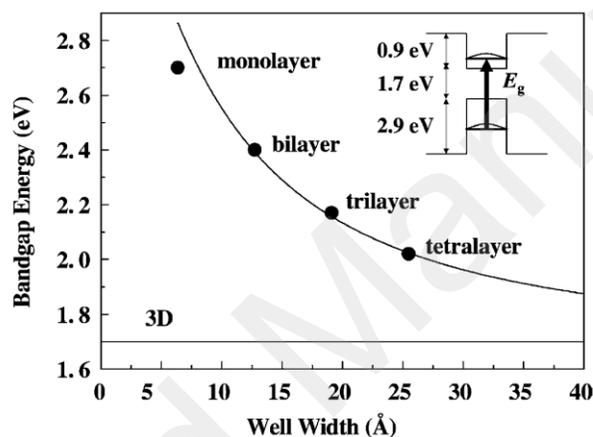
Figure 24. Band gap energy of $(C_6H_{13}NH_3)_2(CH_3NH_3)_nPb_nI_{3n+1}$ as a function of the well width. The solid line represents the band gap energy calculated using a transverse effective-mass approximation. The inset provides the confinement energies and band gap used in the calculation. Reprinted with permission from ref [61]. Copyright © National Institute for Materials Science in partnership with Taylor & Francis, reprinted by permission of Taylor & Francis Ltd, http://www.tandfonline.com on behalf of © National Institute for Materials Science in partnership with Taylor & Francis.

The overestimation of the band gap for the monolayered compound is in fact not a detail. Indeed, any attempt to combine the type I QW picture and confinement potentials with an

effective mass Hamiltonian to better fit the whole curve leads to unrealistic parameters.[94,206] Thus, the transverse effective mass model has no firm theoretical basis for layered halide perovskites, also predicting a strong electronic coupling between QW (perovskite sheets) in contradiction with DFT results (Figure 19).[94] The fundamental reason for this inconsistency is deeply rooted into the classical representation of the electronic states in QW superlattices:[94]

$$\psi_e(r_e) \approx \sum_i F_i(r_e) U_{e,i}(r_e) \qquad (7)$$

where $F_i(r_e)$ are slowly varying envelope functions along the stacking axis and $U_{e,i}(r_e)$ periodic and rapidly oscillating ones. In order to understand the reasons for the failure of the type I QW picture associated to an effective mass model, it is important to realize first that for most multilayered halide perovskites, the actual QW are ultrathin. The equivalent QW thickness L_{QW} in multilayered perovskites of general formula $A'_2A_{n-1}B_nX_{3n+1}$ is typically on the order of $L_{QW}(nm) = n \times 0.6$ while in most cases $n < 3$. Ultrathin QW can also be encountered in conventional semiconductor heterostructures, but then great care should be taken to various effects such as the non-parabolicity of the electronic dispersions that requires to go beyond the effective mass approximation in order to compute the envelope functions $F_i(r_e)$. The second fundamental issue is related to the implicit assumption that the periodic functions of the heterostructure entering formula (7) can be identified to bulk Bloch functions of both W and B partners of the composite structure (Figure 22a) $U_{e,i}(r_e) \approx u_{e,W}(r_e) \approx u_{e,B}(r_e)$. This assumption holds true in many QW superlattices of classical semiconductors, because W and B partners are only slightly different by nature such as in GaAs/AlAs or InGaAs/InP based heterostructures. The truly hybrid character of multilayered halide perovskites, with W being

71

essentially inorganic and B organic (Figure 23c), obviously breaks this assumption. It is especially hard to make a direct connection between the properties of monolayered compounds and the properties of the reference 3D material (*e.g.* MAPbI$_3$). The chemical motif in monolayered compounds contains terminal halides along the stacking axis, by contrast to the corresponding 3D network. For those reasons any reliable theoretical description of hybrid layered halide perovskites should be based on DFT calculations although account of many-body corrections including spin-orbit coupling effect remain challenging.[64,203,205,265,293,305]
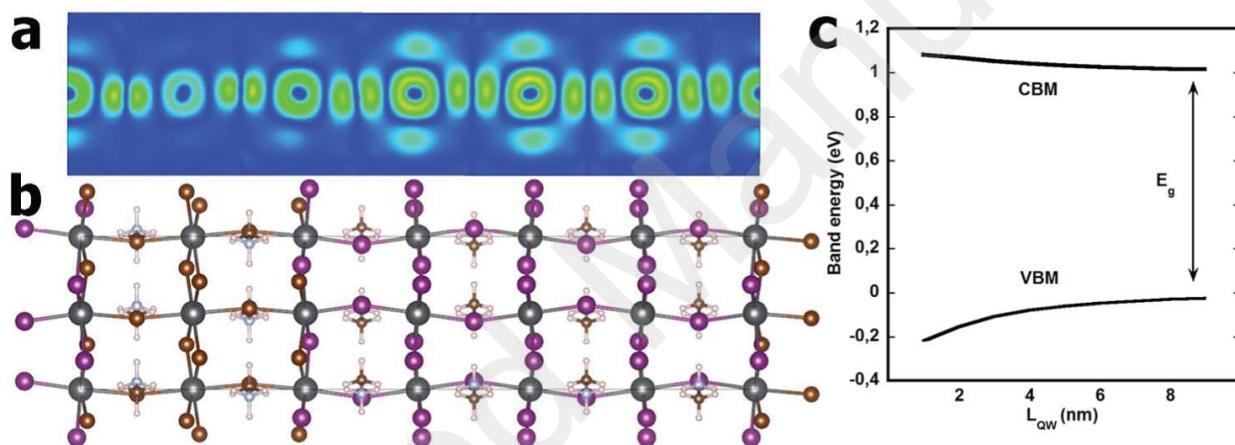
Figure 25. (a) Representation of the electronic density for the VBM of a short superlattice along the [010] direction of the low temperature bulk orthorhombic cell, containing two CH$_3$NH$_3$PbI$_3$ cells and one CH$_3$NH$_3$PbBr$_3$ cell. (b) Overview of the atomic structure. The diagrams are computed at the DFT level with a GGA exchange-correlation functional.[248] SOC is not considered. (c) Electron (CB) and hole (VB) ground-state energies as a function of QW thickness (L$_{QW}$) computed with an empirical effective mass model. Reprinted with permission from ref [67]. Copyright 2015 American Chemical Society.

Figure 25 shows a hypothetic short superlattice containing two $CH_3NH_3PbI_3$ cells and one $CH_3NH_3PbBr_3$ cell. In such a case, both compounds in the well and in the barrier share similar Bloch basis wavefunctions $U_{e,i}(r_e) \approx u_{e,W}(r_e) \approx u_{e,B}(r_e)$ and electronic density undergoes a slow variation along the stacking axis, corresponding to the envelope function picture $F_i(r_e)$. This shows that in such a case, the transverse effective mass approximation is valid, provided that non-parabolicity effects can be neglected.

4. MULTILAYERED HALIDE PEROVSKITES: DIELECTRIC CONFINEMENT

Summary: The localization of charge carriers in halide perovskite is strongly affected by the polarizability of the surrounding polar perovskite lattice. These self-energy contributions are enhanced in low dimensional perovskite structures and nanostructures by dielectric inhomogeneities. The latter also influence electron-hole pair interactions, giving rise to strong excitonic resonances. In this section, the theoretical schemes developed so far are reviewed. Current understanding relies on a combination of first-principles and empirical approaches, including semi-empirical resolution of the Bethe-Salpeter equation. Comparison to Van der Waals ,heterostructures[306] are also emphasized to provide further insight into multilayered halide perovskites.

4.1. Excitons

The enhancement of the electron-hole interaction by dielectric confinement effects has been recognized, in the 1990s, by all the experimental groups working in the field and shown to lead to large binding energies for the exciton in monolayered perovskites. A few modelling attempts were based either on average dielectric constant or more elaborate dielectric well

73

models with abrupt interfaces.[31–33] Since recently, realistic descriptions of the dielectric profiles are affordable thanks to specifically designed DFT-based approaches.[307,81,95,83,69,275,206] It was also shown experimentally for crystals of $(C_6H_{13}NH_3)_2PbI_4$ (Figure 26,[62] and more recently bromide compounds with $((C_4H_9NH_3)_2PbBr_4)$ and $(C_6H_5C_2H_4NH_3)_2PbBr_4))$[308] as well as a $(C_4H_9NH_3)_2PbI_4$ nanosheet (Figure 27,[309]), that the excitonic bound state series (Ns, with N = 1, 2, 3...) exhibits strong deviations from the well-known 2D hydrogenic series, which yields the following expression for the binding energies $E_{b,N}$:

$$E_{b,N} = \frac{Ry}{\left(N-\frac{1}{2}\right)^2} \qquad (8)$$

with Ry being the Rydberg energy of the equivalent 3D hydrogenic system. These deviations were attributed to dielectric confinement effects. The availability of precise crystallographic structures and the development of refined computational techniques for the electronic band structures, now allow addressing quantitatively the problem of the deviation of $E_{b,N}$ from the 2D hydrogenic series in multilayered perovskites (Figure 28). [275]
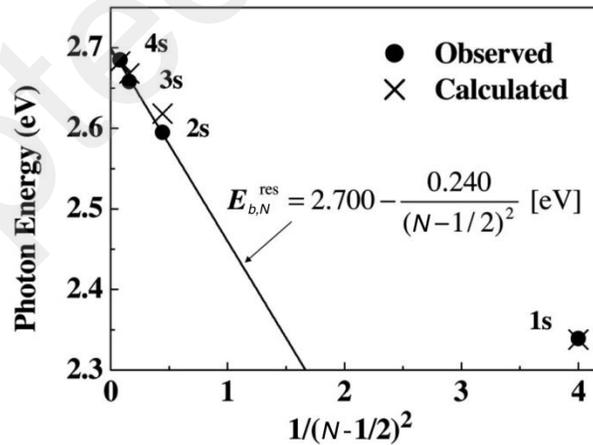
Figure 26. Resonance energies of Wannier-series excitons in $(C_6H_{13}NH_3)_2PbI_4$ as a function of $1/\left(N-\frac{1}{2}\right)^2$. Closed circles and crosses represent the observed and calculated

energies of the excitons, respectively. The solid line shows the fitting based on a simple two-dimensional Wannier exciton model. Reprinted with permission from ref [62]. Copyright 2005 American Physical Society.
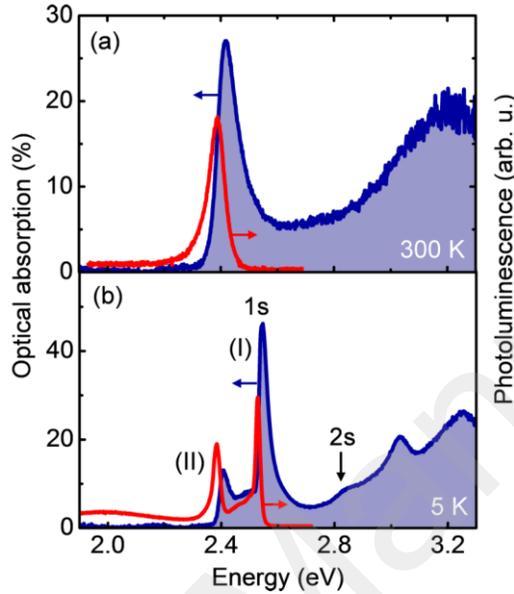
Figure 27. (a) Room-temperature optical absorption and PL spectra of an exfoliated $(C_4H_9NH_3)_2PbI_4$ nanosheet. (b) Optical absorption and PL from an organic-inorganic perovskite crystals nanosheet at 5 K. In about half of the nanosheets, an abrupt 100meV blueshift of the 1s excitonic state is observed at about 250K from position (II) to (I). It is attributed to a structural phase transition. Domains of both phases may coexist within a single flake as reported here. For each nanosheet, the Ns series is related to the dominant 1s excitonic peak at 5K. Reprinted with permission from ref [309]. Copyright 2015 American Physical Society.
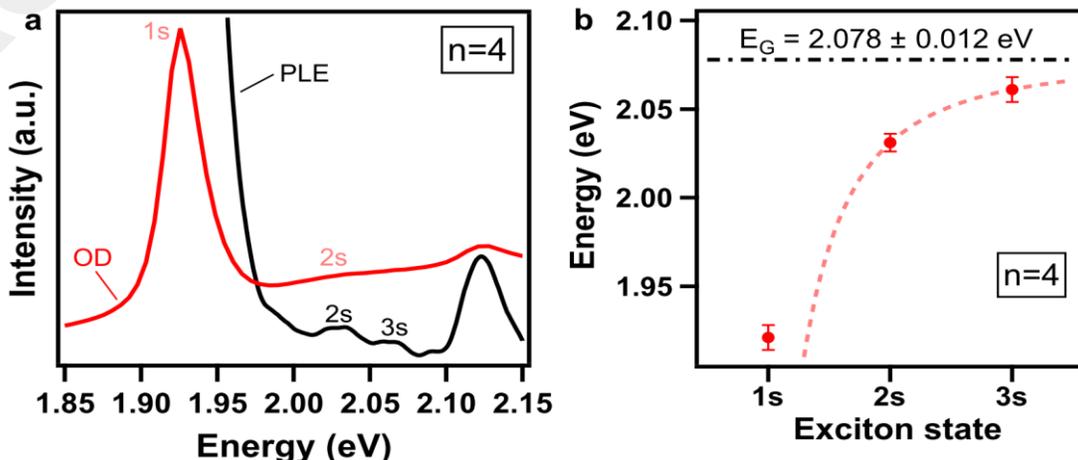
Figure 28. (a) Optical density (OD) and photoluminescence excitation (PLE) of the $(CH_3(CH_2)_3NH_3)(CH_3NH_3)_3Pb_4I_{13}$ multilayered perovskite (n = 4) clearly showing the exciton ground state 1s, the excited exciton states 2s and 3s. (b) Energy of the exciton Rydberg states for the multilayered perovskite n = 4. Dashed line is a fit to the 2s and 3s states with the 2D hydrogen model of exciton Rydberg series. Reprinted with permission from ref [275]. *Copyright 2018 NPG Publishing group.*

4.2. Single particle self-energies and electron-hole pair interactions – Shortcomings of simplified descriptions for layered perovskites

In order to properly understand the concept of dielectric confinement and its impact on the electronic and excitonic properties of composite compounds such as multilayered perovskites, it is important to review first a few basic physical concepts. The textbook of Jackson on classical electrodynamics[310] allows introducing in a simple manner the mutual pair interaction from opposite charges, while single particle self-energy contributions are considered as well. The mutual interaction energy of two point charges $\pm e$ (Figure 29) reads:

$$V(\boldsymbol{r_h}, \boldsymbol{r_e}) = \frac{-e^2}{4\pi \, \varepsilon_M |r_h - r_e|} \,, \qquad (9)$$

where ε_M is the macroscopic dielectric constant.
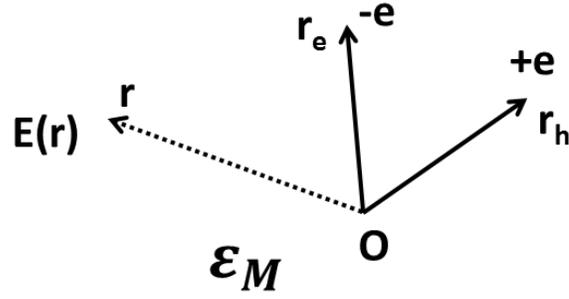
Figure 29. Classical representation of two opposite point charges $\pm e$ (electron (e) and hole (h)) located in a dielectric medium, whose polarizability is represented by a single effective parameter, the macroscopic dielectric constant ε_M. The analytic expression of the electrostatic field $E(r)$ produced by the two charges at a general position r is given by expression (13).

For a Wannier-Mott exciton, the mutual interaction between an electron and a hole is computed from a similar simple expression. It leads to the resolution of a Wannier-Mott equation for the relative motion of the electron-hole pair, which is directly connected in 3D to the well-known solution of the Schrödinger equation describing the electronic states in the hydrogen atom. This approach was generalized for any fractional space dimension α between 1 and 3, leading to the following Schrödinger equation for a Wannier-Mott exciton:[311]

$$\left[\frac{-\hbar^2}{2\mu\rho^{\alpha-1}} \frac{\partial}{\partial\rho} \left[\rho^{\alpha-1} \frac{\partial}{\partial\rho} \right] + \frac{l^2}{2\mu\rho^2} - \frac{e^2}{4\pi\,\varepsilon_M\rho} \right] \psi(\rho,\theta) = \left(E - E_g \right)\psi(\rho,\theta) \qquad (10)$$

where E_g is the electronic band gap of the semiconductor, μ is the reduced mass $\left(\frac{1}{\mu} = \frac{1}{m_e} + \frac{1}{m_h} \right)$, l^2 corresponds to the angular-momentum operator, $\rho = |r_h - r_e|$ is the radial distance between the electron and hole ($0 \leq \rho \leq \infty$) and θ the related angle ($0 \leq \theta \leq \pi$). The discrete bound state energies are given by a generalized Rydberg series:

$$E_{b,N} = \frac{Ry}{\left(N + \frac{\alpha-3}{2} \right)^2} \qquad (11)$$

77

where N =1,2,3…. This expression allows recovering the 2D and 3D hydrogenic series respectively for $\alpha = 2$ and $\alpha = 3$, and also conveniently provides a simple way to analyze anisotropic or confined systems considering α as an adjustable parameter, including a complete calculation of the absorption spectrum.[311] This method was used by Tanaka and coworkers [59] to analyze spectroscopy results on the 1s and 2s exciton resonances in $(C_6H_{13}NH_3)_2PbI_4$ leading to a fractional dimension $\alpha = 2.3$. In classical semiconductor QW it is in principle further possible to account for both the effect of finite thickness and reduced mass mismatch between the well and barrier materials, by using expressions such as $\alpha = 3 - e^{-\frac{L}{2a_B}}$ where a_B is the Bohr radius and L an effective thickness.[312] This approach was recently refined to study the 1s exciton bound state energy variation as a function of the number of inorganic layers (QW thickness) in halide perovskite multilayered perovskites, by tuning the value of α as a function of the QW thickness with (Figure 30):[275]

$$\alpha = 3 - \gamma e^{-\frac{L_W}{2a_B}} \qquad (12)$$

The additional empirical factor γ was introduced to better account for the dielectric confinement effect and for the deviation from a pure quantum confinement enhancement of the exciton binding energy.
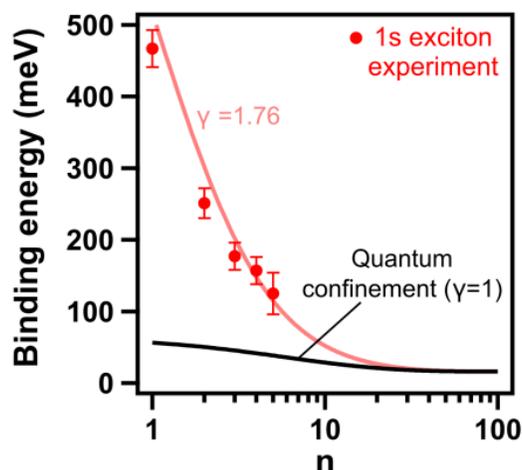
Figure 30. Results for the binding energy of the exciton ground state, showing the enhancement of the binding energy due to dielectric confinement. The black curve corresponds to the scaling law using expression (11) with γ = 1 in expression (12). The red curve gives the general scaling law of the exciton binding energy with the perovskite layer thickness using γ = 1.76. Ry = 16 meV, a_0 = 4.6 nm, and L_w = 0.6292 × n in nanometers. Reprinted with permission from ref [275]. Copyright 2018 NPG Publishing group.

It allows predicting that the exciton binding energy in multilayered perovskites is larger than room temperature thermal fluctuations up to n~20 (equivalent QW thickness of ~12.6 nm). A fine description of the complete series of the Ns resonances as a function of the QW thickness is not possible and the effect of dielectric confinement is not correctly captured by such simplified approaches.

More, the underlying representation of electron and hole as point charges, which corresponds to a convenient expression of the mutual interaction potential, simultaneously leads to a major physical inconsistency on the associated self-energies. As quoted by Jackson in his textbook,[310] a negative potential energy is in apparent contradiction with the positive expression of the

electrostatic energy density $w(\boldsymbol{r}) = \frac{\varepsilon_M \mathrm{E}(r)^2}{2}$. The total electric field $\mathrm{E}(\mathbf{r})$ produced by the two

opposite charges (Figure 29) is indeed:

$$E(\boldsymbol{r}) = \mathrm{e}\frac{\mathbf{r}-r_h}{4\pi\,\varepsilon_M|\mathbf{r}-r_h|^3} - \mathrm{e}\frac{\mathbf{r}-r_e}{4\pi\,\varepsilon_M|\mathbf{r}-r_e|^3} \qquad (13)$$

leading to three terms for the electrostatic energy density:

$$w(\boldsymbol{r}) = \frac{\mathrm{e}^2}{32\pi^2\,\varepsilon_M|\mathbf{r}-r_h|^4} + \frac{\mathrm{e}^2}{32\pi^2\,\varepsilon_M|\mathbf{r}-r_e|^4} - \frac{\mathrm{e}^2(\mathbf{r}-r_h).(\mathbf{r}-r_e)}{16\pi^2\,\varepsilon_M|\mathbf{r}-r_h|^3|\mathbf{r}-r_e|^3} \qquad (14)$$

The last term is negative and, after integration over space, allows recovering the mutual

interaction energy between the two charges (expression (9)). The first two terms are positive

making the sum of the three terms positive. They are thus necessary to solve the above-

mentioned paradox. These first two terms are only related to one charge (either $+e$ or $-e$) and

called for that reason self-energies. They correspond to the interaction of a single charge with the

background medium, represented by the electron gas in the VB of a semiconductor when

considering $\varepsilon_M = \varepsilon_\infty$. At this level of theory, a major problem arises, as the integration of the

first and second terms over space diverges. This inconsistency is related to the representation of

the interacting electron and hole by point charges, and quantum theory approaches are required

for a proper description. It also indicates that the simple representation of the mutual interaction

between the electron and hole in a Wannier-Mott equation for the exciton can only be considered

as an approximation.

More, the representation of the medium polarizability by a single dielectric parameter ε_M

is not suited for complex situations such as the one encountered in multilayered halide

perovskites. Indeed, these materials are composite and inhomogeneous materials at the atomic

scale (*e.g.* Figure 23a,c). In the framework of electrodynamics, the retarded response of the

polarization induced in a medium by an electric field is expressed by:

$$P(r, t) = \varepsilon_0 \iint \chi(r, r', t, t') E(r', t') d^3 r' dt' \qquad (15)$$

where $\chi(r, r', t, t')$ is the two-point susceptibility. For a system at equilibrium, this quantity can be considered homogeneous in time, depending only on $t - t'$. For a continuous dielectric medium, spatial homogeneity leads in addition to a $r - r'$ dependence of the susceptibility $\chi(r - r', t - t')$. After double Fourier transform, a linear expression can be obtained:

$$P(q, \omega) = \varepsilon_0 \chi(q, \omega) E(q, \omega) \qquad (16)$$

It shows that a better description of the problem relies on a refined expression of the macroscopic dielectric tensor $\varepsilon_M(q, \omega)$, including wave vector q and frequency ω dependencies. However, for planar systems at the nanometer scale, such as QWs, the spatial homogeneity assumption breaks down.[313] This assumption is related to neglecting wavelength components smaller than the lattice parameter in periodic solids, which can more or less be justified in bulk solids in some situations (vide infra), but not in dielectric heterostructures especially close to the interfaces. This is at the heart of the so-called "dielectric confinement" effect.

At the atomic scale in solids, the concept of homogeneity is related to the crystal lattice periodicity. In a bulk periodic solid, the local 'microscopic' electric field is given at the atomic scale by (time dependence is not written for sake of clarity):

$$E(r + R) = \sum_{q, G} e^{iG.r} E_G(q) \qquad (17)$$

where R is a crystal lattice vector, G a wavevector of the associated reciprocal lattice, r a vector representing a position within the primitive cell and q a wavevector within the BZ. The 'macroscopic' electric field $E_M(R)$ is defined at the nanoscale by averaging the local field over the primitive cell: $E_M(R) = \frac{1}{V_{cell}} \int_{cell} E(r + R) d^3 r$. The Fourier transform of the 'macroscopic' electric field is then defined by retaining only the $G = 0$ component of the 'microscopic' electric

field in momentum space $E_M(q) = E_{G=0}(q)$. The q dependence allows spatial variation of the 'macroscopic' electric field over distances greater than the primitive cell dimension. Similar considerations for the 'microscopic' two-point dielectric permittivity in a periodic solid $\varepsilon(r + R, r' + R')$, where R, R' are lattice vectors, leads to the definition of a matrix $\varepsilon_{G,G'}(q)$ after Fourier transform $\varepsilon(q + G, q' + G') = \varepsilon_{G,G'}(q)\delta_{q,q'}$. The 'macroscopic' dielectric constant is then defined by $\varepsilon_M^{-1}(q) = \varepsilon^{-1}{}_{G=0,G'=0}(q)$. Notice that the value of $\varepsilon_M(q)$ is related to a single component of the inverse of the dielectric matrix $\varepsilon^{-1}{}_{G=0,G'=0}(q)$ and not of the matrix itself $\varepsilon_M(q) \neq \varepsilon_{G=0,G'=0}(q)$. This stems from inclusion of local field effects.[314]   It shows that considering 'macroscopic' dielectric constants in dielectric heterostructures instead of truly 'microscopic' quantities, may lead to severe approximations if the averaging of the properties over distances on the order of a unit cell or a bond length in a covalent solid is not justified. In such cases, it is necessary to consider advanced descriptions of the electronic structures in order to better account for the dielectric properties. This is precisely one of the issues, when considering composite hybrid materials such as layered halide perovskites, with strong inhomogeneities over short length scales.

4.3. Many-body approaches to the single particle self-energies and electron-hole interaction

In quantum many-body theory of bulk materials, single particle self-energies can be calculated in the GW approximation from :[315]

$$\Sigma(r, r', \omega) = i \int \frac{dE'}{2\pi} e^{-i\delta E'} G(r, r', E - E') W(r, r', E') \tag{18}$$

where $\delta = 0^+$ (approaches zero from positive values), $G(\mathbf{r}, \mathbf{r}', E - E')$ is the single-particle Green's function and $W(\mathbf{r}, \mathbf{r}', E')$ the screened Coulomb interaction W. The screened Coulomb interaction $W(\mathbf{r}, \mathbf{r}', \omega)$ can be computed from the unscreened interaction $V(\mathbf{r}, \mathbf{r}', \omega)$ when the two-point 'microscopic' dielectric permittivity is known:

$$W(\mathbf{r}, \mathbf{r}', \omega) = \int \varepsilon^{-1}(\mathbf{r}, \mathbf{r}'', \omega) V(\mathbf{r}'', \mathbf{r}', \omega) \, d^3\mathbf{r}'' \qquad (19)$$

Nowadays, single particle self-energies are often used to successfully correct the well-known under-estimation of the electronic band gaps of bulk semiconductors computed at the DFT atomistic level.[301] However performing such calculations for very large heterostructures, like layered halide perovskites, has a high and unaffordable computational cost, including the computation of the 'microscopic' two-point dielectric permittivity $\varepsilon(\mathbf{r}, \mathbf{r}'', \omega)$. More, the physical meaning of the dielectric confinement effect appears more clearly in simpler semi-empirical approaches (vide infra). Although the proper evaluation of $\varepsilon(\mathbf{r}, \mathbf{r}'', \omega)$ is a major issue from the computational view point, it shall not be forgotten that any modification of the dielectric permittivity by carrier injection, dielectric confinement effect or coupling to optical phonons shall affect the exciton binding energy, but also the single particle self-energies and thus in turn the electronic band gap.

In quantum many-body approaches of the two particles problem for an electron and a hole, the BSE yields the exciton energies and wavefunctions.[254] It can be solved in various ways, by iterative inversion of a Dyson-like equation or by constructing the exciton wavefunction as a sum of electronic transitions between VB and CB states obtained from a DFT+GW initial calculation:[316]

$$\psi(\mathbf{r}_e, \mathbf{r}_h) = \sum_{vck} A^{vck} \, \psi_{v\mathbf{k}}{}^*(\mathbf{r}_h) \psi_{c\mathbf{k}}(\mathbf{r}_e) \qquad (20)$$

where A^{vck} is the exciton envelope function, $\psi_{ck}(\boldsymbol{r_e})$ $(\psi_{vk}(\boldsymbol{r_h}))$ the CB (VB) monoelectronic state wavefunctions. An effective Hamiltonian is obtained for the envelope function containing a diagonal related to the single particle eigenstates and a nondiagonal part, including both a statically screened Coulomb interaction and an unscreened exchange interaction (this last contribution is not reported here):

$$\widehat{\mathrm{H}}_{c'v'}^{cv}(\boldsymbol{k},\boldsymbol{k'}) = \big(E_c(\boldsymbol{k}) - E_v(\boldsymbol{k})\big)\delta_{c,c'}\delta_{v,v'}\delta_{k,k'} + W_{c'v'}^{cv}(\boldsymbol{k},\boldsymbol{k'}) \tag{21}$$

where the screening of the Coulomb interaction $W_{c'v'}^{cv}(\boldsymbol{k},\boldsymbol{k'})$ is again related to the inverse of the dielectric matrix $\varepsilon^{-1}{}_{G,G'}(\boldsymbol{q})$ ($\boldsymbol{q} = \boldsymbol{k} - \boldsymbol{k'}$). This approach was used for the exciton in 3D perovskites in 2016,[317] but similar theoretical analyses of the exciton in layered perovskites are extremely rare due to the large size of the system. It was performed only for a few monolayered compounds (see (EDBE)PbX$_4$ (EDBE = 2,2-(ethylenedioxy)bis-(ethylammonium), X = Cl, Br) on Figure 31).[240,304,318]
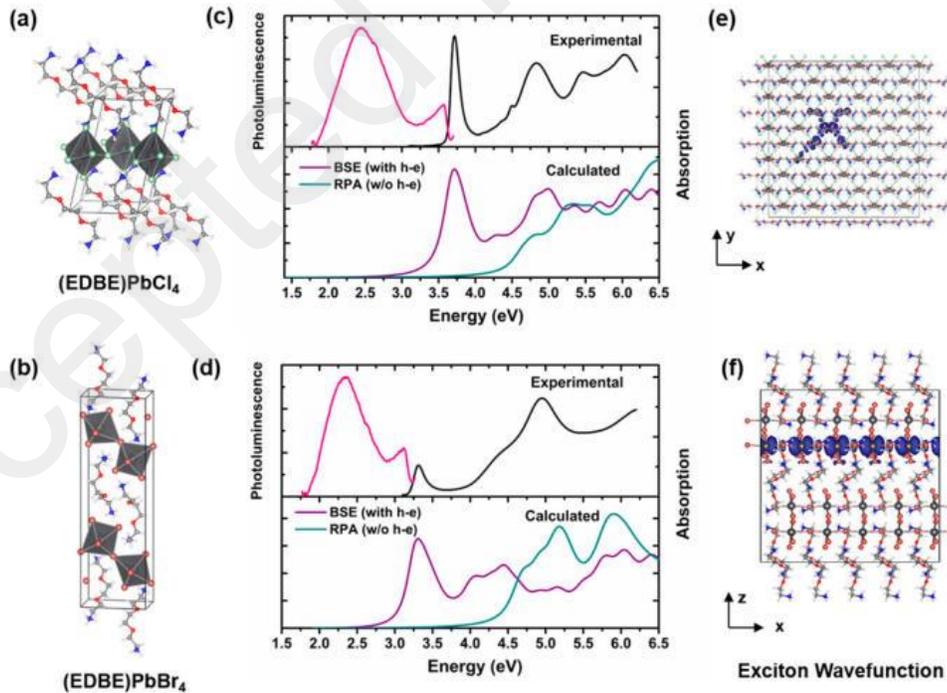
Figure 31. Crystallographic, optical, and excitonic characteristics of the two-dimensional (EDBE)PbCl4 and (EDBE)PbCl₄ hybrid perovskites: (a,b) crystal structures; (c,d) experimental absorption and PL spectra at room temperature (upper panel) and calculated absorption spectra with and without consideration of hole−electron (h−e) interactions (bottom panel); and (e,f) illustration of the exciton wave functions corresponding to the excitonic peaks. Reprinted with permission from ref [304]. Copyright 2017 American Chemical Society.

Large exciton binding energies were obtained from the calculation for 1s resonance in reasonable agreement with the experimental results, but no results related to the higher orders (2s,3s, …) of the exciton resonances were given and the broadening of the 1s exciton resonance was also overestimated (Figure 31). More, due to the large size of the systems, single particle *energies* $E_c(\mathbf{k}), E_v(\mathbf{k})$ and wavefunctions were only evaluated at the DFT level. Adhoc scissor corrections on the electronic band gaps were then applied to match the experimental absorption spectra. This interesting contribution clearly shows the possibilities and the limitations of such DFT-based atomistic approaches to scrutinize the exciton in layered halide perovskites.

A simplified Hamiltonian can be used to reduce the computational complexity: [316]

$$\widehat{H}_{c'v'}^{cv}(\mathbf{k}, \mathbf{k}') = \left(E_g + \frac{\hbar^2 k^2}{2\mu}\right)\delta_{c,c'}\delta_{v,v'}\delta_{\mathbf{k},\mathbf{k}'} - \frac{e^2}{\varepsilon_\infty q^2} \qquad (22)$$

After Fourier transform of the corresponding Schrödinger equation, the 3D Wannier-Mott equation in position space is recovered.[316] The electronic band gap E_g can be either evaluated from a DFT calculation including self-energy corrections or considered as an empirical input parameter. The reduced effective mass μ and the macroscopic dielectric constant ε_∞ may also be considered as empirical inputs.

In parallel with the development of many-body theories based on DFT, semiconductor Bloch equations were proposed to study the influence of many-body effects on the optoelectronic properties of semiconductors.[313] These equations describe the optical response of semiconductors under low or high levels of excitation and can be coupled to Maxwell's equations. The single particle energies are usually computed from the empirical effective mass approximation for single band Hamiltonians or from the **k.p** approximation for multiband empirical Hamiltonians. At low carrier injection and considering non-interacting electron-hole pairs, an effective Hamiltonian is obtained for the envelope function:

$$\widehat{H}_{c'v'}^{cv}(\boldsymbol{k}, \boldsymbol{k}') = \left(E_g + \frac{\hbar^2 k^2}{2\mu}\right)\delta_{c,c'}\delta_{v,v'}\delta_{k,k'} + W_{c'v'}^{cv}(\boldsymbol{k}, \boldsymbol{k}') \tag{23}$$

This effective Hamiltonian is similar to the previous one, but allows mixing an empirical description of the monoelectronic states with refined expressions of the electron-hole pair interaction in momentum space beyond the expression suited for 3D Wannier-Mott equation ($W_{c'v'}^{cv}(\boldsymbol{k}, \boldsymbol{k}') = -\frac{e^2}{\varepsilon_\infty |\boldsymbol{k}-\boldsymbol{k}'|^2}$). The excitons can be studied in 3D bulk semiconductors, but also in QWs provided that the proper expression of the screened interaction is used.[319] An equivalent approach at the same level of theory consists in computing the exciton Green function $G(\boldsymbol{k}, \hbar\omega + i\Gamma)$ from a Dyson like equation by iterative inversion to describe bulk 3D[320] or QW[321] semiconductors:

$$G(\boldsymbol{k}, \hbar\omega + i\Gamma) = G_0(\boldsymbol{k}, \hbar\omega + i\Gamma) + \frac{1}{\mu(\boldsymbol{k})}\sum_{\boldsymbol{k}'} G_0(\boldsymbol{k}, \hbar\omega + i\Gamma)W(\boldsymbol{k}, \boldsymbol{k}')G(\boldsymbol{k}', \hbar\omega + i\Gamma) \tag{24}$$

where Γ is a broadening factor, $\mu(\boldsymbol{k})$ is the dipole matrix element characteristic of the oscillator strength of the optical transition between the CB and VB and $G_0(\boldsymbol{k}, \hbar\omega + i\Gamma) = \frac{\mu(\boldsymbol{k})}{\left(E_g + \frac{\hbar^2 k^2}{2\mu} - \hbar\omega - i\Gamma\right)}$ is the Green function for interband free carrier transitions.

For 3D semiconductors the optical susceptibility is computed using the $G(\boldsymbol{k}, \hbar\omega + i\Gamma)$ solution from: $\varepsilon_0 \chi(\hbar\omega) = \frac{2}{V}\sum_{\boldsymbol{k}} \mu^*(\boldsymbol{k}) G(\boldsymbol{k}, \hbar\omega + i\Gamma)$ where V is a normalization volume. This method was used for 3D perovskites[322] (Figure 32) and for monolayered perovskites[76,69,275] including the effect of dielectric confinement in $W(\boldsymbol{k}, \boldsymbol{k}')$ (Figure 33).
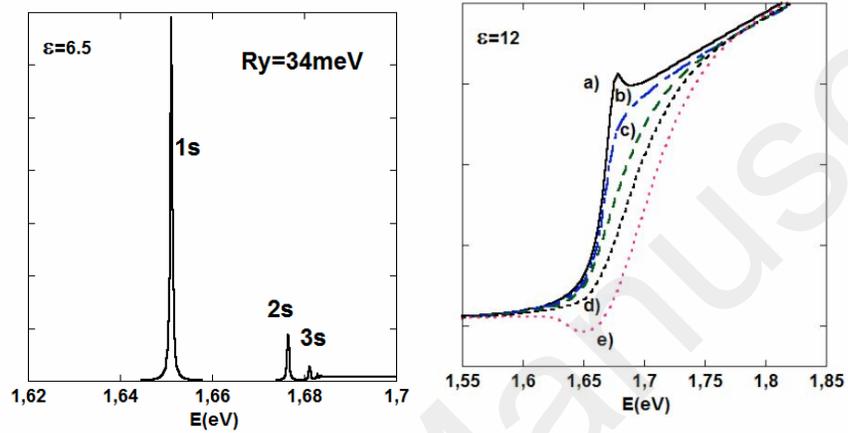
*Figure 32. (left) The optical absorption of MAPbI₃ computed using the BSE and the exciton Green's function in the linear regime at low temperature. An empirical basis of electron and hole monoelectronic states obtained with the **k.p** method close to the R point is used to compute the exciton Green's function. The e-h Coulomb interaction is computed with an effective dielectric constant equal to 6.5. 1s-3s exciton resonances are shown (the electronic band gap is set at 1.685eV). (right) Optical absorption of MAPbI₃ computed using the BSE and the exciton Green's function in the non-linear regime at T=160K. The concentration of free carriers is equal to: a) 0, b) $10^{17} cm^{-3}$, c) $5.10^{17} cm^{-3}$, d) $10^{18} cm^{-3}$, e) $2.10^{18} cm^{-3}$. Reprinted from ref[322]. Copyright 2016 Society of Photo Optical Instrumentation Engineers (SPIE).*
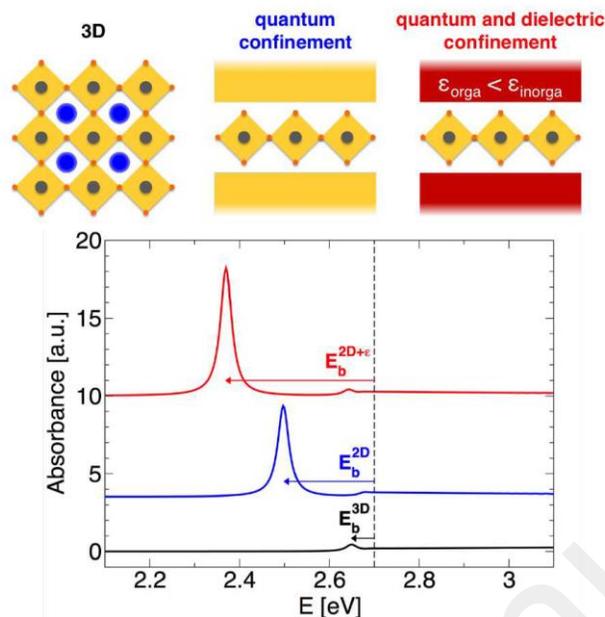
*Figure 33. Optical absorption computed using the **k·p**/BSE approach for a model halide perovskite material considered as a 3D material with $\epsilon_\infty = 5.0$ (black line), a 2D material with only quantum confinement, and $\epsilon_\infty = 5.0$ (blue line), a 2D material with both quantum and dielectric confinement (red line). In the latter, the computed dielectric profile of (Decyl-NH$_3$)$_2$PbI$_4$ is used. In all cases, the band gap is set to 2.7 eV, being the value extrapolated at room temperature from available experimental data, and the reduced effective mass is set to 0.093. Reprinted with permission from ref [76]. Copyright 2016 American Chemical Society.*

More recently the complete series of Ns states was analyzed with the same method for the (C$_4$H$_9$NH$_3$)$_2$(CH$_3$NH$_3$)$_{n-1}$Pb$_n$I$_{3n+1}$ multilayered perovskites with n =1-4.[275] To achieve a quantitative agreement between theory and experiment, it was necessary to refine the method by computing for each n value, the electronic density and dielectric constant profiles from DFT calculations and extract the reduced effective mass from a simulation of the experimental diamagnetic shift (Table 2).

Finally, let's mention that more advanced problems of excitons in 3D can be easily treated using the exciton Green function $G(\boldsymbol{k}, \hbar\omega + i\Gamma)$ within the framework of the theory of the optical Bloch equations. It is for example possible to consider the screening of the electron-hole interaction by a gas of free carriers in the Thomas-Fermi approximation $W(\boldsymbol{k}, \boldsymbol{k}') = -\frac{e^2}{\varepsilon_\infty(|\boldsymbol{k}-\boldsymbol{k}'|^2 + 1/\lambda^2)}$, where λ is the screening length.[313] It corresponds in the position space to the famous Yukawa's potential $V(\boldsymbol{r_h}, \boldsymbol{r_e}) = \frac{-e^2}{4\pi\,\varepsilon_\infty|\boldsymbol{r_h}-\boldsymbol{r_e}|} e^{-|\boldsymbol{r_h}-\boldsymbol{r_e}|/\lambda}$. It is important to notice that either in the simple electrostatic potential or in Yukawa's potential, both potentials depend solely on the relative distance $\rho = |\boldsymbol{r_h} - \boldsymbol{r_e}|$. These potentials could alternatively be represented using a single variable $V(\boldsymbol{\rho})$ that is similar to a 'local' potential for the relative electron-hole motion. Conversely, the local potentials in momentum space are represented using only $\boldsymbol{q} = \boldsymbol{k} - \boldsymbol{k}'$ by $W(\boldsymbol{k}, \boldsymbol{k}') = W(\boldsymbol{q})$. The dielectric confinement effect in layered systems is related to the non-locality of the electron-hole interaction potential, but this effect can be conveniently treated using the framework of the optical Bloch equations (Figures 32,33).

4.4. Image charges and dielectric confinement

The image charge method is a classical method designed to handle the problem of planar interfaces between dielectrics, as well as other simple dielectric heterostructures.[310,323] In order to compute in position space, the electrostatic potential due to a test charge e_0 located on one side of a planar interface separating two semi-infinite dielectric mediums, it is possible to include two fictitious 'image' charges e'_0 and e''_0, located respectively at z = -a and z = a (Figure 34). e'_0 allows computing the additional contribution to the homogeneous potential on the positive side (z > 0) of the interface, whereas e''_0 allows computing the correct value of the potential on the

negative side ($z < 0$). In the case of an electron-hole pair, the test charge e_0 can be either the electron or the hole and the computed electrostatic potential is multiplied by the other charge to deduce the mutual interaction electrostatic energy.
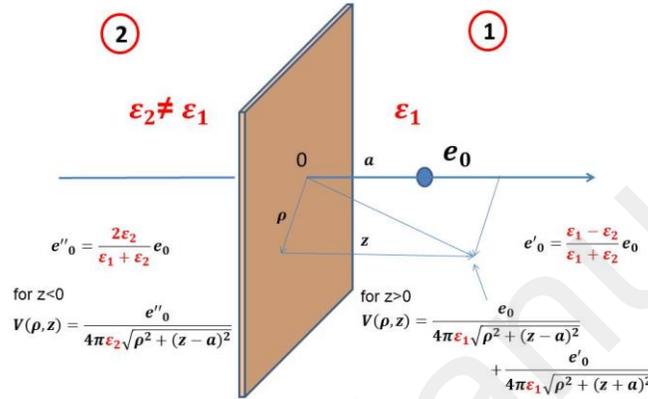
Figure 34. Electrostatic potential due to a test charge e_0 located on one side of a planar interface separating two semi-infinite dielectric mediums. e'_0 and e''_0 are two fictitious 'image' charges located respectively at $z = -a$ and $z = a$. e'_0 allows computing the additional contribution to the homogeneous potential on the positive side ($z>0$) of the interface, whereas e''_0 allows computing the correct value of the potential on the negative side ($z<0$).

In order to apply the same method for a dielectric well (DW) with abrupt interfaces (Figure 35), it is necessary to consider infinite series of image charges.[324] For example, if the test charge e_0 is located inside a DW of thickness L_w ($-L_w/2 < z_0 < L_w/2$) surrounded by two semi-infinite dielectric mediums, the image charges are located at positions $z_n = nL_w + (-1)^n z_0$, $n = \pm 1, \pm 2, \pm 3$ .... The electrostatic potential is non-local because the expressions of the image charges are not equivalent if the potential is computed outside or inside the DW. In the

latter case and for a symmetric DW ($\varepsilon_2 = \varepsilon_3 = \varepsilon_b$ in the barrier and $\varepsilon_1 = \varepsilon_w$ in the well), the image charges located at positions z_n are given by $e_n = \left(\frac{\varepsilon_w - \varepsilon_b}{\varepsilon_w + \varepsilon_b}\right)^{|n|} e_0$. This approach was used initially by Hong and coworkers[31] to explain the binding energies of the exciton for monolayered $(C_6H_5NH_3)_2PbI_4$ and $(C_{10}H_{21}NH_3)_2PbI_4$, and bilayered compounds $(C_6H_5NH_3)_2(CH_3NH_3)Pb_2I_7$ compounds. Unfortunately, a simple exciton wavefunction trial was used, relying on electron and hole monoelectronic wavefunctions computed for an infinite QW. The number of unknown parameters is important for this purely empirical method: ε_w, ε_b, L_w (Figure 22a). More, layered halide perovskites are rather dielectric superlattices (DSL) and an additional dielectric barrier thickness L_b must be introduced in that case (Figure 22a).[32,33] This additional parameter may be deduced from the lattice periodicity $L_w + L_b$ along the stacking axis measured by X-ray diffraction. Using further the schematic picture of a composite DSL, a simple formula can be proposed for the average dielectric constant $\overline{\varepsilon_\infty} = \frac{\varepsilon_w L_w + \varepsilon_b L_b}{L_w + L_b}$.[46] It is not relevant to analyze the enhancement of the exciton binding energy by the dielectric confinement effect, but it shows that dielectric measurements can be used to reduce the number of unknown parameters to two.[31] $\overline{\varepsilon_\infty} = 4.41$ and $\overline{\varepsilon_\infty} = 3.39$ were obtained experimentally for $(C_6H_5NH_3)_2PbI_4$ and $(C_{12}H_{25}NH_3)_2PbI_4$.[31] Finally, the dielectric constant in the DW was considered to be the one of PbI_2 in some cases ($\varepsilon_w = 6.1$) [31,46], or the one of $CH_3NH_3PbI_3$ ($\varepsilon_w = 6.1$) in other cases,[33] but without clear justifications. It was in fact shown recently by using DFT approaches that the dielectric composite picture breaks down for low n values,[81,206] and that smaller ε_w values than the above mentioned ones must be considered for monolayered compounds. In fact, in $CH_3NH_3PbI_3$ and PbI_2 covalent structures, all the iodine atoms are bonded to two Pb atoms. But, on one hand, in layered halide perovskites, the inorganic layers are disconnected along the stacking axis, with terminal iodides having a different electronic environment than the equatorial

ones. On the other hand, in 3D $CH_3NH_3PbI_3$ as well as in PbI_2, all iodine atoms have similar chemical and electronic environments, being connected to two Pb atoms. Similar issues exist for the determination of the effective barrier dielectric constant in a DW or DSL model. The choice of the barrier reference material is somehow arbitrary, especially when the equivalent barrier thickness L_b is small as in the multilayered perovskites based on the BA cation, or even smaller for 3AMP, 4AMP and Gua/MA cations.[83,204]

In most cases, the well thickness L_w was directly related to the lattice periodicity within the inorganic layer ($L_w = n \times 6.36\,\text{Å}$) and the experimental exciton binding energies were fitted. From empirical resolution of the BSE, predicted reduced effective masses were nevertheless highly dispersed among the various authors, depending on the theoretical description ranging from $\mu = 0.09 \times m_0$,[31] $\mu = 0.12 \times m_0$,[33] to $\mu = 0.17 \times m_0$.[32] More recent approaches based on exciton diamagnetic shift measurements combined with DFT theoretical calculations for the dielectric profiles and electronic density profiles derived from the complex spinor Bloch functions densities,[275] give $\mu = 0.221 \times m_0$ for $(C_4H_9NH_3)_2PbI_4$ (Table 2). The effective mass slightly decreases down to $\mu = 0.186 \times m_0$ when the number of layers in the QW increases up to n = 5.
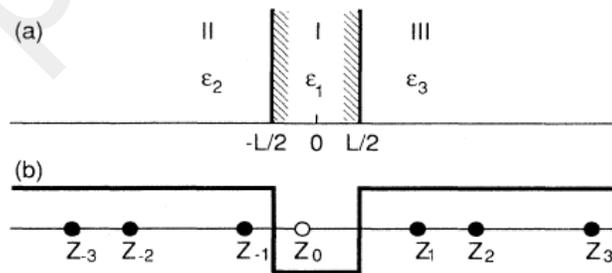
Figure 35. (a) Schematic structure of a general three-layer dielectric well (DW). (b) Typical configurations of the real (Z_0) and image charges are shown for the cases when a charged particle is in the well layer. The original charge is indicated by an open circle and the

Despite some issues related to unknown physical parameters , the DW model[31] or DSL model[32,33] with abrupt interfaces, afford convenient ways to go beyond the Wannier-Mott description and take into account advanced features such as the non-locality of the electron-hole interaction.

However a numerical intrinsic weakness of models based on abrupt dielectric interfaces is the divergence of the dielectric self-energy correction close to the interfaces ($z_0 = \pm L_w/2$ for a DW).[307,81] This issue is related to the self-energy correction resulting from dielectric inhomogeneities:

$$\delta\Sigma = lim_{r \to r_0} \frac{1}{2} e_0 \big(V_{DWorDSL}(r, r_0) - V_{bulk}(r, r_0) \big) \qquad (25)$$

which can be directly evaluated from image charge models.[324] The bulk self-energy $V_{bulk}(r, r_0)$ is expected to be included in the well and barrier bulk single particle energies and electronic band gaps. The numerical divergence of the $\delta\Sigma$ correction at an abrupt dielectric interface leads to serious numerical issues when the monoelectronic wavefunctions extend over both the well and the barrier. A numerical trick consists in shifting the position of the interfaces[324,32] or assuming that the electronic states are totally confined in the well.[31,33] Another deficiency of the image charge method is the implicit assumption of isotropy for both materials forming the well and the barrier, which is obviously not fulfilled for the organic part, but also for the inorganic part due to the presence of terminal halides only along the stacking axis. Therefore, the relation for the above mentioned average dielectric constant only holds for the in-plane component $\overline{\varepsilon_{\infty,\parallel}} = \frac{\varepsilon_{w,\parallel}L_w + \varepsilon_{b,\parallel}L_b}{L_w + L_b}$. The average dielectric constant along the stacking axis, which is also responsible for the enhancement of the exciton binding energy, is instead given

by $1/\overline{\varepsilon_{\infty,\perp}} = \frac{L_w/\varepsilon_{w,\perp}+L_b/\varepsilon_{b,\perp}}{L_w+L_b}$. Notice that $\overline{\varepsilon_{\infty,\perp}} = \overline{\varepsilon_{\infty,\parallel}}$ holds only in the $L_w/L_b \gg 1$ limit, and

for a bulk inorganic part corresponding to 3D halide perovskite in the cubic phase.

In order to avoid the problems related to abrupt interfaces, a more general method may consist in using a partial Fourier transform of the inhomogeneous Poisson equation with a test charge e_0 at $(\boldsymbol{r_{t0}, z_0})$:

$$\frac{\partial}{\partial z}\left(\varepsilon_\perp(z)\frac{\partial}{\partial z}\left(V(q_t,z,z_0)\right)\right) - q_t{}^2 \varepsilon_\parallel(z)V(q_t,z,z_0) = -e_0\delta(z-z_0)e^{-iq_t\cdot r_{t0}} \qquad (26)$$

where $V(\boldsymbol{q_t}, z) = \iint d^2\boldsymbol{\rho}\, e^{iq_t\cdot\rho}V(\boldsymbol{\rho,z})$. Without loss of generality, it is possible to put the test charge on the reference axis ($e^{iq_t\cdot r_{t0}} = 1$). For a homogeneous bulk material ($\varepsilon_\perp(z) = \varepsilon_\perp$ and $\varepsilon_\parallel(z) = \varepsilon_\parallel$) the solution reads $V_{bulk}(\boldsymbol{q_t},z,z_0) = \frac{e_0}{2\sqrt{\varepsilon_\perp\varepsilon_\parallel}q_t}e^{-iq_t\cdot r_{t0}}e^{-\sqrt{\frac{\varepsilon_\parallel}{\varepsilon_\perp}}q_t|z-z_0|}$, and

$V_{bulk}(\boldsymbol{q_t},z,z_0) = e^{-iq_t\cdot r_{t0}}\frac{e_0}{2\varepsilon q_t}e^{-q_t|z-z_0|}$ in the isotropic case ($\varepsilon_\perp = \varepsilon_\parallel = \varepsilon$). The self-energy correction can be analytically or numerically computed from:[307]

$$\delta\Sigma(z) = lim_{z\to z_0}\frac{e_0}{4\pi}\int_0^\infty \left(V_{DWorDSL}(q_t,z,z_0) - V_{bulk}(q_t,z,z_0)\right)q_t dq_t \qquad (27)$$

considering $\varepsilon_\perp(z)$ and $\varepsilon_\parallel(z)$ in the expression of the $V_{bulk}(q_t,z,z_0)$ bulk solution.[81,69,275]

More, recently a new numerical method was proposed to extract from DFT calculations and at low computational cost, $\varepsilon_\perp(z)$ profiles without any experimental input. It was applied to various multilayered perovskite phases (Figure 36).[69,81,83,84,206,275]
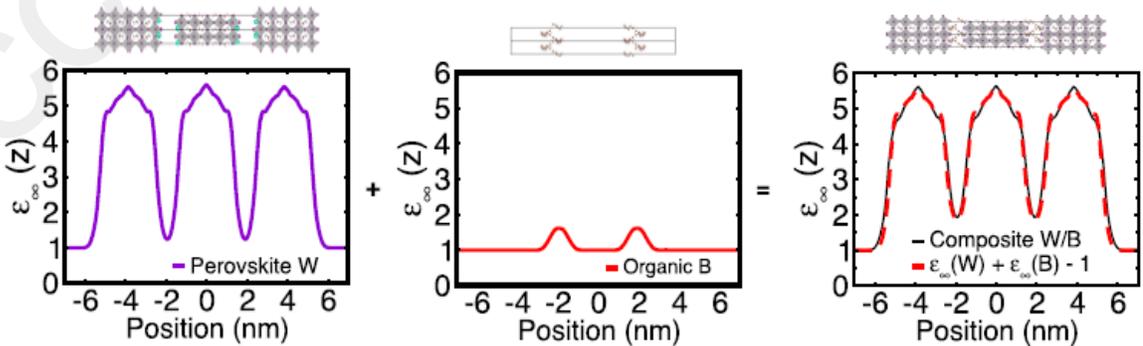
Figure 36. Dielectric profiles computed for each of the sections of a slab of the layered hybrid perovskite (BA)$_2$(MA)$_4$Pb$_5$I$_{16}$) (Figure 23c): (left) for the perovskite well (W) and (middle) for the organic barrier (B). (right) The dielectric profile of the real composite structure W/B computed for (BA)$_2$(MA)$_4$Pb$_5$I$_{16}$ is compared to the sum of the individual components W and B. It reveals the composite nature of the dielectric profiles for the five-octahedron thick layered perovskite. Reprinted with permission from Ref. [206] *Copyright 2018 American Chemical Society.*

This method reveals the composite nature of the dielectric profiles for multilayered perovskites, but also shows that the 3D perovskite $CH_3NH_3PbI_3$ or PbI_2 cannot be considered as the reference material in the DW for small n values. The dielectric profiles do not exhibit abrupt interfaces (Figure 36), and complex situations can be analyzed theoretically such as the inversion of dielectric mismatch when I_2 molecules intercalated in the barrier (Figure 20).[69] However, the $\varepsilon_\parallel(z)$ profile is usually not computed and the $\varepsilon_\parallel(z) = \varepsilon_\perp(z)$ condition was assumed for the calculations of the exciton state resonance in monolayered compounds[69] and multilayered ones.[275] Noteworthy, the partial Fourier transform method was also used to analyze the exciton binding energy in DSL but including empirical bulk parameters.[32]

A precise analysis of the exciton in multilayered halide perovskites also requires an accurate description of the single particle spinor states, as shown in the expression of the electron-hole interaction potential for a DW with abrupt interfaces:

$$V(q_t, z_e, z_h) =$$

$$\frac{-e^2}{2\varepsilon_w q_t} \iint_{\frac{-L_w}{2}, \frac{-L_w}{2}}^{\frac{L_w}{2}, \frac{L_w}{2}} \rho_e(z_e)\rho_h(z_h)\left[e^{-q_t|z_e-z_h|} + \Delta\chi\left(e^{-q_t|z_e+z_h-d|}+e^{-q_t|z_e+z_h+d|}\right) + \right.$$

$$\left. \Delta\chi^2\left(e^{-q_t|z_e-z_h-2d|}+e^{-q_t|z_h-z_e-2d|}\right)\right]dz_e dz_h \qquad (28)$$

where $\rho_e(z_e)$ and $\rho_h(z_h)$ are the electron and hole density profiles, $\Delta = (1 - \chi^2 e^{-2q_t d})^{-1}$, and $\chi = \frac{\varepsilon_w - \varepsilon_b}{\varepsilon_w + \varepsilon_b}$. We may notice that this formula leads to:

$$V(q_t) = \frac{-e^2}{2\varepsilon q_t} \iint \rho_e(z_e)\rho_h(z_h) e^{-q_t|z_e - z_h|} dz_e dz_h \qquad (29)$$

without dielectric confinement ($\varepsilon_w = \varepsilon_b = \varepsilon$).

Here the DW expression is strictly valid when the particles are completely confined in the well ($-L_w/2 < z_e < L_w/2$ and $-L_w/2 < z_h < L_w/2$), but refined expressions can be used when the electronic density profiles exhibit leakage in the barrier.[325,275] Some of the oldest approaches assume simple expressions for the single particle wavefunctions derived from infinite confinement potentials,[31,33] and still one relies on a more elaborate method including an Hamiltonian with effective masses along the stacking axis and finite confinement potentials corrected by self-energy expressions.[32] The larger reduced effective mass found in this last case ($\mu = 0.17 \times m_0$) by comparison with the others[31,33] is indeed in better agreement with a recent work including DFT results (Table 2).[275] However the effective mass method for the carrier motion along the stacking axis is known to suffer from serious issues leading to the prediction of unphysical superlattice effects and dispersion non-parabolicity.[94] We stress that very large effective masses were considered for the barrier materials and the tunneling between neighboring layers was enforced.[32] The most recent study derives the electronic density profiles from DFT calculation without relying on empirical effective masses approaches: [275]

$$\psi_{e,\boldsymbol{k}_t}(\boldsymbol{r}_{te}, z_e) = \frac{e^{-i\boldsymbol{k}_t \cdot \boldsymbol{r}_{te}}}{\sqrt{A}} u_{e,\boldsymbol{k}_t=0}(\boldsymbol{r}_{te}, z_e)$$
$$\psi_{h,\boldsymbol{k}_t}(\boldsymbol{r}_{th}, z_h) = \frac{e^{-i\boldsymbol{k}_t \cdot \boldsymbol{r}_{th}}}{\sqrt{A}} u_{h,\boldsymbol{k}_t=0}(\boldsymbol{r}_{th}, z_h), \qquad (30)$$

where $u_{e,\boldsymbol{k}_t=0}(\boldsymbol{r}_{te}, z_e)$ ($u_{h,\boldsymbol{k}_t=0}(\boldsymbol{r}_{th}, z_h)$) are the electron (hole) ground-state, complex spinor Bloch functions at the BZ center. The electron and hole probability density profiles along the

stacking axis are derived by in-plane averaging of the Bloch functions (see Figure 16f and 19b for corresponding LDOS):

$$\rho_e(z_e) = \iint |u_{e,\boldsymbol{k}_t=0}|^2 \, d^2\boldsymbol{r}_{te} \text{ and } \rho_h(z_h) = \iint |u_{h,\boldsymbol{k}_t=0}|^2 \, d^2\boldsymbol{r}_{th}. \tag{31}$$

4.5. Comparison to dielectric confinement effect in Van der Waals heterostructures

Atomically thin layer Van der Waals heterostructures, such as transition metal dichalcogenides, are known to exhibit very large exciton binding energies and self-energy effects as a result of dielectric confinement.[326] It leads to deviations from the Ns series of resonance energies of 2D excitons similar to the ones reported in free standing monolayered iodide perovskites,[309] monolayered iodide and bromide perovskite crystals[62,308] and multilayered iodide perovskite crystals.[275]

The initial empirical analysis of the 2D dielectric confinement effect in ultrathin dielectric sheets was performed by Keldysh and coworkers,[327] but recent developments for monolayered Van der Waals heterostructures aim at proposing connections between empirical and DFT approaches.[328–332] A theoretical framework mixing empirical and DFT approaches was also proposed recently for halide perovskites[76,69,275] following the pioneer work based on purely empirical approaches.[31–33] However there are some differences between the two families of layered materials that deserve to be stressed.

Let's first consider the complete empirical relation proposed above for halide perovskites:[275]

$$V(q_t, z_e, z_h) =$$

$$\frac{-e^2}{2\varepsilon_w q_t} \iint_{-\frac{L_w}{2}, -\frac{L_w}{2}}^{\frac{L_w}{2}, \frac{L_w}{2}} \rho_e(z_e)\rho_h(z_h)\big[e^{-q_t|z_e-z_h|} + \Delta\chi\big(e^{-q_t|z_e+z_h-d|} + e^{-q_t|z_e+z_h+d|}\big) +$$

$$\Delta\chi^2\big(e^{-q_t|z_e-z_h-2d|} + e^{-q_t|z_h-z_e-2d|}\big)\big]dz_e dz_h \tag{32}$$

This momentum space formula is similar to the one reported by Keldysh in his seminal paper:[327]

$$V(q_t, z_e, z_h) = \frac{-e^2}{2\varepsilon_w q_t} \iint_{\frac{-L_w}{2}, \frac{-L_w}{2}}^{\frac{L_w}{2}, \frac{L_w}{2}} \left[e^{-q_t|z_e - z_h|} + \Delta\chi\left(e^{-q_t|z_e + z_h - d|} + e^{-q_t|z_e + z_h + d|}\right) + \right.$$

$$\left. \Delta\chi^2\left(e^{-q_t|z_e - z_h - 2d|} + e^{-q_t|z_h - z_e - 2d|}\right)\right]dz_e dz_h, \tag{33}$$

assuming homogeneous electron and hole densities $(\rho_e(z_e) = \rho_h(z_h) = {}^1\!/\!_{L_w})$ within the DW with no electronic leakage in the dielectric barrier. Thus, it is implicitly matching the DW and QW thicknesses. DFT calculations on layered halide perovskites have shown that the shape of the density distributions may deviate from a rectangular distribution, with especially out-of-plane contributions of the iodine atoms for the hole density.[64,206,275] By comparison, Van der Waals heterostructures exhibit a higher carrier confinement and are closer to the simplifying hypothesis of Keldysh's theory on carrier densities (Figure 19b, bottom).[326] Assuming instead a QW with vanishing thicknesses for the confinement of the band edge states $(\rho_e(z_e) = \delta_{z_e}$ and $\rho_h(z_h) = \delta_{z_h})$ while the DW has a non-zero thickness L_w:

$$V(q_t) = \frac{-e^2}{2\varepsilon_w q_t} \frac{1 + \chi e^{-q_t L_w}}{1 - \chi e^{-q_t L_w}} \tag{34}$$

which is equivalent to an effective 2D dielectric function of the form:

$$\varepsilon_{2D}(q_t) = \varepsilon_w \frac{1 - \chi e^{-q_t L_w}}{1 + \chi e^{-q_t L_w}} \tag{35}$$

Considering the approximation valid for 2D Wannier exciton $q_t L_w \ll 1$:

$$\varepsilon_{2D}(q_t) \approx \varepsilon_b + \frac{(\varepsilon_w^2 - \varepsilon_b^2)}{2\varepsilon_w} q_t L_w. \tag{36}$$

For a large dielectric mismatch $\varepsilon_w \gg \varepsilon_b$:[275]

$$\varepsilon_{2D}(q_t) \approx \varepsilon_b + \frac{\varepsilon_w q_t L_w}{2}. \tag{37}$$

The most popular formula of Keldysh's theory is usually given in position space.[326] It is

based on a number of additional approximations neglecting z_e and z_h dependences. Similar

approximations for halide perovskites lead to:

$$V(q_t) = \frac{-e^2}{2\varepsilon_w q_t} \frac{1+\chi e^{-q_t L_w}}{1-\chi e^{-q_t L_w}}. \tag{38}$$

The second approximation of Keldysh's paper ($q_t L_w \ll 1$) corresponds to a long-range

electron-hole interaction (small in-plane wavevectors), thus well suited for 2D Wannier-like

excitons and materials such as Van der Waals heterostructures or layered halide perovskites. It

leads to an expression in position space after Fourier transform:

$$V(r_t) = \frac{-e^2 \varepsilon_w}{2\pi(\varepsilon_w{}^2-\varepsilon_b{}^2)} \int_0^\infty \frac{1}{t+\frac{2\varepsilon_w \varepsilon_b}{\varepsilon_w{}^2-\varepsilon_b{}^2}\frac{r_t}{L_w}} J_0(t)dt =$$

$$\frac{-e^2 \varepsilon_w}{4(\varepsilon_w{}^2-\varepsilon_b{}^2)}\left[H_0\left(\frac{2\varepsilon_w \varepsilon_b}{\varepsilon_w{}^2-\varepsilon_b{}^2}\frac{r_t}{L_w}\right) - N_0\left(\frac{2\varepsilon_w \varepsilon_b}{\varepsilon_w{}^2-\varepsilon_b{}^2}\frac{r_t}{L_w}\right)\right].$$

$$\tag{39}$$

Finally, assuming a large dielectric contrast $\varepsilon_w \gg \varepsilon_b$:

$$V(r_t) = \frac{-e^2}{4\varepsilon_w}\left[H_0\left(\frac{2\varepsilon_b}{\varepsilon_w}\frac{r_t}{L_w}\right) - N_0\left(\frac{2\varepsilon_b}{\varepsilon_w}\frac{r_t}{L_w}\right)\right], \tag{40}$$

which is the original approximate formula of Keldysh in position space.[327] We may first notice

that the approximation $\varepsilon_w \gg \varepsilon_b$ is less justified for monolayered halide perovskite crystals, than

for free-standing mono-layered systems (the in-plane dielectric constant of bulk MoS_2 is on the

order of 13-15).[328,329]

Finally let's discuss a more fundamental difference between Van der Waals

heterostructures and multilayered halide perovskites. In monolayered sheets related to Van der

Waals heterostructures, a microscopic in-plane polarization $\vec{P}_{DW}$ was introduced, instead of

considering two different macroscopic dielectric constants. Indeed, a microscopically derived

99

polarizability makes more sense because the notion of the bulk dielectric constant has no clear meaning in atomically thin layers (Figure 37).[328]
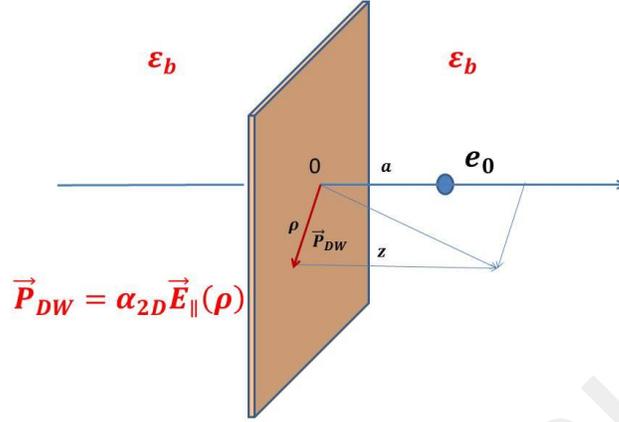
Figure 37. Schematic representation of a test charge e_0 located on a side of an ultrathin DW inducing an in-plane polarization related to a microscopic polarizability α_{2D}. ε_b is the barrier dielectric constant.

Starting from the partial Fourier transform of the inhomogeneous Poisson equation with a test charge e_0 at $(\boldsymbol{r_{t0}}, \boldsymbol{z_0})$:

$$\varepsilon_b \frac{\partial}{\partial z}\left(\frac{\partial}{\partial z}\left(V(q_t, z, z_0)\right)\right) - q_t^2 \varepsilon_b V(q_t, z, z_0) = -e_0 \delta(z - z_0)e^{-iq_t.r_{t0}} +$$

$$\alpha_{2D} q_t^2 V(q_t, z, z_0)\delta(z), \qquad (41)$$

where the last term is the 2D induced charge at the well position ($z = 0$) related to the 2D polarization $\boldsymbol{P_{DW}} = \alpha_{2D}\boldsymbol{E}_\parallel(\boldsymbol{\rho})$. The solution for a test charge on the reference axis ($e^{iq_t.r_{t0}} = 1$) and in the DW ($z_0 = 0$) is:

$$V(\boldsymbol{q_t}, z, z_0) = \frac{e_0}{2\varepsilon_b q_t \left(1 + \frac{q_t \alpha_{2D}}{2}\right)} \qquad (42)$$

The effective 2D dielectric constant is thus

$$\varepsilon_{2D}(q_t) \approx \varepsilon_b + \frac{\varepsilon_b q_t \alpha_{2D}}{2} \qquad (43)$$

which can be compared to the above derived purely empirical relation: [275]

$$\varepsilon_{2D}(q_t) \approx \varepsilon_b + \frac{\varepsilon_w q_t L_w}{2} \; when \; \varepsilon_w \gg \varepsilon_b \qquad (44)$$

The in-plane polarization of the related 3D crystal can be estimated in Van der Waals heterostructures as an average over the number of monolayers,[328,329] thus affording a convenient way to extract the value of the 2D in-plane polarizability α_{2D} from first-principles calculations of the 3D dielectric matrix. These methods were recently refined in the quasi-2D approach of Latini and coworkers.[330] Actual density profiles were used to compute the screened electron-hole interaction in reciprocal space and the effect of the dielectric mismatch was introduced through a proper 2D transformation of the 3D bulk dielectric, accounting for local field effects. In the DFT approaches on layered perovskites,[81,69,275] a direct computation of the dielectric profile was performed for each phase, due to the absence of a 3D reference system. In the 3D compound (MAPbI$_3$) that might be considered as a reference for many multilayered systems, covalent bonds are present along the stacking axis. On the other hand, only terminal iodides are present in the monolayered structures along the same axis. Thus, the MAPbI$_3$ crystal cannot be considered as a simple assembly of perovskite monolayers. This discrepancy is in fact related to the failure of the $\varepsilon_{\parallel}(z) = \varepsilon_{\perp}(z)$ condition. It shows that further progresses must be performed to better account for the anisotropy of the dielectric properties of the layered perovskite heterostructures.

4.6. Experimental results on the exciton fine structure and higher excitations in layered halide perovskites

As shown in the previous section, the increase of the 1s exciton binding energy and oscillator strength related to the dielectric confinement effect in layered halide perovskites is now a well-established general feature, leading for example to PL at room temperature and

distinct signatures in optical absorption. It was demonstrated for a large number of chemical compositions and extensive investigations on the optical characteristics of the 1s exciton in these systems were performed since the 1980s by many experimental groups. Progresses on the understanding of the quantum and dielectric confinements may benefit from recent results obtained for monolayered compounds such as, the exciton fine structure,[49,333,334,308] multiexcitonic effects.[47,54,60,335–337] Additional information may also come from various observations related to strong exciton-photon coupling in optical cavities,[74,75,338,339] the influence of chirality,[340] electrooptic effects,[333,341] or spin-selective optical Stark effects.[342]

We will focus in this part on a brief overview of the experimental works dedicated to the exciton fine structure of monolayered perovskites. In fact, in-depths analyses have been proposed over the last two decades on the exciton fine structures of monolayered bromide and iodide compounds (Table 3).

Table 3: Table summarizing some important spectroscopy results on the exciton fine structure in monolayered halide perovskites.

$(C_jH_{2j+1}NH_3)_2PbBr_4$ (j = 4)	Biexciton binding energy E_{bXX} = 60meV	Kato et al, solid state comm 2003[60]
$(C_jH_{2j+1}NH_3)_2PbBr_4$ (j = 4)	Exciton fine structure model	Tanaka et al, Jap. J. Appl. Phys. 2005[333]
$(C_jH_{2j+1}NH_3)_2PbBr_4$ (j = 4)	Exciton fine structure model	Ema et al, Phys. Rev. B 2006[334]
$(CH_3C_6H_4CH_2NH_3)_2PbBr_4$	Exciton and biexciton localization	Goto et al, Phys. Rev. B 2006[336]
$(C_jH_{2j+1}NH_3)_2PbBr_4$ (j = 8)	Temperature study	Kitazawa et al, Thin Solid Films 2006[343]
$(C_jH_{2j+1}NH_3)_2PbBr_4$ (j = 4, 5, 7, 12)	Influence of the organic barrier	Kitazawa et al, Thin Solid Films 2010[344]
$(C_6H_5C_jH_{2j}NH_3)_2PbBr_4$	Temperature study	Kitazawa et al, J. Phys.

(j =1-4)		Chem. Solids 2010[345]
$(C_jH_{2j+1}NH_3)_2PbBr_4$ (j = 4)	Biexciton Exciton fine structure model	Yamamoto et al, Phys. Status solidi C 2012[346]
$(C_6H_5C_jH_{2j}NH_3)_2PbBr_4$ (j = 2) $(C_6H_5C_jH_{2j}NH_3)_2PbI_4$ (j = 2)	Comparison between Bromide and iodide compounds	Kitazawa et al, Mater. Chem. Phys. 2012[347]
$(C_jH_{2j+1}NH_3)_2PbBr_4$ (j = 4) $(C_6H_5C_jH_{2j}NH_3)_2PbBr_4$ (j = 2)	Influence of the organic barrier Exciton fine structure model	Takagi et al, Phys. Rev. B 2013[308]
$(C_jH_{2j+1}NH_3)_2PbI_4$ (j = 4, 8, 9, 10, 12)	Exciton fine structure (not analyzed)	Ishihara et al, Phys. Rev. B 1990[46]
$(C_jH_{2j+1}NH_3)_2PbI_4$ (j = 10) $(C_6H_5C_jH_{2j}NH_3)_2PbI_4$ (j = 2)	Biexciton binding energy E_{bXX} = 50meV	Ishihara et al, Surf. Sci. 1992[47]
$(C_jH_{2j+1}NH_3)_2PbI_4$ (j = 6)	Magneto-optical study Exciton fine structure model	Kataoka et al, Phys. Rev. B 1993[48]
$(C_jH_{2j+1}NH_3)_2PbI_4$ (j = 6)	Biexciton lasing Biexciton binding energy E_{bXX} = 40meV	Kondo et al, Solid State. Comm. 1998[54]
$(C_jH_{2j+1}NH_3)_2PbI_4$ (j = 6) $(C_6H_5C_jH_{2j}NH_3)_2PbI_4$ (j = 2)	Influence of the organic barrier	Shimizu et al, Phys. Rev. B 2005[335]
$(C_6H_5C_jH_{2j}NH_3)_2PbI_4$ (j = 2)	Triexciton	Shimizu et al, Phys. Rev. B 2006[337]
$(C_6H_5C_jH_{2j}NH_3)_2PbI_4$ (j = 2)	Exciton splitting at low temperature	Gauthron et al, Optics express 2010[348]
$(C_jH_{2j+1}NH_3)_2PbI_4$ (j = 4, 5, 7, 8, 9)	PL dynamics depending on the organic cation	Kitazawa et al, J. Phys. Chem. Solids 2011[349]
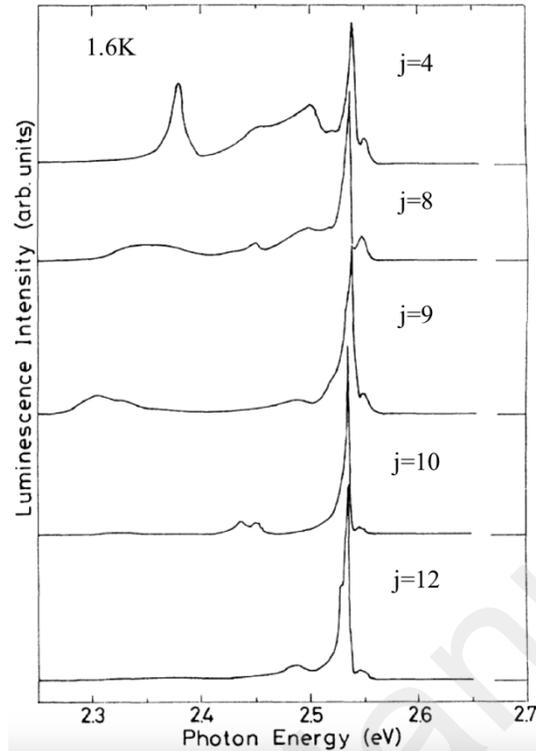
Figure 38. PL spectra in single crystals of $(C_jH_{2j+1}NH_3)_2PbI_4$ with j = 4, 8, 9, 10, and 12 at 1.6 K Reprinted with permission from [46] *Copyright 1990 American Physical Society.*

The first paper showing evidence of exciton fine structures at low temperature in monolayered halide perovskites was published by Ishihara and coworkers in 1990 (Figure 38),[46] although no analysis was provided. The paper was merely focused on the dielectric confinement enhancement of the exciton binding energy. The next important step was the observation of an additional broad contribution at high optical excitation in $(C_{10}H_{21}NH_3)_2PbI_4$.[47] This new band (M band on Figure 39) appears about 50 meV below the free exciton band (F on Figure 39). It grows as the square of the excitation intensity. As reported by the authors, the ratio of the binding energy of the biexciton to that of the exciton (50/320~0.16) is typical of QW-like structures. A lower biexciton binding energy of 40 meV was reported later on for $(C_6H_{13}NH_3)_2PbI_4$.[54] The large value of the biexciton binding energy is favorable for the observation of biexciton lasing,

which was observed up to 40K by Kondo and coworkers in 1998 in $(C_6H_{13}NH_3)_2PbI_4$ under optical pumping.[54] Moreover, as shown on Figure 39, other contributions are present in between the F and M peaks, but could not be resolved in the early study on $(C_{10}H_{21}NH_3)_2PbI_4$.[47] Due to smaller dielectric constants, bromide compounds exhibit somewhat larger exciton binding energy than iodide compounds. A larger biexciton binding energy was measured as well for $(C_4H_9NH_3)_2PbBr_4$ (Figure 39).[60] Noteworthy the intermediate contribution in between the EX and M peaks are better resolved and interpreted as exchange splitting states (referred to as Q on Figure 39), whereas the high energy peak is related to a singlet state. We may also notice that the Q peak contains in fact two contributions. The observation of triexciton formation with a dissociation energy of 14 meV was reported $(C_6H_5C_2H_4NH_3)_2PbI_4$ by Shimizu and coworkers.[337] This energy was not directly determined from peak splitting, but estimated from the temperature dependence of the triexciton peak intensity.
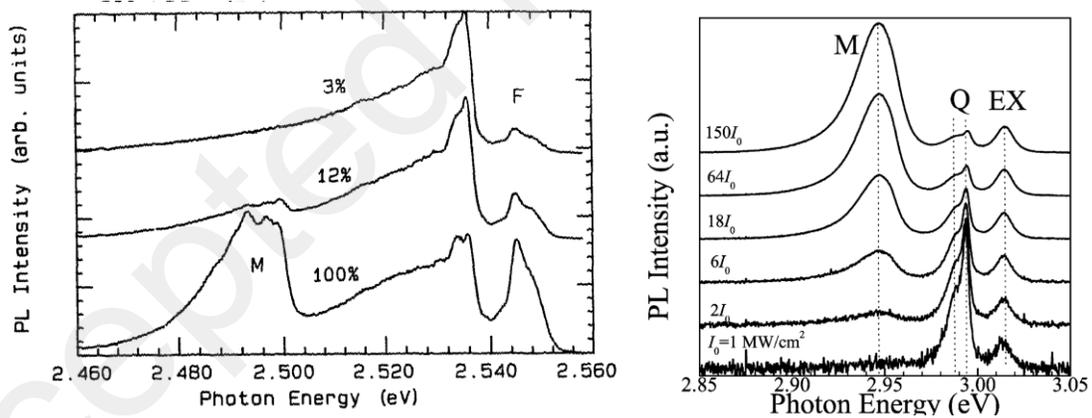
Figure 39. (left) PL spectra of $(C_{10}H_{21}NH_3)_2PbI_4$ at 2 K for different excitation levels. Highest intensity is estimated to be 100 kW/cm². Ref [47] Copyright 1992, with permission from Elsevier. (right) PL spectra of a $(C_4H_9NH_3)_2PbBr_4$ single crystal at 10 K for various excitation intensities. EX and Q denote the exciton luminescence from the singlet state and the exchange splitting

A magneto-optical study was performed on polycristalline films of $(C_6H_{13}NH_3)_2PbI_4$ by Kataoka and coworkers combining Voigt and Faraday configurations.[49] A model was proposed for the first time for the exciton fine structure. This model was designed for a Frenkel exciton, but interestingly takes into account the strong SOC of the CB, as well as the double degeneracy of the in-plane p-orbitals of Pb atoms.[64] The additional CB states related to out of plane Pb p-orbitals which have a higher energy than in-planar Pb p-orbitals, are also taken into account through a crystal field term. This model was extensively used leading to precise peak assignments for bromide compounds.[333,334,346,308] Figure 40a illustrates such analysis for $(C_4H_9NH_3)_2PbBr_4$ and $(C_6H_5C_2H_4NH_3)_2PbBr_4$ single crystals at T=10K. The computation of the exciton fine structure accounts for Coulomb interaction but also an exchange term (Figure 40b). Γ^-_5 is a doubly degenerate excitonic state (in the approximation of a tetragonal unit cell) with an optical activity corresponding to an in-plane electric field polarization (TE). Γ^-_1 is a dark state with no optical activity, and Γ^-_2 is a bright state corresponding to an out of-plane electric field polarization (TM), that may however appear dark in many experimental situations. The peak splitting appears much larger than in 3D halide perovskites or $CsPbBr_3$ QD,[350] which is interpreted as a result of an exchange energy greatly enhanced (28 to 32 meV according to Ema et al[334]) by strong confinement and by image charge effects. Quantitative simulations of the splitting observed in the exciton fine structure of monolayered perovskites are still lacking.

.
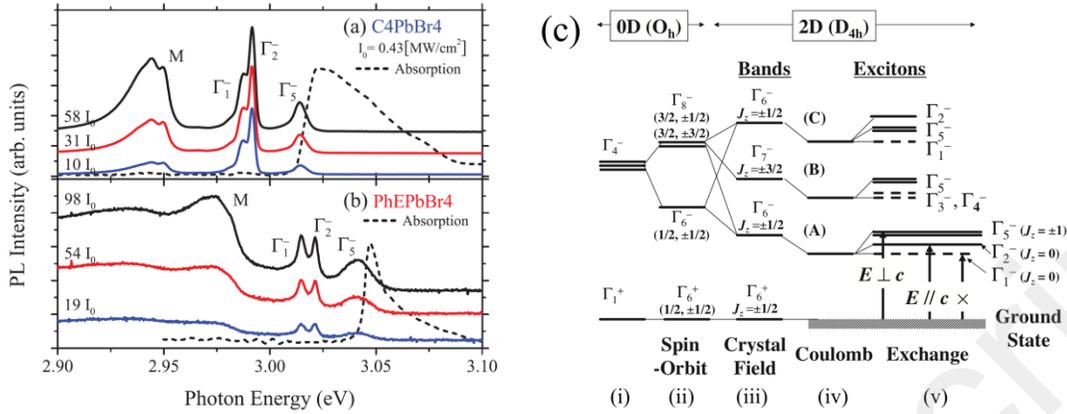
Figure 40. (a) and (b) PL spectra of (a) (C₄H₉NH₃)₂PbBr₄ (C4PbBr4) and (b)

(C₆H₅C₂H₄NH₃)₂PbBr₄ (PhEPbBr4) single crystals at 10 K for various excitation intensities.

There are four main peaks in both samples. The assignments of these four peaks are described in

the text. Dashed lines show absorption spectra obtained by the Kramers-Kronig relation of

reflection spectra. Ref. [308] Copyright 2013 American physical society. (c) Schematic energy

diagram of two-dimensional crystal (C₄H₉NH₃)₂ PbBr₄ at Γ point of the BZ. (i) The CBM and

VBM states of the [PbBr₆] octahedron have Γ_4^- and Γ_1^+ symmetries, respectively. (ii) With spin–

orbit interaction and (iii) tetragonal crystal field, the CBM state splits into the three bands A, B,

and C, while the VBM state is not split. The excitons in each band are split by the (iv) Coulomb

and (v) exchange interactions. Only the selection rules to the lowest-energy excitons (A band)

are described. Ref. [333]. Copyright 2005 The Japan Society of Applied Physics.

The situation is less clear for iodide compounds.[49]A possible explanation may rely on

dark exciton and biexciton localization in bromide compounds.[336] It is consistent with a

comparative study of $(C_6H_5C_2H_4NH_3)_2PbBr_4$ and $(C_6H_5C_2H_4NH_3)_2PbI_4$ using temperature

dependent time–resolved PL.[347] It shows an apparent long lifetime for the dark exciton line in the

bromide compound, not observed in the iodide one. The internal strain of the structure seems to

play a major role for the exciton localization. The size of the halogen atom as well as the internal dynamics of the organic cation may lead to large difference in the local structure as probed by NMR studies.[290,351] Another study on $(C_jH_{2j+1}NH_3)_2PbI_4$ compounds with j = 4, 5, 7, 8, 9 shows that the PL dynamics is strongly affected by seemingly small changes of the organic cation in the barrier.[349]

More generally, the localization of charge carriers has been little explored from the fundamental viewpoint in multilayered halide perovskites, although it is obviously important to explain various experimental results and may lead to additional applications for white light emission.[336,202,352,84,89,303,304,353–355]

5. CONFINEMENT EFFECTS IN COLLOIDAL NANOSTRUCTURES

Summary: Recent results obtained for colloidal perovskites nanostructures are reviewed. The analysis of confinement effects deserves additional research efforts to reach a suitable level of description on par with other colloidal systems or multilayered perovskite structures.

5.1. Introduction

Experimental studies on colloidal nanostructures of halide perovskite materials started very recently (2015), but they revealed almost immediately the good potential of these nanostructures for light emission. The development of perovskite colloidal QD solar cells made a significant step one year later, and these nanostructures are currently leading the sector of QD photovoltaics.[166,21,167,356,168,22] New synthesis methods were proposed allowing virtually all perovskite chemical compositions to be explored with various nanostructure shapes, sizes and electronic dimensionalities ranging from QD, QWr, QR to QNPL.[21,166–168,309,350,357–396] Inorganic

CsPbX$_3$ QD (X=I, Br, Cl or alloys) exhibit presently the most important potential for applications both for light emission and photovoltaics. Now, hybrid halide perovskites colloidal nanostructures deserve further investigations and present room for chemical engineering.

Most experimental studies on halide perovskite colloidal structures show that carrier confinement significantly improves the optoelectronic properties by comparison to the related bulk perovskite compounds, leading for example to enhanced and stable narrow-band emission, with suppressed blinking and small spectral diffusion at low temperature.[366] However, the literature on quantum and dielectric confinement effects in halide perovskite nanostructures is still scarce. We present in the next section a short review of this topic that will certainly undergo a quick development in the near future.

5.2. Quantum and dielectric confinements
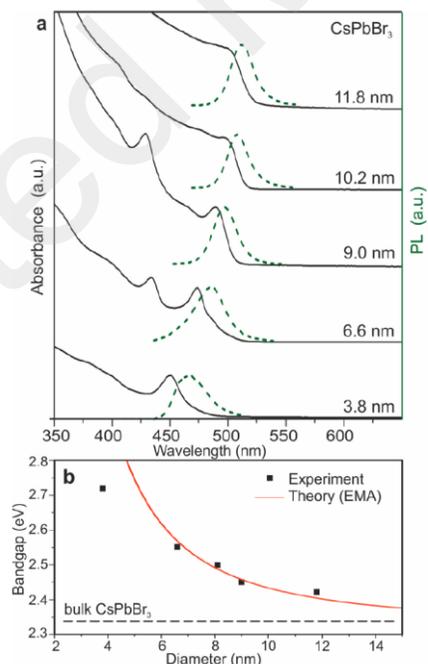
Figure 41. Quantum-size effects in the absorption and emission spectra of 5−12 nm CsPbBr$_3$ QD. (b) Experimental versus theoretical (effective mass approximation, EMA) size

dependence of the band gap energy. Reprinted with permission from ref [166]. Copyright 2015 American Chemical Society.

The experimental studies dedicated to these effects essentially report on the optical band gap variations as a function of the nanostructure size. Such variations were clearly observed in the first paper on $CsPbX_3$ QD (Figure 41).[166] An effective mass approximation was used to analyze the quantum confinement effect. The dielectric confinement effect was not considered (vide infra).
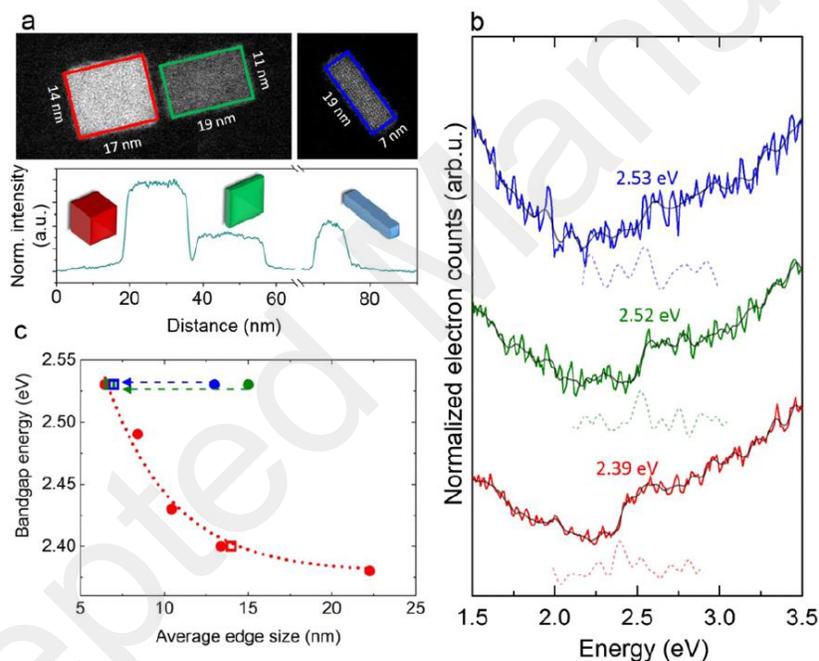
Figure 42. Shape-dependent energy band gap of isolated single nanostructures. (a) Z-contrast annular dark-field (ADF) images of three QD that have different shapes. Two edge lengths can be derived from the ADF image, while the thickness is estimated based on the normalized ADF image intensity as shown in the panel underneath. The thickness of each nanostructure is estimated qualitatively to be 13−14 nm (cube, red), 6−7 nm (QNPL, green), and 8−9 nm (QR, blue). (b) The low-loss EEL spectra of the corresponding nanostructure with

their band gap energies given. The semitransparent black solid lines are the smoothed spectra and the dashed lines their first derivatives. (c) A schematic comparison of the "average" edge size, as solely determined from the ADF image, vs band gap energy for these three shapes (solid dots) showing a clear discrepancy for the QNPL and QR. The average edge size of a (non cubic) nanostructure is determined as the square root of the surface. Taking now the thickness into account, the actual shortest edge of the nanostructure can be considered where subsequently the band gap values of the plate and rod-shaped nanostructures agree well with earlier observations (open squares). Reprinted with permission from ref [365]. Copyright 2016 American Chemical Society.

Other authors report on variations of the optical band gaps when the chemical synthesis is used to tune the sizes and shapes of perovskite nanostructures. However, quantum and dielectric confinement effects are not yet analyzed using geometrical and material parameters (Figures 42 and 43). [365,380]
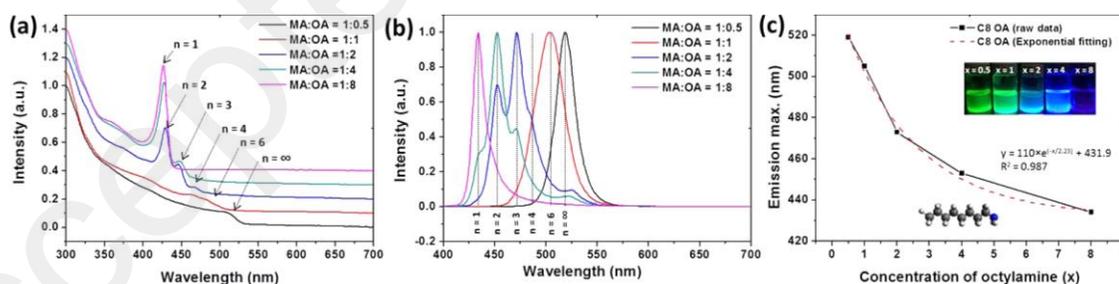
Figure 43. (a) UV−visible absorption spectra and (b) PLE spectra plotted for varying MA/RA ratios (RA is alkylamine) when octyl-alkylammonium ligand (C8 OA) is used as the capping ligand. The PL spectra have been normalized to a unitary intensity to illustrate variations of the peak maxima. (c) Plot of the peak position of the primary PLE band as a

function of the relative OA concentration. An exponential fit to the data yields a R^2 value of 0.987. The inset to panel c indicates a digital photograph of 2D QNPL capped with OA prepared at different concentrations of the capping ligand upon excitation with a 365 nm UV light source. Reprinted with permission from ref [380]. Copyright 2016 American Chemical Society.

In QNPL, the confinement effect is somehow simpler to analyze. The confinement effect due to the lateral dimensions can be neglected provided that the lateral size exceeds about 15nm (Figure 44).[385] Confinement effects have been observed in colloidal QNPL made of various bulk compounds including $CsPbX_3$ and $MAPbX_3$, but also $CsSnI_3$ (Figure 45)[386], or layered perovskites $(C_4H_9NH_3)_2PbBr_4$ (Figure 46)[397] and $(C_4H_9NH_3)_2PbI_4$.[309]
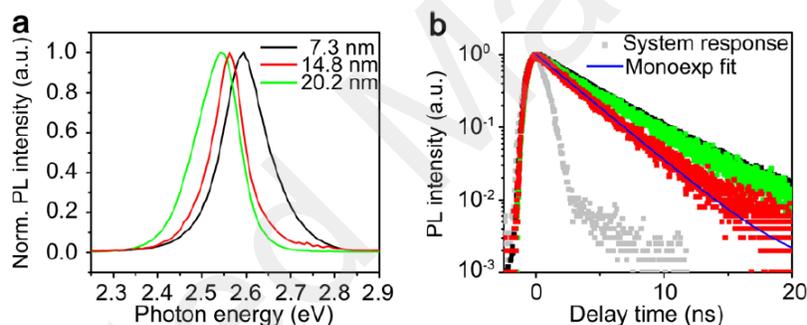
Figure 44. PL properties of the $CsPbBr_3$ QNPL. (a) PL spectra of the 7.3, 14.8, and 20.2 nm QNPLs. (b) PL decay traces of the 7.3, 14.8, and 20.2 nm QNPL. The system response is also plotted as the gray line. Reprinted with permission from ref [385]. Copyright 2017 American Chemical Society.
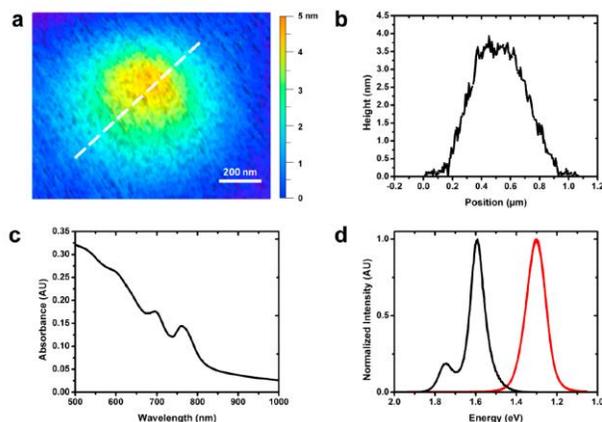
Figure 45. Confinement in CsSnI₃ studied by thickness measurements and optical characterization. (a) Atomic force microscopy (AFM) image of a single CsSnI₃ QNPL as measured in non-contact mode in an air-free cell. (b) AFM height profile across a single, isolated CsSnI₃ QNPL as shown in panel a by the dashed line. (c) Absorbance spectrum of CsSnI₃ QNPL. (d) PL spectra of quantum-confined CsSnI₃ QNPL (black) and bulk CsSnI₃ (red). Reprinted with permission from ref [386]. *Copyright 2018 American Chemical Society.*
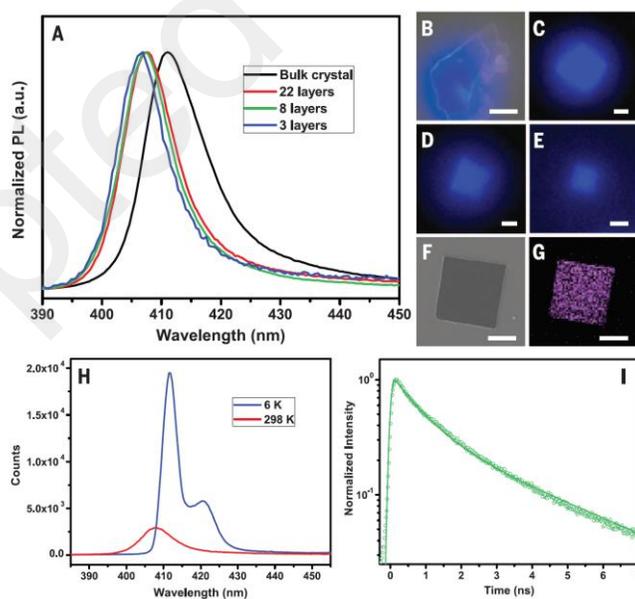
Figure 46.   PL properties of the 2D ($C_4H_9NH_3$)$_2$PbBr$_4$ sheets. (A) Steady-state PL spectrum of a piece of bulk crystal and several 2D sheets. (B) The corresponding optical image of the bulk crystal under excitation. Scale bar, 20 mm. (C to E) Optical images of the 2D sheets with 22 layers, 8 layers, and 3 layers. Scale bars, 2 mm. (F) SEM image of a 2D sheet. Scale bar, 2 mm. (G) The corresponding cathodoluminescence image showing the emission (with a 40-nm bandpass filter centered at 415 nm). (H) PL spectra of a 2D sheet at 298 and 6 K. (I) Time-resolved PL measurements showing a bi-exponential decay. From ref[397]. Reprinted with permission from AAAS.

A purely DFT-based theoretical approach of the optoelectronic properties of halide perovskite nanostructures is not yet possible due to the very large number of atoms and electrons to be considered. It can be performed for very small nanostructures,[376] but at a level of theory (without including many-body effects) where the description of bulk materials still deserves improvements. More importantly, the actual crystallographic structure inside a nanostructure may be different from the one of the bulk compound at the same temperature. The cubic phase is the crystallographic phase at high temperatures for all CsPbX$_3$ compounds, but they exhibit various structural phase transitions leading to tetragonal phases or orthorhombic perovskite as well as non perovskite phases. The case of CsPbBr$_3$ QD is the one with the most precise description and illustrates some of the possible issues. Some of the early works[166,358] indeed report on a cubic phase at room temperature in contradiction with the known bulk orthorhombic phase from room down to very low temperatures [395] and with other experimental results on QD.[362] Refined analysis of 12.5nm QD crystallographic structures at room temperature by X-ray diffraction indicates that the crystal structure is unequivocally an orthorhombic perovskite phase.[364] However, the analysis of the exciton fine structure of a large number of CsPbBr$_3$ QD at

low temperature (Figure 47), shows that they may exhibit a tetragonal or orthorhombic phase.[350,398] A further reduction of symmetry leading to a Rashba effect is also possible.[379] More, the existence of coherent nanotwins was demonstrated in $CsPbX_3$ QD.[374] These nanotwins together with dynamic disorder may results in an apparent higher-symmetry structure.
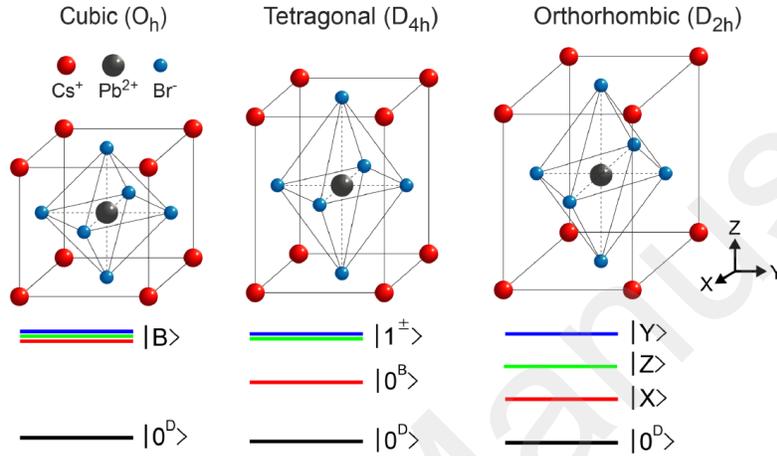
Figure 47. Diagrams of energy levels of the band-edge exciton fine structure of CsPbBr₃ perovskites for three different crystal structures. The lowest state is a dark state while the others are optically active. For the cubic phase, B represents a triply degenerate bright energy-level. Reprinted with permission from ref [350]. Copyright 2017 American Chemical Society.

A DFT-based theoretical analysis of quantum confinement effects is simpler in QNPL assuming lattice periodicity in the two directions perpendicular to the smallest dimension (Figure 48)? [81,382] Sizeable increase of the electronic band gap by comparison to bulk materials is predicted for thicknesses of QNPL smaller than about 8-10 monolayers (about 6nm depending on the material). The variation of the band gap with the number of layers n, $E_g(n)$, can be expressed as: $E_g(n) = E_{g,bulk} + \delta E_g(n)$ where $E_{g,bulk}$ is the band gap of the bulk core material and $\delta E_g(n)$ stems from confinement effects. Although DFT-based many-body corrections are not

possible for such nanostructures, it is possible to propose an approximated decomposition of the various contributions: $E_g(n) = E_{g,DFT,bulk} + \delta E_{g,DFT}(n) + \Sigma_{bulk} + \delta\Sigma(n)$ where $E_{g,DFT,bulk}$ and Σ_{bulk} are respectively the bulk band gap evaluated at the DFT level and the self-energy corrections due to many-body effects. The band gap can also be extracted from experimental data.

The effect of quantum confinement can be estimated from $\delta E_{g,DFT}(n)$, provided that the effective masses of the bulk materials are not strongly affected by the underestimation of the band gap at the DFT level. SOC is in principle necessary for a precise determination of the electronic properties of halide perovskite (Table 4 and section 3.1.3).[64,91] But a crude approximation of the electronic band gap variation may be obtained in many cases by neglecting the SOC, due to an error cancellation between SOC and many-body corrections (vide supra). However, one must keep in mind that the degeneracy of the CB is not correctly predicted.
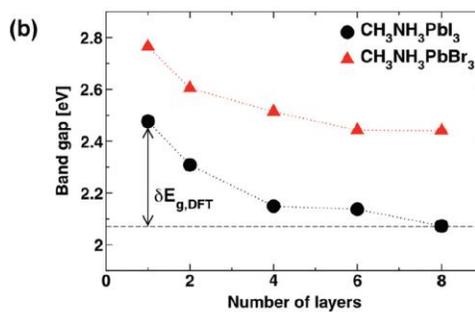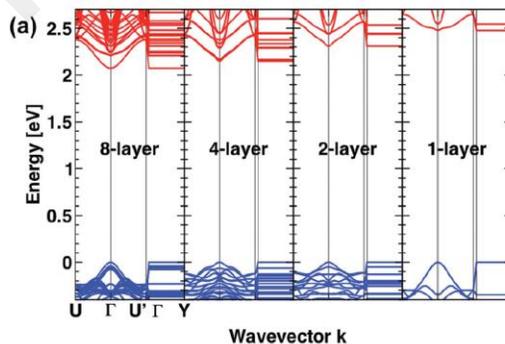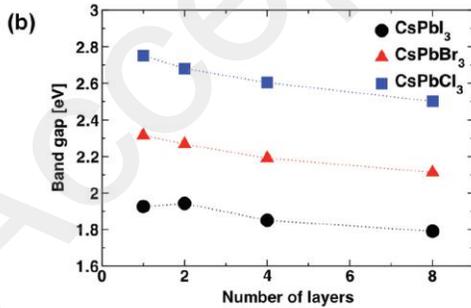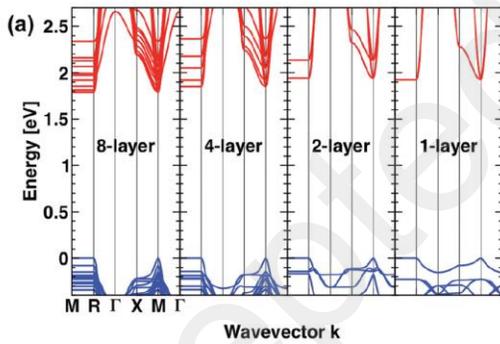
Figure 48. (left) (a) Band structures for slabs of CsPbI₃. (b) Band gaps with respect to the slab thickness of CsPbX₃ (X = I, Br, Cl). (right) (a) Band structures for slabs of CH₃NH₃PbI₃ with various thicknesses. (b) Band gaps with respect to the slab thickness of CH₃NH₃PbX₃ (X = I, Br). From ref [81] *– Published by the Royal Society of Chemistry.*

Table 4: SOC-DFT calculated band gap $E_{g,DFT}$, electron/hole effective masses and reduced masses. Reprinted with permission from ref [382]. *Copyright 2016 American Chemical Society.*

n	$E_g{}^a$ (eV)	m_h/m_0	m_e/m_0	μ/m_0
1	2.84	0.246	0.242	0.122
3	2.67	0.224	0.226	0.112
5	2.59	0.211	0.215	0.107
11	2.51	0.198	0.202	0.100
15	2.47	0.191	0.195	0.096
∞	2.36	0.172	0.171	0.086

^{a}The calculated band gap values were rescaled by 2.09 eV to match the measured PL band gap for the bulk.

The variation of the self-energy correction $\delta\Sigma(n)$ cannot be evaluated directly from GW computations. An alternative semi-empirical evaluation of this correction, similar to the one used for layered perovskites, is possible. A detailed description of the dielectric profile is needed for that purpose. DFT calculations on the in-plane and out-plane dielectric constants was performed considering the stacks of CH₃NH₃PbBr₃ perovskites with capping ligand octylammonium (CH₃(CH₂)₇NH₃⁺) layers as a single object (Figure 49.)[384] It shows that a small dielectric anisotropy is present for thicknesses larger than 10 monolayers, whereas quantum confinement effects are expected to vanish beyond this limit. More importantly the average dielectric constant is smaller than the bulk one, thus leading to the prediction of an enhancement of the exciton binding energy.
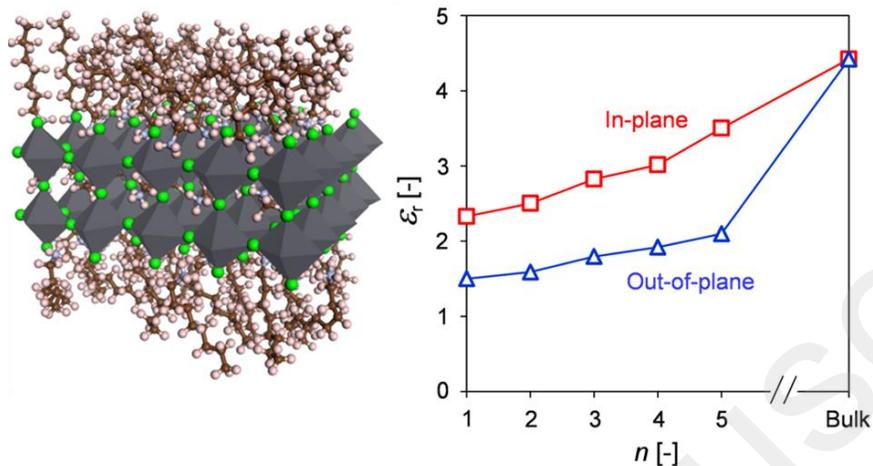
Figure 49. (left) Computer-generated molecular model (carbon, brown; hydrogen, pink; bromine, green; nitrogen, sky blue) of a 2D perovskite with n = 2 from CH₃NH₃PbBr₃. (right) DFT-calculated out-of-plane and in-plane relative permittivity ε_r as a function of n. Reprinted with permission from ref [384]. Copyright 2016 American Chemical Society.

A DFT computation of the dielectric profiles in QNPL was proposed for the first time by Sapori and coworkers[81] and applied to many different halide perovskites (Figure 50.)[206] This approach is able to predict a dielectric confinement in various situations including QNPL made of bulk 3D halide perovskites such as $CsPbX_3$ or $MAPbX_3$ compounds. It shows that the dielectric constant at the center of a QNPL is significantly smaller than the bulk dielectric constant for thickness smaller than about 8 monolayers (5nm). The binding energy of the 2D exciton is thus expected to be enhanced in thin QNPL both by a lower perovskite dielectric constant and by the dielectric mismatch with the external layer.

118
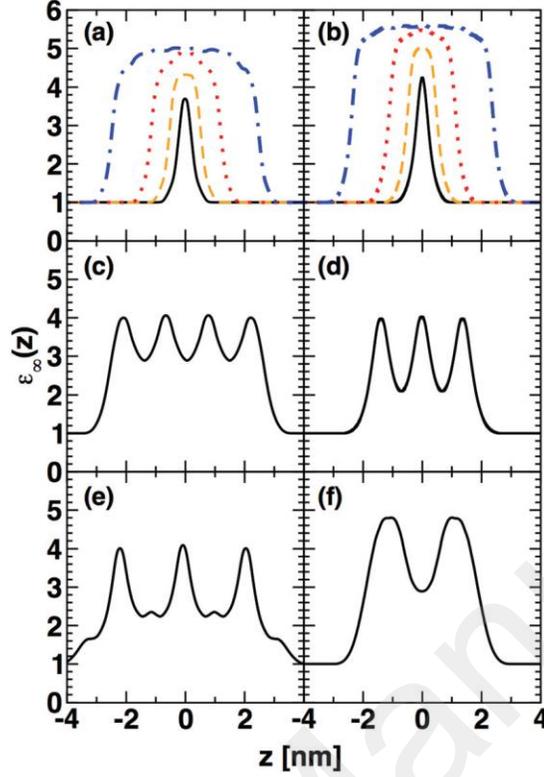
Figure 50. High frequency dielectric profiles $\varepsilon_\infty(z)$ for slabs of (a) CsPbI$_3$, (b) CH$_3$NH$_3$PbI$_3$ (in the [010] direction). Black, orange, red and blue lines correspond to 1, 2, 4 and 8-layer slabs, respectively. $\varepsilon_\infty(z)$ for (c) the 2D halide perovskite with an aromatic cation (C$_7$H$_{10}$N)$_2$PbI4, the 2D halide perovskite with aliphatic cations (d) (C$_4$H$_{12}$N)$_2$PbI$_4$, and (e) (C$_{10}$H$_{24}$N)$_2$PbI$_4$. (f) Same for the bilayered (n = 2) halide perovskite (C$_{10}$H$_{24}$N)$_2$PbI$_3$CH$_3$NH$_3$PbI$_4$. From ref [81] – Published by The Royal Society of Chemistry.

In order to evaluate the impact of dielectric self-energy correction on single particle states, the self-energy profiles may be deduced after a partial Fourier transform of the Poisson equation as previously described for layered perovskites:

$$\delta\Sigma(z) = \lim_{z \to z_0} \frac{e_0}{4\pi} \int_0^\infty \left(V_{QNPL}(q_t, z, z_0) - V_{bulk}(q_t, z, z_0) \right) q_t dq_t \qquad (45)$$

119

In order to properly evaluate the $\delta\Sigma(n)$ correction, the self-energy profile $\delta\Sigma(z)$ shall be a weighted average over the electron or hole densities, but this has not yet been performed. A rough estimate of $\delta\Sigma(n)$ can be obtained by considering the profile value at the middle of the QNPL $\delta\Sigma(z = 0)$ (Figure 51). This approximation is strictly valid for ultrathin QNPL and considering single particle states highly confined inside the perovskite sheet ($\rho_e(z_e) = \delta_{z_e}$ and $\rho_h(z_h) = \delta_{z_h}$) It yields thus an upper limit for the self-energy correction in monolayered QNPL on the order of 0.3 eV for a single particle state and of 0.6 eV for the band gap. In principle this value should be added to the $\delta E_{g,DFT}(n)$ correction which is on the order of about 0.4 eV. The exciton binding energy which depends on the QNPL thickness as well ($E_{b,X}(n)$) must be substracted from the electronic band gap formula:

$$E_{g,opt}(n) = E_{g,DFT,bulk} + \delta E_{g,DFT}(n) + \Sigma_{bulk} + \delta\Sigma(n) - E_{b,X}(n) \qquad (46)$$

Experimental or theoretical studies on the enhancement of the exciton binding energies in QNPL $E_{b,X}(n)$ are scarce, by comparison to layered perovskites. Li and coworkers[385] report a binding energy of about 120 meV for $CsPbBr_3$ QNPL with thicknesses on the order of 5-7 monolayers and larger lateral sizes, that is on the same order as the one predicted for layered perovskites with n = 5-7.[275] More systematic studies will be certainly fruitfull. Yaffe and coworkers[309] indeed show that the binding energy of a free-standing monolayered perovskite sheet may be as high as 490 meV, which is slightly larger than the binding energy of the same compounds in bulk monolayered perovskites (467 meV)[275].
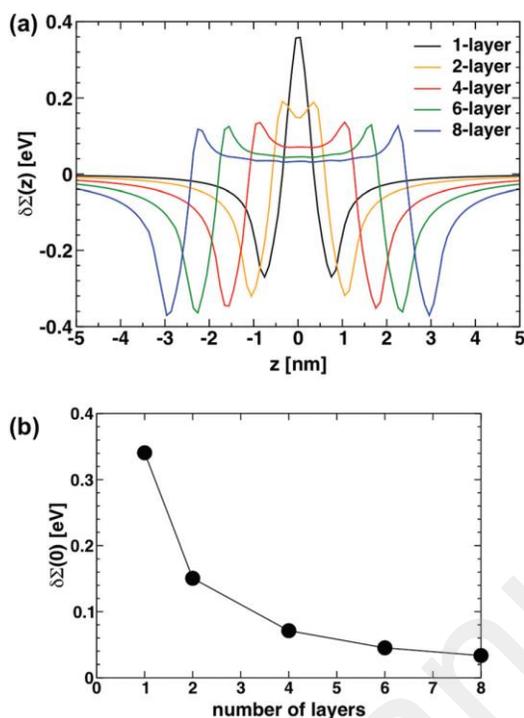
Figure 51. (a) Self-energy profile δΣ(z) for slabs of $CH_3NH_3PbI_3$. (b) Self-energy taken at the slab centre δΣ(0). From ref [81] *– Published by The Royal Society of Chemistry.*

6. CONCLUSION

Despite decades of research on layered halide perovskites and the recent surge of interest on colloidal perovskite nanostructures, understanding on the seemingly well-defined quantum and dielectric confinement concepts in the context of halide perovskites is still scarce. Noteworthy, some basic optoelectronic properties of 3D bulk halide perovskites are still shrouded in mystery.[399–404] Therefore, multilayered halide perovskites and colloidal perovskite nanostructures represent nano-objects of great complexity. Theoretical descriptions may hardly rely only on brute force atomistic methods based on DFT. Precise full DFT-based calculations based on the BSE equation will require significant progresses on the numerical side in order to address the

121

excitations in such big systems. From the review on the dielectric confinement effect in layered perovskites (section 4), we suggest some perspectives on the theoretical approaches of the dielectric properties of multilayered halide perovskites. The progresses on the understanding of these effects will probably rely first on the Poisson equation and more systematic investigations of the dielectric profiles using DFT including anisotropy effects ($\varepsilon_\parallel(z) \neq \varepsilon_\perp(z)$). DFT shall also be useful to obtain a proper description of single particle spinors. Mixing empirical approaches with modern DFT methods, as well as drawing analogies with classical semiconductor heterostructures or van der Waals heterostructures, is a more practical way to achieve quantitative and predictive descriptions. The success of nowadays studies will inevitably rely on precise structural characterizations and modern spectroscopy tools. Recent investigations of various families of natural multilayered halide perovskite (innate heterostructures) and exfoliated crystals allow making systematic variations of relevant important physical parameters, such as the QW thickness or the dielectric mismatch between the QW and the barrier. Furthermore, whereas most of the existing layered perovskites consist in type I inorganic quantum wells, engineering of the spacer cations that stabilize the perovskite slabs leaves room for significant diversification and improvement, raising issues of dimensionality (e.g. structural versus electronic) and/or energy or charge transfer phenomena. Similar questions are also to be anticipated in the realm of perovskite nanostructures, for instance with the ongoing development of core-shell nano-objects and the ever-growing list of materials and chemical moieties that are combined to perovskites to enrich their properties. We believe that this exciting class of materials provides an impressive playground both for new discoveries in fundamental science but also in the prospect to establish new stable and environmental friendly devices.

ACKNOWLEDGEMENTS

ABBREVIATIONS

0D,1D, 2D, 3D	zero-, one-, two-, three-dimensional
3AMP	3-(methylammonium)piperidinium
4AMP	4-(methylammonium)piperidinium
5FPEA	2,3,4,5,6-pentafluorophenethylammonium
ac-BA	ammonium 4-butyric acid
ADF	annular dark field
AESBT	5-ammoniumethylsulfanyl-2,2'-bithiophene
AFM	atomic force microscopy
API	ammonium-propyl-imidazole
BA	butylammonium
BSE	Bethe–Salpeter equation
BZ	Brillouin zone
CB	conduction band
CBM	conduction band minimum
CIGS	solid solution of copper, indium, gallium and selenide used for thin-film solar cell technology
DFT	density functional theory

123

DOS	density of states
DPDA	N,N-dimethylphenylene-p-diammonium
DSL	dielectric superlattice
DW	dielectric well
EA	ethylammonium
EDBE	2,2'-(ethylenedioxy)bis(ethylammonium)
EEL	electron energy loss spectroscopy
ETH	extended Hückel tight-binding model
FA	formamidinium
GGA	generalized gradient approximation to the exchange–correlation energy functional in density functional theory including the density and its first derivative
GKS	generalized Kohn – Sham
GUA	guanidinium
GW	approximation of the self-energy of a many-body system of electrons as a product between the single particle Green's function G and the screened Coulomb interaction W
G_0W_0	first order perturbation of the GW approximation
H2D2c	N-methylethane-1,2-diammonium
HEA	ethanolammonium
HOMO	highest occupied molecular orbital

HSE	exchange–correlation energy functional incorporating a portion of exact exchange from Hartree–Fock theory proposed by Heyd, Scuseria and Ernzerhof in 2003
IC6	iodohexylammonium
IPES	inverse photoemission spectroscopy
KS	Kohn – Sham
LCAO	linear combination of atomic orbitals
LDA	local density approximation to the exchange–correlation energy functional in density functional theory
LDOS	local density of states
LUMO	lowest unoccupied molecular orbital
MA	methylammonium
NAMD	non-adiabatic molecular dynamics
NEA	2-naphtylenethylammonium
OA	octyl-alkylammonium
OD	optical density
PEA	phenethylammonium
PBE	generalized gradient approximation proposed by Perdew, Burke and Ernzerhof in 1996
PL	photoluminescence
PLE	photoluminescence excitation
QD	quantum dot
QNPL	quantum nanoplatelet

QR	quantum rod
QW	quantum well
QWr	quantum wire
RA	alkylamine
Sc-GW	self-consistent GW approximation
SEM	scanning electron microscopy
SOC	spin-orbit coupling
TB	tight binding
TD-DFT	time-dependent density functional theory
ThMA	2-methylammonium thiophene
UPS	ultraviolet photoelectron spectroscopy
UV	ultraviolet
VB	valence band
VBM	valence band maximum

SHORT BIOS

Claudine Katan

Dr. Claudine Katan, born Hoerner, is a CNRS Research Investigator since 1993 in France. She has a broad experience in interdisciplinary collaborative research thanks to her subsequent position at the Physics and Chemistry Departments of Rennes interspersed by a two year stay at FOTON Institute as well as fruitful international collaborations. Her theoretical research is usually conducted in close collaboration with experimentalists and covered structural and electronic properties of molecular charge-transfer crystals, linear/non-linear optical properties of molecular chromophores for various applications, including two-photon uncaging. Currently, understanding the physical and photo-physical properties of hybrid and all-inorganic metal-halide perovskites is her major theme. Those materials have recently demonstrated great potential for various sustainable technologies, including light emitting and photovoltaic devices, raising in turn many fundamental issues in Physics and Materials Science.

Nicolas Mercier

Nicolas Mercier is full Professor at the University of Angers (France). He obtained his PhD in 1994 from the University of Le Mans (France), under the supervision of Pr. M. Leblanc in Pr. G. Ferey's group. In 1996, he was an assistant professor in the chemistry department of Angers University. His major interests include the synthesis, crystallography, structure-property relationships of organic-inorganic hybrid materials. He started working in the field of hybrid perovskites (HPs) in 2002, showing the key role of organic cations to tune the band gap of 2D HPs, the potential of such hybrids in the field of SHG switchable materials and in the field of ferroelectrics. Recently, he has discovered the new family of lead and iodide deficient hybrid perovskites (d-HPs). His activity is also dedicated to viologen based photochromic materials, porous coordination polymers and mechanochromic luminescent hybrid materials.

Jacky Even

Jacky Even is full Professor at INSA Rennes engineering school since 1999 and senior member of Institut Universitaire de France (IUF). He received a PhD in Physics from the University of Paris VI in 1992. He was assistant professor at the Physics Department of Rennes University (1992−1999), where he gained broad experience in phase transitions and solid-state chemical reactions in molecular materials, using theoretical and experimental approaches: neutron and X-ray scattering, Raman/FTIR spectroscopy, calorimetry, among others. In 1999, he created FOTON's simulation team, to address fundamental questions on semiconductors at the atomistic level as well as to perform optoelectronic device simulation. Besides halide perovskites, his theoretical activity is dedicated to semiconductor buried nanostructures, colloidal nanostructures, photovoltaic and light-emitting (LED, laser, ...) devices for silicon photonics, and optical telecommunications.

References

(1)   Kojima, A.; Teshima, K.; Shirai, Y.; Miyasaka, T. Organometal Halide Perovskites as Visible-Light Sensitizers for Photovoltaic Cells. *J. Am. Chem. Soc.* **2009**, *131* (17), 6050–6051. https://doi.org/10.1021/ja809598r.

(2)   Im, J.-H.; Lee, C.-R.; Lee, J.-W.; Park, S.-W.; Park, N.-G. 6.5% Efficient Perovskite Quantum-Dot-Sensitized Solar Cell. *Nanoscale* **2011**, *3* (10), 4088–4093. https://doi.org/10.1039/c1nr10867k.

(3)   Lee, M. M.; Teuscher, J.; Miyasaka, T.; Murakami, T. N.; Snaith, H. J. Efficient Hybrid Solar Cells Based on Meso-Superstructured Organometal Halide Perovskites. *Science* **2012**, *338* (6107), 643–647. https://doi.org/10.1126/science.1228604.

(4)   Kim, H.-S.; Lee, C.-R.; Im, J.-H.; Lee, K.-B.; Moehl, T.; Marchioro, A.; Moon, S.-J.; Humphry-Baker, R.; Yum, J.-H.; Moser, J. E.; et al. Lead Iodide Perovskite Sensitized All-Solid-State Submicron Thin Film Mesoscopic Solar Cell with Efficiency Exceeding 9%. *Sci. Rep.* **2012**, *2* (1), 591. https://doi.org/10.1038/srep00591.

(5)   Correa-Baena, J.-P.; Saliba, M.; Buonassisi, T.; Grätzel, M.; Abate, A.; Tress, W.; Hagfeldt, A. Promises and Challenges of Perovskite Solar Cells. *Science* **2017**, *358* (6364), 739–744. https://doi.org/10.1126/science.aam6323.

(6)   NREL Chart.

(7)   Snaith, H. J. Present Status and Future Prospects of Perovskite Photovoltaics. *Nat. Mater.* **2018**, *17* (5), 372–376. https://doi.org/10.1038/s41563-018-0071-z.

(8)   Yang, W. S.; Park, B.-W.; Jung, E. H.; Jeon, N. J.; Kim, Y. C.; Lee, D. U.; Shin, S. S.; Seo, J.; Kim, E. K.; Noh, J. H.; et al. Iodide Management in Formamidinium-Lead-Halide–Based Perovskite Layers for Efficient Solar Cells. *Science* **2017**, *356* (6345), 1376–1379. https://doi.org/10.1126/science.aan2301.

(9)   Tsai, H.; Asadpour, R.; Blancon, J.-C.; Stoumpos, C. C.; Durand, O.; Strzalka, J. W.; Chen, B.; Verduzco, R.; Ajayan, P. M.; Tretiak, S.; et al. Light-Induced Lattice Expansion Leads to High-Efficiency Perovskite Solar Cells. *Science* **2018**, *360* (6384), 67–70. https://doi.org/10.1126/science.aap8671.

(10) Saliba, M.; Matsui, T.; Domanski, K.; Seo, J.-Y.; Ummadisingu, A.; Zakeeruddin, S. M.; Correa-Baena, J.-P.; Tress, W. R.; Abate, A.; Hagfeldt, A.; et al. Incorporation of Rubidium Cations into Perovskite Solar Cells Improves Photovoltaic Performance. *Science* **2016**, *354* (6309), 206–209. https://doi.org/10.1126/science.aah5557.

(11) Nie, W.; Tsai, H.; Asadpour, R.; Blancon, J.-C.; Neukirch, A. J.; Gupta, G.; Crochet, J. J.; Chhowalla, M.; Tretiak, S.; Alam, M. A.; et al. High-Efficiency Solution-Processed Perovskite Solar Cells with Millimeter-Scale Grains. *Science* **2015**, *347* (6221), 522–525. https://doi.org/10.1126/science.aaa0472.

(12) Eperon, G. E.; Leijtens, T.; Bush, K. A.; Prasanna, R.; Green, T.; Wang, J. T.-W.; McMeekin, D. P.; Volonakis, G.; Milot, R. L.; May, R.; et al. Perovskite-Perovskite Tandem Photovoltaics with Optimized Band Gaps. *Science* **2016**, *354* (6314), 861–865. https://doi.org/10.1126/science.aaf9717.

(13) Fu, F.; Feurer, T.; Weiss, T. P.; Pisoni, S.; Avancini, E.; Andres, C.; Buecheler, S.; Tiwari, A. N. High-Efficiency Inverted Semi-Transparent Planar Perovskite Solar Cells in Substrate Configuration. *Nat. Energy* **2016**, *2* (1), 16190. https://doi.org/10.1038/nenergy.2016.190.

(14) Bush, K. A.; Palmstrom, A. F.; Yu, Z. J.; Boccard, M.; Cheacharoen, R.; Mailoa, J. P.; McMeekin, D. P.; Hoye, R. L. Z.; Bailie, C. D.; Leijtens, T.; et al. 23.6%-Efficient

Monolithic Perovskite/Silicon Tandem Solar Cells with Improved Stability. *Nat. Energy* **2017**, *2* (4), 17009. https://doi.org/10.1038/nenergy.2017.9.

(15) Sahli, F.; Werner, J.; Kamino, B. A.; Bräuninger, M.; Monnard, R.; Paviet-Salomon, B.; Barraud, L.; Ding, L.; Diaz Leon, J. J.; Sacchetto, D.; et al. Fully Textured Monolithic Perovskite/Silicon Tandem Solar Cells with 25.2% Power Conversion Efficiency. *Nat. Mater.* **2018**, *17*, 820–826. https://doi.org/10.1038/s41563-018-0115-4.

(16) Duong, T.; Wu, Y.; Shen, H.; Peng, J.; Fu, X.; Jacobs, D.; Wang, E.-C.; Kho, T. C.; Fong, K. C.; Stocks, M.; et al. Rubidium Multication Perovskite with Optimized Bandgap for Perovskite-Silicon Tandem with over 26% Efficiency. *Adv. Energy Mater.* **2017**, *7* (14), 1700228. https://doi.org/10.1002/aenm.201700228.

(17) Ramírez Quiroz, C. O.; Shen, Y.; Salvador, M.; Forberich, K.; Schrenker, N.; Spyropoulos, G. D.; Heumüller, T.; Wilkinson, B.; Kirchartz, T.; Spiecker, E.; et al. Balancing Electrical and Optical Losses for Efficient 4-Terminal Si–Perovskite Solar Cells with Solution Processed Percolation Electrodes. *J. Mater. Chem. A* **2018**, *6* (8), 3583–3592. https://doi.org/10.1039/C7TA10945H.

(18) Smith, I. C.; Hoke, E. T.; Solis-Ibarra, D.; McGehee, M. D.; Karunadasa, H. I. A Layered Hybrid Perovskite Solar-Cell Absorber with Enhanced Moisture Stability. *Angew. Chem. Int. Ed.* **2014**, *53* (42), 11232–11235. https://doi.org/10.1002/anie.201406466.

(19) Cao, D. H.; Stoumpos, C. C.; Farha, O. K.; Hupp, J. T.; Kanatzidis, M. G. 2D Homologous Perovskites as Light-Absorbing Materials for Solar Cell Applications. *J. Am. Chem. Soc.* **2015**, *137* (24), 7843–7850. https://doi.org/10.1021/jacs.5b03796.

(20) Tsai, H.; Nie, W.; Blancon, J.-C.; Stoumpos, C. C.; Asadpour, R.; Harutyunyan, B.; Neukirch, A. J.; Verduzco, R.; Crochet, J. J.; Tretiak, S.; et al. High-Efficiency Two-Dimensional Ruddlesden–Popper Perovskite Solar Cells. *Nature* **2016**, *536* (7616), 312–316. https://doi.org/10.1038/nature18306.

(21) Swarnkar, A.; Marshall, A. R.; Sanehira, E. M.; Chernomordik, B. D.; Moore, D. T.; Christians, J. A.; Chakrabarti, T.; Luther, J. M. Quantum Dot-Induced Phase Stabilization of -CsPbI3 Perovskite for High-Efficiency Photovoltaics. *Science* **2016**, *354* (6308), 92–95. https://doi.org/10.1126/science.aag2700.

(22) Bian, H.; Bai, D.; Jin, Z.; Wang, K.; Liang, L.; Wang, H.; Zhang, J.; Wang, Q.; Liu, S. (Frank). Graded Bandgap CsPbI 2+x Br 1−x Perovskite Solar Cells with a Stabilized Efficiency of 14.4%. *Joule* **2018**, *2*, 1500–1510. https://doi.org/10.1016/j.joule.2018.04.012.

(23) Papavassiliou, G. C. Three- and Low-Dimensional Inorganic Semiconductors. *Prog. Solid State Chem.* **1997**, *25* (3–4), 125–270. https://doi.org/10.1016/S0079-6786(97)80886-2.

(24) Mitzi, D. B. Synthesis, Structure, and Properties of Organic-Inorganic Perovskites and Related Materials. In *Progress in Inorganic Chemistry*; Karlin, K. D., Ed.; John Wiley & Sons, Inc.: Hoboken, NJ, USA, 1999; pp 1–121. https://doi.org/10.1002/9780470166499.ch1.

(25) Saparov, B.; Mitzi, D. B. Organic–Inorganic Perovskites: Structural Versatility for Functional Materials Design. *Chem. Rev.* **2016**, *116*, 4558–4596. https://doi.org/10.1021/acs.chemrev.5b00715.

(26) Ishihara, T.; Takahashi, J.; Goto, T. Exciton State in Two-Dimensional Perovskite Semiconductor (C10H21NH3)2PbI4. *Solid State Commun.* **1989**, *69* (9), 933–936. https://doi.org/10.1016/0038-1098(89)90935-6.

(27) Xu, C.; Kondo, T.; Sakakura, H.; Kumata, K.; Takahashi, Y.; Ito, R. Optical Third-Harmonic Generation in Layered Perovskite-Type Material (C10H21NH3)2PbI4. *Solid State Commun.* **1991**, *79* (3), 245–248. https://doi.org/10.1016/0038-1098(91)90643-A.

(28) Calabrese, J.; Jones, N. L.; Harlow, R. L.; Herron, N.; Thorn, D. L.; Wang, Y. Preparation and Characterization of Layered Lead Halide Compounds. *J. Am. Chem. Soc.* **1991**, *113* (6), 2328–2330. https://doi.org/10.1021/ja00006a076.

(29) Papavassiliou, G. C.; Patsis, A. P.; Lagouvardos, D. J.; Koutselas, I. B. Spectroscopic Studies of (C10H21NH3)2PbI4, (CH3NH3)(C10H21NH3)2Pb2I7, (CH3NH3) PbI3, and Similar Compounds. *Synth. Met.* **1993**, *57* (1), 3889–3894. https://doi.org/10.1016/0379-6779(93)90530-A.

(30) Mitzi, D. B.; Chondroudis, K.; Kagan, C. R. Organic-Inorganic Electronics. *IBM J. Res. Dev.* **2001**, *45* (1), 29–45. https://doi.org/10.1147/rd.451.0029.

(31) Hong, X.; Ishihara, T.; Nurmikko, A. V. Dielectric Confinement Effect on Excitons in PbI 4 -Based Layered Semiconductors. *Phys. Rev. B* **1992**, *45* (12), 6961–6964. https://doi.org/10.1103/PhysRevB.45.6961.

(32) Muljarov, E. A.; Tikhodeev, S. G.; Gippius, N. A.; Ishihara, T. Excitons in Self-Organized Semiconductor/Insulator Superlattices: PbI-Based Perovskite Compounds. *Phys. Rev. B* **1995**, *51* (20), 14370–14378. https://doi.org/10.1103/PhysRevB.51.14370.

(33) Koutselas, I. B.; Ducasse, L.; Papavassiliou, G. C. Electronic Properties of Three- and Low-Dimensional Semiconducting Materials with Pb Halide and Sn Halide Units. *J. Phys. Condens. Matter* **1996**, *8* (9), 1217–1227. https://doi.org/10.1088/0953-8984/8/9/012.

(34) Mitzi, D. B.; Feild, C. A.; Harrison, W. T. A.; Guloy, A. M. Conducting Tin Halides with a Layered Organic-Based Perovskite Structure. *Nature* **1994**, *369* (6480), 467–469. https://doi.org/10.1038/369467a0.

(35) Mitzi, D. B.; Wang, S.; Feild, C. A.; Chess, C. A.; Guloy, A. M. Conducting Layered Organic-Inorganic Halides Containing -Oriented Perovskite Sheets. *Science* **1995**, *267* (5203), 1473–1476. https://doi.org/10.1126/science.267.5203.1473.

(36) Kagan, C. R.; Mitzi, D. B.; Dimitrakopoulos, C. D. Organic-Inorganic Hybrid Materials as Semiconducting Channels in Thin-Film Field-Effect Transistors. *Science* **1999**, *286* (5441), 945–947. https://doi.org/10.1126/science.286.5441.945.

(37) Mitzi, D. B.; Dimitrakopoulos, C. D.; Kosbar, L. L. Structurally Tailored Organic−Inorganic Perovskites: Optical Properties and Solution-Processed Channel Materials for Thin-Film Transistors. *Chem. Mater.* **2001**, *13* (10), 3728–3740. https://doi.org/10.1021/cm010105g.

(38) Papavassiliou, G. C.; Koutselas, I. B.; Terzis, A.; Whangbo, M.-H. Structural and Electronic Properties of the Natural Quantum-Well System (C6H5CH2CH2NH3)2SnI4. *Solid State Commun.* **1994**, *91* (9), 695–698. https://doi.org/10.1016/0038-1098(94)00435-8.

(39) Papavassiliou, G. C.; Koutselas, I. B. Structural, Optical and Related Properties of Some Natural Three- and Lower-Dimensional Semiconductor Systems. *Synth. Met.* **1995**, *71* (1–3), 1713–1714. https://doi.org/10.1016/0379-6779(94)03017-Z.

(40) Koutselas, I.; Bampoulis, P.; Maratou, E.; Evagelinou, T.; Pagona, G.; Papavassiliou, G. C. Some Unconventional Organic−Inorganic Hybrid Low-Dimensional Semiconductors and Related Light-Emitting Devices. *J. Phys. Chem. C* **2011**, *115* (17), 8475–8483. https://doi.org/10.1021/jp111881b.

(41)   Papavassiliou, G. C. Synthetic Three-and Lower-Dimensional Semiconductors Based on Inorganic Units. *Mol. Cryst. Liq. Cryst. Sci. Technol. Sect. Mol. Cryst. Liq. Cryst.* **1996**, *286* (1), 231–238. https://doi.org/10.1080/10587259608042291.

(42)   Papavassiliou, G. C.; Mousdis, G. A.; Raptopoulou, C. P.; Terzis, A. Some New Luminescent Compounds Based on 4-Methylbenzylamine and Lead Halides. *Z. Für Naturforschung B* **2000**, *55* (6), 536– 540. https://doi.org/10.1515/znb-2000-0615.

(43)   Mousdis, G. A.; Gionis, V.; Papavassiliou, G. C.; Raptopoulou, C. P.; Terzis, A. Preparation, Structure and Optical Properties of [CH3SC(□NH2)NH2]3PbI5, [CH3SC(□NH2)NH2]4Pb2Br8and [CH3SC(□NH2)NH2]3PbCl5·CH3SC(□NH2)NH2Cl. *J. Mater. Chem.* **1998**, *8* (10), 2259–2262. https://doi.org/10.1039/a802926a.

(44)   Papavassiliou, G. C.; Koutselas, I. B.; Lagouvardos, D. J.; Kapoutsis, J.; Terzis, A.; Papaioannou, G. J. Optical and Related Properties of Some Natural Three and Lower Dimensional Semiconductor Systems. *Mol. Cryst. Liq. Cryst. Sci. Technol. Sect. Mol. Cryst. Liq. Cryst.* **1994**, *253* (1), 103–112. https://doi.org/10.1080/10587259408055249.

(45)   Papavassiliou, G. C.; Mousdis, G. A.; Koutselas, I. B. Excitonic Bands in the Spectra of Some Organic-Inorganic Hybrid Compounds Based on Metal Halide Units. In *Molecular Materials and Functional Polymers*; Blau, W. J., Lianos, P., Schubert, U., Eds.; Springer Vienna: Vienna, 2001; pp 113–119. https://doi.org/10.1007/978-3-7091-6276-7_11.

(46)   Ishihara, T.; Takahashi, J.; Goto, T. Optical Properties Due to Electronic Transitions in Two-Dimensional Semiconductors (C n H 2 n + 1 NH 3) 2 PbI 4 . *Phys. Rev. B* **1990**, *42* (17), 11099–11107. https://doi.org/10.1103/PhysRevB.42.11099.

(47)   Ishihara, T.; Hong, X.; Ding, J.; Nurmikko, A. V. Dielectric Confinement Effect for Exciton and Biexciton States in PbI4-Based Two-Dimensional Semiconductor Structures. *Surf. Sci.* **1992**, *267* (1–3), 323–326. https://doi.org/10.1016/0039-6028(92)91147-4.

(48)   Kataoka, T.; Kondo, T.; Ito, R.; Sasaki, S.; Uchida, K.; Miura, N. Magneto-Optical Study on the Excitonic Spectrum of (C6H13NH3)2PbI4. *Phys. B Condens. Matter* **1993**, *184* (1–4), 132–136. https://doi.org/10.1016/0921-4526(93)90336-5.

(49)   Kataoka, T.; Kondo, T.; Ito, R.; Sasaki, S.; Uchida, K.; Miura, N. Magneto-Optical Study on Excitonic Spectra in (C 6 H 13 NH 3) 2 PbI 4. *Phys. Rev. B* **1993**, *47* (4), 2010– 2018. https://doi.org/10.1103/PhysRevB.47.2010.

(50)   Hirasawa, M.; Ishihara, T.; Goto, T.; Uchida, K.; Miura, N. Magnetoabsorption of the Lowest Exciton in Perovskite-Type Compound (CH3NH3)PbI3. *Phys. B Condens. Matter* **1994**, *201*, 427–430. https://doi.org/10.1016/0921-4526(94)91130-4.

(51)   Ishihara, T. Optical Properties of PbI-Based Perovskite Structures. *J. Lumin.* **1994**, *60– 61*, 269–274. https://doi.org/10.1016/0022-2313(94)90145-7.

(52)   Kataoka, T.; Kondo, T.; Ito, R.; Sasaki, S.; Uchida, K.; Miura, N. Magneto-Optical Effects of Excitons in the Layered Perovskite-Type Material (C6H13NH3)2(CH3NH3)Pb2I7. *Phys. B Condens. Matter* **1994**, *201*, 423–426. https://doi.org/10.1016/0921-4526(94)91129-0.

(53)   Kondo, T.; Iwamoto, S.; Hayase, S.; Tanaka, K.; Ishi, J.; Mizuno, M.; Ema, K.; Ito, R. Resonant Third-Order Optical Nonlinearity in the Layered Perovskite-Type Material (C6H13NH3)2PbI4. *Solid State Commun.* **1998**, *105* (8), 503–506. https://doi.org/10.1016/S0038-1098(97)10166-1.

(54)   Kondo, T.; Azuma, T.; Yuasa, T.; Ito, R. Biexciton Lasing in the Layered Perovskite-Type Material (C6H13NH3)2PbI4. *Solid State Commun.* **1998**, *105* (4), 253–255. https://doi.org/10.1016/S0038-1098(97)10085-0.

(55)   Matsuishi, K.; Suzuki, T.; Onari, S.; Gregoryanz, E.; Hemley, R. J.; Mao, H. K. Excitonic States of Alkylammonium Lead-Iodide Layered Perovskite Semiconductors under Hydrostatic Pressure to 25 GPa. *Phys. Status Solidi B* **2001**, *223* (1), 177–182. https://doi.org/10.1002/1521-3951(200101)223:1<177::AID-PSSB177>3.0.CO;2-J.

(56)   Matsuishi, K.; Ishihara, T.; Onari, S.; Chang, Y. H.; Park, C. H. Optical Properties and Structural Phase Transitions of Lead-Halide Based Inorganic–Organic 3D and 2D Perovskite Semiconductors under High Pressure. *Phys. Status Solidi B* **2004**, *241* (14), 3328–3333. https://doi.org/10.1002/pssb.200405229.

(57)   Fujita, T.; Nakashima, H.; Hirasawa, M.; Ishihara, T. Ultrafast Photoluminescence from (C6H5C2H4NH3)2PbI4. *J. Lumin.* **2000**, *87–89*, 847–849. https://doi.org/10.1016/S0022-2313(99)00437-8.

(58)   Shimizu, M.; Gippius, N. A.; Tikhodeev, S. G.; Ishihara, T. Coulomb Correction to the Dressed Exciton in an Inorganic-Organic Layered Semiconductor: Detuning Dependence of the Stark Shift. *Phys. Rev. B* **2004**, *69* (15), 155201. https://doi.org/10.1103/PhysRevB.69.155201.

(59)   Tanaka, K.; Sano, F.; Takahashi, T.; Kondo, T.; Ito, R.; Ema, K. Two-Dimensional Wannier Excitons in a Layered-Perovskite-Type Crystal (C6H13NH3)2PbI4. *Solid State Commun.* **2002**, *122* (5), 249–252. https://doi.org/10.1016/S0038-1098(02)00126-6.

(60)   Kato, Y.; Ichii, D.; Ohashi, K.; Kunugita, H.; Ema, K.; Tanaka, K.; Takahashi, T.; Kondo, T. Extremely Large Binding Energy of Biexcitons in an Organic–Inorganic Quantum-Well Material (C4H9NH3)2PbBr4. *Solid State Commun.* **2003**, *128* (1), 15–18. https://doi.org/10.1016/S0038-1098(03)00626-4.

(61)   Tanaka, K.; Kondo, T. Bandgap and Exciton Binding Energies in Lead-Iodide-Based Natural Quantum-Well Crystals. *Sci. Technol. Adv. Mater.* **2003**, *4* (6), 599–604. https://doi.org/10.1016/j.stam.2003.09.019.

(62)   Tanaka, K.; Takahashi, T.; Kondo, T.; Umebayashi, T.; Asai, K.; Ema, K. Image Charge Effect on Two-Dimensional Excitons in an Inorganic-Organic Quantum-Well Crystal. *Phys. Rev. B* **2005**, *71* (4), 045312. https://doi.org/10.1103/PhysRevB.71.045312.

(63)   Braun, M.; Frey, W. Crystal Structure of Bis(Benzylammonium) Lead Tetrachloride, (C7H7NH3)2PbCl4. *Z. Für Krist. - New Cryst. Struct.* **1999**, *214* (3), 331–332. https://doi.org/10.1515/ncrs-1999-0318.

(64)   Even, J.; Pedesseau, L.; Dupertuis, M.-A.; Jancu, J.-M.; Katan, C. Electronic Model for Self-Assembled Hybrid Organic/Perovskite Semiconductors: Reverse Band Edge Electronic States Ordering and Spin-Orbit Coupling. *Phys. Rev. B* **2012**, *86* (20), 205301. https://doi.org/10.1103/PhysRevB.86.205301.

(65)   Pedesseau, L.; Jancu, J.-M.; Rolland, A.; Deleporte, E.; Katan, C.; Even, J. Electronic Properties of 2D and 3D Hybrid Organic/Inorganic Perovskites for Optoelectronic and Photovoltaic Applications. *Opt. Quantum Electron.* **2014**, *46* (10), 1225–1232. https://doi.org/10.1007/s11082-013-9823-9.

(66)   Kepenekian, M.; Robles, R.; Katan, C.; Sapori, D.; Pedesseau, L.; Even, J. Rashba and Dresselhaus Effects in Hybrid Organic–Inorganic Perovskites: From Basics to Devices. *ACS Nano* **2015**, *9* (12), 11557–11567. https://doi.org/10.1021/acsnano.5b04409.

(67) Even, J.; Pedesseau, L.; Katan, C.; Kepenekian, M.; Lauret, J.-S.; Sapori, D.; Deleporte, E. Solid-State Physics Perspective on Hybrid Perovskite Semiconductors. *J. Phys. Chem. C* **2015**, *119* (19), 10161–10177. https://doi.org/10.1021/acs.jpcc.5b00695.

(68) Lemmerer, A.; Billing, D. G. Synthesis, Characterization and Phase Transitions of the Inorganic–Organic Layered Perovskite-Type Hybrids [(C $_n$ H $_{2n+1}$ NH $_3$) $_2$ PbI $_4$], n = 7, 8, 9 and 10. *Dalton Trans* **2012**, *41* (4), 1146–1157. https://doi.org/10.1039/C0DT01805H.

(69) Smith, M. D.; Pedesseau, L.; Kepenekian, M.; Smith, I. C.; Katan, C.; Even, J.; Karunadasa, H. I. Decreasing the Electronic Confinement in Layered Perovskites through Intercalation. *Chem. Sci.* **2017**, *8* (3), 1960–1968. https://doi.org/10.1039/C6SC02848A.

(70) Kikuchi, K.; Takeoka, Y.; Rikukawa, M.; Sanui, K. Structure and Optical Properties of Lead Iodide Based Two-Dimensional Perovskite Compounds Containing Fluorophenethylamines. *Curr. Appl. Phys.* **2004**, *4* (6), 599–602. https://doi.org/10.1016/j.cap.2004.01.027.

(71) Lanty, G.; Bréhier, A.; Parashkov, R.; Lauret, J. S.; Deleporte, E. Strong Exciton–Photon Coupling at Room Temperature in Microcavities Containing Two-Dimensional Layered Perovskite Compounds. *New J. Phys.* **2008**, *10* (6), 065007. https://doi.org/10.1088/1367-2630/10/6/065007.

(72) Billing, D. G.; Lemmerer, A. Synthesis, Characterization and Phase Transitions in the Inorganic–Organic Layered Perovskite-Type Hybrids [(C $_n$ H $_{2n+1}$ NH $_3$) $_2$ PbI $_4$], *n* = 4, 5 and 6. *Acta Crystallogr. B* **2007**, *63* (5), 735–747. https://doi.org/10.1107/S0108768107031758.

(73) Lanty, G.; Jemli, K.; Wei, Y.; Leymarie, J.; Even, J.; Lauret, J.-S.; Deleporte, E. Room-Temperature Optical Tunability and Inhomogeneous Broadening in 2D-Layered Organic–Inorganic Perovskite Pseudobinary Alloys. *J. Phys. Chem. Lett.* **2014**, *5* (22), 3958–3963. https://doi.org/10.1021/jz502086e.

(74) Brehier, A.; Parashkov, R.; Lauret, J. S.; Deleporte, E. Strong Exciton-Photon Coupling in a Microcavity Containing Layered Perovskite Semiconductors. *Appl. Phys. Lett.* **2006**, *89* (17), 171110. https://doi.org/10.1063/1.2369533.

(75) Wenus, J.; Parashkov, R.; Ceccarelli, S.; Brehier, A.; Lauret, J.-S.; Skolnick, M. S.; Deleporte, E.; Lidzey, D. G. Hybrid Organic-Inorganic Exciton-Polaritons in a Strongly Coupled Microcavity. *Phys. Rev. B* **2006**, *74* (23), 235212. https://doi.org/10.1103/PhysRevB.74.235212.

(76) Pedesseau, L.; Sapori, D.; Traore, B.; Robles, R.; Fang, H.-H.; Loi, M. A.; Tsai, H.; Nie, W.; Blancon, J.-C.; Neukirch, A.; et al. Advances and Promises of Layered Halide Hybrid Perovskite Semiconductors. *ACS Nano* **2016**, *10* (11), 9776–9786. https://doi.org/10.1021/acsnano.6b05944.

(77) Miura, T.; Takeoka, Y.; Sato, M.; Kunugita, H.; Ema, K. Well-Width Dependence of Excitonic Properties in Organic-Inorganic Hybrid Quantum Well Materials: Well-Width Dependence of Excitonic Properties in Organic-Inorganic Hybrid Quantum Well Materials. *Phys. Status Solidi C* **2011**, *8* (9), 2752–2755. https://doi.org/10.1002/pssc.201084076.

(78) Wu, X.; Trinh, M. T.; Niesner, D.; Zhu, H.; Norman, Z.; Owen, J. S.; Yaffe, O.; Kudisch, B. J.; Zhu, X.-Y. Trap States in Lead Iodide Perovskites. *J. Am. Chem. Soc.* **2015**, *137* (5), 2089–2096. https://doi.org/10.1021/ja512833n.

(79) Wu, X.; Trinh, M. T.; Zhu, X.-Y. Excitonic Many-Body Interactions in Two-Dimensional Lead Iodide Perovskite Quantum Wells. *J. Phys. Chem. C* **2015**, *119* (26), 14714–14721. https://doi.org/10.1021/acs.jpcc.5b00148.

(80) Stoumpos, C. C.; Cao, D. H.; Clark, D. J.; Young, J.; Rondinelli, J. M.; Jang, J. I.; Hupp, J. T.; Kanatzidis, M. G. Ruddlesden–Popper Hybrid Lead Iodide Perovskite 2D Homologous Semiconductors. *Chem. Mater.* **2016**, *28*, 2852–2867. https://doi.org/10.1021/acs.chemmater.6b00847.

(81) Sapori, D.; Kepenekian, M.; Pedesseau, L.; Katan, C.; Even, J. Quantum Confinement and Dielectric Profiles of Colloidal Nanoplatelets of Halide Inorganic and Hybrid Organic–Inorganic Perovskites. *Nanoscale* **2016**, *8* (12), 6369–6378. https://doi.org/10.1039/C5NR07175E.

(82) Stoumpos, C. C.; Soe, C. M. M.; Tsai, H.; Nie, W.; Blancon, J.-C.; Cao, D. H.; Liu, F.; Traoré, B.; Katan, C.; Even, J.; et al. High Members of the 2D Ruddlesden-Popper Halide Perovskites: Synthesis, Optical Properties, and Solar Cells of $(CH_3(CH_2)_3NH_3)_2(CH_3NH_3)_4Pb_5I_{16}$. *Chem* **2017**, *2* (3), 427–440. https://doi.org/10.1016/j.chempr.2017.02.004.

(83) Soe, C. M. M.; Stoumpos, C. C.; Kepenekian, M.; Traoré, B.; Tsai, H.; Nie, W.; Wang, B.; Katan, C.; Seshadri, R.; Mohite, A. D.; et al. New Type of 2D Perovskites with Alternating Cations in the Interlayer Space, $(C(NH_2)_3)(CH_3NH_3)_n Pb_n I_{3n+1}$: Structure, Properties, and Photovoltaic Performance. *J. Am. Chem. Soc.* **2017**, *139* (45), 16297–16309. https://doi.org/10.1021/jacs.7b09096.

(84) Mao, L.; Wu, Y.; Stoumpos, C. C.; Traore, B.; Katan, C.; Even, J.; Wasielewski, M. R.; Kanatzidis, M. G. Tunable White-Light Emission in Single-Cation-Templated Three-Layered 2D Perovskites $(CH_3CH_2NH_3)_4Pb_3Br_{10-x}Cl_x$. *J. Am. Chem. Soc.* **2017**, *139* (34), 11956–11963. https://doi.org/10.1021/jacs.7b06143.

(85) Yu, Y.; Zhang, D.; Yang, P. Ruddlesden–Popper Phase in Two-Dimensional Inorganic Halide Perovskites: A Plausible Model and the Supporting Observations. *Nano Lett.* **2017**, *17* (9), 5489–5494. https://doi.org/10.1021/acs.nanolett.7b02146.

(86) Cao, D. H.; Stoumpos, C. C.; Yokoyama, T.; Logsdon, J. L.; Song, T.-B.; Farha, O. K.; Wasielewski, M. R.; Hupp, J. T.; Kanatzidis, M. G. Thin Films and Solar Cells Based on Semiconducting Two-Dimensional Ruddlesden–Popper $(CH_3(CH_2)_3NH_3)_2(CH_3NH_3)_{n-1}Sn_nI_{3n+1}$ Perovskites. *ACS Energy Lett.* **2017**, *2* (5), 982–990. https://doi.org/10.1021/acsenergylett.7b00202.

(87) Soe, C. M. M.; Nie, W.; Stoumpos, C. C.; Tsai, H.; Blancon, J.-C.; Liu, F.; Even, J.; Marks, T. J.; Mohite, A. D.; Kanatzidis, M. G. Understanding Film Formation Morphology and Orientation in High Member 2D Ruddlesden-Popper Perovskites for High-Efficiency Solar Cells. *Adv. Energy Mater.* **2018**, *8* (1), 1700979. https://doi.org/10.1002/aenm.201700979.

(88) Tsai, H.; Nie, W.; Blancon, J.-C.; Stoumpos, C. C.; Soe, C. M. M.; Yoo, J.; Crochet, J.; Tretiak, S.; Even, J.; Sadhanala, A.; et al. Stable Light-Emitting Diodes Using Phase-Pure Ruddlesden-Popper Layered Perovskites. *Adv. Mater.* **2018**, 1704217. https://doi.org/10.1002/adma.201704217.

(89) Blancon, J.-C.; Tsai, H.; Nie, W.; Stoumpos, C. C.; Pedesseau, L.; Katan, C.; Kepenekian, M.; Soe, C. M. M.; Appavoo, K.; Sfeir, M. Y.; et al. Extremely Efficient Internal Exciton Dissociation through Edge States in Layered 2D Perovskites. *Science* **2017**, *355* (6331), 1288–1292. https://doi.org/10.1126/science.aal4211.

(90) Even, J.; Pedesseau, L.; Katan, C. Theoretical Insights into Multibandgap Hybrid Perovskites for Photovoltaic Applications. In *Proc. SPIE 9140*; Wehrspohn, R. B., Gombert, A., Eds.; 2014; Vol. 9140, p 91400Y. https://doi.org/10.1117/12.2052375.

(91) Even, J.; Pedesseau, L.; Jancu, J.-M.; Katan, C. Importance of Spin–Orbit Coupling in Hybrid Organic/Inorganic Perovskites for Photovoltaic Applications. *J. Phys. Chem. Lett.* **2013**, *4* (17), 2999–3005. https://doi.org/10.1021/jz401532q.

(92) Even, J.; Pedesseau, L.; Katan, C. Analysis of Multivalley and Multibandgap Absorption and Enhancement of Free Carriers Related to Exciton Screening in Hybrid Perovskites. *J. Phys. Chem. C* **2014**, *118* (22), 11566–11572. https://doi.org/10.1021/jp503337a.

(93) Even, J.; Pedesseau, L.; Jancu, J.-M.; Katan, C. DFT and k · p Modelling of the Phase Transitions of Lead and Tin Halide Perovskites for Photovoltaic Cells. *Phys. Status Solidi RRL - Rapid Res. Lett.* **2014**, *8* (1), 31–35. https://doi.org/10.1002/pssr.201308183.

(94) Even, J.; Pedesseau, L.; Katan, C. Understanding Quantum Confinement of Charge Carriers in Layered 2D Hybrid Perovskites. *ChemPhysChem* **2014**, *15* (17), 3733–3741. https://doi.org/10.1002/cphc.201402428.

(95) Mao, L.; Wu, Y.; Stoumpos, C. C.; Wasielewski, M. R.; Kanatzidis, M. G. White-Light Emission and Structural Distortion in New Corrugated Two-Dimensional Lead Bromide Perovskites. *J. Am. Chem. Soc.* **2017**, *139* (14), 5210–5215. https://doi.org/10.1021/jacs.7b01312.

(96) Mao, L.; Tsai, H.; Nie, W.; Ma, L.; Im, J.; Stoumpos, C. C.; Malliakas, C. D.; Hao, F.; Wasielewski, M. R.; Mohite, A. D.; et al. Role of Organic Counterion in Lead- and Tin-Based Two-Dimensional Semiconducting Iodide Perovskites and Application in Planar Solar Cells. *Chem. Mater.* **2016**, *28* (21), 7781–7792. https://doi.org/10.1021/acs.chemmater.6b03054.

(97) Ma, C.; Leng, C.; Ji, Y.; Wei, X.; Sun, K.; Tang, L.; Yang, J.; Luo, W.; Li, C.; Deng, Y.; et al. 2D/3D Perovskite Hybrids as Moisture-Tolerant and Efficient Light Absorbers for Solar Cells. *Nanoscale* **2016**, *8* (43), 18309–18314. https://doi.org/10.1039/C6NR04741F.

(98) Koh, T. M.; Shanmugam, V.; Guo, X.; Lim, S. S.; Filonik, O.; Herzig, E. M.; Müller-Buschbaum, P.; Swamy, V.; Chien, S. T.; Mhaisalkar, S. G.; et al. Enhancing Moisture Tolerance in Efficient Hybrid 3D/2D Perovskite Photovoltaics. *J. Mater. Chem. A* **2018**, *6*, 2122–2128. https://doi.org/10.1039/C7TA09657G.

(99) Jung, M.-H. Photovoltaic Effect of 2D Homologous Perovskites. *Electrochimica Acta* **2017**, *240*, 98–107. https://doi.org/10.1016/j.electacta.2017.04.067.

(100) Wang, N.; Cheng, L.; Ge, R.; Zhang, S.; Miao, Y.; Zou, W.; Yi, C.; Sun, Y.; Cao, Y.; Yang, R.; et al. Perovskite Light-Emitting Diodes Based on Solution-Processed Self-Organized Multiple Quantum Wells. *Nat. Photonics* **2016**, *10* (11), 699–704. https://doi.org/10.1038/nphoton.2016.185.

(101) Liao, J.-F.; Rao, H.-S.; Chen, B.-X.; Kuang, D.-B.; Su, C.-Y. Dimension Engineering on Cesium Lead Iodide for Efficient and Stable Perovskite Solar Cells. *J. Mater. Chem. A* **2017**, *5* (5), 2066–2072. https://doi.org/10.1039/C6TA09582H.

(102) Cohen, B.-E.; Wierzbowska, M.; Etgar, L. High Efficiency Quasi 2D Lead Bromide Perovskite Solar Cells Using Various Barrier Molecules. *Sustain. Energy Fuels* **2017**, *1* (9), 1935–1943. https://doi.org/10.1039/C7SE00311K.

(103) Li, M.; Gao, Q.; Liu, P.; Liao, Q.; Zhang, H.; Yao, J.; Hu, W.; Wu, Y.; Fu, H. Amplified Spontaneous Emission Based on 2D Ruddlesden-Popper Perovskites. *Adv. Funct. Mater.* **2018**, 1707006. https://doi.org/10.1002/adfm.201707006.

(104) Hu, H.; Salim, T.; Chen, B.; Lam, Y. M. Molecularly Engineered Organic-Inorganic Hybrid Perovskite with Multiple Quantum Well Structure for Multicolored Light-Emitting Diodes. *Sci. Rep.* **2016**, *6* (1), 33546. https://doi.org/10.1038/srep33546.

(105) Chen, Z.; Zhang, C.; Jiang, X.-F.; Liu, M.; Xia, R.; Shi, T.; Chen, D.; Xue, Q.; Zhao, Y.-J.; Su, S.; et al. High-Performance Color-Tunable Perovskite Light Emitting Devices through Structural Modulation from Bulk to Layered Film. *Adv. Mater.* **2017**, *29* (8), 1603157. https://doi.org/10.1002/adma.201603157.

(106) Zou, W.; Li, R.; Zhang, S.; Liu, Y.; Wang, N.; Cao, Y.; Miao, Y.; Xu, M.; Guo, Q.; Di, D.; et al. Minimising Efficiency Roll-off in High-Brightness Perovskite Light-Emitting Diodes. *Nat. Commun.* **2018**, *9* (1), 608. https://doi.org/10.1038/s41467-018-03049-7.

(107) Yang, X.; Zhang, X.; Deng, J.; Chu, Z.; Jiang, Q.; Meng, J.; Wang, P.; Zhang, L.; Yin, Z.; You, J. Efficient Green Light-Emitting Diodes Based on Quasi-Two-Dimensional Composition and Phase Engineered Perovskite with Surface Passivation. *Nat. Commun.* **2018**, *9* (1), 570. https://doi.org/10.1038/s41467-018-02978-7.

(108) Yuan, M.; Quan, L. N.; Comin, R.; Walters, G.; Sabatini, R.; Voznyy, O.; Hoogland, S.; Zhao, Y.; Beauregard, E. M.; Kanjanaboos, P.; et al. Perovskite Energy Funnels for Efficient Light-Emitting Diodes. *Nat. Nanotechnol.* **2016**, *11*, 872–877. https://doi.org/10.1038/nnano.2016.110.

(109) Grancini, G.; Roldán-Carmona, C.; Zimmermann, I.; Mosconi, E.; Lee, X.; Martineau, D.; Narbey, S.; Oswald, F.; De Angelis, F.; Graetzel, M.; et al. One-Year Stable Perovskite Solar Cells by 2D/3D Interface Engineering. *Nat. Commun.* **2017**, *8*, 15684. https://doi.org/10.1038/ncomms15684.

(110) Liao, Y.; Liu, H.; Zhou, W.; Yang, D.; Shang, Y.; Shi, Z.; Li, B.; Jiang, X.; Zhang, L.; Quan, L. N.; et al. Highly Oriented Low-Dimensional Tin Halide Perovskites with Enhanced Stability and Photovoltaic Performance. *J. Am. Chem. Soc.* **2017**, *139* (19), 6693–6699. https://doi.org/10.1021/jacs.7b01815.

(111) Shao, S.; Liu, J.; Portale, G.; Fang, H.-H.; Blake, G. R.; ten Brink, G. H.; Koster, L. J. A.; Loi, M. A. Highly Reproducible Sn-Based Hybrid Perovskite Solar Cells with 9% Efficiency. *Adv. Energy Mater.* **2017**, 1702019. https://doi.org/10.1002/aenm.201702019.

(112) Wang, Z.; Lin, Q.; Chmiel, F. P.; Sakai, N.; Herz, L. M.; Snaith, H. J. Efficient Ambient-Air-Stable Solar Cells with 2D–3D Heterostructured Butylammonium-Caesium-Formamidinium Lead Halide Perovskites. *Nat. Energy* **2017**, *2* (9), 17135. https://doi.org/10.1038/nenergy.2017.135.

(113) Qing, J.; Liu, X.-K.; Li, M.; Liu, F.; Yuan, Z.; Tiukalova, E.; Yan, Z.; Duchamp, M.; Chen, S.; Wang, Y.; et al. Aligned and Graded Type-II Ruddlesden-Popper Perovskite Films for Efficient Solar Cells. *Adv. Energy Mater.* **2018**, 1800185. https://doi.org/10.1002/aenm.201800185.

(114) Ishi, J.; Kunugita, H.; Ema, K.; Ban, T.; Kondo, T. Time-to-Space Conversion of Tbits/s Optical Pulses Using a Self-Organized Quantum-Well Material. *Appl. Phys. Lett.* **2000**, *77* (22), 3487–3489. https://doi.org/10.1063/1.1328365.

(115) Zhang, S.; Lanty, G.; Lauret, J.-S.; Deleporte, E.; Audebert, P.; Galmiche, L. Synthesis and Optical Properties of Novel Organic–Inorganic Hybrid Nanolayer Structure

Semiconductors. *Acta Mater.* **2009**, *57* (11), 3301–3309. https://doi.org/10.1016/j.actamat.2009.03.037.

(116) Pradeesh, K.; Baumberg, J. J.; Prakash, G. V. Exciton Switching and Peierls Transitions in Hybrid Inorganic-Organic Self-Assembled Quantum Wells. *Appl. Phys. Lett.* **2009**, *95* (17), 173305. https://doi.org/10.1063/1.3257725.

(117) Billing, D. G.; Lemmerer, A. Synthesis, Characterization and Phase Transitions of the Inorganic–Organic Layered Perovskite-Type Hybrids [(CnH2n+1NH3)2PbI4] (n = 12, 14, 16 and 18). *New J. Chem.* **2008**, *32* (10), 1736. https://doi.org/10.1039/b805417g.

(118) Quan, L. N.; Yuan, M.; Comin, R.; Voznyy, O.; Beauregard, E. M.; Hoogland, S.; Buin, A.; Kirmani, A. R.; Zhao, K.; Amassian, A.; et al. Ligand-Stabilized Reduced-Dimensionality Perovskites. *J. Am. Chem. Soc.* **2016**, *138* (8), 2649–2655. https://doi.org/10.1021/jacs.5b11740.

(119) Koh, T. M.; Shanmugam, V.; Schlipf, J.; Oesinghaus, L.; Müller-Buschbaum, P.; Ramakrishnan, N.; Swamy, V.; Mathews, N.; Boix, P. P.; Mhaisalkar, S. G. Nanostructuring Mixed-Dimensional Perovskites: A Route Toward Tunable, Efficient Photovoltaics. *Adv. Mater.* **2016**, *28* (19), 3653–3661. https://doi.org/10.1002/adma.201506141.

(120) Ahmad, S.; Kanaujia, P. K.; Beeson, H. J.; Abate, A.; Deschler, F.; Credgington, D.; Steiner, U.; Prakash, G. V.; Baumberg, J. J. Strong Photocurrent from Two-Dimensional Excitons in Solution-Processed Stacked Perovskite Semiconductor Sheets. *ACS Appl. Mater. Interfaces* **2015**, *7* (45), 25227–25236. https://doi.org/10.1021/acsami.5b07026.

(121) Sanehira, Y.; Numata, Y.; Ikegami, M.; Miyasaka, T. Photovoltaic Properties of Two-Dimensional (CH$_3$(CH$_2$)$_3$NH$_3$)$_2$PbI$_4$ Perovskite Crystals Oriented with TiO$_2$ Nanowire Array. *Chem. Lett.* **2017**, *46* (8), 1204–1206. https://doi.org/10.1246/cl.170428.

(122) Wang, J.; Leng, J.; Liu, J.; He, S.; Wang, Y.; Wu, K.; Jin, S. Engineered Directional Charge Flow in Mixed Two-Dimensional Perovskites Enabled by Facile Cation-Exchange. *J. Phys. Chem. C* **2017**, *121* (39), 21281–21289. https://doi.org/10.1021/acs.jpcc.7b08535.

(123) Abdelwahab, I.; Grinblat, G.; Leng, K.; Li, Y.; Chi, X.; Rusydi, A.; Maier, S. A.; Loh, K. P. Highly Enhanced Third-Harmonic Generation in 2D Perovskites at Excitonic Resonances. *ACS Nano* **2017**, *12*, 644–650. https://doi.org/10.1021/acsnano.7b07698.

(124) Ma, L.; Dai, J.; Zeng, X. C. Two-Dimensional Single-Layer Organic-Inorganic Hybrid Perovskite Semiconductors. *Adv. Energy Mater.* **2017**, *7* (7), 1601731. https://doi.org/10.1002/aenm.201601731.

(125) Chung, H.; Sun, X.; Mohite, A. D.; Singh, R.; Kumar, L.; Alam, M. A.; Bermel, P. Modeling and Designing Multilayer 2D Perovskite / Silicon Bifacial Tandem Photovoltaics for High Efficiencies and Long-Term Stability. *Opt. Express* **2017**, *25* (8), A311. https://doi.org/10.1364/OE.25.00A311.

(126) Zhou, N.; Shen, Y.; Li, L.; Tan, S.; Liu, N.; Zheng, G.; Chen, Q.; Zhou, H. Exploration of Crystallization Kinetics in Quasi Two-Dimensional Perovskite and High Performance Solar Cells. *J. Am. Chem. Soc.* **2018**, *140* (1), 459–465. https://doi.org/10.1021/jacs.7b11157.

(127) Liu, G.; Kong, L.; Guo, P.; Stoumpos, C. C.; Hu, Q.; Liu, Z.; Cai, Z.; Gosztola, D. J.; Mao, H.; Kanatzidis, M. G.; et al. Two Regimes of Bandgap Red Shift and Partial

Ambient Retention in Pressure-Treated Two-Dimensional Perovskites. *ACS Energy Lett.* **2017**, *2* (11), 2518–2524. https://doi.org/10.1021/acsenergylett.7b00807.

(128) Peng, W.; Yin, J.; Ho, K.-T.; Ouellette, O.; De Bastiani, M.; Murali, B.; El Tall, O.; Shen, C.; Miao, X.; Pan, J.; et al. Ultralow Self-Doping in Two-Dimensional Hybrid Perovskite Single Crystals. *Nano Lett.* **2017**, *17* (8), 4759–4767. https://doi.org/10.1021/acs.nanolett.7b01475.

(129) Iagher, L.; Etgar, L. Effect of Cs on the Stability and Photovoltaic Performance of 2D/3D Perovskite-Based Solar Cells. *ACS Energy Lett.* **2018**, 366–372. https://doi.org/10.1021/acsenergylett.7b01196.

(130) Chen, Y.; Sun, Y.; Peng, J.; Zhang, W.; Su, X.; Zheng, K.; Pullerits, T.; Liang, Z. Tailoring Organic Cation of 2D Air-Stable Organometal Halide Perovskites for Highly Efficient Planar Solar Cells. *Adv. Energy Mater.* **2017**, *7* (18), 1700162. https://doi.org/10.1002/aenm.201700162.

(131) Liu, B.; Soe, C. M. M.; Stoumpos, C. C.; Nie, W.; Tsai, H.; Lim, K.; Mohite, A. D.; Kanatzidis, M. G.; Marks, T. J.; Singer, K. D. Optical Properties and Modeling of 2D Perovskite Solar Cells. *Sol. RRL* **2017**, *1* (8), 1700062. https://doi.org/10.1002/solr.201700062.

(132) Lédée, F.; Trippé-Allard, G.; Diab, H.; Audebert, P.; Garrot, D.; Lauret, J.-S.; Deleporte, E. Fast Growth of Monocrystalline Thin Films of 2D Layered Hybrid Perovskite. *CrystEngComm* **2017**, *19* (19), 2598–2602. https://doi.org/10.1039/C7CE00240H.

(133) Ma, D.; He, Y. Syntheses of Needle-Shaped Layered Perovskite (C 6 H 5 CH 2 NH 3) 2 PbI 4 Bundles via a Two-Step Processing Technique. *J. Alloys Compd.* **2017**, *696*, 1213–1219. https://doi.org/10.1016/j.jallcom.2016.12.090.

(134) Hamaguchi, R.; Yoshizawa-Fujita, M.; Miyasaka, T.; Kunugita, H.; Ema, K.; Takeoka, Y.; Rikukawa, M. Formamidine and Cesium-Based Quasi-Two-Dimensional Perovskites as Photovoltaic Absorbers. *Chem. Commun.* **2017**, *53* (31), 4366–4369. https://doi.org/10.1039/C7CC00921F.

(135) Bai, Y.; Xiao, S.; Hu, C.; Zhang, T.; Meng, X.; Lin, H.; Yang, Y.; Yang, S. Dimensional Engineering of a Graded 3D-2D Halide Perovskite Interface Enables Ultrahigh V_{Oc} Enhanced Stability in the p-i-n Photovoltaics. *Adv. Energy Mater.* **2017**, *7* (20), 1701038. https://doi.org/10.1002/aenm.201701038.

(136) Cheng, P.; Wu, T.; Zhang, J.; Li, Y.; Liu, J.; Jiang, L.; Mao, X.; Lu, R.-F.; Deng, W.-Q.; Han, K. (C 6 H 5 C 2 H 4 NH 3) 2 GeI 4 : A Layered Two-Dimensional Perovskite with Potential for Photovoltaic Applications. *J. Phys. Chem. Lett.* **2017**, *8* (18), 4402–4406. https://doi.org/10.1021/acs.jpclett.7b01985.

(137) Wang, J.; Li, J.; Tan, Q.; Li, L.; Zhang, J.; Zang, J.; Tan, P.; Zhang, J.; Li, D. Controllable Synthesis of Two-Dimensional Ruddlesden–Popper-Type Perovskite Heterostructures. *J. Phys. Chem. Lett.* **2017**, *8* (24), 6211–6219. https://doi.org/10.1021/acs.jpclett.7b02843.

(138) Ma, D.; Fu, Y.; Dang, L.; Zhai, J.; Guzei, I. A.; Jin, S. Single-Crystal Microplates of Two-Dimensional Organic–Inorganic Lead Halide Layered Perovskites for Optoelectronics. *Nano Res.* **2017**, *10* (6), 2117–2129. https://doi.org/10.1007/s12274-016-1401-6.

(139) Congreve, D. N.; Weidman, M. C.; Seitz, M.; Paritmongkol, W.; Dahod, N. S.; Tisdale, W. A. Tunable Light-Emitting Diodes Utilizing Quantum-Confined Layered Perovskite

Emitters. *ACS Photonics* **2017**, *4* (3), 476–481. https://doi.org/10.1021/acsphotonics.6b00963.

(140) Li, T.; Dunlap-Shohl, W. A.; Han, Q.; Mitzi, D. B. Melt Processing of Hybrid Organic–Inorganic Lead Iodide Layered Perovskites. *Chem. Mater.* **2017**, *29* (15), 6200–6204. https://doi.org/10.1021/acs.chemmater.7b02363.

(141) Tu, Q.; Spanopoulos, I.; Hao, S.; Wolverton, C.; Kanatzidis, M. G.; Shekhawat, G. S.; Dravid, V. P. Out-of-Plane Mechanical Properties of 2D Hybrid Organic–Inorganic Perovskites by Nanoindentation. *ACS Appl. Mater. Interfaces* **2018**, *10*, 22167–22173. https://doi.org/10.1021/acsami.8b05138.

(142) Ramirez, D.; Uribe, J. I.; Francaviglia, L.; Romero-Gomez, P.; Fontcuberta i Morral, A.; Jaramillo, F. Photophysics behind Highly Luminescent Two-Dimensional Hybrid Perovskite $(CH_3 (CH_2)_2 NH_3)_2 (CH_3 NH_3)_2 Pb_3 Br_{10}$ Thin Films. *J. Mater. Chem. C* **2018**, *6* (23), 6216–6221. https://doi.org/10.1039/C8TC01582A.

(143) Chen, J.; Wang, Y.; Gan, L.; He, Y.; Li, H.; Zhai, T. Generalized Self-Doping Engineering towards Ultrathin and Large-Sized Two-Dimensional Homologous Perovskites. *Angew. Chem.* **2017**, *129* (47), 15089–15093. https://doi.org/10.1002/ange.201708434.

(144) Shi, E.; Gao, Y.; Finkenauer, B. P.; Akriti, A.; Coffey, A. H.; Dou, L. Two-Dimensional Halide Perovskite Nanomaterials and Heterostructures. *Chem. Soc. Rev.* **2018**, *47*, 6046–6072. https://doi.org/10.1039/C7CS00886D.

(145) Zheng, K.; Chen, Y.; Sun, Y.; Chen, J.; Chábera, P.; Schaller, R.; Al-Marri, M. J.; Canton, S. E.; Liang, Z.; Pullerits, T. Inter-Phase Charge and Energy Transfer in Ruddlesden–Popper 2D Perovskites: Critical Role of the Spacing Cations. *J. Mater. Chem. A* **2018**, *6* (15), 6244–6250. https://doi.org/10.1039/C8TA01518J.

(146) Zhang, Y.; Sahoo, M. P. K.; Shimada, T.; Kitamura, T.; Wang, J. Strain-Induced Improper Ferroelectricity in Ruddlesden-Popper Perovskite Halides. *Phys. Rev. B* **2017**, *96* (14), 144110. https://doi.org/10.1103/PhysRevB.96.144110.

(147) Zhang, L.; Liang, W. How the Structures and Properties of Two-Dimensional Layered Perovskites $MAPbI_3$ and $CsPbI_3$ Vary with the Number of Layers. *J. Phys. Chem. Lett.* **2017**, *8* (7), 1517–1523. https://doi.org/10.1021/acs.jpclett.6b03005.

(148) Milot, R. L.; Sutton, R. J.; Eperon, G. E.; Haghighirad, A. A.; Martinez Hardigree, J.; Miranda, L.; Snaith, H. J.; Johnston, M. B.; Herz, L. M. Charge-Carrier Dynamics in 2D Hybrid Metal–Halide Perovskites. *Nano Lett.* **2016**, *16* (11), 7001–7007. https://doi.org/10.1021/acs.nanolett.6b03114.

(149) Gélvez-Rueda, M. C.; Hutter, E. M.; Cao, D. H.; Renaud, N.; Stoumpos, C. C.; Hupp, J. T.; Savenije, T. J.; Kanatzidis, M. G.; Grozema, F. C. Interconversion between Free Charges and Bound Excitons in 2D Hybrid Lead Halide Perovskites. *J. Phys. Chem. C* **2017**, *121* (47), 26566–26574. https://doi.org/10.1021/acs.jpcc.7b10705.

(150) Shang, Q.; Wang, Y.; Zhong, Y.; Mi, Y.; Qin, L.; Zhao, Y.; Qiu, X.; Liu, X.; Zhang, Q. Unveiling Structurally Engineered Carrier Dynamics in Hybrid Quasi-Two-Dimensional Perovskite Thin Films toward Controllable Emission. *J. Phys. Chem. Lett.* **2017**, *8* (18), 4431–4438. https://doi.org/10.1021/acs.jpclett.7b01857.

(151) Liu, J.; Leng, J.; Wu, K.; Zhang, J.; Jin, S. Observation of Internal Photoinduced Electron and Hole Separation in Hybrid Two-Dimentional Perovskite Films. *J. Am. Chem. Soc.* **2017**, *139* (4), 1432–1435. https://doi.org/10.1021/jacs.6b12581.

(152) Kawano, N.; Koshimizu, M.; Sun, Y.; Yahaba, N.; Fujimoto, Y.; Yanagida, T.; Asai, K. Effects of Organic Moieties on Luminescence Properties of Organic–Inorganic Layered Perovskite-Type Compounds. *J. Phys. Chem. C* **2014**, *118* (17), 9101–9106. https://doi.org/10.1021/jp4114305.

(153) Yangui, A.; Pillet, S.; Mlayah, A.; Lusson, A.; Bouchez, G.; Triki, S.; Abid, Y.; Boukheddaden, K. Structural Phase Transition Causing Anomalous Photoluminescence Behavior in Perovskite (C6H11NH3)2[PbI4]. *J. Chem. Phys.* **2015**, *143* (22), 224201. https://doi.org/10.1063/1.4936776.

(154) Yangui, A.; Sy, M.; Li, L.; Abid, Y.; Naumov, P.; Boukheddaden, K. Rapid and Robust Spatiotemporal Dynamics of the First-Order Phase Transition in Crystals of the Organic-Inorganic Perovskite (C12H25NH3)2PbI4. *Sci. Rep.* **2015**, *5*, 16634. https://doi.org/10.1038/srep16634.

(155) Dammak, T.; Boughzala, H.; Mlayah, A.; Abid, Y. Elaboration, Structural, Vibrational and Optical Investigation of a Two-Dimensional Self-Assembled Organic-Inorganic Hybrid Compound. *J. Lumin.* **2016**, *173*, 213–217. https://doi.org/10.1016/j.jlumin.2015.10.057.

(156) Abid, H.; Samet, A.; Dammak, T.; Mlayah, A.; Hlil, E. K.; Abid, Y. Electronic Structure Calculations and Optical Properties of a New Organic–Inorganic Luminescent Perovskite: (C9H19NH3)2PbI2Br2. *J. Lumin.* **2011**, *131* (8), 1753–1757. https://doi.org/10.1016/j.jlumin.2011.03.034.

(157) Era, M.; Yasuda, T.; Mori, K.; Tomotsu, N.; Kawano, N.; Koshimizu, M.; Asai, K. PbBr-Based Layered Perovskite Organic–Inorganic Superlattice Having Carbazole Chromophore; Hole-Mobility and Quantum Mechanical Calculation. *J. Nanosci. Nanotechnol.* **2016**, *16* (4), 3159–3167. https://doi.org/10.1166/jnn.2016.12320.

(158) Yao, K.; wang, X.; Xu, Y.; Li, F.; Zhou, L. Multilayered Perovskite Materials Based on Polymeric-Ammonium Cations for Stable Large-Area Solar Cell. *Chem. Mater.* **2016**. https://doi.org/10.1021/acs.chemmater.6b00711.

(159) Gan, L.; Li, J.; Fang, Z.; He, H.; Ye, Z. Effects of Organic Cation Length on Exciton Recombination in Two-Dimensional Layered Lead Iodide Hybrid Perovskite Crystals. *J. Phys. Chem. Lett.* **2017**, *8* (20), 5177–5183. https://doi.org/10.1021/acs.jpclett.7b02083.

(160) Dwivedi, V. K.; Vijaya Prakash, G. Fabrication and Room-Temperature Exciton Photoluminescence Stability Studies of Inorganic–Organic Hybrid (C12H25NH3)2SnI4 Thin Films. *Solid State Sci.* **2014**, *27*, 60–64. https://doi.org/10.1016/j.solidstatesciences.2013.11.009.

(161) Abdel-Baki, K.; Boitier, F.; Diab, H.; Lanty, G.; Jemli, K.; Lédée, F.; Garrot, D.; Deleporte, E.; Lauret, J. S. Exciton Dynamics and Non-Linearities in Two-Dimensional Hybrid Organic Perovskites. *J. Appl. Phys.* **2016**, *119* (6), 064301. https://doi.org/10.1063/1.4941345.

(162) Guo, Z.; Wu, X.; Zhu, T.; Zhu, X.; Huang, L. Electron–Phonon Scattering in Atomically Thin 2D Perovskites. *ACS Nano* **2016**, *10* (11), 9992–9998. https://doi.org/10.1021/acsnano.6b04265.

(163) Huang, C.; Gao, Y.; Wang, S.; Zhang, C.; Yi, N.; Xiao, S.; Song, Q. Giant Blueshifts of Excitonic Resonances in Two-Dimensional Lead Halide Perovskite. *Nano Energy* **2017**, *41*, 320–326. https://doi.org/10.1016/j.nanoen.2017.09.048.

(164) Cortecchia, D.; Lew, K. C.; So, J.-K.; Bruno, A.; Soci, C. Cathodoluminescence of Self-Organized Heterogeneous Phases in Multidimensional Perovskite Thin Films. *Chem. Mater.* **2017**, *29* (23), 10088–10094. https://doi.org/10.1021/acs.chemmater.7b03851.

(165) Yu, D.; Yin, C.; Cao, F.; Zhu, Y.; Ji, J.; Cai, B.; Liu, X.; Wang, X.; Zeng, H. Enhancing Optoelectronic Properties of Low-Dimensional Halide Perovskite via Ultrasonic-Assisted Template Refinement. *ACS Appl. Mater. Interfaces* **2017**, *9* (45), 39602–39609. https://doi.org/10.1021/acsami.7b12048.

(166) Protesescu, L.; Yakunin, S.; Bodnarchuk, M. I.; Krieg, F.; Caputo, R.; Hendon, C. H.; Yang, R. X.; Walsh, A.; Kovalenko, M. V. Nanocrystals of Cesium Lead Halide Perovskites (CsPbX$_3$, X = Cl, Br, and I): Novel Optoelectronic Materials Showing Bright Emission with Wide Color Gamut. *Nano Lett.* **2015**, *15* (6), 3692–3696. https://doi.org/10.1021/nl5048779.

(167) Kovalenko, M. V.; Protesescu, L.; Bodnarchuk, M. I. Properties and Potential Optoelectronic Applications of Lead Halide Perovskite Nanocrystals. *Science* **2017**, *358* (6364), 745–750. https://doi.org/10.1126/science.aam7093.

(168) Akkerman, Q. A.; Rainò, G.; Kovalenko, M. V.; Manna, L. Genesis, Challenges and Opportunities for Colloidal Lead Halide Perovskite Nanocrystals. *Nat. Mater.* **2018**, *17* (5), 394–405. https://doi.org/10.1038/s41563-018-0018-4.

(169) Mitzi, D. B. Templating and Structural Engineering in Organic–Inorganic Perovskites. *J. Chem. Soc. Dalton Trans.* **2001**, No. 1, 1–12. https://doi.org/10.1039/b007070j.

(170) Giustino, F.; Snaith, H. J. Toward Lead-Free Perovskite Solar Cells. *ACS Energy Lett.* **2016**, *1* (6), 1233–1240. https://doi.org/10.1021/acsenergylett.6b00499.

(171) Xiao, Z.; Meng, W.; Wang, J.; Mitzi, D. B.; Yan, Y. Searching for Promising New Perovskite-Based Photovoltaic Absorbers: The Importance of Electronic Dimensionality. *Mater. Horiz.* **2017**, *4* (2), 206–216. https://doi.org/10.1039/C6MH00519E.

(172) Tulsky, E. G.; Long, J. R. Dimensional Reduction: A Practical Formalism for Manipulating Solid Structures. *Chem. Mater.* **2001**, *13* (4), 1149–1166. https://doi.org/10.1021/cm0007858.

(173) Mitzi, D. . A Layered Solution Crystal Growth Technique and the Crystal Structure of (C6H5C2H4NH3)2PbCl4. *J. Solid State Chem.* **1999**, *145* (2), 694–704. https://doi.org/10.1006/jssc.1999.8281.

(174) Szafrański, M.; Katrusiak, A. Phase Transitions in the Layered Structure of Diguanidinium Tetraiodoplumbate. *Phys. Rev. B* **2000**, *61* (2), 1026–1035. https://doi.org/10.1103/PhysRevB.61.1026.

(175) Stoumpos, C. C.; Mao, L.; Malliakas, C. D.; Kanatzidis, M. G. Structure–Band Gap Relationships in Hexagonal Polytypes and Low-Dimensional Structures of Hybrid Tin Iodide Perovskites. *Inorg. Chem.* **2017**, *56* (1), 56–73. https://doi.org/10.1021/acs.inorgchem.6b02764.

(176) Mitzi, D. B.; Liang, K.; Wang, S. Synthesis and Characterization of [NH$_2$C(I)NH$_2$]$_2$ASnI$_5$ with A = Iodoformamidinium or Formamidinium: The Chemistry of Cyanamide and Tin(II) Iodide in Concentrated Aqueous Hydriodic Acid Solutions. *Inorg. Chem.* **1998**, *37* (2), 321–327. https://doi.org/10.1021/ic971332g.

(177) Ishihara, H.; Watanabe, K.; Iwata, A.; Yamada, K.; Kinoshita, Y.; Okuda, T.; Krishnan, V. G.; Dou, S.; Weiss, A. NQR and X-Ray Studies of [N(CH3)4]3M2X9 and (CH3NH3)3M2X9 (M = Sb,Bi; X = Cl,Br). *Z. Für Naturforschung A* **1992**, *47* (1–2), 65–74. https://doi.org/10.1515/zna-1992-1-213.

(178) Zhang, H.; Fang, L.; Yuan, R.-Z. Triammonium Nonaiododiantimonate(III), (NH$_4$)$_3$ [Sb$_2$I$_9$]. *Acta Crystallogr. Sect. E Struct. Rep. Online* **2005**, *61* (5), i70–i72. https://doi.org/10.1107/S1600536805011098.

(179) Suzuki, Y.; Kubo, H. Distribution of Cl⁻ and Br⁻ Ions in Mixed Crystals (CH$_3$NH$_3$)$_2$ Cu(Cl$_{1-x}$Br$_x$)$_4$. *J. Phys. Soc. Jpn.* **1983**, *52* (4), 1420–1426. https://doi.org/10.1143/JPSJ.52.1420.

(180) Staulo, G.; Bellitto, C. (C6H5CH2NH3)2CrBr3.3I0.7: A New Insulating Ferromagnet with a Curie Temperature of 51 K. *J. Mater. Chem.* **1991**, *1* (6), 915–918. https://doi.org/10.1039/jm9910100915.

(181) Kitazawa, N. Optical Absorption and Photoluminescence Properties of Pb(I, Br)-Based Two-Dimensional Layered Perovskite. *Jpn. J. Appl. Phys.* **1997**, *36* (Part 1, No. 4A), 2272–2276. https://doi.org/10.1143/JJAP.36.2272.

(182) Kitazawa, N. Excitons in Two-Dimensional Layered Perovskite Compounds: (C6H5C2H4NH3)2Pb(Br,I)4 and (C6H5C2H4NH3)2Pb(Cl,Br)4. *Mater. Sci. Eng. B* **1997**, *49* (3), 233–238. https://doi.org/10.1016/S0921-5107(97)00132-3.

(183) Daub, M.; Hillebrecht, H. Synthesis, Single-Crystal Structure and Characterization of (CH$_3$NH$_3$)$_2$Pb(SCN)$_2$I$_2$. *Angew. Chem. Int. Ed.* **2015**, *54* (38), 11016–11017. https://doi.org/10.1002/anie.201506449.

(184) Jiang, Q.; Rebollar, D.; Gong, J.; Piacentino, E. L.; Zheng, C.; Xu, T. Pseudohalide-Induced Moisture Tolerance in Perovskite CH$_3$NH$_3$Pb(SCN)$_2$I Thin Films. *Angew. Chem. Int. Ed.* **2015**, *54* (26), 7617–7620. https://doi.org/10.1002/anie.201503038.

(185) Umeyama, D.; Lin, Y.; Karunadasa, H. I. Red-to-Black Piezochromism in a Compressible Pb–I–SCN Layered Perovskite. *Chem. Mater.* **2016**, *28*, 3241–3244. https://doi.org/10.1021/acs.chemmater.6b01147.

(186) Xiao, Z.; Meng, W.; Saparov, B.; Duan, H.-S.; Wang, C.; Feng, C.; Liao, W.; Ke, W.; Zhao, D.; Wang, J.; et al. Photovoltaic Properties of Two-Dimensional (CH$_3$NH$_3$)$_2$ Pb(SCN)$_2$I$_2$ Perovskite: A Combined Experimental and Density Functional Theory Study. *J. Phys. Chem. Lett.* **2016**, *7* (7), 1213–1218. https://doi.org/10.1021/acs.jpclett.6b00248.

(187) Guan, J.; Tang, Z.; Guloy, A. M. α-[NH3(CH2)5NH3]SnI4: A New Layered Perovskite Structure. *Chem. Commun.* **1999**, No. 18, 1833–1834. https://doi.org/10.1039/a905323i.

(188) Nazarenko, O.; Kotyrba, M. R.; Yakunin, S.; Aebli, M.; Rainò, G.; Benin, B. M.; Wörle, M.; Kovalenko, M. V. Guanidinium-Formamidinium Lead Iodide: A Layered Perovskite-Related Compound with Red Luminescence at Room Temperature. *J. Am. Chem. Soc.* **2018**, *140* (11), 3850–3853. https://doi.org/10.1021/jacs.8b00194.

(189) Leblanc, A.; Mercier, N.; Allain, M.; Dittmer, J.; Fernandez, V.; Pauporté, T. Lead- and Iodide-Deficient (CH$_3$NH$_3$)PbI$_3$ (*d*-MAPI): The Bridge between 2D and 3D Hybrid Perovskites. *Angew. Chem. Int. Ed.* **2017**, *56* (50), 16067–16072. https://doi.org/10.1002/anie.201710021.

(190) Mercier, N.; Barres, A.-L.; Giffard, M.; Rau, I.; Kajzar, F.; Sahraoui, B. Conglomerate-to-True-Racemate Reversible Solid-State Transition in Crystals of an Organic Disulfide-Based Iodoplumbate. *Angew. Chem. Int. Ed.* **2006**, *45* (13), 2100–2103. https://doi.org/10.1002/anie.200503423.

(191) Corradi, A. B.; Ferrari, A. M.; Pellacani, G. C.; Saccani, A.; Sandrolini, F.; Sgarabotto, P. Structural and Electrical Characterization of Polymeric Haloplumbate(II) Systems. *Inorg. Chem.* **1999**, *38* (4), 716–721. https://doi.org/10.1021/ic980893k.

(192) Louvain, N.; Bi, W.; Mercier, N.; Buzar?, J.-Y.; Legein, C.; Corbel, G. PbnI4n+2(2n+2)? Ribbons (n = 3, 5) as Dimensional Reductions of 2D Perovskite Layers in Cystamine Cation Based Hybrids, Also Incorporating Iodine Molecules or Reversible Guest Water Molecules. *Dalton Trans.* **2007**, No. 9, 965–970. https://doi.org/10.1039/b617225c.

(193) Kamminga, M. E.; Fang, H.-H.; Filip, M. R.; Giustino, F.; Baas, J.; Blake, G. R.; Loi, M. A.; Palstra, T. T. M. Confinement Effects in Low-Dimensional Lead Iodide Perovskite Hybrids. *Chem. Mater.* **2016**, *28*, 4554–4562. https://doi.org/10.1021/acs.chemmater.6b00809.

(194) Zhu, X.-H.; Mercier, N.; Frère, P.; Blanchard, P.; Roncali, J.; Allain, M.; Pasquier, C.; Riou, A. Effect of Mono- versus Di-Ammonium Cation of 2,2'-Bithiophene Derivatives on the Structure of Organic−Inorganic Hybrid Materials Based on Iodo Metallates. *Inorg. Chem.* **2003**, *42* (17), 5330–5339. https://doi.org/10.1021/ic034235y.

(195) Smith, M. D.; Watson, B. L.; Dauskardt, R. H.; Karunadasa, H. I. Broadband Emission with a Massive Stokes Shift from Sulfonium Pb–Br Hybrids. *Chem. Mater.* **2017**, *29* (17), 7083–7087. https://doi.org/10.1021/acs.chemmater.7b02594.

(196) Que, C.-J.; Mo, C.-J.; Li, Z.-Q.; Zhang, G.-L.; Zhu, Q.-Y.; Dai, J. Perovskite-Like Organic–Inorganic Hybrid Lead Iodide with a Large Organic Cation Incorporated within the Layers. *Inorg. Chem.* **2017**, *56* (5), 2467–2472. https://doi.org/10.1021/acs.inorgchem.6b02550.

(197) Xu, Z.; Mitzi, D. B. [CH$_3$(CH$_2$)$_{11}$NH$_3$]SnI$_3$: A Hybrid Semiconductor with MoO$_3$-Type Tin(II) Iodide Layers. *Inorg. Chem.* **2003**, *42* (21), 6589–6591. https://doi.org/10.1021/ic0347081.

(198) Krautscheid, H.; Vielsack, F. [Pb18I44]8−–An Iodoplumbate with an Unusual Structure. *Angew. Chem. Int. Ed. Engl.* **1995**, *34* (18), 2035–2037. https://doi.org/10.1002/anie.199520351.

(199) Stoumpos, C. C.; Malliakas, C. D.; Kanatzidis, M. G. Semiconducting Tin and Lead Iodide Perovskites with Organic Cations: Phase Transitions, High Mobilities, and Near-Infrared Photoluminescent Properties. *Inorg. Chem.* **2013**, *52* (15), 9019–9038. https://doi.org/10.1021/ic401215x.

(200) Zhu, X.-H.; Mercier, N.; Riou, A.; Blanchard, P.; Frère, P. (C$_4$H$_3$SCH$_2$NH$_3$)$_2$(CH$_3$NH$_3$)Pb$_2$I$_7$: Non-Centrosymmetrical Crystal Structure of a Bilayer Hybrid Perovskite. *Chem Commun* **2002**, No. 18, 2160–2161. https://doi.org/10.1039/B205543K.

(201) Barman, S.; Venkataraman, N. V.; Vasudevan, S.; Seshadri, R. Phase Transitions in the Anchored Organic Bilayers of Long-Chain Alkylammonium Lead Iodides (C$_n$H$_{2n+1}$NH$_3$)$_2$PbI$_4$; n = 12, 16, 18. *J. Phys. Chem. B* **2003**, *107* (8), 1875–1883. https://doi.org/10.1021/jp026879h.

(202) Dohner, E. R.; Jaffe, A.; Bradshaw, L. R.; Karunadasa, H. I. Intrinsic White-Light Emission from Layered Hybrid Perovskites. *J. Am. Chem. Soc.* **2014**, *136* (38), 13154–13157. https://doi.org/10.1021/ja507086b.

(203) Knutson, J. L.; Martin, J. D.; Mitzi, D. B. Tuning the Band Gap in Hybrid Tin Iodide Perovskite Semiconductors Using Structural Templating. *Inorg. Chem.* **2005**, *44* (13), 4699–4705. https://doi.org/10.1021/ic050244q.

(204) Mao, L.; Ke, W.; Pedesseau, L.; Wu, Y.; Katan, C.; Even, J.; Wasielewski, M. R.; Stoumpos, C. C.; Kanatzidis, M. G. Hybrid Dion–Jacobson 2D Lead Iodide Perovskites. *J. Am. Chem. Soc.* **2018**, *140* (10), 3775–3783. https://doi.org/10.1021/jacs.8b00542.

(205) Sourisseau, S.; Louvain, N.; Bi, W.; Mercier, N.; Rondeau, D.; Boucher, F.; Buzaré, J.-Y.; Legein, C. Reduced Band Gap Hybrid Perovskites Resulting from Combined Hydrogen and Halogen Bonding at the Organic−Inorganic Interface. *Chem. Mater.* **2007**, *19* (3), 600–607. https://doi.org/10.1021/cm062380e.

(206) Traore, B.; Pedesseau, L.; Assam, L.; Che, X.; Blancon, J.-C.; Tsai, H.; Nie, W.; Stoumpos, C. C.; Kanatzidis, M. G.; Tretiak, S.; et al. Composite Nature of Layered Hybrid Perovskites: Assessment on Quantum and Dielectric Confinements and Band Alignment. *ACS Nano* **2018**, *12* (4), 3321–3332. https://doi.org/10.1021/acsnano.7b08202.

(207) Tang, Z.; Guan, J.; Guloy, A. M. Synthesis and Crystal Structure of New Organic-Based Layered Perovskites with 2,2′-Biimidazolium Cations. *J. Mater. Chem.* **2001**, *11* (2), 479–482. https://doi.org/10.1039/b007639m.

(208) Li, Y.; Zheng, G.; Lin, C.; Lin, J. New Organic–Inorganic Perovskite Materials with Different Optical Properties Modulated by Different Inorganic Sheets. *Cryst. Growth Des.* **2008**, *8* (6), 1990–1996. https://doi.org/10.1021/cg800047p.

(209) Hautzinger, M. P.; Dai, J.; Ji, Y.; Fu, Y.; Chen, J.; Guzei, I. A.; Wright, J. C.; Li, Y.; Jin, S. Two-Dimensional Lead Halide Perovskites Templated by a Conjugated Asymmetric Diammonium. *Inorg. Chem.* **2017**, *56* (24), 14991–14998. https://doi.org/10.1021/acs.inorgchem.7b02285.

(210) Nazarenko, O.; Kotyrba, M. R.; Wörle, M.; Cuervo-Reyes, E.; Yakunin, S.; Kovalenko, M. V. Luminescent and Photoconductive Layered Lead Halide Perovskite Compounds Comprising Mixtures of Cesium and Guanidinium Cations. *Inorg. Chem.* **2017**, *56* (19), 11552–11564. https://doi.org/10.1021/acs.inorgchem.7b01204.

(211) Rodríguez-Romero, J.; Hames, B. C.; Mora-Seró, I.; Barea, E. M. Conjugated Organic Cations to Improve the Optoelectronic Properties of 2D/3D Perovskites. *ACS Energy Lett.* **2017**, *2* (9), 1969–1970. https://doi.org/10.1021/acsenergylett.7b00654.

(212) Xu, Z.; Mitzi, D. B.; Dimitrakopoulos, C. D.; Maxcy, K. R. Semiconducting Perovskites $(2\text{-}XC_6H_4C_2H_4NH_3)_2SnI_4$ (X = F, Cl, Br): Steric Interaction between the Organic and Inorganic Layers. *Inorg. Chem.* **2003**, *42* (6), 2031–2039. https://doi.org/10.1021/ic0261474.

(213) Du, K.; Tu, Q.; Zhang, X.; Han, Q.; Liu, J.; Zauscher, S.; Mitzi, D. B. Two-Dimensional Lead(II) Halide-Based Hybrid Perovskites Templated by Acene Alkylamines: Crystal Structures, Optical Properties, and Piezoelectricity. *Inorg. Chem.* **2017**, *56* (15), 9291–9302. https://doi.org/10.1021/acs.inorgchem.7b01094.

(214) Mitzi, D. B.; Chondroudis, K.; Kagan, C. R. Design, Structure, and Optical Properties of Organic−Inorganic Perovskites Containing an Oligothiophene Chromophore. *Inorg. Chem.* **1999**, *38* (26), 6246–6256. https://doi.org/10.1021/ic991048k.

(215) Mitzi, D. B.; Medeiros, D. R.; Malenfant, P. R. L. Intercalated Organic−Inorganic Perovskites Stabilized by Fluoroaryl−Aryl Interactions. *Inorg. Chem.* **2002**, *41* (8), 2134–2145. https://doi.org/10.1021/ic011190x.

(216) Lemmerer, A.; Billing, D. G. Effect of Heteroatoms in the Inorganic–Organic Layered Perovskite-Type Hybrids $[(ZC_nH_{2n}NH_3)_2PbI_4]$, n = 2, 3, 4, 5, 6; Z = OH, Br and I; and $[(H_3NC_2H_4S_2C_2H_4NH_3)PbI_4]$. *CrystEngComm* **2010**, *12* (4), 1290–1301. https://doi.org/10.1039/B917824D.

(217) Wang, Q.; Jiang, C.; Zhang, P.; Hamann, T. W. Overcoming Bulk Recombination Limits of Layered Perovskite Solar Cells with Mesoporous Substrates. *J. Phys. Chem. C* **2018**, *122*, 14177–14185. https://doi.org/10.1021/acs.jpcc.8b01592.

(218) Li, Y.; Zheng, G.; Lin, J. Synthesis, Structure, and Optical Properties of a Contorted - Oriented Layered Hybrid Perovskite: C3H11SN3PbBr4. *Eur. J. Inorg. Chem.* **2008**, *2008* (10), 1689–1692. https://doi.org/10.1002/ejic.200700927.

(219) Li, Y. Y.; Lin, C. K.; Zheng, G. L.; Cheng, Z. Y.; You, H.; Wang, W. D.; Lin, J. Novel 〈 110 〉 -Oriented Organic−Inorganic Perovskite Compound Stabilized by *N* -(3-Aminopropyl)Imidazole with Improved Optical Properties. *Chem. Mater.* **2006**, *18* (15), 3463–3469. https://doi.org/10.1021/cm060714u.

(220) Lai, H.; Kan, B.; Liu, T.; Zheng, N.; Xie, Z.; Zhou, T.; Wan, X.; Zhang, X.; Liu, Y.; Chen, Y. Two-Dimensional Ruddlesden–Popper Perovskite with Nanorod-like Morphology for Solar Cells with Efficiency Exceeding 15%. *J. Am. Chem. Soc.* **2018**, *140* (37), 11639–11646. https://doi.org/10.1021/jacs.8b04604.

(221) Zhang, X.; Wu, G.; Fu, W.; Qin, M.; Yang, W.; Yan, J.; Zhang, Z.; Lu, X.; Chen, H. Orientation Regulation of Phenylethylammonium Cation Based 2D Perovskite Solar Cell with Efficiency Higher Than 11%. *Adv. Energy Mater.* **2018**, *8* (14), 1702498. https://doi.org/10.1002/aenm.201702498.

(222) Zhang, X.; Ren, X.; Liu, B.; Munir, R.; Zhu, X.; Yang, D.; Li, J.; Liu, Y.; Smilgies, D.-M.; Li, R.; et al. Stable High Efficiency Two-Dimensional Perovskite Solar Cells via Cesium Doping. *Energy Environ. Sci.* **2017**, *10* (10), 2095–2102. https://doi.org/10.1039/C7EE01145H.

(223) Fu, W.; Wang, J.; Zuo, L.; Gao, K.; Liu, F.; Ginger, D. S.; Jen, A. K.-Y. Two-Dimensional Perovskite Solar Cells with 14.1% Power Conversion Efficiency and 0.68% External Radiative Efficiency. *ACS Energy Lett.* **2018**, *3* (9), 2086–2093. https://doi.org/10.1021/acsenergylett.8b01181.

(224) Li, L.; Shang, X.; Wang, S.; Dong, N.; Ji, C.; Chen, X.; Zhao, S.; Wang, J.; Sun, Z.; Hong, M.; et al. Bilayered Hybrid Perovskite Ferroelectric with Giant Two-Photon Absorption. *J. Am. Chem. Soc.* **2018**, *140* (22), 6806–6809. https://doi.org/10.1021/jacs.8b04014.

(225) Mercier, N. (HO2C(CH2)3NH3)2(CH3NH3)Pb2I7: A Predicted Non-Centrosymmetrical Structure Built up from Carboxylic Acid Supramolecular Synthons and Bilayer Perovskite Sheets. *CrystEngComm* **2005**, *7* (70), 429–432. https://doi.org/10.1039/b504342e.

(226) Li, X.; Hoffman, J.; Ke, W.; Chen, M.; Tsai, H.; Nie, W.; Mohite, A. D.; Kepenekian, M.; Katan, C.; Even, J.; et al. Two-Dimensional Halide Perovskites Incorporating Straight Chain Symmetric Diammonium Ions, $(NH_3C_mH_{2m}NH_3)(CH_3NH_3)_{n-1}Pb_nI_{3n+1}$ (m = 4–9; n = 1–4). *J. Am. Chem. Soc.* **2018**, *140* (38), 12226–12238. https://doi.org/10.1021/jacs.8b07712.

(227) Li, L.; Sun, Z.; Wang, P.; Hu, W.; Wang, S.; Ji, C.; Hong, M.; Luo, J. Tailored Engineering of an Unusual $(C_4H_9NH_3)_2(CH_3NH_3)_2Pb_3Br_{10}$ Two-Dimensional Multilayered Perovskite Ferroelectric for a High-Performance Photodetector. *Angew. Chem. Int. Ed.* **2017**, *56* (40), 12150–12154. https://doi.org/10.1002/anie.201705836.

(228) Quarti, C.; Mosconi, E.; De Angelis, F. Interplay of Orientational Order and Electronic Structure in Methylammonium Lead Iodide: Implications for Solar Cell Operation. *Chem. Mater.* **2014**, *26* (22), 6557–6569. https://doi.org/10.1021/cm5032046.

(229) Leblanc, N.; Mercier, N.; Zorina, L.; Simonov, S.; Auban-Senzier, P.; Pasquier, C. Large Spontaneous Polarization and Clear Hysteresis Loop of a Room-Temperature Hybrid Ferroelectric Based on Mixed-Halide [BiI$_3$Cl$_2$] Polar Chains and Methylviologen Dication. *J. Am. Chem. Soc.* **2011**, *133* (38), 14924–14927. https://doi.org/10.1021/ja206171s.

(230) Sun, Z.; Liu, X.; Khan, T.; Ji, C.; Asghar, M. A.; Zhao, S.; Li, L.; Hong, M.; Luo, J. A Photoferroelectric Perovskite-Type Organometallic Halide with Exceptional Anisotropy of Bulk Photovoltaic Effects. *Angew. Chem. Int. Ed.* **2016**, *55* (22), 6545–6550. https://doi.org/10.1002/anie.201601933.

(231) Liao, W.-Q.; Zhang, Y.; Hu, C.-L.; Mao, J.-G.; Ye, H.-Y.; Li, P.-F.; Huang, S. D.; Xiong, R.-G. A Lead-Halide Perovskite Molecular Ferroelectric Semiconductor. *Nat. Commun.* **2015**, *6*, 7338. https://doi.org/10.1038/ncomms8338.

(232) Kohn, W.; Sham, L. J. Self-Consistent Equations Including Exchange and Correlation Effects. *Phys. Rev.* **1965**, *140* (4A), A1133–A1138. https://doi.org/10.1103/PhysRev.140.A1133.

(233) Grüning, M.; Marini, A.; Rubio, A. Density Functionals from Many-Body Perturbation Theory: The Band Gap for Semiconductors and Insulators. *J. Chem. Phys.* **2006**, *124* (15), 154108. https://doi.org/10.1063/1.2189226.

(234) Hedin, L. New Method for Calculating the One-Particle Green's Function with Application to the Electron-Gas Problem. *Phys. Rev.* **1965**, *139* (3A), A796–A823. https://doi.org/10.1103/PhysRev.139.A796.

(235) Macfarlane, G. G.; McLean, T. P.; Quarrington, J. E.; Roberts, V. Fine Structure in the Absorption-Edge Spectrum of Ge. *Phys. Rev.* **1957**, *108* (6), 1377–1383. https://doi.org/10.1103/PhysRev.108.1377.

(236) Whitcher, T. J.; Zhu, J.-X.; Chi, X.; Hu, H.; Zhao, D.; Asmara, T. C.; Yu, X.; Breese, M. B. H.; Castro Neto, A. H.; Lam, Y. M.; et al. Importance of Electronic Correlations and Unusual Excitonic Effects in Formamidinium Lead Halide Perovskites. *Phys. Rev. X* **2018**, *8* (2), 021034. https://doi.org/10.1103/PhysRevX.8.021034.

(237) Brivio, F.; Butler, K. T.; Walsh, A.; van Schilfgaarde, M. Relativistic Quasiparticle Self-Consistent Electronic Structure of Hybrid Halide Perovskite Photovoltaic Absorbers. *Phys. Rev. B* **2014**, *89* (15), 155204. https://doi.org/10.1103/PhysRevB.89.155204.

(238) Huang, L.; Lambrecht, W. R. L. Electronic Band Structure, Phonons, and Exciton Binding Energies of Halide Perovskites CsSnCl 3 , CsSnBr 3 , and CsSnI 3. *Phys. Rev. B* **2013**, *88* (16), 165203. https://doi.org/10.1103/PhysRevB.88.165203.

(239) Menéndez-Proupin, E.; Palacios, P.; Wahnón, P.; Conesa, J. C. Self-Consistent Relativistic Band Structure of the CH 3 NH 3 PbI 3 Perovskite. *Phys. Rev. B* **2014**, *90* (4), 045207. https://doi.org/10.1103/PhysRevB.90.045207.

(240) Leveillee, J.; Katan, C.; Zhou, L.; Mohite, A. D.; Even, J.; Tretiak, S.; Schleife, A.; Neukirch, A. J. Influence of π -Conjugated Cations and Halogen Substitution on the Optoelectronic and Excitonic Properties of Layered Hybrid Perovskites. *Phys. Rev. Mater.* **2018**, *2* (10), 105406. https://doi.org/10.1103/PhysRevMaterials.2.105406.

(241) Slater, J. C.; Koster, G. F. Simplified LCAO Method for the Periodic Potential Problem. *Phys. Rev.* **1954**, *94* (6), 1498–1524. https://doi.org/10.1103/PhysRev.94.1498.

(242) Hoffmann, R. An Extended Hückel Theory. I. Hydrocarbons. *J. Chem. Phys.* **1963**, *39* (6), 1397–1412. https://doi.org/10.1063/1.1734456.

(243) Hoffmann, R. Extended Hückel Theory. II. σ Orbitals in the Azines. *J. Chem. Phys.* **1964**, *40* (9), 2745–2745. https://doi.org/10.1063/1.1725601.

(244) Hoffmann, R. Extended Hückel Theory. III. Compounds of Boron and Nitrogen. *J. Chem. Phys.* **1964**, *40* (9), 2474–2480. https://doi.org/10.1063/1.1725550.

(245) Goringe, C. M.; Bowler, D. R.; Hernández, E. Tight-Binding Modelling of Materials. *Rep. Prog. Phys.* **1997**, *60* (12), 1447–1512. https://doi.org/10.1088/0034-4885/60/12/001.

(246) Perdew, J. P.; Zunger, A. Self-Interaction Correction to Density-Functional Approximations for Many-Electron Systems. *Phys. Rev. B* **1981**, *23* (10), 5048–5079. https://doi.org/10.1103/PhysRevB.23.5048.

(247) Ceperley, D. M.; Alder, B. J. Ground State of the Electron Gas by a Stochastic Method. *Phys. Rev. Lett.* **1980**, *45* (7), 566–569. https://doi.org/10.1103/PhysRevLett.45.566.

(248) Perdew, J. P.; Burke, K.; Ernzerhof, M. Generalized Gradient Approximation Made Simple. *Phys. Rev. Lett.* **1996**, *77* (18), 3865–3868. https://doi.org/10.1103/PhysRevLett.77.3865.

(249) Perdew, J. P.; Yang, W.; Burke, K.; Yang, Z.; Gross, E. K. U.; Scheffler, M.; Scuseria, G. E.; Henderson, T. M.; Zhang, I. Y.; Ruzsinszky, A.; et al. Understanding Band Gaps of Solids in Generalized Kohn–Sham Theory. *Proc. Natl. Acad. Sci.* **2017**, *114* (11), 2801–2806. https://doi.org/10.1073/pnas.1621352114.

(250) Seidl, A.; Görling, A.; Vogl, P.; Majewski, J. A.; Levy, M. Generalized Kohn-Sham Schemes and the Band-Gap Problem. *Phys. Rev. B* **1996**, *53* (7), 3764–3774. https://doi.org/10.1103/PhysRevB.53.3764.

(251) Yang, Z.; Peng, H.; Sun, J.; Perdew, J. P. More Realistic Band Gaps from Meta-Generalized Gradient Approximations: Only in a Generalized Kohn-Sham Scheme. *Phys. Rev. B* **2016**, *93* (20), 205205. https://doi.org/10.1103/PhysRevB.93.205205.

(252) Heyd, J.; Scuseria, G. E.; Ernzerhof, M. Hybrid Functionals Based on a Screened Coulomb Potential. *J. Chem. Phys.* **2003**, *118* (18), 8207–8215. https://doi.org/10.1063/1.1564060.

(253) Even, J.; Pedesseau, L.; Katan, C. Comment on "Density Functional Theory Analysis of Structural and Electronic Properties of Orthorhombic Perovskite CH$_3$NH$_3$PbI$_3$" by Y. Wang et Al., Phys. Chem. Chem. Phys., 2014, **16**, 1424–1429. *Phys Chem Chem Phys* **2014**, *16* (18), 8697–8698. https://doi.org/10.1039/C3CP55006K.

(254) Rohlfing, M.; Louie, S. G. Electron-Hole Excitations and Optical Spectra from First Principles. *Phys. Rev. B* **2000**, *62* (8), 4927–4944. https://doi.org/10.1103/PhysRevB.62.4927.

(255) Runge, E.; Gross, E. K. U. Density-Functional Theory for Time-Dependent Systems. *Phys. Rev. Lett.* **1984**, *52* (12), 997–1000. https://doi.org/10.1103/PhysRevLett.52.997.

(256) Casida, M. E. Time-Dependent Density Functional Response Theory for Molecules. In *Recent Advances in Computational Chemistry*; WORLD SCIENTIFIC, 1995; Vol. 1, pp 155–192. https://doi.org/10.1142/9789812830586_0005.

(257) Onida, G.; Reining, L.; Rubio, A. Electronic Excitations: Density-Functional versus Many-Body Green's-Function Approaches. *Rev. Mod. Phys.* **2002**, *74* (2), 601–659. https://doi.org/10.1103/RevModPhys.74.601.

(258) De Angelis, F. Modeling Materials and Processes in Hybrid/Organic Photovoltaics: From Dye-Sensitized to Perovskite Solar Cells. *Acc. Chem. Res.* **2014**, *47* (11), 3349–3360. https://doi.org/10.1021/ar500089n.

(259) Hakamata, T.; Shimamura, K.; Shimojo, F.; Kalia, R. K.; Nakano, A.; Vashishta, P. The Nature of Free-Carrier Transport in Organometal Halide Perovskites. *Sci. Rep.* **2016**, *6* (1), 19599. https://doi.org/10.1038/srep19599.

(260) Yin, J.; Maity, P.; De Bastiani, M.; Dursun, I.; Bakr, O. M.; Brédas, J.-L.; Mohammed, O. F. Molecular Behavior of Zero-Dimensional Perovskites. *Sci. Adv.* **2017**, *3* (12), e1701793. https://doi.org/10.1126/sciadv.1701793.

(261) Long, R.; Liu, J.; Prezhdo, O. V. Unravelling the Effects of Grain Boundary and Chemical Doping on Electron-Hole Recombination in CH3NH3PbI3 Perovskite by Time-Domain Atomistic Simulation. *J. Am. Chem. Soc.* **2016**, *138*, 3884–3890. https://doi.org/10.1021/jacs.6b00645.

(262) Quarti, C.; Marchal, N.; Beljonne, D. Tuning the Optoelectronic Properties of Two-Dimensional Hybrid Perovskite Semiconductors with Alkyl Chain Spacers. *J. Phys. Chem. Lett.* **2018**, *9* (12), 3416–3424. https://doi.org/10.1021/acs.jpclett.8b01309.

(263) Feng, H.-J.; Paudel, T. R.; Tsymbal, E. Y.; Zeng, X. C. Tunable Optical Properties and Charge Separation in $CH_3NH_3Sn_xPb_{1-x}I_3$/TiO_2-Based Planar Perovskites Cells. *J. Am. Chem. Soc.* **2015**, *137* (25), 8227–8236. https://doi.org/10.1021/jacs.5b04015.

(264) Nan, G.; Zhang, X.; Abdi-Jalebi, M.; Andaji-Garmaroudi, Z.; Stranks, S. D.; Lu, G.; Beljonne, D. How Methylammonium Cations and Chlorine Dopants Heal Defects in Lead Iodide Perovskites. *Adv. Energy Mater.* **2018**, *8* (13), 1702754. https://doi.org/10.1002/aenm.201702754.

(265) Umebayashi, T.; Asai, K.; Kondo, T.; Nakao, A. Electronic Structures of Lead Iodide Based Low-Dimensional Crystals. *Phys. Rev. B* **2003**, *67* (15), 155405. https://doi.org/10.1103/PhysRevB.67.155405.

(266) Silver, S.; Yin, J.; Li, H.; Brédas, J.-L.; Kahn, A. Characterization of the Valence and Conduction Band Levels of $n = 1$ 2D Perovskites: A Combined Experimental and Theoretical Investigation. *Adv. Energy Mater.* **2018**, 1703468. https://doi.org/10.1002/aenm.201703468.

(267) Zhou, L.; Neukirch, A. J.; Vogel, D. J.; Kilin, D. S.; Pedesseau, L.; Carignano, M. A.; Mohite, A. D.; Even, J.; Katan, C.; Tretiak, S. Density of States Broadening in $CH_3NH_3PbI_3$ Hybrid Perovskites Understood from Ab Initio Molecular Dynamics Simulations. *ACS Energy Lett.* **2018**, *3* (4), 787–793. https://doi.org/10.1021/acsenergylett.8b00166.

(268) Kang, J.; Wang, L.-W. Dynamic Disorder and Potential Fluctuation in Two-Dimensional Perovskite. *J. Phys. Chem. Lett.* **2017**, *8* (16), 3875–3880. https://doi.org/10.1021/acs.jpclett.7b01501.

(269) Ema, K.; Inomata, M.; Kato, Y.; Kunugita, H.; Era, M. Nearly Perfect Triplet-Triplet Energy Transfer from Wannier Excitons to Naphthalene in Organic-Inorganic Hybrid Quantum-Well Materials. *Phys. Rev. Lett.* **2008**, *100* (25), 257401. https://doi.org/10.1103/PhysRevLett.100.257401.

(270) Straus, D. B.; Kagan, C. R. Electrons, Excitons, and Phonons in Two-Dimensional Hybrid Perovskites: Connecting Structural, Optical, and Electronic Properties. *J. Phys. Chem. Lett.* **2018**, *9* (6), 1434–1447. https://doi.org/10.1021/acs.jpclett.8b00201.

(271) Chondroudis, K.; Mitzi, D. B. Electroluminescence from an Organic−Inorganic Perovskite Incorporating a Quaterthiophene Dye within Lead Halide Perovskite Layers. *Chem. Mater.* **1999**, *11* (11), 3028–3030. https://doi.org/10.1021/cm990561t.

(272) Liu, C.; Huhn, W.; Du, K.-Z.; Vazquez-Mayagoitia, A.; Dirkes, D.; You, W.; Kanai, Y.; Mitzi, D. B.; Blum, V. Tunable Semiconductors: Control over Carrier States and

Excitations in Layered Hybrid Organic-Inorganic Perovskites. *Phys. Rev. Lett.* **2018**, *121* (14), 146401. https://doi.org/10.1103/PhysRevLett.121.146401.

(273) Braun, M.; Tuffentsammer, W.; Wachtel, H.; Wolf, H. C. Pyrene as Emitting Chromophore in Organic–Inorganic Lead Halide-Based Layered Perovskites with Different Halides. *Chem. Phys. Lett.* **1999**, *307* (5–6), 373–378. https://doi.org/10.1016/S0009-2614(99)00526-6.

(274) Braun, M.; Tuffentsammer, W.; Wachtel, H.; Wolf, H. C. Tailoring of Energy Levels in Lead Chloride Based Layered Perovskites and Energy Transfer between the Organic and Inorganic Planes. *Chem. Phys. Lett.* **1999**, *303* (1–2), 157–164. https://doi.org/10.1016/S0009-2614(99)00205-5.

(275) Blancon, J.-C.; Stier, A. V.; Tsai, H.; Nie, W.; Stoumpos, C. C.; Traoré, B.; Pedesseau, L.; Kepenekian, M.; Katsutani, F.; Noe, G. T.; et al. Scaling Law for Excitons in 2D Perovskite Quantum Wells. *Nat. Commun.* **2018**, *9* (1), 2254. https://doi.org/10.1038/s41467-018-04659-x.

(276) Agranovich, V. M.; Basko, D. M.; Rocca, G. C. L.; Bassani, F. Excitons and Optical Nonlinearities in Hybrid Organic-Inorganic Nanostructures. *J. Phys. Condens. Matter* **1998**, *10* (42), 9369–9400. https://doi.org/10.1088/0953-8984/10/42/005.

(277) Agranovich, V. M.; Gartstein, Y. N.; Litinskaya, M. Hybrid Resonant Organic–Inorganic Nanostructures for Optoelectronic Applications. *Chem. Rev.* **2011**, *111* (9), 5179–5214. https://doi.org/10.1021/cr100156x.

(278) Heidrich, K.; Künzel, H.; Treusch, J. Optical Properties and Electronic Structure of CsPbCl3 and CsPbBr3. *Solid State Commun.* **1978**, *25* (11), 887–889. https://doi.org/10.1016/0038-1098(78)90294-6.

(279) Katan, C.; Pedesseau, L.; Kepenekian, M.; Rolland, A.; Even, J. Interplay of Spin–Orbit Coupling and Lattice Distortion in Metal Substituted 3D Tri-Chloride Hybrid Perovskites. *J. Mater. Chem. A* **2015**, *3* (17), 9232–9240. https://doi.org/10.1039/C4TA06418F.

(280) Heidrich, K.; Schäfer, W.; Schreiber, M.; Söchtig, J.; Trendel, G.; Treusch, J.; Grandke, T.; Stolz, H. J. Electronic Structure, Photoemission Spectra, and Vacuum-Ultraviolet Optical Spectra of CsPb Cl 3 and CsPb Br 3. *Phys. Rev. B* **1981**, *24* (10), 5642–5649. https://doi.org/10.1103/PhysRevB.24.5642.

(281) Boyer-Richard, S.; Katan, C.; Traoré, B.; Scholz, R.; Jancu, J.-M.; Even, J. Symmetry-Based Tight Binding Modeling of Halide Perovskite Semiconductors. *J. Phys. Chem. Lett.* **2016**, *7* (19), 3833–3840. https://doi.org/10.1021/acs.jpclett.6b01749.

(282) Mitzi, D. B. Synthesis, Crystal Structure, and Optical and Thermal Properties of (C $_4$ H $_9$ NH $_3$) $_2$ MI $_4$ (M = Ge, Sn, Pb). *Chem. Mater.* **1996**, *8* (3), 791–800. https://doi.org/10.1021/cm9505097.

(283) Amat, A.; Mosconi, E.; Ronca, E.; Quarti, C.; Umari, P.; Nazeeruddin, M. K.; Grätzel, M.; De Angelis, F. Cation-Induced Band-Gap Tuning in Organohalide Perovskites: Interplay of Spin–Orbit Coupling and Octahedra Tilting. *Nano Lett.* **2014**, *14* (6), 3608–3616. https://doi.org/10.1021/nl5012992.

(284) Tanaka, K.; Takahashi, T.; Ban, T.; Kondo, T.; Uchida, K.; Miura, N. Comparative Study on the Excitons in Lead-Halide-Based Perovskite-Type Crystals CH3NH3PbBr3 CH3NH3PbI3. *Solid State Commun.* **2003**, *127* (9–10), 619–623. https://doi.org/10.1016/S0038-1098(03)00566-0.

(285) Even, J. Pedestrian Guide to Symmetry Properties of the Reference Cubic Structure of 3D All-Inorganic and Hybrid Perovskites. *J. Phys. Chem. Lett.* **2015**, *6* (12), 2238–2242. https://doi.org/10.1021/acs.jpclett.5b00905.

(286) Bala, A.; Deb, A. K.; Kumar, V. Atomic and Electronic Structure of Two-Dimensional Inorganic Halide Perovskites A$_{n+1}$ M$_n$ X$_{3n+1}$ (n = 1–6, A = Cs, M = Pb and Sn, and X = Cl, Br, and I) from *Ab Initio* Calculations. *J. Phys. Chem. C* **2018**, *122* (13), 7464–7473. https://doi.org/10.1021/acs.jpcc.7b11322.

(287) Kawaguchi, Y.; Nitta, M.; Ueda, M. Knots in a Spinor Bose-Einstein Condensate. *Phys. Rev. Lett.* **2008**, *100* (18), 180403. https://doi.org/10.1103/PhysRevLett.100.180403.

(288) Liu, Y.-K.; Yang, S.-J. Three-Dimensional Dimeron as a Stable Topological Object. *Phys. Rev. A* **2015**, *91* (4), 043616. https://doi.org/10.1103/PhysRevA.91.043616.

(289) Song, S.-W.; Sun, R.; Zhao, H.; Wang, X.; Han, B.-Z. Weakly Interacting Spinor Bose–Einstein Condensates with Three-Dimensional Spin–Orbit Coupling. *Chin. Phys. B* **2016**, *25* (4), 040305. https://doi.org/10.1088/1674-1056/25/4/040305.

(290) Ueda, T.; Omo, M.; Shimizu, K.; Ohki, H.; Okuda, T. Ionic Motion of Phenethylammonium Ion in [C6H5CH2CH2NH3]2 PbX4 (X = Cl, Br, I) as Studied by 1 H NMR. *Z. Für Naturforschung A* **1997**, *52* (6–7), 502–508. https://doi.org/10.1515/zna-1997-6-706.

(291) Fraccarollo, A.; Marchese, L.; Cossi, M. Ab Initio Design of Low Band Gap 2D Tin Organohalide Perovskites. *J. Phys. Chem. C* **2018**, *122* (7), 3677–3689. https://doi.org/10.1021/acs.jpcc.7b08928.

(292) Huan, T. D.; Tuoc, V. N.; Minh, N. V. Layered Structures of Organic/Inorganic Hybrid Halide Perovskites. *Phys. Rev. B* **2016**, *93* (9), 094105. https://doi.org/10.1103/PhysRevB.93.094105.

(293) Fraccarollo, A.; Cantatore, V.; Boschetto, G.; Marchese, L.; Cossi, M. Ab Initio Modeling of 2D Layered Organohalide Lead Perovskites. *J. Chem. Phys.* **2016**, *144* (16), 164701. https://doi.org/10.1063/1.4947305.

(294) Azarhoosh, P.; McKechnie, S.; Frost, J. M.; Walsh, A.; van Schilfgaarde, M. Research Update: Relativistic Origin of Slow Electron-Hole Recombination in Hybrid Halide Perovskite Solar Cells. *APL Mater.* **2016**, *4* (9), 091501. https://doi.org/10.1063/1.4955028.

(295) Motta, C.; El-Mellouhi, F.; Kais, S.; Tabet, N.; Alharbi, F.; Sanvito, S. Revealing the Role of Organic Cations in Hybrid Halide Perovskite CH3NH3PbI3. *Nat. Commun.* **2015**, *6* (1). https://doi.org/10.1038/ncomms8026.

(296) Giorgi, G.; Yamashita, K. Organic–Inorganic Halide Perovskites: An Ambipolar Class of Materials with Enhanced Photovoltaic Performances. *J. Mater. Chem. A* **2015**, *3* (17), 8981–8991. https://doi.org/10.1039/C4TA05046K.

(297) Kepenekian, M.; Even, J. Rashba and Dresselhaus Couplings in Halide Perovskites: Accomplishments and Opportunities for Spintronics and Spin–Orbitronics. *J. Phys. Chem. Lett.* **2017**, *8* (14), 3362–3370. https://doi.org/10.1021/acs.jpclett.7b01015.

(298) Zhai, Y.; Baniya, S.; Zhang, C.; Li, J.; Haney, P.; Sheng, C.-X.; Ehrenfreund, E.; Vardeny, Z. V. Giant Rashba Splitting in 2D Organic-Inorganic Halide Perovskites Measured by Transient Spectroscopies. *Sci. Adv.* **2017**, *3* (7), e1700704. https://doi.org/10.1126/sciadv.1700704.

(299) Chen, X.; Lu, H.; Li, Z.; Zhai, Y.; Ndione, P. F.; Berry, J. J.; Zhu, K.; Yang, Y.; Beard, M. C. Impact of Layer Thickness on the Charge Carrier and Spin Coherence Lifetime in

Two-Dimensional Layered Perovskite Single Crystals. *ACS Energy Lett.* **2018**, *3* (9), 2273–2279. https://doi.org/10.1021/acsenergylett.8b01315.

(300) Filip, M. R.; Verdi, C.; Giustino, F. *GW* Band Structures and Carrier Effective Masses of CH $_3$ NH $_3$ PbI $_3$ and Hypothetical Perovskites of the Type APbI $_3$: A = NH $_4$, PH $_4$, AsH $_4$, and SbH $_4$. *J. Phys. Chem. C* **2015**, *119* (45), 25209–25219. https://doi.org/10.1021/acs.jpcc.5b07891.

(301) van Schilfgaarde, M.; Kotani, T.; Faleev, S. Quasiparticle Self-Consistent G W Theory. *Phys. Rev. Lett.* **2006**, *96* (22), 226402. https://doi.org/10.1103/PhysRevLett.96.226402.

(302) Miyata, A.; Mitioglu, A.; Plochocka, P.; Portugall, O.; Wang, J. T.-W.; Stranks, S. D.; Snaith, H. J.; Nicholas, R. J. Direct Measurement of the Exciton Binding Energy and Effective Masses for Charge Carriers in Organic–Inorganic Tri-Halide Perovskites. *Nat. Phys.* **2015**, *11* (7), 582–587. https://doi.org/10.1038/nphys3357.

(303) Cortecchia, D.; Neutzner, S.; Srimath Kandada, A. R.; Mosconi, E.; Meggiolaro, D.; De Angelis, F.; Soci, C.; Petrozza, A. Broadband Emission in Two-Dimensional Hybrid Perovskites: The Role of Structural Deformation. *J. Am. Chem. Soc.* **2017**, *139* (1), 39–42. https://doi.org/10.1021/jacs.6b10390.

(304) Yin, J.; Li, H.; Cortecchia, D.; Soci, C.; Brédas, J.-L. Excitonic and Polaronic Properties of 2D Hybrid Organic–Inorganic Perovskites. *ACS Energy Lett.* **2017**, *2* (2), 417–423. https://doi.org/10.1021/acsenergylett.6b00659.

(305) Fraccarollo, A.; Canti, L.; Marchese, L.; Cossi, M. First Principles Study of 2D Layered Organohalide Tin Perovskites. *J. Chem. Phys.* **2017**, *146* (23), 234703. https://doi.org/10.1063/1.4985054.

(306) Tan, C.; Cao, X.; Wu, X.-J.; He, Q.; Yang, J.; Zhang, X.; Chen, J.; Zhao, W.; Han, S.; Nam, G.-H.; et al. Recent Advances in Ultrathin Two-Dimensional Nanomaterials. *Chem. Rev.* **2017**, *117* (9), 6225–6331. https://doi.org/10.1021/acs.chemrev.6b00558.

(307) Even, J.; Pedesseau, L.; Kepenekian, M. Electronic Surface States and Dielectric Self-Energy Profiles in Colloidal Nanoscale Platelets of CdSe. *Phys Chem Chem Phys* **2014**, *16* (45), 25182–25190. https://doi.org/10.1039/C4CP03267E.

(308) Takagi, H.; Kunugita, H.; Ema, K. Influence of the Image Charge Effect on Excitonic Energy Structure in Organic-Inorganic Multiple Quantum Well Crystals. *Phys. Rev. B* **2013**, *87* (12), 125421. https://doi.org/10.1103/PhysRevB.87.125421.

(309) Yaffe, O.; Chernikov, A.; Norman, Z. M.; Zhong, Y.; Velauthapillai, A.; van der Zande, A.; Owen, J. S.; Heinz, T. F. Excitons in Ultrathin Organic-Inorganic Perovskite Crystals. *Phys. Rev. B* **2015**, *92* (4), 045414. https://doi.org/10.1103/PhysRevB.92.045414.

(310) Jackson, J. D. *Classical Electrodynamics*, 3. ed., [Nachdr.].; Wiley: Hoboken, NY, 2009.

(311) He, X.-F. Excitons in Anisotropic Solids: The Model of Fractional-Dimensional Space. *Phys. Rev. B* **1991**, *43* (3), 2063–2069. https://doi.org/10.1103/PhysRevB.43.2063.

(312) Mathieu, H.; Lefebvre, P.; Christol, P. Simple Analytical Method for Calculating Exciton Binding Energies in Semiconductor Quantum Wells. *Phys. Rev. B* **1992**, *46* (7), 4092–4101. https://doi.org/10.1103/PhysRevB.46.4092.

(313) Haug, H.; Koch, S. W. *Quantum Theory of the Optical and Electronic Properties of Semiconductors*, 4. ed., repr.; World Scientific: New Jersey, NJ, 2005.

(314) Adler, S. L. Quantum Theory of the Dielectric Constant in Real Solids. *Phys. Rev.* **1962**, *126* (2), 413–420. https://doi.org/10.1103/PhysRev.126.413.

(315) Hybertsen, M. S.; Louie, S. G. Electron Correlation in Semiconductors and Insulators: Band Gaps and Quasiparticle Energies. *Phys. Rev. B* **1986**, *34* (8), 5390–5413. https://doi.org/10.1103/PhysRevB.34.5390.

(316) Fuchs, F.; Rödl, C.; Schleife, A.; Bechstedt, F. Efficient O (N 2) Approach to Solve the Bethe-Salpeter Equation for Excitonic Bound States. *Phys. Rev. B* **2008**, *78* (8), 085103. https://doi.org/10.1103/PhysRevB.78.085103.

(317) Bokdam, M.; Sander, T.; Stroppa, A.; Picozzi, S.; Sarma, D. D.; Franchini, C.; Kresse, G. Role of Polar Phonons in the Photo Excited State of Metal Halide Perovskites. *Sci. Rep.* **2016**, *6* (1), 28618. https://doi.org/10.1038/srep28618.

(318) Giorgi, G.; Yamashita, K.; Palummo, M. Nature of the Electronic and Optical Excitations of Ruddlesden–Popper Hybrid Organic–Inorganic Perovskites: The Role of the Many-Body Interactions. *J. Phys. Chem. Lett.* **2018**, *9* (19), 5891–5896. https://doi.org/10.1021/acs.jpclett.8b02653.

(319) Chow, W. W.; Koch, S. W. *Semiconductor-Laser Fundamentals: Physics of the Gain Materials ; with 3 Tables*; Springer: Berlin, 1999.

(320) Schmitt-Rink, S.; Löwenau, J.; Haug, H. Theory of Absorption and Refraction of Direct-Gap Semiconductors with Arbitrary Free-Carrier Concentrations. *Z. Für Phys. B Condens. Matter* **1982**, *47* (1), 13–17. https://doi.org/10.1007/BF01686177.

(321) Chuang, S.-L.; Schmitt-Rink, S.; Miller, D. A. B.; Chemla, D. S. Exciton Green's-Function Approach to Optical Absorption in a Quantum Well with an Applied Electric Field. *Phys. Rev. B* **1991**, *43* (2), 1500–1509. https://doi.org/10.1103/PhysRevB.43.1500.

(322) Even, J.; Boyer-Richard, S.; Carignano, M.; Pedesseau, L.; Jancu, J.-M.; Katan, C. Theoretical Insights into Hybrid Perovskites for Photovoltaic Applications; Witzigmann, B., Osiński, M., Arakawa, Y., Eds.; 2016; Vol. Proc. SPIE 9742, p 97421A. https://doi.org/10.1117/12.2213135.

(323) Benchamekh, R.; Gippius, N. A.; Even, J.; Nestoklon, M. O.; Jancu, J.-M.; Ithurria, S.; Dubertret, B.; Efros, A. L.; Voisin, P. Tight-Binding Calculations of Image-Charge Effects in Colloidal Nanoscale Platelets of CdSe. *Phys. Rev. B* **2014**, *89* (3), 035307. https://doi.org/10.1103/PhysRevB.89.035307.

(324) Kumagai, M.; Takagahara, T. Excitonic and Nonlinear-Optical Properties of Dielectric Quantum-Well Structures. *Phys. Rev. B* **1989**, *40* (18), 12359–12381. https://doi.org/10.1103/PhysRevB.40.12359.

(325) Barrera, R. G.; Guzmán, O.; Balaguer, B. Point Charge in a Three-dielectric Medium with Planar Interfaces. *Am. J. Phys.* **1978**, *46* (11), 1172–1179. https://doi.org/10.1119/1.11501.

(326) Wang, G.; Chernikov, A.; Glazov, M. M.; Heinz, T. F.; Marie, X.; Amand, T.; Urbaszek, B. Excitons in Atomically Thin Transition Metal Dichalcogenides. *Rev. Mod. Phys.* **2018**, *90* (2), 021001. https://doi.org/10.1103/RevModPhys.90.021001.

(327) Keldysh, leonid. Coulomb Interaction in Thin Film Semiconductor and Semimetal Films. *JETP Lett.* **1979**, *29* (11), 716–719.

(328) Cudazzo, P.; Tokatly, I. V.; Rubio, A. Dielectric Screening in Two-Dimensional Insulators: Implications for Excitonic and Impurity States in Graphane. *Phys. Rev. B* **2011**, *84* (8), 085406. https://doi.org/10.1103/PhysRevB.84.085406.

(329) Berkelbach, T. C.; Hybertsen, M. S.; Reichman, D. R. Theory of Neutral and Charged Excitons in Monolayer Transition Metal Dichalcogenides. *Phys. Rev. B* **2013**, *88* (4). https://doi.org/10.1103/PhysRevB.88.045318.

(330) Latini, S.; Olsen, T.; Thygesen, K. S. Excitons in van Der Waals Heterostructures: The Important Role of Dielectric Screening. *Phys. Rev. B* **2015**, *92* (24), 245123. https://doi.org/10.1103/PhysRevB.92.245123.

(331) Rösner, M.; Şaşıoğlu, E.; Friedrich, C.; Blügel, S.; Wehling, T. O. Wannier Function Approach to Realistic Coulomb Interactions in Layered Materials and Heterostructures. *Phys. Rev. B* **2015**, *92* (8), 085102. https://doi.org/10.1103/PhysRevB.92.085102.

(332) Olsen, T.; Latini, S.; Rasmussen, F.; Thygesen, K. S. Simple Screened Hydrogen Model of Excitons in Two-Dimensional Materials. *Phys. Rev. Lett.* **2016**, *116* (5), 056401. https://doi.org/10.1103/PhysRevLett.116.056401.

(333) Tanaka, K.; Takahashi, T.; Kondo, T.; Umeda, K.; Ema, K.; Umebayashi, T.; Asai, K.; Uchida, K.; Miura, N. Electronic and Excitonic Structures of Inorganic–Organic Perovskite-Type Quantum-Well Crystal (C $_4$ H $_9$ NH $_3$) $_2$ PbBr $_4$. *Jpn. J. Appl. Phys.* **2005**, *44* (8), 5923–5932. https://doi.org/10.1143/JJAP.44.5923.

(334) Ema, K.; Umeda, K.; Toda, M.; Yajima, C.; Arai, Y.; Kunugita, H.; Wolverson, D.; Davies, J. J. Huge Exchange Energy and Fine Structure of Excitons in an Organic-Inorganic Quantum Well Material. *Phys. Rev. B* **2006**, *73* (24), 241310. https://doi.org/10.1103/PhysRevB.73.241310.

(335) Shimizu, M.; Fujisawa, J.-I.; Ishi-Hayase, J. Influence of Dielectric Confinement on Excitonic Nonlinearity in Inorganic-Organic Layered Semiconductors. *Phys. Rev. B* **2005**, *71* (20), 205306. https://doi.org/10.1103/PhysRevB.71.205306.

(336) Goto, T.; Makino, H.; Yao, T.; Chia, C. H.; Makino, T.; Segawa, Y.; Mousdis, G. A.; Papavassiliou, G. C. Localization of Triplet Excitons and Biexcitons in the Two-Dimensional Semiconductor (C H 3 C 6 H 4 C H 2 N H 3) 2 Pb Br 4. *Phys. Rev. B* **2006**, *73* (11), 115206. https://doi.org/10.1103/PhysRevB.73.115206.

(337) Shimizu, M.; Fujisawa, J.; Ishihara, T. Photoluminescence of the Inorganic-Organic Layered Semiconductor (C 6 H 5 C 2 H 4 N H 3) 2 Pb I 4 : Observation of Triexciton Formation. *Phys. Rev. B* **2006**, *74* (15), 155206. https://doi.org/10.1103/PhysRevB.74.155206.

(338) Pradeesh, K.; Baumberg, J. J.; Prakash, G. V. Strong Exciton-Photon Coupling in Inorganic-Organic Multiple Quantum Wells Embedded Low-Q Microcavity. *Opt. Express* **2009**, *17* (24), 22171. https://doi.org/10.1364/OE.17.022171.

(339) Wei, Y.; Lauret, J. S.; Galmiche, L.; Audebert, P.; Deleporte, E. Strong Exciton-Photon Coupling in Microcavities Containing New Fluorophenethylamine Based Perovskite Compounds. *Opt. Express* **2012**, *20* (9), 10399. https://doi.org/10.1364/OE.20.010399.

(340) Ahn, J.; Lee, E.; Tan, J.; Yang, W.; Kim, B.; Moon, J. A New Class of Chiral Semiconductors: Chiral-Organic-Molecule-Incorporating Organic–Inorganic Hybrid Perovskites. *Mater. Horiz.* **2017**, *4* (5), 851–856. https://doi.org/10.1039/C7MH00197E.

(341) Amerling, E.; Baniya, S.; Lafalce, E.; Zhang, C.; Vardeny, Z. V.; Whittaker-Brooks, L. Electroabsorption Spectroscopy Studies of (C $_4$ H $_9$ NH $_3$) $_2$ PbI $_4$ Organic–Inorganic Hybrid Perovskite Multiple Quantum Wells. *J. Phys. Chem. Lett.* **2017**, *8* (18), 4557–4564. https://doi.org/10.1021/acs.jpclett.7b01741.

(342) Giovanni, D.; Chong, W. K.; Dewi, H. A.; Thirumal, K.; Neogi, I.; Ramesh, R.; Mhaisalkar, S.; Mathews, N.; Sum, T. C. Tunable Room-Temperature Spin-Selective Optical Stark Effect in Solution-Processed Layered Halide Perovskites. *Sci. Adv.* **2016**, *2* (6), e1600477–e1600477. https://doi.org/10.1126/sciadv.1600477.

(343) Kitazawa, N.; Ito, T.; Sakasegawa, D.; Watanabe, Y. Excitons in Self-Organized Layered Perovskite Films Prepared by the Two-Step Growth Process. *Thin Solid Films* **2006**, *500* (1–2), 133–137. https://doi.org/10.1016/j.tsf.2005.11.053.

(344) Kitazawa, N.; Aono, M.; Watanabe, Y. Excitons in Organic–Inorganic Hybrid Compounds (CnH2n+1NH3)2PbBr4 (N=4, 5, 7 and 12). *Thin Solid Films* **2010**, *518* (12), 3199–3203. https://doi.org/10.1016/j.tsf.2009.09.014.

(345) Kitazawa, N.; Watanabe, Y. Optical Properties of Natural Quantum-Well Compounds (C6H5-CnH2n-NH3)2PbBr4 (N=1–4). *J. Phys. Chem. Solids* **2010**, *71* (5), 797–802. https://doi.org/10.1016/j.jpcs.2010.02.006.

(346) Yamamoto, Y.; Oohata, G.; Mizoguchi, K.; Ichida, H.; Kanematsu, Y. Photoluminescence of Excitons and Biexcitons in (C$_4$H$_9$NH$_3$)$_2$PbBr$_4$ Crystals under High Excitation Density: Photoluminescence of Excitons and Biexcitons in (C$_4$H$_9$NH$_3$)$_2$PbBr$_4$ Crystals under High Excitation Density. *Phys. Status Solidi C* **2012**, *9* (12), 2501–2504. https://doi.org/10.1002/pssc.201200314.

(347) Kitazawa, N.; Aono, M.; Watanabe, Y. Temperature-Dependent Time-Resolved Photoluminescence of (C6H5C2H4NH3)2PbX4 (X=Br and I). *Mater. Chem. Phys.* **2012**, *134* (2–3), 875–880. https://doi.org/10.1016/j.matchemphys.2012.03.083.

(348) Gauthron, K.; Lauret, J.-S.; Doyennette, L.; Lanty, G.; Al Choueiry, A.; Zhang, S. J.; Brehier, A.; Largeau, L.; Mauguin, O.; Bloch, J.; et al. Optical Spectroscopy of Two-Dimensional Layered (C_6H_5C_2H_4-NH_3)_2-PbI_4 Perovskite. *Opt. Express* **2010**, *18* (6), 5912. https://doi.org/10.1364/OE.18.005912.

(349) Kitazawa, N.; Aono, M.; Watanabe, Y. Synthesis and Luminescence Properties of Lead-Halide Based Organic–Inorganic Layered Perovskite Compounds (CnH2n+1NH3)2PbI4 (N=4, 5, 7, 8 and 9). *J. Phys. Chem. Solids* **2011**, *72* (12), 1467–1471. https://doi.org/10.1016/j.jpcs.2011.08.029.

(350) Fu, M.; Tamarat, P.; Huang, H.; Even, J.; Rogach, A. L.; Lounis, B. Neutral and Charged Exciton Fine Structure in Single Lead Halide Perovskite Nanocrystals Revealed by Magneto-Optical Spectroscopy. *Nano Lett.* **2017**, *17* (5), 2895–2901. https://doi.org/10.1021/acs.nanolett.7b00064.

(351) Ueda, T.; Shimizu, K.; Ohki, H.; Okuda, T. 13CP/MAS NMR Study of Motion and Local Structure of Phenethyl- Ammonium Ion in [C6H5CH2CH2 NH3]2PbX4(X = Cl, Br, I). *Z. Für Naturforschung A* **1998**, *53* (12), 983–988. https://doi.org/10.1515/zna-1998-1209.

(352) Hu, T.; Smith, M. D.; Dohner, E. R.; Sher, M.-J.; Wu, X.; Trinh, M. T.; Fisher, A.; Corbett, J.; Zhu, X.-Y.; Karunadasa, H. I.; et al. Mechanism for Broadband White-Light Emission from Two-Dimensional (110) Hybrid Perovskites. *J. Phys. Chem. Lett.* **2016**, 2258–2263. https://doi.org/10.1021/acs.jpclett.6b00793.

(353) Elkins, M. H.; Pensack, R.; Proppe, A. H.; Voznyy, O.; Quan, L. N.; Kelley, S. O.; Sargent, E. H.; Scholes, G. D. Biexciton Resonances Reveal Exciton Localization in Stacked Perovskite Quantum Wells. *J. Phys. Chem. Lett.* **2017**, *8* (16), 3895–3901. https://doi.org/10.1021/acs.jpclett.7b01621.

(354) Thirumal, K.; Chong, W. K.; Xie, W.; Ganguly, R.; Muduli, S. K.; Sherburne, M.; Asta, M.; Mhaisalkar, S.; Sum, T. C.; Soo, H. S.; et al. Morphology-Independent Stable White-Light Emission from Self-Assembled Two-Dimensional Perovskites Driven by Strong Exciton–Phonon Coupling to the Organic Framework. *Chem. Mater.* **2017**, *29* (9), 3947–3953. https://doi.org/10.1021/acs.chemmater.7b00073.

(355) Wu, Z.; Ji, C.; Sun, Z.; Wang, S.; Zhao, S.; Zhang, W.; Li, L.; Luo, J. Broadband White-Light Emission with a High Color Rendering Index in a Two-Dimensional Organic–Inorganic Hybrid Perovskite. *J. Mater. Chem. C* **2018**, *6*, 1171–1175. https://doi.org/10.1039/C7TC04868H.

(356) Sanehira, E. M.; Marshall, A. R.; Christians, J. A.; Harvey, S. P.; Ciesielski, P. N.; Wheeler, L. M.; Schulz, P.; Lin, L. Y.; Beard, M. C.; Luther, J. M. Enhanced Mobility CsPbI $_3$ Quantum Dot Arrays for Record-Efficiency, High-Voltage Photovoltaic Cells. *Sci. Adv.* **2017**, *3* (10), eaao4204. https://doi.org/10.1126/sciadv.aao4204.

(357) Vybornyi, O.; Yakunin, S.; Kovalenko, M. V. Polar-Solvent-Free Colloidal Synthesis of Highly Luminescent Alkylammonium Lead Halide Perovskite Nanocrystals. *Nanoscale* **2016**, *8*, 6278–6283. https://doi.org/10.1039/C5NR06890H.

(358) Bekenstein, Y.; Koscher, B. A.; Eaton, S. W.; Yang, P.; Alivisatos, A. P. Highly Luminescent Colloidal Nanoplates of Perovskite Cesium Lead Halide and Their Oriented Assemblies. *J. Am. Chem. Soc.* **2015**, *137*, 16008–16011. https://doi.org/10.1021/jacs.5b11199.

(359) Park, Y.-S.; Guo, S.; Makarov, N. S.; Klimov, V. I. Room Temperature Single-Photon Emission from Individual Perovskite Quantum Dots. *ACS Nano* **2015**, *9* (10), 10386–10393. https://doi.org/10.1021/acsnano.5b04584.

(360) Yakunin, S.; Protesescu, L.; Krieg, F.; Bodnarchuk, M. I.; Nedelcu, G.; Humer, M.; De Luca, G.; Fiebig, M.; Heiss, W.; Kovalenko, M. V. Low-Threshold Amplified Spontaneous Emission and Lasing from Colloidal Nanocrystals of Caesium Lead Halide Perovskites. *Nat. Commun.* **2015**, *6*, 8056. https://doi.org/10.1038/ncomms9056.

(361) Hu, F.; Zhang, H.; Sun, C.; Yin, C.; Lv, B.; Zhang, C.; Yu, W. W.; Wang, X.; Zhang, Y.; Xiao, M. Superior Optical Properties of Perovskite Nanocrystals as Single Photon Emitters. *ACS Nano* **2015**, *9* (12), 12410–12416. https://doi.org/10.1021/acsnano.5b05769.

(362) Swarnkar, A.; Chulliyil, R.; Ravi, V. K.; Irfanullah, M.; Chowdhury, A.; Nag, A. Colloidal CsPbBr $_3$ Perovskite Nanocrystals: Luminescence beyond Traditional Quantum Dots. *Angew. Chem.* **2015**, *127* (51), 15644–15648. https://doi.org/10.1002/ange.201508276.

(363) Bhaumik, S.; Veldhuis, S.; Ng, Y. F.; Li, M.; Muduli, S. K.; Sum, T. C.; Damodaran, B.; Mhaisalkar, S. G.; Mathews, N. Highly Stable, Luminescent Core-Shell Type Methylammonium-Octylammonium Lead Bromide Layered Perovskite Nanoparticles. *Chem Commun* **2016**, *52*, 7118–7121. https://doi.org/10.1039/C6CC01056C.

(364) Cottingham, P.; Brutchey, R. L. On the Crystal Structure of Colloidally Prepared CsPbBr $_3$ Quantum Dots. *Chem. Commun.* **2016**, *52* (30), 5246–5249. https://doi.org/10.1039/C6CC01088A.

(365) Lin, J.; Gomez, L.; de Weerd, C.; Fujiwara, Y.; Gregorkiewicz, T.; Suenaga, K. Direct Observation of Band Structure Modifications in Nanocrystals of CsPbBr $_3$ Perovskite. *Nano Lett.* **2016**, *16* (11), 7198–7202. https://doi.org/10.1021/acs.nanolett.6b03552.

(366) Rainò, G.; Nedelcu, G.; Protesescu, L.; Bodnarchuk, M. I.; Kovalenko, M. V.; Mahrt, R. F.; Stöferle, T. Single Cesium Lead Halide Perovskite Nanocrystals at Low Temperature: Fast Single-Photon Emission, Reduced Blinking, and Exciton Fine Structure. *ACS Nano* **2016**, *10* (2), 2485–2490. https://doi.org/10.1021/acsnano.5b07328.

(367) Wei, M.; Sun, W.; Liu, Y.; Liu, Z.; Xiao, L.; Bian, Z.; Chen, Z. Highly Luminescent and Stable Layered Perovskite as the Emitter for Light Emitting Diodes: Highly Luminescent
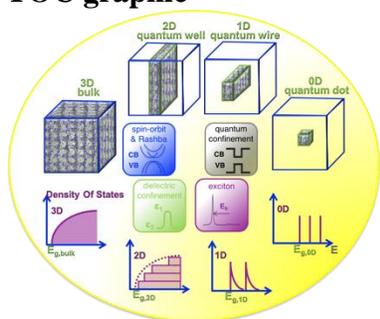
and Stable Layered Perovskite. *Phys. Status Solidi A* **2016**, *213* (10), 2727–2732. https://doi.org/10.1002/pssa.201600246.

(368) Zhang, Q.; Su, R.; Liu, X.; Xing, J.; Sum, T. C.; Xiong, Q. High-Quality Whispering-Gallery-Mode Lasing from Cesium Lead Halide Perovskite Nanoplatelets. *Adv. Funct. Mater.* **2016**, *26*, 6238–6245. https://doi.org/10.1002/adfm.201601690.

(369) Zhang, X.; Lin, H.; Huang, H.; Reckmeier, C.; Zhang, Y.; Choy, W. C. H.; Rogach, A. L. Enhancing the Brightness of Cesium Lead Halide Perovskite Nanocrystal Based Green Light-Emitting Devices through the Interface Engineering with Perfluorinated Ionomer. *Nano Lett.* **2016**, *16*, 1415–1420. https://doi.org/10.1021/acs.nanolett.5b04959.

(370) Chen, W.; Bhaumik, S.; Veldhuis, S. A.; Xing, G.; Xu, Q.; Grätzel, M.; Mhaisalkar, S.; Mathews, N.; Sum, T. C. Giant Five-Photon Absorption from Multidimensional Core-Shell Halide Perovskite Colloidal Nanocrystals. *Nat. Commun.* **2017**, *8*, 15198. https://doi.org/10.1038/ncomms15198.

(371) Chen, J.; Žídek, K.; Chábera, P.; Liu, D.; Cheng, P.; Nuuttila, L.; Al-Marri, M. J.; Lehtivuori, H.; Messing, M. E.; Han, K.; et al. Size- and Wavelength-Dependent Two-Photon Absorption Cross-Section of CsPbBr$_3$ Perovskite Quantum Dots. *J. Phys. Chem. Lett.* **2017**, *8* (10), 2316–2321. https://doi.org/10.1021/acs.jpclett.7b00613.

(372) Isarov, M.; Tan, L. Z.; Bodnarchuk, M. I.; Kovalenko, M. V.; Rappe, A. M.; Lifshitz, E. Rashba Effect in a Single Colloidal CsPbBr$_3$ Perovskite Nanocrystal Detected by Magneto-Optical Measurements. *Nano Lett.* **2017**, *17* (8), 5020–5026. https://doi.org/10.1021/acs.nanolett.7b02248.

(373) Protesescu, L.; Yakunin, S.; Kumar, S.; Bär, J.; Bertolotti, F.; Masciocchi, N.; Guagliardi, A.; Grotevent, M.; Shorubalko, I.; Bodnarchuk, M. I.; et al. Dismantling the "Red Wall" of Colloidal Perovskites: Highly Luminescent Formamidinium and Formamidinium–Cesium Lead Iodide Nanocrystals. *ACS Nano* **2017**, *11* (3), 3119–3134. https://doi.org/10.1021/acsnano.7b00116.

(374) Bertolotti, F.; Protesescu, L.; Kovalenko, M. V.; Yakunin, S.; Cervellino, A.; Billinge, S. J. L.; Terban, M. W.; Pedersen, J. S.; Masciocchi, N.; Guagliardi, A. Coherent Nanotwins and Dynamic Disorder in Cesium Lead Halide Perovskite Nanocrystals. *ACS Nano* **2017**, *11* (4), 3819–3831. https://doi.org/10.1021/acsnano.7b00017.

(375) Lee, J.-W.; Choi, Y. J.; Yang, J.-M.; Ham, S.; Jeon, S. K.; Lee, J. Y.; Song, Y.-H.; Ji, E. K.; Yoon, D.-H.; Seo, S.; et al. *In-Situ* Formed Type I Nanocrystalline Perovskite Film for Highly Efficient Light-Emitting Diode. *ACS Nano* **2017**, *11* (3), 3311–3319. https://doi.org/10.1021/acsnano.7b00608.

(376) Vogel, D. J.; Kryjevski, A.; Inerbaev, T.; Kilin, D. S. Photoinduced Single- and Multiple-Electron Dynamics Processes Enhanced by Quantum Confinement in Lead Halide Perovskite Quantum Dots. *J. Phys. Chem. Lett.* **2017**, *8* (13), 3032–3039. https://doi.org/10.1021/acs.jpclett.6b03048.

(377) Yin, C.; Chen, L.; Song, N.; Lv, Y.; Hu, F.; Sun, C.; Yu, W. W.; Zhang, C.; Wang, X.; Zhang, Y.; et al. Bright-Exciton Fine-Structure Splittings in Single Perovskite Nanocrystals. *Phys. Rev. Lett.* **2017**, *119* (2), 026401. https://doi.org/10.1103/PhysRevLett.119.026401.

(378) Li, J.; Gan, L.; Fang, Z.; He, H.; Ye, Z. Bright Tail States in Blue-Emitting Ultrasmall Perovskite Quantum Dots. *J. Phys. Chem. Lett.* **2017**, *8* (24), 6002–6008. https://doi.org/10.1021/acs.jpclett.7b02786.

(379) Becker, M. A.; Vaxenburg, R.; Nedelcu, G.; Sercel, P. C.; Shabaev, A.; Mehl, M. J.; Michopoulos, J. G.; Lambrakos, S. G.; Bernstein, N.; Lyons, J. L.; et al. Bright Triplet Excitons in Caesium Lead Halide Perovskites. *Nature* **2018**, *553* (7687), 189–193. https://doi.org/10.1038/nature25147.

(380) Cho, J.; Choi, Y.-H.; O'Loughlin, T. E.; De Jesus, L.; Banerjee, S. Ligand-Mediated Modulation of Layer Thicknesses of Perovskite Methylammonium Lead Bromide Nanoplatelets. *Chem. Mater.* **2016**, *28* (19), 6909–6916. https://doi.org/10.1021/acs.chemmater.6b02241.

(381) Yuan, Z.; Shu, Y.; Xin, Y.; Ma, B. Highly Luminescent Nanoscale Quasi-2D Layered Lead Bromide Perovskites with Tunable Emissions. *Chem. Commun.* **2016**, *52* (20), 3887–3890. https://doi.org/10.1039/C5CC09762B.

(382) Akkerman, Q. A.; Motti, S. G.; Srimath Kandada, A. R.; Mosconi, E.; D'Innocenzo, V.; Bertoni, G.; Marras, S.; Kamino, B. A.; Miranda, L.; De Angelis, F.; et al. Colloidal Cesium Lead Halide Perovskite Nanoplatelets with Monolayer-Level Thickness Control by a Solution Synthesis Approach. *J. Am. Chem. Soc.* **2016**, *138*, 1010–1016. https://doi.org/10.1021/jacs.5b12124.

(383) Kumar, S.; Jagielski, J.; Kallikounis, N.; Kim, Y.-H.; Wolf, C.; Jenny, F.; Tian, T.; Hofer, C. J.; Chiu, Y.-C.; Stark, W. J.; et al. Ultrapure Green Light-Emitting Diodes Using Two-Dimensional Formamidinium Perovskites: Achieving Recommendation 2020 Color Coordinates. *Nano Lett.* **2017**, *17* (9), 5277–5284. https://doi.org/10.1021/acs.nanolett.7b01544.

(384) Kumar, S.; Jagielski, J.; Yakunin, S.; Rice, P.; Chiu, Y.-C.; Wang, M.; Nedelcu, G.; Kim, Y.; Lin, S.; Santos, E. J. G.; et al. Efficient Blue Electroluminescence Using Quantum-Confined Two-Dimensional Perovskites. *ACS Nano* **2016**, *10* (10), 9720–9729. https://doi.org/10.1021/acsnano.6b05775.

(385) Li, J.; Luo, L.; Huang, H.; Ma, C.; Ye, Z.; Zeng, J.; He, H. 2D Behaviors of Excitons in Cesium Lead Halide Perovskite Nanoplatelets. *J. Phys. Chem. Lett.* **2017**, *8* (6), 1161–1168. https://doi.org/10.1021/acs.jpclett.7b00017.

(386) Wong, A. B.; Bekenstein, Y.; Kang, J.; Kley, C. S.; Kim, D.; Gibson, N. A.; Zhang, D.; Yu, Y.; Leone, S. R.; Wang, L.-W.; et al. Strongly Quantum Confined Colloidal Cesium Tin Iodide Perovskite Nanoplates: Lessons for Reducing Defect Density and Improving Stability. *Nano Lett.* **2018**, *18* (3), 2060–2066. https://doi.org/10.1021/acs.nanolett.8b00077.

(387) Yang, Z.; Wang, M.; Qiu, H.; Yao, X.; Lao, X.; Xu, S.; Lin, Z.; Sun, L.; Shao, J. Engineering the Exciton Dissociation in Quantum-Confined 2D CsPbBr$_3$ Nanosheet Films. *Adv. Funct. Mater.* **2018**, *28* (14), 1705908. https://doi.org/10.1002/adfm.201705908.

(388) Yu, D.; Cao, F.; Gao, Y.; Xiong, Y.; Zeng, H. Room-Temperature Ion-Exchange-Mediated Self-Assembly toward Formamidinium Perovskite Nanoplates with Finely Tunable, Ultrapure Green Emissions for Achieving Rec. 2020 Displays. *Adv. Funct. Mater.* **2018**, *28* (19), 1800248. https://doi.org/10.1002/adfm.201800248.

(389) Zhu, H.; Fu, Y.; Meng, F.; Wu, X.; Gong, Z.; Ding, Q.; Gustafsson, M. V.; Trinh, M. T.; Jin, S.; Zhu, X.-Y. Lead Halide Perovskite Nanowire Lasers with Low Lasing Thresholds and High Quality Factors. *Nat. Mater.* **2015**, *14* (6), 636–642. https://doi.org/10.1038/nmat4271.

(390) Liu, J.; Xue, Y.; Wang, Z.; Xu, Z.-Q.; Zheng, C.; Weber, B.; Song, J.; Wang, Y.; Lu, Y.; Zhang, Y.; et al. Two-Dimensional CH$_3$NH$_3$PbI$_3$ Perovskite: Synthesis and Optoelectronic Application. *ACS Nano* **2016**, *10*, 3536–3542. https://doi.org/10.1021/acsnano.5b07791.

(391) Zhang, D.; Eaton, S. W.; Yu, Y.; Dou, L.; Yang, P. Solution-Phase Synthesis of Cesium Lead Halide Perovskite Nanowires. *J. Am. Chem. Soc.* **2015**, *137* (29), 9230–9233. https://doi.org/10.1021/jacs.5b05404.

(392) Aharon, S.; Etgar, L. Two Dimensional Organometal Halide Perovskite Nanorods with Tunable Optical Properties. *Nano Lett.* **2016**, 3230–3235. https://doi.org/10.1021/acs.nanolett.6b00665.

(393) Ning, Z.; Gong, X.; Comin, R.; Walters, G.; Fan, F.; Voznyy, O.; Yassitepe, E.; Buin, A.; Hoogland, S.; Sargent, E. H. Quantum-Dot-in-Perovskite Solids. *Nature* **2015**, *523* (7560), 324–328. https://doi.org/10.1038/nature14563.

(394) Yang, Z.; Voznyy, O.; Walters, G.; Fan, J. Z.; Liu, M.; Kinge, S.; Hoogland, S.; Sargent, E. H. Quantum Dots in Two-Dimensional Perovskite Matrices for Efficient Near-Infrared Light Emission. *ACS Photonics* **2017**, *4* (4), 830–836. https://doi.org/10.1021/acsphotonics.6b00865.

(395) Stoumpos, C. C.; Malliakas, C. D.; Peters, J. A.; Liu, Z.; Sebastian, M.; Im, J.; Chasapis, T. C.; Wibowo, A. C.; Chung, D. Y.; Freeman, A. J.; et al. Crystal Growth of the Perovskite Semiconductor CsPbBr$_3$: A New Material for High-Energy Radiation Detection. *Cryst. Growth Des.* **2013**, *13* (7), 2722–2727. https://doi.org/10.1021/cg400645t.

(396) Weidman, M. C.; Seitz, M.; Stranks, S. D.; Tisdale, W. A. Highly Tunable Colloidal Perovskite Nanoplatelets through Variable Cation, Metal, and Halide Composition. *ACS Nano* **2016**, *10* (8), 7830–7839. https://doi.org/10.1021/acsnano.6b03496.

(397) Dou, L.; Wong, A. B.; Yu, Y.; Lai, M.; Kornienko, N.; Eaton, S. W.; Fu, A.; Bischak, C. G.; Ma, J.; Ding, T.; et al. Atomically Thin Two-Dimensional Organic-Inorganic Hybrid Perovskites. *Science* **2015**, *349* (6255), 1518–1521. https://doi.org/10.1126/science.aac7660.

(398) Ramade, J.; Andriambariarijaona, L. M.; Steinmetz, V.; Goubet, N.; Legrand, L.; Barisien, T.; Bernardot, F.; Testelin, C.; Lhuillier, E.; Bramati, A.; et al. Fine Structure of Excitons and Electron–Hole Exchange Energy in Polymorphic CsPbBr$_3$ Single Nanocrystals. *Nanoscale* **2018**, *10* (14), 6393–6401. https://doi.org/10.1039/C7NR09334A.

(399) Martiradonna, L. Riddles in Perovskite Research. *Nat. Mater.* **2018**, *17* (5), 377–377. https://doi.org/10.1038/s41563-018-0072-y.

(400) Miyata, K.; Zhu, X.-Y. Ferroelectric Large Polarons. *Nat. Mater.* **2018**, *17* (5), 379–381. https://doi.org/10.1038/s41563-018-0068-7.

(401) Stranks, S. D.; Plochocka, P. The Influence of the Rashba Effect. *Nat. Mater.* **2018**, *17* (5), 381–382. https://doi.org/10.1038/s41563-018-0067-8.

(402) Fleig, J.; Kubicek, M. Light May Harm or Help. *Nat. Mater.* **2018**, *17* (5), 389–391. https://doi.org/10.1038/s41563-018-0052-2.

(403) De Angelis, F.; Petrozza, A. Clues from Defect Photochemistry. *Nat. Mater.* **2018**, *17* (5), 383–384. https://doi.org/10.1038/s41563-018-0069-6.

(404) Katan, C.; Mohite, A. D.; Even, J. Entropy in Halide Perovskites. *Nat. Mater.* **2018**, *17* (5), 377–379. https://doi.org/10.1038/s41563-018-0070-0.

TOC graphic